Iridium-based synthetic ferrimagnets for spintronics

Thibaud Fache

To cite this version:

Thibaud Fache. Iridium-based synthetic ferrimagnets for spintronics. Physics [physics]. Université de Lorraine, 2020. English. NNT : 2020LORR0011 . tel-02863420

HAL Id: tel-02863420
https://hal.univ-lorraine.fr/tel-02863420v1

Submitted on 11 Jan 2022

THÈSE

pour l'obtention du titre de

DOCTEUR DE L'UNIVERSITÉ DE LORRAINE

SPÉCIALITÉ : PHYSIQUE

présentée et soutenue publiquement par

THIBAUD FACHE

le 2 mars 2020

Iridium-based synthetic ferrimagnets for spintronics

Matériaux ferrimagnétiques de synthèse à base d'iridium pour l'électronique de spin

---

Jury

Mme Liza Herrera Diez	Chercheuse CNRS – C2N Université Paris Saclay	Rapporteur
Mme Claire Baraduc	Chercheuse CEA – SPINTEC CEA Grenoble	Rapporteur
M. Michel Viret	Chercheur CEA – LNO CEA Paris Saclay	Examinateur
M. Pietro Gambardella	Professeur – ETH Zürich	Examinateur
M. Stéphane Mangin	Professeur – Université de Lorraine	Directeur de thèse
M. Sébastien Petit-Watelot	Maître de conférences – Université de Lorraine	Co-directeur de thèse

Institut Jean Lamour
UMR 7198 – Université de Lorraine
Département de Physique de la Matière et des Matériaux

Contents

Remerciements

Le travail publié dans le présent manuscrit a été rendu possible par le concours de nombreuses personnes. J'aimerais tout d'abord remercier les membres du jury, Liza Herrera Diez, Claire Baraduc, Pietro Gambardella et Michel Viret, qui ont accepté d'évaluer mon travail, et dont les nombreux commentaires, tant sur le manuscrit que lors des discussions scientifiques, ont été pour moi autant de clefs de compréhension et de connaissance.

Je dois également le succès de ma thèse de doctorat à un encadrement de grande qualité. Stéphane, tu as été au cours de ces années, d'abord d'études aux mines et de stage à New York, puis pendant ma thèse, un guide avisé et présent. Que ce soit pour la recherche ou la course à pied, quel coach formidable !

Sébastien, ta grande curiosité et ta patience m'ont permis d'aborder des domaines scientifiques vastes et variés. Je te remercie d'avoir passé du temps à maniper avec moi, et de m'avoir expliqué tant d'éléments de science, dans une ambiance toujours rigoureuse et constructive, mais sereine et conviviale !

Je tiens également à faire part de ma gratitude envers les membres de l'entreprise Vinci Technologies. En particulier, merci à Renaud Presberg qui m'a fait confiance pour réussir cette thèse, ainsi qu'à Jean Marcel Vannieuwenhuyse et Christine Walsh pour leur management souple et la liberté qu'ils m'ont donnée dans le cadre de mes activités. Je remercie également Emmanuel et Jean-Jacques, pour leur bon accueil et leur disponibilité de chaque instant. J'ai également une pensée spéciale pour Olivier Lerbet qui m'a en de nombreuses occasions apporté son expertise et a dépensé son temps sans compter pour m'aider à installer la PVD Vinci, et gérer les petits incidents techniques.

Je souhaite désormais remercier les membres de l'institut Jean Lamour qui m'ont grandement aidé au cours de ces trois années. Je suis en particulier reconnaissant envers Michel Hehn, qui a passé de nombreuses heures à m'enseigner l'art de la PVD et mille autres connaissances sur la croissance de matériaux. Je remercie également Carlos Rojas-Sánchez qui a également été très présent pour m'expliquer des concepts tant techniques que théoriques sur le SOT. Je tiens également à mentionner la précieuse aide des personnels de la salle blanche, Gwladys Lengaine, François Montaigne, Carlos et Laurent Badie qui m'ont permis de bénéficier d'équipements de grande qualité, ainsi que Danielle Pierre, Ludovic Pasquier, David Pilloud, et Alexandre Bouché qui ont été d'un soutien précieux en de nombreuses occasions, dans la salle expérimentale dans laquelle j'ai passé tant de temps. Je remercie en particulier Laurent pour sa disponibilité et son excellent conseil sur les Bordeaux. Je remercie également tous les autres membres de l'équipe 101 qui m'ont aidé à un moment ou un autre, et qui ont été des collègues de travail agréables et disponibles : Stéphane Andrieu, Christine Bellouard, Olivier Copie, Karine Dumesnil, Hélène Fischer, Isabelle Fournelle, Jon Gorchon, Thomas Hauet, Julius Hohlfeld, Daniel Lacour et Grégory Malinowski.

I would like also to thank Jieiy Liu for the time spent working with me and introducing me to Cambridge student's life during my short stay, Heisemberg Tarazona who could reproduce every of my experiments through impressive simulations, and the team of Roman Morgunov, with whom it is always a pleasure to work and interact!

Je tiens également à mentionner le soutien moral que j'ai obtenu d'Aurore Calmels et Sylvie

Robert, qui ont toujours une parole bienveillante et motivante dans les moments de doute. Merci !

Cette thèse n'aurait pas été la même sans la bonne entente entre jeunes, thésards, postdocs... qui a régné dans le labo. Je tiens donc à remercier Sarah, Christopher, Ludovic, Guillaume, Vincent et Arnaud pour les bons moments passés à faire du tennis ou des pauses café, ou encore de la pétanque. Je suis également reconnaissant envers Sébastien, Catalina, Thiago, Dominique, Huyen, Julien, Aurelia pour le soutien permanent et le bon esprit dans lequel nous avons partagé tant de bons moments. Je remercie également Yassine, Marion, Gauthier, Huyen, Kaushalya, Junta, Fan, et Boris, avec lesquels j'ai eu l'opportunité de partager un bureau et des instants de partage intellectuels et alimentaires. Je pense également à mes collègues de conférence Charles, Thai-Ha, Maryam, Jean-Loïs, Gauthier, Boyu et Yong. Je tiens également à remercier Kosseila, avec qui il faudra bien qu'on se départage un jour autour d'un échiquier.

D'un point de vue plus extérieur à mon travail de thèse, je remercie tous ceux qui m'acceptèrent comme colocataire ou hôte au cours de ces années Nancéennes : en particulier Charlie et Vincent, puis Marion, Alexandre et Pierre (malgré des incidents de machine à laver, *fluctuat nec mergitur* !), Philippe (les soirs de chant) et enfin Kathleen et Miguel, pour la fin de la fin. Vous avez été, par votre patience bienveillante, la source de ma sérénité et de mon savoir être lorrain.

Merci également à ma deuxième maison d'accueil lyonnaise constituée de Célia, Cat, Vincent, Estelle et Joe, et agréablement complétée de Loreena, Simon et Gabriel.

J'ai également une pensée pour mes supporters nantais, en particulier Benoît, Pauline, Héloise, Christopher, Jean, Marine, Bruno et Simon.

Pour finir, un grand merci à ma famille qui me soutient et m'encourage depuis tant d'années malgré mon exil en terres orientales.

Introduction

Since the beginning the 1960's, the information storage has gathered the interest of a large part of the scientific community. From the use of punch cards at the very beginning to hard disk drives, the technological improvement in this industrial field have been outstanding, with an exponential increase of the mass storage per surface unit, the decrease of the cost of memory, and the enhancement of reading and writing technologies. In the meantime, the needs for digital memory have skyrocketed due to the multiplication of numeric devices, and the development of the internet to such an extent that the challenge of improving the speed, the size, and the energy consumption of memory devices has never been harder to handle. In the past few decades, two crucial keystones have lead to the modern magnetic memories that are used nowadays: the discovery of giant magneto resistance, and the enhancement of the materials growth techniques. Let us present shortly these two major steps in the history of digital memories.

The main discovery that has been made in this field is undoubtedly the discovery of the giant magneto resistance (GMR) by Albert Fert [1] and Peter Grunberg [2]. Both researchers' teams found simultaneously this phenomenon that was awarded the Nobel Prize of Physics for the year 2007. The concept is based on the spin dependent transport in magnetic materials. In the GMR, the dependence is used as follows: in a magnetic multilayered structure, the electric resistance of the material depends on the respective orientations of the magnetisations of both magnetic layers. Indeed, a parallel configuration gives rise to a low resistance state in comparison with the antiparallel configuration, which leads to a high resistance state. This phenomenon is of major importance: the control by any means of one layer's magnetisation while the other one is pinned enables the control of the resistance state of the material. This step can be understood as the writing of a remanent information through the magnetic configuration of a multilayer. Independently, the resistance state is accessible by basic electric measurements that do not change the magnetic state of the magnetic system. This part can be interpreted as the reading of the information wrapped in the magnetic state. These two configurations accessible were largely used to code for magnetic information, with the lower and upper resistance states representing "0" and "1" digital bits. The discovery of GMR has lead to the rise of spintronics.

Additionally, some other scientific progress lead the researchers to be able to use practically this phenomenon in actual devices. The improvement of thin film deposition has been the key technological advance that lead to the growth of magnetic layers that were adequate for memory device fabrication. Indeed, many experimental techniques allow us to grow high quality thin films in the subnanometer scale. Amongst them, the magnetron sputtering is one of the most popular due to the reliability for the thicknesses grown, and the deposition rate.

In this scientific context, my Ph. D is the result of the collaboration between Vinci Technologies, one of the world's major companies in the field of ultra high vacuum deposition tools, and the Institut Jean Lamour, one of the leading laboratories in the domain of materials, nanomagnetism and spintronics. The company Vinci Technologies, major actor of the French and international industry, is divided in two main branches. One of its field of activities is the development of equipment for the oil extraction industry. The second main branch of Vinci Technologies is what was called Meca 2000 earlier. Its main goal is to provide the most efficient deposition and growth tools under ultra high vacuum for industrial purposes as well as for fundamental research applications. The success of the company, and the high precision of the equipment that is produced enabled the Institut Jean Lamour to fabricate efficiently high quality thin films, that enable an in-depth study of the properties of the magnetic sub-nanometer multilayers. In this frame, the Ph. D work that is presented here is the result of an academic/industrial fruitful collaboration that was funded by Vinci Technologies along with the ANRT (Association Nationale Recherche Technologie), in which the characterisation of the thin films grown on the tools provided by Vinci Technologies could lead to an optimisation of the growth devices.

VINCI
TECHNOLOGIES

Figure 1: Logo of the company Vinci Technologies

The experimental works presented in this manuscript correspond to experiments that were carried out on thin films that were deposited in the magnetron sputtering tool developed by Vinci Technologies, which chamber is presented on the figure 2.

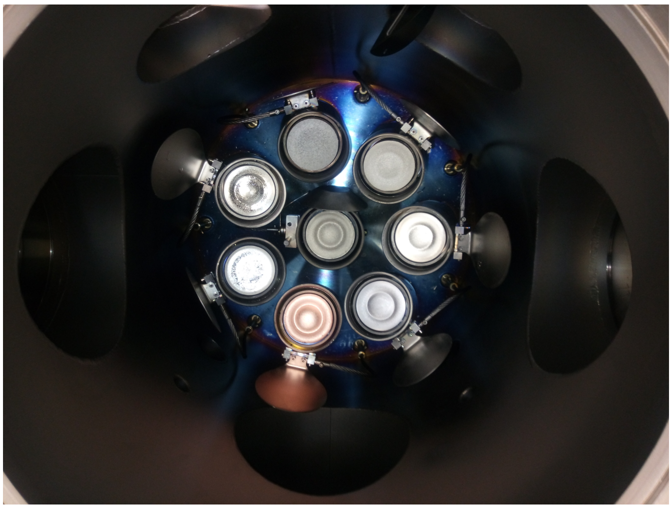

Figure 2: Top view of the inside of the sputtering chamber: we can distinguish eight 2-inch elemental materials targets, from which the thin films can be grown.

In that frame, Vinci Technologies' magnetron sputtering device provides ideal conditions for a high precision deposition. The quality of the thin films grown by magnetron sputtering is greatly impacted by the base vacuum reached in the chamber. The system that we are presenting can reach until 5×10^{-9} mbar, that is to say an order of magnitude lower than the adequate base pressure value. Furthermore, the number of targets that can be put in the chamber simultaneously (8) enable the growth of complex heterostructures, using all of these materials. We can also notice that many alloys can be grown using a co-sputtering process in which several targets are sputtered at the same time. Many magnetic alloys were deposited beyond the scope of this manuscript: we can especially mention the binary magnetic alloy Co_xTb_{1-x} [3, 4], or the ternary magnetic alloy $GdFeCo$. The precision of the composition that can be achieved is the percent of atomic composition, leading to a great reliability in the quality of the depositions made.

The quality of the deposition that is reached nowadays provides easy means to study very thin films, in which many interfacial effects like surface anisotropies or indirect exchange coupling can be used and optimised (as shown in this manuscript). This was one of the last technological bottlenecks that needed to be overcome to develop new spintronics concepts.

In this context, S. S. Parkin and his research group in IBM have proposed a new architecture concerning the random access magnetic memories (MRAM), called “racetrack memory” [5], involving new paradigms. Instead of displacing a reading head over a hard drive where the information is written, the magnetic information is coded by small domains that can be displaced by electric means towards the reading head that is fixed, as shown in figure 3. Therefore, the information is coded in a sequential way, and the writing of the information can occur at the same time as the reading, but in a different location.

This new method would present numerous advantages. First, it would avoid any mechanical motion during the reading and writing of the information. Indeed, the information is displaced through the circuit, and there is no need to displace the reading head to the relevant bit to access the information. Furthermore, this new technology relies on spin current generation and spin torques acting on the magnetisation, which could lead to a small loss of energy by Joule effect. This could lead to an energetic efficiency of the devices that could improve the energy consumption from what is currently used. Eventually, in the best case, this memory could be achieved in a three dimension geometry, by choosing adequately the architecture of the racetrack. As a consequence, racetrack memories could be a way to increase significantly the magnetic memory storage density.

A comparative study of the racetrack memory and spin transfer torque magnetic random access memory (STT MRAM) has been carried out in [6], which enlightens the numerous improvements that could be obtained thanks to racetrack memory. The features compared are the size, the energetic consumption and the system efficiency, and both criteria are considerably enhanced in the case of racetrack memory, which advocates for a further study in this field.

However, he concept of racetrack memory can thrive only if several technological challenges can be overcome. This application needs at least two types of materials: a magnetic material which magnetisation is supposed to contain the digital information, and a material that can generate a spin current so as to manipulate the magnetisation of the latter. Therefore, the study of both materials is the first step to the success of a device.

Parkin came up with the concept of racetrack memories in a certain context. Current-induced domain wall motion had been predicted for decades by Berger [8–11], Slonczewski [12, 13], Zhang and Li [14], and Tatara and Kohno [15]. These theoreticians had understood that an electric current can act on the magnetisation and magnetic domains through angular moment and spin transfer torques, which was the first step towards applications and experimental exploration. Later, numerous studies concerning current-induced domain wall motion were carried out, showing a dramatic enhancement of the domain wall motion by adding current to an applied magnetic field [16, 17] and current-induced domain wall motion without any applied magnetic field [18–20], leading to a record current-induced domain wall speed of 110 $m.s^{-1}$ [21]. The progress made on the topic was quick, with a first proof of creation and displacement of a series of domain walls with current pulses of a few tens of nanoseconds was achieved in 2008 by Hayashi, Parkin *et al.* [22]. Numerous studies followed, achieving current-induced domain wall motion thanks to spin torques, with Rashba effect [23], chiral spin torques [24, 25]. These scientific advances have lead Parkin's research group to patent numerous technological applications, starting from the depinning of domain walls using current pulses [26, 27], a unidirectional racetrack memory device [28] (for which new possibilities by means of Dzyaloshinskii–Moriya interaction were investigated later by [29]), magnetic racetrack memory devices in an undulating energy landscape [30, 31]. Later, with the discovery of incredible current induced domain wall speeds in synthetic ferrimagnets, IBM also patented domain wall motion in multilayers [32] and more especially synthetic ferrimagnets [33], and eventually spin current switcheable memory elements and their integration and fabrication [34]. An article was published later to announce

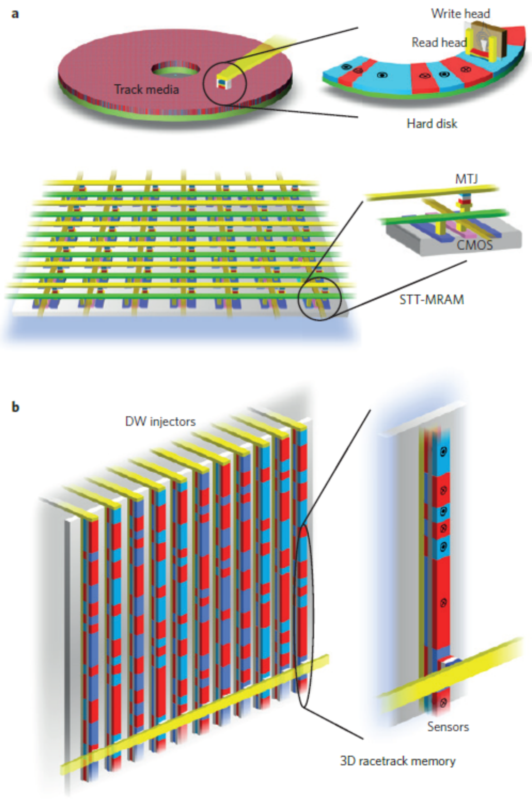

Figure 3: (**Excerpt from** [7]) Schematic and concept of magnetic memories: (a) top: representation of a hard disk: the information is written in the orientation of the magnetisation in domains, and a sensor can read the corresponding information; bottom: representation of a spin transfer torque Magnetic Random Access Memory (MRAM). (b): detailed view of the reading/writing parts of a racetrack memory: the information is coded in the orientation of magnetic domains that can be moved towards a sensor without any mechanical means. In all these images, the orientation of magnetisation within domains is represented by the colours red and blue.

the fabrication of highly efficient domain wall injectors, that would thus be the writing part of the racetrack memory in [35].

This field of research was also very trendy amongst other research groups worldwide, with some studies about the fabrication and the feasibility of racetrack memory of small dimensions, around 40nm [36], and also the implementation of racetrack memory with perpendicular magnetic anisotropy [37]. We can especially notice that the CoFeB alloy was temporarily considered to be the magnetic material carrying the information of the racetrack memory in nanowires [38, 39].

Furthermore, the propagation of magnetic domain walls thanks to the spin currents is the driving force of the magnetic memory cell that we plan to achieve. This phenomenon can be optimised through a deep and thorough materials study, involving numerous properties of thin multilayers. Lately, huge improvements have been achieved through the introduction of new types of magnetic heterostructures, called synthetic ferrimagnets. Especially, the research group of S. Parkin has investigated the magnetic domain wall propagation in ruthenium-based synthetic ferrimagnets, achieving a record speed of 750 $m.s^{-1}$ [40]. During the Ph.D that is presented in this manuscript, higher domain wall speeds have even been observed in nearly compensated ferrimagnets [41], setting the new speed record to 1.3 $km.s^{-1}$.

In the most recent articles concerning racetrack memories, the latest alternative is to change the magnetic object representing the magnetic information. Instead of displacing domain walls, Geng and Jin [42] proposed to displace magnetic vortices, which are magnetic structures that can be stabilised and displaced with current. In line with this, the intensive study of magnetic skyrmions has lead to the possibility to use this topologically protected magnetic configuration to be propagated in racetracks using current pulses or voltage control [43–46]. In this frame, the article of [41] also proposes the displacement of magnetic skyrmions in racetracks, pointing out the enhancement that would be enabled by using this new magnetic object.

Even though the most promising ways to improve racetrack memory seems to be the study of current-induced skyrmions motion, we have not explored this horizon, neither did we have time to perform current-induced domain wall propagation studies. The aim we focused on in this manuscript is the behaviour of similar heterostructures to those that were used by Parkin's team (that is to say ruthenium-based synthetic ferrimagnets), by replacing ruthenium with iridium. This choice is motivated by similar properties of iridium and ruthenium concerning the synthetic ferrimagnetic structure, as shown in [47,48] and a better spin current generation in iridium than in ruthenium, which would lead to more efficient racetrack memories. The conclusions that could be drawn from literature concerning the spin current generation in iridium and ruthenium before our works are scarce, due to very little experimental results in iridium [43, 49], and absolutely no results for ruthenium. However, the spin current generation depends directly on the spin orbit interaction, which is known to be linked to the atomic number as $(Z - Z_0)^4$ [50]. The same dependence has been shown for the charge-to-spin conversion efficiency [51],

Therefore, the problematic of this manuscript is the study of iridium-based synthetic ferrimagnets by characterising on the one hand magnetic properties of the stacks, and on the other hand, the spin current generation and transport in iridium so as to optimise the domain wall propagation conditions in these structures. Thus, the results of this manuscript are organised in the following way: in the first chapter, we present the relevant properties of the two types of materials that are needed for a racetrack memory. Then, for the magnetic materials, we describe the macrospin approximation through which we interpret several of our results, as well as the magnetisation dynamics equations that rule the magnetisation behaviour in our samples. The non magnetic materials are presented with the spin current generation effects, as well as the indirect exchange that they can provide. Eventually, we display relevant results already obtained in the literature for the current-induced domain wall motion, and we use these to justify the synthetic ferrimagnetic heterostructure of the samples that we chose to study.

The second chapter is devoted to the presentation of experimental techniques and setups that are used in order to establish the results presented in the manuscript. First, we present the main experimental technique used to grow ultra thin layers with a great quality and purity of the materials. Then, we show the methods that can be used to measure a magnetic hysteresis loop of a material, especially vibrating sample measurements and magneto-optical microscopy. Eventually, we describe two methods that can lead to the determination of spin transport parameters of a material through ferromagnetic resonance, namely the spin transfer torque and spin pumping ferromagnetic resonances. We provide a deeper understanding of the undelying physics of these experimental methods in the fourth chapter.

In the third chapter, we show the results of the magnetic study of synthetic ferrimagnets that we grew thanks to a magnetron sputtering equipment. We characterise first the magnetic properties as a function of the thickness of ferromagnetic and non magnetic layers. Afterwards, we modify the macrospin model used until then to add the temperature as a new parameter, and study the synthetic ferrimagnets magnetic behaviour as a function of the temperature. We distinguish in particular three main regimes corresponding to the magnetic transitions and accessible magnetic states by sweeping the magnetic field. Eventually, after presenting literature results about field-induced magnetic domain wall motion on synthetic ferrimagnets, we disclose the results of an in-depth experimental study of the magnetic relaxation on such materials, so as to explore new non monotonic magnetic relaxation that can occur at the limits between the two temperature regimes observed earlier. We find especially unusual non monotonic time dependence magnetisations that we are able to understand using a two spin model presented in the previous chapter.

The fourth chapter is devoted to the spin currents in a non magnetic material due to direct and inverse spin Hall effects (SHE). We first introduce two wide spread ferromagnetic resonance techniques to probe the SHE: spin torque and spin pumping ferromagnetic resonances (ST-FMR and SP-FMR). Then, we present an extensive study of the ferromagnetic resonance using the most general framework possible: spherical coordinates and an arbitrary energy density to take into account various interactions. We use the results displayed here to make an accurate comparison between ST- and SP- FMR, and provide general formulas, as functions of the geometry of the experimental setup, in order to provide at the end of this chapter a comparative analysis of the spin Hall effect in iridium and platinum.

Despite the fact that we did not treat skyrmion racetrack memory in this manuscript, let us point out that the works that have been carried out can still be transposed to any magnetic object carrying a magnetic information in a racetrack memory. Indeed, as long as the means through which the magnetic objects motion is controlled is mainly the spin currents, obtained by spin orbit torques, the results proposed in this manuscript can be used. Furthermore, it is relevant to notice that beyond this scope, synthetic antiferromagnetics spintronics is still a vivid research field [52], for which many contributions are expected for the next decade.

Résumé

Les technologies de l'information ont toujours eu une place stratégique dans les sociétés humaines. Depuis l'avènement de l'écriture, la transmission des savoirs et des idées à grandes échelles spatiales et temporelles est possible. En conséquence, les progrès des connaissances ont connu une évolution exponentielle, entre autres grâce à l'amélioration continue des technologies de l'information. Si, dans les premiers temps, celle-ci a été rendue possible grâce à des papyrus ou des tablettes d'argile dans le bassin méditerranéen au cours de l'Antiquité, l'invention de l'imprimerie par Gutemberg au XV^e siècle a permis un de réaliser un saut technologique qui ne fut surpassé que plusieurs siècles plus tard, avec le développement des technologies magnétiques au XX^e siècle. Après les bandes magnétiques, furent utilisées des supports numériques que nous connaissons aujourd'hui, comprenant entre autres les disques durs et clefs USB. Aujourd'hui omniprésents, de tels objets d'utilisation courante sont issus d'un travail de recherche de longue haleine, partant de la révolution quantique du début du siècle dernier jusqu'à des découvertes telles celle de la magnétorésistance géante, qui valut à Albert Fert et Peter Grunberg le prix Nobel de physique en 2007.

Ce domaine industriel et scientifique est à l'heure actuelle encore très actif : depuis les années 1960, les progrès ont permis de maintenir une augmentation des performances, tant en termes de densité de stockage de l'information que dans le prix par unité de mémoire, à un rythme exponentiel, connu sous le nom de loi de Moore. Aujourd'hui, si les préoccupations de taille et de coût sont encore importantes, les limites physiques de la miniaturisation sont en passe d'être atteintes, et les progrès futurs sont vraisemblablement amenés à considérer l'utilisation de la troisième dimension, par opposition avec les systèmes plans que l'on utilise encore actuellement.

Historiquement, la découverte du magnétisme remonte au moins à l'Antiquité. On attribue généralement à Thalès de Millet et Aristote les premières discussions scientifiques concernant le magnétisme, au V^e siècle avant notre ère. Par ailleurs, les propriétés magnétiques des matériaux furent utilisées largement pendant le Moyen Âge, notamment à travers l'usage des boussoles dans le domaine de la navigation. Les explorateurs constatent à travers cela la rémanence magnétique, c'est-à-dire d'une certaine façon, le stockage d'une information correspondant à la position du pôle magnétique nord du globe terrestre. Bien qu'alors, les humains étaient plus enclins à donner des interprétations mystiques que scientifiques au magnétisme, l'observation et l'expérience de ces phénomènes était établie.

Ce n'est qu'avec l'avènement de la physique quantique, et en particulier la découverte du spin de l'électron comme quantité intrinsèque sans analogue classique, qu'un formalisme scientifique rigoureux permet d'appréhender le magnétisme. Ainsi, les découvertes s'enchaînent, et les modèles proposés pour expliquer les comportements des différents matériaux sont de plus en plus précis. On observe notamment le ferrimagnétisme et l'antiferromagnétisme dont les preuves expérimentales étaient plus difficiles à soupçonner que dans le cas du ferromagnétisme.

Les avancées dans le domaine de la croissance des matériaux permettent dès les années 1960 de songer à réaliser des mémoires magnétiques en utilisant des aimants de petites dimensions. L'aimantation est alors manipulée avec des champs magnétiques, et l'information est codée par l'orientation de l'aimantation. Pour la lecture de l'information, le phénomène physique qui est utilisé couramment de nos jours est la magnétorésistance géante : une alternance d'orientations

de l'aimantation induit une résistance plus forte qu'une succession de couches avec des aimantations alignées dans la même direction. Ce phénomène physique de la plus haute importance est découvert en 1988, et permet le développement du disque dur.

Les avancées dans les technologies de l'information ne sont rendues possible que du fait d'une amélioration vertigineuse des techniques de croissance des matériaux en couches minces qui s'opèrent dans le même temps. Les possibilités offertes par le dépôt par voie physique, notamment la pulvérisation cathodique magnétron, permettent entre autres de réaliser des dépôts de matière de haute qualité avec des hauteurs très faibles, ce qui permet de réduire les épaisseurs jusqu'à des échelles nanométriques.

Cette technologie fait également surgir des effets de surface et d'interfaces qui ne sont visibles que dans des systèmes à très faible épaisseur. On utilise donc les propriétés de matériaux qui sont quasiment en deux dimensions. Parmi les nombreux effets étudiés en particulier dans ce manuscrit, on peut citer en particulier les anisotropies magnétocristallines de surface, qui permettent en particulier d'obtenir des systèmes dont l'aimantation est perpendiculaire au plan de dépôt de la couche mince, et également le couplage RKKY (du nom des découvreurs Ruderman, Kittel, Kasuya et Yosida), permettant de maîtriser l'influence de deux couches adjacentes l'une sur l'autre.

Enfin, à la suite de travaux théoriques prédisant la possibilité de manipuler l'aimantation à l'aide de courants polarisés en spin dans les années 1970, en particulier grâce à des couples de transfert de spin, les progrès techniques ont engagé des recherches expérimentales dans cette direction. Les expériences et théories mettant en jeu des courants électriques polarisés en spin constituent à elles seules une nouvelle branche de la physique, nommée électronique de spin ou spintronique. Une nouvelle étape a été franchie avec la découverte de purs courants de spin, ne mettant plus en jeu de déplacement d'électrons, et diminuant d'autant les pertes énergétiques par effet Joule. La génération de ce type de courants a été portée entre autres par les techniques de pompage de spin, liées à la dynamique de l'aimantation, champ de la physique un peu plus ancien, déjà exploré dans les années 1940.

Pour la spintronique, la diminution des dimensions a été l'un des plus importants leviers de développement, puisque l'une des particularités de cette branche de la physique est d'utiliser un courant polarisé en spin pour agir sur l'aimantation d'un matériau magnétique. Un des enjeux expérimentaux était donc la densité de courant polarisé qui était nécessaire pour parvenir à des expériences concluantes. La faible taille des matériaux magnétiques sur lesquels on souhaitait agir était également un prérequis, pour minimiser l'amplitude des couples à appliquer à l'aimantation. Les premiers articles théoriques parlaient de plusieurs ampères pour observer une interaction entre l'aimantation et les courants, ce qui était absolument inenvisageable en l'état. La miniaturisation a donc eu également le bénéfice de permettre l'avènement de l'électronique de spin dans les années 1990.

Cette génération de courants de spin est actuellement un sujet actuel dans le domaine du nanomagnétisme, et les expérimentateurs d'évertuent à synthétiser les matériaux les plus prometteurs à cet effet, dans le but de réaliser des dispositifs d'électronique de spin plus performants, et moins gourmands en énergie. Dans ce cadre, la comparaison entre différents matériaux est un sujet épineux du fait de la variété des méthodes expérimentales permettant de mesurer les propriétés de transport de courant de spin des matériaux. Il est en effet notoire que les valeurs obtenues par différents groupes de recherche dans le monde peuvent varier de plus d'un ordre de grandeur, malgré des conditions expérimentales censées être quasiment identiques. Malgré l'affinement progressif des modèles, certaines hypothèses ne sont pas encore questionnées, et ce manuscrit en adresse certaines par un examen précis de deux techniques expérimentales, comme précisé ci-dessous.

Dans ce cadre technologique et académique, l'entreprise Vinci Technologies a pris un rôle moteur, en étant à la pointe de la réalisation d'équipements de dépôts de matériaux de hautes performances. Scindée en quatre divisions principales, cette entreprise a en effet incorporé la société MECA2000 pour en faire sa division “Thin film deposition – Ultra high vacuum – Nanotechnology”, ce qui lui permet d’être un acteur majeur du domaine, proposant des équipements destinés tant aux industriels qu’aux établissements académiques. En maîtrisant les technologies de l’ultra vide, ainsi que les techniques de croissance des matériaux, cette compagnie est capable de produire parmi les meilleurs équipements de pulvérisation magnétron disponibles sur le marché.

Du fait de cette position particulière, l’entreprise Vinci Technologies a financé, avec l’aide de l’Agence Nationale Recherche Technologie (A.N.R.T.) la thèse présentée dans ce manuscrit, dans le but d’optimiser les outils de dépôt de matériaux pour l’électronique de spin, notamment pour le dépôt de terres rares comme le gadolinium et le terbium. Ce travail de recherche et développement d’outils de pointe a une visée double. D’une part, il permet d’accroître la qualité des moyens dédiés à la recherche académique dans des domaines de pointe, et d’autre part, il permet d’obtenir des qualifications d’un outil utilisé de manière habituelle dans un cadre industriel, du fait de la bonne connaissance du procédé, de sa fiabilité et de sa précision.

Le cadre technologique plus spécifique dans lequel s’inscrit ce travail de doctorat est celui des mémoires de type racetrack. Cette alternative technologique consiste à réaliser une technologie de stockage de l’information basée sur le déplacement de parois magnétiques. Introduite par l’équipe de recherche de Stuart Parkin dans les années 2000, cette méthode présente plusieurs avantages. Tout d’abord, un déplacement de l’information contenue dans une structure magnétique telle une paroi de domaine permet d’éviter les déplacements mécaniques qui existent dans les systèmes actuels, où l’information est localisée, et le lecteur d’information doit se déplacer jusqu’à la cellule d’information pour la lire. Il est également notable que cette technologie fonctionnerait principalement par l’action de couples sur l’aimantation par de purs courants de spin, n’impliquant pas de déplacement de charges. De ce fait, la dissipation d’énergie par effet Joule serait limitée, ce qui améliorerait sensiblement l’efficacité énergétique des dispositifs. Enfin, l’une des plus grandes forces de cette innovation est la possibilité, à terme, d’utiliser les trois dimensions, pour peu que l’on soit capable de réaliser une piste sur laquelle propager une structure magnétique sur une surface non plane. De la sorte, les problématiques de densité de stockage de l’information trouveraient une solution idoine.

Les travaux réalisés sur la propagation de parois magnétiques dans des couches minces ont permis de déterminer que les matériaux dits ferrimagnétiques de synthèse faisaient partie des candidats les plus prometteurs pour les mémoires magnétiques de type racetrack. Ces matériaux sont constitués de deux couches minces magnétiques séparées par une fine couche d’un matériau donnant lieu à un couplage indirect entre les deux couches magnétiques.

Dans ce manuscrit, nous avons exploré les propriétés des matériaux ferrimagnétiques de synthèse dans lesquels l’iridium a été choisi pour séparer deux couches magnétiques de cobalt dans un système à aimantation perpendiculaire. L’intérêt que nous portons dans ce cas à l’iridium est dû à plusieurs éléments. D’une part, l’iridium est connu pour la grande amplitude de couplage indirect qu’il offre quand il est placé entre deux couches magnétiques. Il est donc aisé de réaliser des matériaux ferrimagnétiques de synthèse à base d’iridium. D’autre part, l’iridium permet de promouvoir l’aimantation perpendiculaire dans les interfaces avec le cobalt, ce qui nous donne un couple de matériaux satisfaisants pour lancer notre étude. Enfin, l’iridium a une grande valeur de couplage spin-orbite, ce qui permet d’envisager que c’est un matériau de choix pour la génération de purs courants de spin. Ce serait donc une brique triplement active dans les multicouches que nous souhaitons étudier. Nous proposons donc une étude des matériaux ferrimagnétiques de synthèse visant à caractériser le potentiel de ces matériaux à réaliser des mémoires magnétiques de type racetrack, et d’une manière plus générale, leurs propriétés pour l’électronique de spin.

Dans un premier chapitre, nous présentons des concepts de base de nanomagnétisme permettant une bonne compréhension des problématiques traitées dans le reste du manuscrit. Nous donnons entre autres des résultats bibliographiques pour positionner notre étude dans le cadre de la recherche actuelle. En particulier, après un rappel des notions de moment magnétique et d'aimantation, nous présentons une représentation des interactions magnétiques en utilisant un formalisme de densités d'énergie, puis en déduisons les structures magnétiques que l'on peut trouver dans un matériau ferromagnétique classique (comme des parois de domaine), ainsi que dans le cas d'un matériau ferrimagnétique de synthèse.

À partir de cela, nous caractérisons un système modèle de matériau ferrimagnétique de synthèse à base d'iridium optimisé pour l'application de mémoires magnétiques de type racetrack. Nous donnons des spécifications concernant les champs magnétiques de renversement de l'aimantation dans une configuration de cycle magnétique avec champ appliqué dans un axe de facile aimantation. Cette étude sert de base au chapitre suivant, dont l'objet est entre autres la réalisation expérimentale de ce système modèle.

Le deuxième chapitre est consacré à la description de techniques expérimentales utilisées pour obtenir les résultats présentés dans le manuscrit. Nous décrivons tout d'abord la pulvérisation cathodique magnétron, méthode de dépôt qui a permis la croissance de tous les échantillons étudiés. Nous présentons également les différentes méthodes permettant de réaliser une courbe d'aimantation, mesude sur laquelle sont basés les résultats du troisième chapitre. Enfin, nous décrivons deux méthodes permettant de mesurer les propriétés de transport de spin des matériaux, la résonance ferromagnétique par couple de transfert de spin, et par pompage de spin. Nous revenons plus en détail sur les phénomènes physiques mis en jeu dans le quatrième chapitre.

Dans le troisième chapitre, nous présentons les résultats relatifs à la croissance de matériaux ferrimagnétiques de synthèse. Nous nous intéressons particulièrement à l'optimisation de l'épaisseur des différentes couches constitutives du matériau, dans le but de réaliser un système modèle possédant a priori les meilleures propriétés pour des applications de mémoires magnétiques de type racetrack. Nos résultats permettent d'étudier l'influence de plusieurs paramètres de cette hétérostructure, et permettent d'obtenir des conditions de croissance optimales en termes de propriétés magnétiques en vue de réalisation de mémoires magnétiques de type racetrack. Ces résultats basés sur des mesures de cycles magnétiques dans des axes de facile aimantation donnent également un moyen d'établir des caractéristiques des matériaux déposés à l'aide du modèle de Stoner Wohlfarth.

Nous proposons ensuite la réalisation d'un diagramme d'état d'une hétérostructure ferrimagnétique de synthèse à base d'iridium en fonction du champ magnétique appliqué et de la température. Cette étude nous permet d'établir avec précision les conditions expérimentales et les paramètres matériaux souhaités pour obtenir un système modèle

Nous consacrons également une partie de ce chapitre à l'étude de la propagation de parois de domaines magnétiques sous champ dans les échantillons de matériaux ferrimagnetiques de synthèse réalisés. Des mesures de traînage magnétique sont réalisées en collaboration avec l'équipe de Pr. Roman Morgunov et celle de Pr. Crispin Barnes, qui utilisent entre autres des moyens de mesures magnétiques à basse température. Ces expériences font l'objet d'une découverte inattendue de transitions magnétiques non monotones, qui limitent le potentiel des hétérostructures réalisées en vue d'applications de mémoires racetrack. C'est cependant l'occasion de caractériser les hétérostructures de manière précise et d'obtenir un bon niveau de compréhension des phénomènes physiques mis en jeu. D'autres résultats expérimentaux sont également obtenus, portant notamment sur l'influence de la vitesse de balayage du champ (magnetic field sweeping rate) sur les transitions magnétiques obtensibles sur des matériaux ferrimagnétiques de synthèse.

Dans le quatrième et dernier chapitre, nous réalisons une étude comparative des techniques expérimentales de résonance ferromagnétique par pompage de spin et par couple de transfert de spin. En réalisant des calculs analytiques, nous proposons une analyse de la résonance ferromagnétique générale, en base sphérique, pour ne plus avoir à subir les limites des formules souvent proposées dans la littérature pour des géométries cartésiennes. Nous étudions en profondeur les aspects de symétrie usuellement évoqués dans le traitement de la résonance ferromagnétique par couple de transfert de spin et montrons dans quelle limite ces approximations sont valides.

Ceci nous conduit à envisager une autre méthode pour évaluer les propriétés de génération de courant de spin de l'iridium. Nous présentons en conséquence la méthode de résonance ferromagnétique par pompage de spin, pour laquelle nous détaillons les calculs qui permettent d'obtenir des résultats conformes à ce qui est présenté dans la littérature. Nous en déduisons une méthode robuste pour pouvoir étudier avec fiabilité la génération de courant de spin de manière comparative dans deux matériaux, ainsi que le transport de courants de spin au sein de ces matériaux. Nous choisissons d'appliquer cette méthode à l'iridium en comparaison avec le platine, matériau déjà étudié de manière extensive dans la littérature. En conclusion, nous observons que même si l'iridium est un matériau dont les propriétés de génération et transport de courant de spin sont très inférieures à celles du platine, celles-ci sont tout de même suffisantes pour envisager de les utiliser dans le cadre d'applications d'électronique de spin, en particulier parce que ces performances s'ajoutent à des propriétés de couplage d'échange indirect et d'anisotropie magnétocristalline.

Bien que ce travail s'inscrive dans la recherche et le développement de la technologie de mémoires magnétiques de type racetrack, le présent travail ne rend pas compte d'expériences de propagations de parois magnétiques induites par courant. Ces expériences seront l'objet de travaux futurs réalisés dans l'équipe d'électronique de spin et de nanomagnétisme de l'institut Jean Lamour de Nancy.

Chapter I

A few useful concepts of magnetism

I.1 Introduction

This chapter aims at two main purposes. First, we are presenting the main physical notions that are useful for the understanding of the rest of this manuscript. Then, we want to describe the chronological advances concerning the domain wall motion in magnetic materials that lead us to consider for this manuscript the study of iridium-based synthetic ferrimagnets amongst all the magnetic heterostructures that can be grown in 2020.

This chapter is divided in three main parts. First, we describe the magnetic interactions that govern the properties of the multilayers that we study. Then, we present the equations Landau-Lifshitz-Gilbert (LLG) and Landau-Lifshitz-Gilbert-Slonczewski (LLGS) that rule the magnetisation dynamics, and the main ways to describe the different terms involved. Afterwards, we display a study of a ferromagnet behaviour as a function of a static applied magnetic field, using a Stoner Wohlfarth description. Using these results, we present previous studies that focus on the field and current induced domain wall motion in ferromagnetic layers, and especially the Walker breakdown phenomenon. Eventually, we disclose predictions and experimental results of current induced domain wall propagation in synthetic ferrimagnets extracted from the literature, which encourages us to choose this type of materials as a good candidate for current induced domain wall propagation. Therefore, we finish this chapter by presenting a field study of a synthetic ferrimagnet by using a 2-spin model inspired from the usual Stoner Wohlfarth approach.

I.2 Magnetic moment and interactions

Magnetised matter is subjected to numerous interactions that generate various specific behaviours and properties. In this section, we first introduce the concept of magnetisation, and then we select the most relevant magnetic interactions present in magnetic thin films and multilayers.

I.2.1 Magnetic moment of an atom

Within the matter, electrons can be characterised partly by two quantities: their angular moment $\boldsymbol{L}$ and their spin moment $\boldsymbol{S}$, to which we associate the corresponding operators $\hat{\boldsymbol{L}}$ and $\hat{\boldsymbol{S}}$. The angular moment of the electron is defined in an analogous way to the classical angular moment as a function of the position $\hat{\boldsymbol{r}}$ and impulsion $\hat{\boldsymbol{p}}$ operators, that is to say as $\hat{\boldsymbol{L}} = \hat{\boldsymbol{r}} \times \hat{\boldsymbol{p}}$. Since the electron is a charged particle, the operator corresponding to this magnetic moment, called orbital magnetic moment, is expressed as:

$$\hat{\boldsymbol{\mu}}_L = -\mu_B g_L \hat{\boldsymbol{L}}$$

Where μ_B is the Bohr magneton defined as $\mu_B = \frac{e\hbar}{4\pi}$, and g_L is the orbital Landé factor, equal to 1. However, the spin magnetic moment $\boldsymbol{S}$ cannot be understood in terms of classical physics. This quantity is an intrinsic kinetic moment that was evidenced by Stern and Gerlach in 1922, and give rise, in an analogous way to the angular momentum, to a magnetic moment as follows:

$$\hat{\boldsymbol{\mu}}_S = -\mu_B g_S \hat{\boldsymbol{S}}$$

where g_S is the spin Landé factor, approximately equal to 2 for the electrons. Then, the operator corresponding to the local magnetic moment carried by an atom $\hat{\boldsymbol{\mu}}_{at}$ corresponds to the composition of the orbital and spin magnetic moments of all the electrons composing the atom:

$$\hat{\boldsymbol{\mu}}_{at} = \sum_{e^-} (\hat{\boldsymbol{\mu}}_L + \hat{\boldsymbol{\mu}}_S)$$

The expected value of the magnetic momentum of an atom can thus be represented as a function of the wave function representing the system ψ as: $\boldsymbol{\mu}_{at} = \langle \psi | \hat{\boldsymbol{\mu}} | \psi \rangle$. We can then define the magnetisation $\boldsymbol{M}$ of a material. This quantity is a local value that represents the amount of magnetic moment per unit volume. Let us call l_{ex} the typical length at which the interactions between two magnetic moments vanish. We can define the local magnetisation at a position $\boldsymbol{r}$ as the volume average of magnetic atomic momenta in the vicinity of volume Ω of $\boldsymbol{r}$

$$\boldsymbol{M}(\boldsymbol{r}) = \frac{1}{\Omega} \sum_{\boldsymbol{\mu}_{at} \in \Omega} \boldsymbol{\mu}_{at}$$

Another quantity of interest is the saturation magnetisation M_S. It corresponds to the value of the magnetisation that can be observed when all the moments are aligned in the same direction. Since this quantity depends on the electrons carried by the atoms, this quantity is constant in homogeneous materials. In that case, it can be defined simply as:

$$M_S = \max ||\boldsymbol{M}||$$

Furthermore, in the cases where all the atomic magnetic moments are aligned, due for instance to an external field, or an exchange interaction, it can be convenient to consider the reduced magnetisation $\boldsymbol{m}$, that is to say the ratio between the magnetisation and the saturation magnetisation:

$$\boldsymbol{m} = \frac{\boldsymbol{M}}{M_S}$$

In this case, the reduced magnetisation is a unit vector, and it can be perfectly determined by the Euler angles (θ, φ) as long as the saturation magnetisation is known.

Now that we have defined the notion of magnetic moment and magnetisation, let us describe the various interactions that can affect the magnetisation within the matter in the cases that we study.

I.2.2 Energy and energy density

In the following, we present magnetic interactions that will play a role in the rest of this manuscript. However, two types of representation can be relevant: a local one, depending on the position considered in the material, and a total one, representing the behaviour of the whole system considered. In order to represent this in a proper way, we will introduce three notations. First, one can consider an elementary energy due to the interaction of two moments, or just one moment with external excitations. We will express this in terms of elementary energy δE, that is to say the energy of the interaction between two momenta, or between one momentum and an external excitation. Second, we can treat a large system as a continuous entity on which interactions can be represented using energy densities, that correspond to the volume average of the elementary energies in the vicinity Ω of the position considered. Let us note ε this energy density, which can be expressed as:

$$\varepsilon(\boldsymbol{r}) = \frac{1}{\Omega} \sum_{i \in \Omega} \delta E_i$$

Eventually, the total energy of the system can be considered, because it is usually what will determine the stability of a configuration. We can easily express it as a function of the energy density as:

$$E = \iiint_{System} \varepsilon(\boldsymbol{r}) d^3\boldsymbol{r}$$

Let us note that in the special cases where the energy density does not depend on the position, we can easily define the total energy of the system as: $E = \varepsilon V$ where V is the total volume of the system.

I.2.3 Heisenberg exchange interaction

The electrons spins of two neighbour atoms in a solid interact with each other by what is called the exchange interaction. This interaction is the result of the competition between two phenomena: Pauli's exclusion principle and the Coulomb interaction between electrons of the atoms considered. Pauli's exclusion principle does not allow two fermions (as electrons for instance) to be in the same quantic state. Furthermore, it forces the wave functions representing the electrons to be antisymmetric. The corresponding energy of a two-electron spin system S_1 and S_2:

$$\delta E_H = -J \boldsymbol{S}_1 \cdot \boldsymbol{S}_2 \tag{I.1}$$

In this expression, J is called the exchange integral and can determine the magnetic order in a material. If J is positive, a ferromagnetic order is favoured, whereas the opposite case leads to an antiferromagnetic order. The exchange interaction only lets small variation of the orientation between neighbour spins. In order to observe significant variations in the direction of the spin, one can use the continuous variable of the magnetisation, as long as one of the dimensions of the system at least is larger than the exchange length l_{ex}, which can be expressed as $l_{ex} = \sqrt{\frac{2A_{ex}}{\mu_0 M_S^2}}$ [53]. (In this expression, A_{ex} is the exchange stiffness, which can be determined depending on the symmetries and dimensions of the crystal considered). Under such hypotheses, one can take into account the difference of energy density between a configuration where all the spins are aligned and a configuration with a spin orientation varying with the position as follows [54, 55]:

$$\varepsilon_{Ex}(\boldsymbol{r}) = A_{ex}\left(\nabla \boldsymbol{m}(\boldsymbol{r})\right)^2$$

I.2.4 Zeeman interaction

The first magnetic interaction is the response of a magnetic moment $\boldsymbol{\mu}$ to an external applied magnetic field $\boldsymbol{H}$, called the Zeeman interaction. When subjected to a magnetic field, the magnetisation of a material tends to align with it, as does the magnetised needle of a compass along the Earth's magnetic field. This interaction is described by the Zeeman interaction:

$$\delta E_Z = -\mu_0 \boldsymbol{H} \cdot \boldsymbol{\mu} \tag{I.2}$$

Equivalently, one can consider the energy density:

$$\varepsilon_Z(\boldsymbol{r}) = -\mu_0 \boldsymbol{H}(\boldsymbol{r}) \cdot \boldsymbol{M}(\boldsymbol{r})$$

or the total energy:

$$E = -\mu_0 \iiint \boldsymbol{H}(\boldsymbol{r}) \cdot \boldsymbol{M}(\boldsymbol{r}) d^3\boldsymbol{r}$$

I.2.5 Dipolar interaction

The dipolar interaction is the influence that a magnetic moment $\boldsymbol{\mu}$ has on its environment. This interaction can be understood as follows: a magnetic moment $\boldsymbol{\mu}$ at the position $\boldsymbol{r}_0$ emits a magnetic field H_D, called dipolar field, that can be expressed as a function of the position $\boldsymbol{r}$:

$$\boldsymbol{H}_D(\boldsymbol{r}) = \frac{\mu_0}{4\pi}\left(\frac{3(\boldsymbol{\mu} \cdot (\boldsymbol{r} - \boldsymbol{r}_0))(\boldsymbol{r} - \boldsymbol{r}_0)}{\|\boldsymbol{r} - \boldsymbol{r}_0\|^5} - \frac{\boldsymbol{\mu}}{\|\boldsymbol{r} - \boldsymbol{r}_0\|^3}\right) \tag{I.3}$$

The dipolar field outside of the matter is called "stray field", whereas inside the magnetic material this field is referred to as "demagnetising field". Indeed, the demagnetising field interacts with a moment $\boldsymbol{\mu}_1$ located at the position $\boldsymbol{r}$ with a Zeeman interaction, represented by the elementary energy δE_D:

$$\delta E_D = -\mu_0 \boldsymbol{H}_D \cdot \boldsymbol{\mu}_1$$

Even though this interaction seems easy to apprehend and understand, since it is a long range interaction, its evaluation in an actual magnetic material is very complicated. Indeed, an exact calculation of all the interactions between magnetic moments within the matter would be too demanding in terms of computing resources. However, there is another way to represent this interaction in the case of a uniformly magnetised material. When all the dipolar fields sum up, we can express the total resulting field as follows:

$$\boldsymbol{H}_D^T = -\boldsymbol{N} \cdot \boldsymbol{M}$$

Where $\boldsymbol{N}$ is the demagnetising tensor. This operator can be determined by the shape of the sample considered. The calculation of this tensor can be complicated [56], but it has been approached analytically in the case of ellipsoids [57]. In the case of thin films or patterned wires, which are the only geometries used here, it is then possible to assimilate the samples to ellipsoids with two infinite axes in the plane of the sample, leading to the following expression of the demagnetising tensor in the orthonormal base defined by the axes of the ellipsoid (the latter being the axis orthogonal to the plane of the sample):

$$\boldsymbol{N}_{Thin\ film} = \begin{pmatrix} 0 & 0 & 0 \\ 0 & 0 & 0 \\ 0 & 0 & 1 \end{pmatrix}$$

And:

$$\varepsilon_D = \frac{\mu_0}{2} \boldsymbol{M} \cdot (\boldsymbol{N} \cdot \boldsymbol{M}) \overset{\text{thin film}}{=} \frac{\mu_0}{2} M_z^2$$

$$E_D = \frac{\mu_0 V}{2} \boldsymbol{M} \cdot (\boldsymbol{N} \cdot \boldsymbol{M}) \overset{\text{thin film}}{=} \frac{\mu_0 V}{2} M_z^2 \tag{I.4}$$

The energy previously expressed corresponds to what is called the shape anisotropy. The expression of this energy does only depend on the magnetisation of the material and the shape of the sample. As we can see from eq. (I.4), the shape anisotropy favours an in plane magnetisation for thin films. Indeed, in thin films, the demagnetising energy is maximised when the magnetisation points out of the sample's plane, and minimised when it lies in it.

I.2.6 Magnetocrystalline anisotropy

Bulk magnetocrystalline anisotropy

The symmetries of the crystalline structure of the materials that are grown can give rise to anistropic behaviours, and preferential directions for magnetisation. These material parameters can be expressed as interactions between the lattice and the magnetisation of a sample in many various ways, depending on the materials and the crystal structures.

Amongst the numerous expressions of magnetocrystalline anisotropy that can be found in materials, let us consider the simplest example. In some of our samples, the magnetisation $\boldsymbol{M}$ experiences a uniaxial magnetic anisotropy that sets the magnetisation along a favoured direction $\boldsymbol{u}$. In that specific case, the energy term taking account of the magnetocrystalline anisotropy can be represented as proportional to the volume anisotropy constant K_V (in $J.m^{-3}$), in terms of energy density ε_A and energy E_A in the following way:

$$\varepsilon_A(\boldsymbol{r}) = -K_V \left(\boldsymbol{m}(\boldsymbol{r}) \cdot \boldsymbol{u}\right)^2$$

$$E_A(\boldsymbol{r}) = -K_V \iiint_V \left(\boldsymbol{m}(\boldsymbol{r}) \cdot \boldsymbol{u}\right)^2 d^3\boldsymbol{r}$$

In the case of a uniform magnetisation, the anisotropy energy can be written as:

$$E_A = -K_V V \left(\boldsymbol{m} \cdot \boldsymbol{u}\right)^2 \tag{I.5}$$

In these expressions, we choose the following convention: a positive value of the anisotropy constant $K_V > 0$ implies that the energy given in eq. (I.5) is minimised when $\boldsymbol{m}$ is aligned along $\boldsymbol{u}$, and maximised when $\boldsymbol{u}$ and $\boldsymbol{m}$ are orthogonal. In that case, $\boldsymbol{u}$ represents an easy axis of magnetisation, and the plane to which $\boldsymbol{u}$ is orthogonal is a hard plane of magnetisation. On the oppositve, a negative anisotropy constant $K_V < 0$ lets the anisotropy energy as defined in eq. (I.5) be minimised when $\boldsymbol{m}$ and $\boldsymbol{u}$ are orthogonal, and maximised when $\boldsymbol{m}$ and $\boldsymbol{u}$ are colinear. Therefore, $\boldsymbol{u}$ defines a hard axis of magnetisation, and the plane orthogonal to $\boldsymbol{u}$ is an easy plane of magnetisation.

Interfacial anisotropy

In the past decades, the improvement of growth techniques has led to the growth of very thin layers, in the subnanometer scale. This technical enhancement provided a new way to see interfacial effects. Amongst these, the surface anisotropy was evidenced. This phenomenon can be observed thanks to a hybridization of the orbitals of a ferromagnetic material at the interface with atoms of a material showing a large spin orbit coupling, (like Pt, Ir, Ta), or to a texture given by a buffer layer that changes the growth of the layer that is put above. Due to the spin orbit coupling, the hybridisation of these orbitals results in a preferred direction for the magnetisation. These phenomena result in an interaction that can be described as a surface anisotropy constant K_S (in $J.m^{-2}$). The energy density correspinding to this interaction can be expressed as:

$$\varepsilon_{A,S}(\boldsymbol{r}) = -\frac{K_S}{t_{FM}} \left(\boldsymbol{m}(\boldsymbol{r}) \cdot \boldsymbol{u}\right)^2$$

Where $\boldsymbol{u}$ is the direction of easy anisotropy axis (normal to the interface in the case of perpendicular magnetic anisotropy), and t_{FM} is the thickness of the ferromagnetic layer considered. The corresponding energy can be written in a general way as:

$$E_{A,S} = -\frac{K_S}{t_{FM}} \iiint_V \left(\boldsymbol{m}(\boldsymbol{r}) \cdot \boldsymbol{u}\right)^2 d^3\boldsymbol{r}$$

In the case of a uniform magnetisation, we can rewrite the interfacial anisotropy energy as:

$$E_{A,S} = -\frac{K_S V}{t_{FM}} \left(\boldsymbol{m} \cdot \boldsymbol{u}\right)^2$$

The total magnetic anisotropy is the sum of both the bulk and the interfacial contributions. Since the dipolar interaction in a macrospin point of view can be treated as a shape anisotropy, all three terms are sometimes grouped. In very thin magnetic films, like the synthetic ferrimagnets studied in this manuscript, a surface anisotropy is considered, the bulk anisotropy is neglected, and the dipolar interaction is treated as a demagnetising field. Thus, in the case of perpendicular magnetic anisotropy and uniform magnetisation, the energy density representing all these interactions can be written as:

$$E_{Anis+Demag} = E_{Anis\ eff} = \left(\frac{1}{2}\mu_0 M_S^2 - \frac{K_S}{t_{FM}} - K_V\right) V \left(\boldsymbol{m} \cdot \boldsymbol{z}\right)^2$$

In this expression, we can see that at zero applied magnetic field, the sign of the energy density will determine if the magnetisation points out of the sample's plane or if it lays within it. Indeed, the very thin magnetic layers favour the out of plane magnetisation. For the rest of this chapter, we will use an effective anisotropy constant $K_{eff} = \frac{1}{2}\mu_0 M_S^2 - \frac{K_S}{t_{FM}} - K_V$. In our case, the samples will be assumed to show a perpendicular magnetic anisotropy, which is equivalent, in this formalism, to assume $K_{eff} < 0$.

The magnetic anisotropy creates preferential directions of magnetisation, and directions that will not be reached without magnetic field. The preferential directions of the magnetisation are thus defined by local minima of the energy density when no magnetic field is applied. We will call these peculiar directions **easy axes of magnetisation**. On the opposite, the plane corresponding to local energy density maximum in the absence of magnetic field will be referred to as the **hard plane of magnetisation**. In this representation, all the axes lying in a hard plane of magnetisation are hard axes of magnetisation.

I.2.7 RKKY interaction – indirect coupling

The RKKY interaction is a magnetic exchange interaction which was first predicted by Ruderman and Kittel in 1954 [58] and was later completed by Kasuya in 1956 [59], and Yosida in 1957 [60]. This phenomenon corresponds to spin density oscillations within a spacer separating two magnetic layers. As mentionned by [60], this phenomenon is analogous to the charge density oscillations described by Friedel in a metal next to a charged impurity. The resulting interaction between the two magnetic layers can be understood as interferences between spin density static waves that are formed by each layer due to the Friedel oscillations. In the case of magnetic monodomains in each magnetic layer surrounding the spacer considered, we can represent this interaction in terms of energy density by introducing a surface coupling constant J_E (in $J.m^{-2}$). The interaction depends on the respective orientations of both magnetisations ($\boldsymbol{m}_1$ and $\boldsymbol{m}_2$), as follows:

$$\varepsilon_{RKKY} = \frac{J_E}{t_{FM}}(\boldsymbol{m}_1 \cdot \boldsymbol{m}_2)$$

Where t_{FM} is the total thickness of the magnetic layers. The energy associated is thus:

$$E_{RKKY} = \frac{J_E V_{FM}}{t_{FM}}(\boldsymbol{m}_1 \cdot \boldsymbol{m}_2)$$

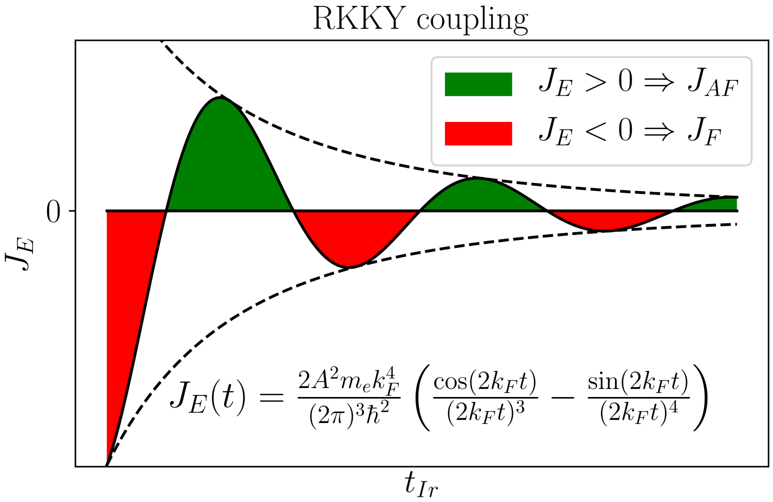

Figure I.1: Evolution of the indirect exchange coupling constant as a function of the thickness of the spacer considered

The RKKY coupling constant J_E (in $J.m^{-2}$) can be expressed as a function of the spacer thickness t and the length of the Fermi wave vector k_F within the metal as [58–61]:

$$J_E(t) = \frac{4A^2 m_e k_F^4}{(2\pi)^3\hbar^2}\left(\frac{\cos(2k_F t)}{(2k_F t)^3} - \frac{\sin(2k_F t)}{(2k_F t)^4}\right) \tag{I.6}$$

In this expression, A is an ajustable parameter that represents the strength of the coupling. This coupling has been widely studied experimentally, for a large variety of materials [47, 48].

I.2.8 Effective field

All the energies that are presented above are an efficient way to represent the interactions that occur in the magnetic matter. If we focus on the orientation of the magnetisation in the case of static field, the energy of the magnetic system is expected to reach a minimum. This minimum can be achieved when the magnetisation aligns in a specific direction. In order to represent that, we can introduce an effective field $\boldsymbol{H}_{eff}$ of the following form:

$$\boldsymbol{H}_{eff} = -\frac{1}{\mu_0 M_S}\boldsymbol{\nabla}_{\boldsymbol{m}}\varepsilon_{tot}$$

This definition of the effective field holds for a single magnetic layer and we will only use it for samples composed of a single layer of magnetic material.

I.2.9 Summary of the interactions

For the sake of clarity, we have summarised all the relevant interactions and their expressions in table I.1.

NAME	Energy E	Energy density ε
Heisenberg exchange	$\iiint_{V_{FM}} A_{ex}\left(\nabla\boldsymbol{m}(\boldsymbol{r})\right)^2 d^3\boldsymbol{r}$	$A_{ex}\left(\nabla\boldsymbol{m}(\boldsymbol{r})\right)^2$
Zeeman	$-\mu_0 M_S \boldsymbol{H}\cdot\boldsymbol{m}V$	$-\mu_0 M_S \boldsymbol{H}\cdot\boldsymbol{m}$
Shape anis.	$\frac{\mu_0 M_S^2 V}{2}\boldsymbol{m}\cdot\boldsymbol{N}\cdot\boldsymbol{m}$	$\frac{\mu_0 M_S^2}{2}\boldsymbol{m}\cdot\boldsymbol{N}\cdot\boldsymbol{m}$
Uniax. magnetocryst. anis.	$-\left(K_V + \frac{K_S}{t_{FM}}\right)V\left(\boldsymbol{m}\cdot\boldsymbol{u}\right)^2$	$-\left(K_V + \frac{K_S}{t_{FM}}\right)\left(\boldsymbol{m}\cdot\boldsymbol{u}\right)^2$
RKKY coupling	$\frac{J_E V_{FM}}{t_{FM}}\left(\boldsymbol{m}_1\cdot\boldsymbol{m}_2\right)$	$\frac{J_E}{t_{FM}}\left(\boldsymbol{m}_1\cdot\boldsymbol{m}_2\right)$

Table I.1: Summary of the various interactions and the energies and associated energy densities in the case of a uniform magnetisation (macrospin approximation).

In the following, we will mostly work with the energy densities.

I.3 Quasistatic magnetisation reversal in a ferromagnetic thin film

Now that the magnetic energies involved in our studies are presented in details, let us find out how this representation helps us describing our magnetic materials. We are considering in a first example the study of a single ferromagnetic layer. For that purpose, we chose the Stoner-Wohlfarth [62] approach: it consists in a macrospin approximation of a magnetic system, considered at a temperature of 0K. Even though this approximation is very rough, it can still be very useful in order to have a first idea of the magnetisation properties of a material. This model turns out to be very efficient in the case of very thin layers, in which case the magnetic domains can be very large, leading to a good agreement between the experimental measurements and the calculations that can be carried out thanks to a comparison between the energies listed above.

In this section, we will be especially interested in the magnetic loops that we can obtain from this model. Within this whole subsection, since the material that we consider is supposed to be uniformly magnetised, we will describe the magnetisation as a vector $\boldsymbol{M}$, and evaluate the relevant interactions so as to represent the effect of a static field on the magnetisation. The magnetisation will thus be perfectly described by the length of the vector (M_S) and its position.

I.3.1 Description of the sample

We will consider here a material showing perpendicular magnetic anisotropy. Indeed, the magnetic interactions that matter in this case are the effect of the field (Zeeman interaction, associated to ε_Z) and the effective anisotropy (described by $\varepsilon_{Anis\ eff}$). The Heisenberg interaction does not play a role here: the hypothesis of a macrospin is equivalent to consider that all the magnetic moments are always aligned, leading to a constant value of the Heisenberg interaction. We shall thus ignore it.

Since the problem that we are considering shows a clear symmetry around the $\boldsymbol{z}$ axis, the only coordinate that we need to describe the magnetisation orientation is the angle between $\boldsymbol{M}$ and $\boldsymbol{z}$. Let us call that angle θ. The major experimental parameter is the orientation of the applied magnetic field with respect to the easy axis of magnetisation of the sample. Let us call θ_H the angle between these two axes.

I.3.2 Easy axis magnetic hysteresis loop measurement ($\theta_H = 0$)

We shall now describe an easy axis of magnetisation hysteresis loop. In that case, the magnetic field is applied along the $\boldsymbol{z}$ axis. Let us first consider the equilibrium positions of the magnetisation as a function of the position. The energy density can be written as:

$$\varepsilon = -\mu_0 M_S \boldsymbol{H} \cdot \boldsymbol{m} + K_{eff} \left(\boldsymbol{m} \cdot \boldsymbol{z}\right)^2 \tag{I.7}$$

Let us express that energy density as a function of the angle θ:

$$\varepsilon(\theta) = -\mu_0 H M_S \cos(\theta) + K_{eff} \cos^2(\theta)$$

The determination of the equilibrium position is obtained when the first derivative of the energy density with respect to the position cancels, and when its second derivative is positive. Let us solve this system, using the convention $2K_{eff} = -\mu_0 H_K M_S$. In order to simplify the notations, we will note the position derivatives of the energy density as follows: $\dfrac{\partial \varepsilon}{\partial \theta} = \varepsilon_\theta$ and $\dfrac{\partial^2 \varepsilon}{\partial \theta^2} = \varepsilon_{\theta\theta}$:

$$\varepsilon_\theta(\theta) = 0 \Leftrightarrow \begin{cases} \theta = 0[\pi] & (\sin(\theta) = 0) \\ \cos(\theta) = -\dfrac{H}{H_K} & \end{cases}$$

Let us call $\theta_m = \arccos\left(-\dfrac{H}{H_K}\right)$

$$\begin{cases} \varepsilon_{\theta\theta}(0) = & \mu_0 M_S(H + H_K) \\ \varepsilon_{\theta\theta}(\pi) = & \mu_0 M_S(-H + H_K) \\ \varepsilon_{\theta\theta}(\theta_m) = & \mu_0 M_S H_K \left(\left(\dfrac{H}{H_K}\right)^2 - 1\right) \end{cases}$$

We can see through these equations that the magnetic field H_K has a crucial importance here. The angles $\theta = 0$ and $\theta = \pi$ are the only equilibrium positions that may be available in this system. Indeed, the other case θ_m presents a non satisfying solution when $H \in [-H_K, H_K]$, and no solution for other values. The solution $\theta = 0$ is an equilibrium position for fields larger than $-H_K$, whereas $\theta = \pi$ corresponds to an equilibrium position for $H < H_K$.

I.3.3 Hard axis magnetic hysteresis loop measurement $\left(\theta_H = \frac{\pi}{2}\right)$

Let us now consider the case of a magnetic loop where the magnetic field is applied in a direction in the plane of the sample. The energy density of the system can still be written as in eq. (I.7), but the angular expression of the Zeeman term is a little different. We can write this angular dependence as follows:

$$\varepsilon(\theta) = -\mu_0 H M_S \sin(\theta) + K_{eff} \cos^2(\theta)$$

The equilibrium position of the magnetisation can thus be found by derivation of ε with respect to θ:

$$\varepsilon_\theta(\theta) = 0 \Leftrightarrow \begin{cases} \theta = \dfrac{\pi}{2}[\pi] \\ \sin(\theta) = \dfrac{H}{H_K} \end{cases}$$

Again, let us consider the second derivatives of the energy density to determine the equilibrium positions of the magnetisation. Let us call θ_n the angle such that $\sin(\theta_n) = \frac{H}{H_K}$:

$$\begin{cases} \varepsilon_{\theta\theta}\left(\dfrac{\pi}{2}\right) = & \mu_0 M_S(H - H_K) \\ \varepsilon_{\theta\theta}\left(-\dfrac{\pi}{2}\right) = & -\mu_0 M_S(H + H_K) \\ \varepsilon_{\theta\theta}(\theta_n) = & \mu_0 M_S H_K \left(1 - \left(\dfrac{H}{H_K}\right)^2\right) \end{cases}$$

This case is significantly different from the previous one: we can clearly see that the equilibrium positions $\theta = \frac{\pi}{2}$ is the equilibrium position for $H > H_K$, and symmetrically, $\theta = -\frac{\pi}{2}$ is the magnetisation position for $H < -H_K$. In between these values, for $|H| < H_K$, the magnetisation position is defined with a linear field dependence of $\sin(\theta)$. Since the projection of the magnetisation along the field axis is given by $\sin(\theta)$, the magnetic hysteresis loop shows two steps and a linear part that joins both plateaus.

I.3.4 Magnetic transitions

The Stoner-Wohlfarth model does not consider temperature. Therefore, we have access to the stable and metastable states, but we do not consider the transitions properly: the transition will be given by the energy barrier, the temperature and the possibility of a domain nucleation and domain wall propagation. Indeed, in the Stoner Wohlfarth model, an energy barrier cannot be crossed. In the hysteresis loop that we are considering, the switching from an equilibrium to the other occurs only when the initial state is not an equilibrium position anymore. This assumption corresponds to a switching at $-H_K$ and H_K. Let us point out here that these values are overestimated in this case. There are several reasons for that. First, for large samples (several mm^2), it is very likely that defects are present in the material. We can also point out that even for small samples, defects are also often present on the edges. Indeed the nucleation of a reversed domain is also very likely, and from that, the propagation of a domain wall can occur easily, at fields that are lower than H_K. Furthermore, let us add that in actual measurement conditions, the temperature is not null. This can lead to spontaneous nucleation of a reversed magnetisation area that can spread and lead the magnetisation switching, despite the existence of a small energy barrier. We represent on fig. I.2 the hysteresis cycles that are obtained in the macrospin approximation and the actual measurements that can be achieved experimentally.

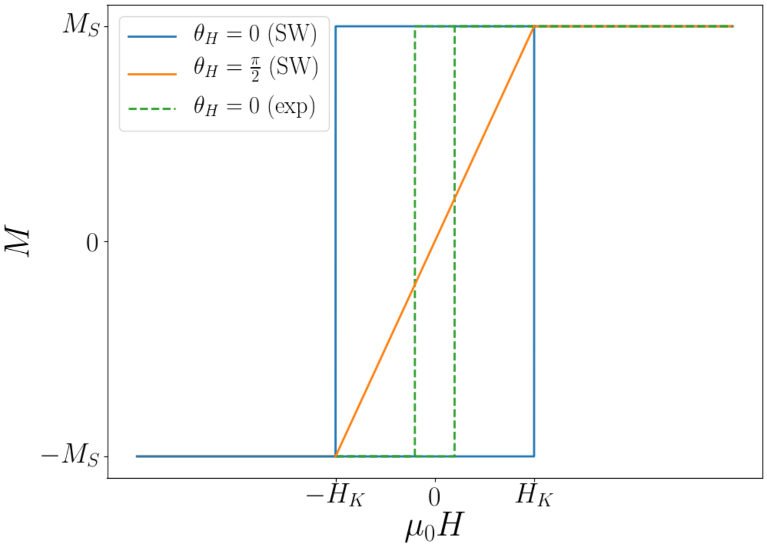

Figure I.2: Magnetic hysteresis loops predicted from the Stoner Wohlfarth approach in the cases of an easy axis of magnetisation ($\theta_H = 0$, blue), and a hard axis of magnetisation ($\theta_H = \frac{\pi}{2}$, orange). We also plot in dashed green lines what an actual experimental easy axis magnetic loop would look like, since there is a large discrepancy with the Stoner Wohlfarth model.

I.4 Spin torques and spin Hall effect (SHE)

In the past few decades, the possibility to generate a spin polarised current has emerged, leading to a new way to manipulate the magnetisation. In this section, we present spin polarised currents, and the effects that generate them.

I.4.1 Spin polarised currents and pure spin currents

Amongst the spin polarised currents, one can distinguish two different categories. On the one hand, the spin polarised charge currents are composed of electrons flowing through a material, which have the property to carry a magnetic moment that is oriented preferentially in one direction. This direction is called the spin polarisation direction, and the amplitude of the polarisation P can be determined by the band structure of the material as follows:

$$P = \frac{k^+ - k-}{k^+ + k-}$$

The spin polarisation can thus vary between 0 and 1. Materials that allow a spin polarisation of 1 are called semi metals. In usual ferromagnetic materials, the spin polarisation is inferior.

On the other hand,it is also possible to generate “pure” spin currents. In that case, the magnetic moment is not carried by a charge current anymore. The impact of this phenomenon is dramatic: it enables to manipulate the magnetisation by spin means, avoiding mainly the Joule effect. Indeed, a method that does not involve charge transport, and thus Joule heating, is promising considering that the energy consumption that would be decreased. Let us precise that the methods used are not absolutely free of Joule effect, since the generation of a pure spin current is usually obtained thanks to the spin Hall effect (see subsection I.4.3). Therefore, a charge current in a material is often mandatory to generate a pure spin current, but it is possible to choose a low resistance material for that purpose, such as platinum. We can also mention the fact that some spin flip mechanisms that are at stake during the propagation of a spin current involve the generation of phonons (like the Elliott Yafet phenomenon [63, 64]), which leads to Joule effect.

In the rest of this section, we will present the effect of the generation of a spin polarised charge current and its effect on the magnetisation (spin transfer torque, STT), and similarly for pure spin currents (spin Hall effect, SHE) and the manipulation of magnetisation through it (spin orbit torque, SOT).

I.4.2 Spin transfer torque

The spin polarisation of a charge current flowing through a magnetic material is due to the band structure of the material. Indeed, the number of available states at the Fermi level can differ depending on the spin of the electrons. Accordingly, we can consider majority and minority spins. The ratio of these populations lead to the spin polarisation of a current flowing through the material: the spin current is polarised in average in the direction of the magnetisation.

Interestingly, when a spin polarised charge current flows through a non uniform magnetisation structure, the momentum carried by the electrons tends to align locally with the effective field that is mainly due to the magnetisation, under zero applied field. However, the laws of conservation of angular momentum lead to a change in the magnetisation. A simple model that considers the action of a spin-polarised charge current inside a magnetic material which magnetisation is not aligned with the spin polarisation is presented by Ralph and Stiles in [65]. The effect of the magnetisation can thus be expressed as:

$$\frac{d\boldsymbol{m}}{dt}_{ST} = \frac{\eta(\theta)\mu_B I}{eV}\boldsymbol{m} \times (\boldsymbol{m} \times \boldsymbol{\sigma})$$

where μ_B is the Bohr magneton, I is the intensity of the current flowing through the material, e is the charge of an electron, V is the volume of magnetic material considered, σ is the unit vector in the direction of the spin polarisation of the charge current, and $\eta(\theta) = \dfrac{q}{A + B\cos(\theta)}$ is an angular function that takes into account all the details of the layer structure considered, through the parameters A, B, and q. It has also been shown that in the geometry where a first magnetic layer acts as a polariser for the charge current which then flows through a magnetic layer oriented in the opposite direction, in a macrospin approach at zero temperature, the switching current can be expressed as [66]:

$$I_c = \frac{2e}{\hbar}\frac{\alpha}{\eta(0)}V\mu_0 M_S H_{eff}$$

where e is the charge of an electron, $\hbar$ is the reduced Planck constant, α is the magnetic damping, V is the volume considered, M_S is the saturation magnetisation of the material considered, and H_{eff} is the amplitude of the effective magnetic field.

Indeed, the spin transfer torque is a promising electrical phenomenon for the manipulation of the magnetisation. We explore a little more into details the case of domain wall propagation by presenting the torques of Zhang and Li in section I.6.4, where the magnetic layer acts as the spin-polariser in the parts where the magnetisation is uniform, and endures the action of the spin current in the non uniformly magnetised zones, namely domain walls.

I.4.3 Spin orbit torque

Origins of spin-Hall effect

The spin-Hall effect is a phenomenon that occurs in conductive materials, typically metals. The microscopic origin of this phenomenon is the spin-orbit interaction between the conductive electrons and the lattice. This effect corresponds to the generation of a spin current when a charge current is flowing through a material. This effect can arise from intrinsic and extrinsic properties of the material.

On the one hand, the intrinsic spin-Hall effect was inspired by the anomalous Hall effect (AHE, where a transverse charge current can stem from the magnetisation of a material). An intrinsic contribution was predicted in the early 1970's by D'Yakonov and Perel [67] considering the properties of an electric current in a 2-dimensional Rashba electron gas. The mechanism proposed was analogous to an asymmetric Mott scattering [68] due to the spin-orbit coupling of the atoms. Another explanation relied on an analogy with AHE, where the role of the magnetisation was replaced by an equivalent force due to the spin orbit interaction in the material, without considering the D'Yakonov and Perel's mechanism [69]. Other extrinsic mechanisms, also analogous to the “side jump” and “skew scattering” introduced in the AHE theory were also evidenced [70].

The description of the SHE and ISHE, however, is achieved regardless of the contributions, since all these can be represented using two phenomenological parameters. In the following, we will characterise the SH/ISH effects in the aim of injecting a spin current to control the magnetisation of a material. The actual mechanism that is responsible for the spin current generation does not play a role in our use of the phenomenon. Therefore, we will focus on the determination of the phenomenological parameters that enable an efficient representation of the spin-Hall effect, and we will not try to dissociate the mechanisms from which it stems from. We represent on fig. I.3 the phenomena occurring in a bilayer composed of a non magnetic material showing SHE and a ferromagnetic layer, and the interplay between the spin currents and the magnetisation.

The main interest of this effect is to be able to inject non locally a pure spin current inside a magnetic material so as to act on its magnetisation. We have indeed to characterise it in order to quantify the spin current that can be injected in a ferromagnetic material thanks to iridium, and therefore, evaluate its ability to be used as a spintronics material.

Phenomenological representation of the effect

As we described, the spin-Hall effect of a material can be attributed to many different origins and materials parameters, including band structure and defects. However, a phenomenological approach leads to an efficient experimental description of all the phenomena observed, regardless on the actual origin of the phenomenon. In order to do so, the whole SHE of a material is usually characterised by two main parameters that are the spin Hall angle θ_{SH} and the spin flip length l_{sf}. When inserted into a device, the addition of the interfaces lead to the addition of a new parameter, namely the spin mixing conductance $g^{\uparrow\downarrow}$ between the material where the spin-Hall effect occurs and the material where the spin current is injected. Let us examine these quantities.

The spin Hall angle θ_{SH}

The spin-Hall angle is the unitless spin-to-charge and charge-to-spin conversion efficiency. Indeed, the SHE and ISHE are rigourously reciprocal effects, thus the efficiency for the direct and the inverse effects are the same. It is thus possible to link the current density $\boldsymbol{j}_c$ and the spin current density $\boldsymbol{j}_s$, depending on the effect that is occurring, using the following relationships:

$$\boldsymbol{j}_c = \theta_{SH}\frac{2e}{\hbar}\boldsymbol{j}_s \times \boldsymbol{\sigma} \qquad (ISHE) \tag{I.8a}$$

$$\boldsymbol{j}_s = -\theta_{SH}\frac{\hbar}{2e}\boldsymbol{j}_c \times \boldsymbol{\sigma} \qquad (SHE) \tag{I.8b}$$

Where $\hbar = \frac{h}{2\pi}$ is the reduced Planck constant, e the electric charge of an electron, and $\boldsymbol{\sigma}$ is the unit vector representing the direction of polarisation of the spin current.

Indeed, the larger the spin-Hall angle the larger the effect. We are thus hoping for the largest value possible for this parameter. Experimentally, the determination of the spin Hall angle of a material is to inject a charge current into the material to probe, and to measure the spin current produced, or to do the opposite, and extract the ratio.

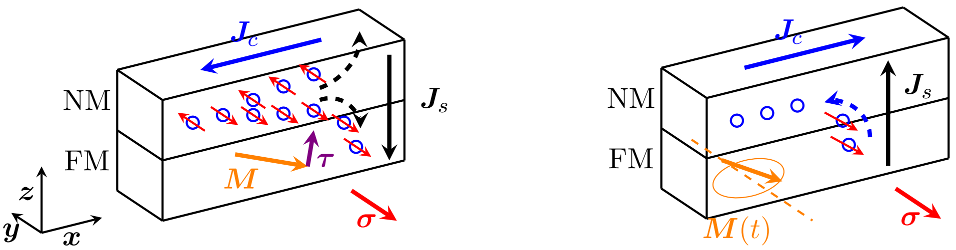

(a) Spin Hall Effect

(b) Inverse Spin Hall Effect

Figure I.3: Illustration of the direct and inverse SHE in a ferromagnetic/nonmagnetic bilayer with a non magnetic material exhibiting SHE: (a) A charge current $\boldsymbol{J}_c$ is applied, which generates a spin current $\boldsymbol{J}_s$ polarised along $\boldsymbol{\sigma}$ that is injected in the ferromagnetic material, applying a torque $\boldsymbol{\tau}$ on the magnetisation M; (b) Coherent precession of the magnetisation $\boldsymbol{M}(t)$ generating a spin current $\boldsymbol{J}_s$ polarised along $\boldsymbol{\sigma}$ by spin pumping effect, which is converted into a charge current $\boldsymbol{J}_c$ by ISHE in the non magnetic material.

In the table I.2, we provide a few values of spin Hall angles for materials that are considered as promising:

Material	$\lvert\theta_{SH}\rvert$ (%)	Sign	References
Pt	0.67 – 12	Positive	[71–85]
Ta	2 – 3	Negative	[71, 86, 87]
W	14	Negative	[88]
Au	0.16 – 1.1	Positive	[73, 78, 81]

Table I.2: Values of spin Hall angles for promising materials

The spin-flip length l_{sf}

The spin flip length represents the decay length of the probability to conserve the spin when it travels through a material. This diffusion length is of major interest in our case: it allows to tune the efficiency of the spin torque we can apply on the magnetisation, for a set current density. If this value is too small, even a large spin-Hall angle value will not be sufficient, because only a very thin part of the material will generate a spin current that will reach the magnetic layer on which it is expected to act. Again, for our purposes, the larger the spin flip length the larger the spin current injection.

Experimentally, the spin flip length can be determined by probing the evolution of the spin-to-charge conversion as a function of the thickness of the material in which the ISHE occurs. What is expected is that for very small thicknesses, all the spin current will be submitted to this conversion, whereas as the thickness is increased, most of the spin current will have flipped before any spin-to-charge conversion occurs.

We display on the following table I.3 some values of spin flip length for the most promising materials studied until now:

Material	l_{sf} (nm)	References
Pt	1.2–12	[71–85, 89–91]
Ta	1.5–1.9	[71, 86, 87]
W	2.1	[88]

Table I.3: Values of spin flip length for promising materials.

The spin-mixing conductance $g^{\uparrow\downarrow}$

When a spin current is generated in a material showing spin Hall effect, one of the main interests is to inject that spin current in a magnetic material so as to act on the magnetisation. However, at the interface, it is likely that all the spin current will not be fully transmitted. The real part of the spin mixing conductance represents the crossing of the interface by the spin current: it acts mainly on the magnetic damping of the magnetic material where the spin current flows. The imaginary part of the spin mixing conductance represents the modification of the precession in terms of gyromagnetic ratio that governs the precession of the magnetisation of the material through which the spin current flows. However, this effect has been shown to be negligible in metallic systems [92, 93] like the ones that are studied in this manuscript.

I.5 Magnetisation equations of motion

The magnetisation dyamics of a sample can be described using the Landau-Lifshitz-Gilbert equation that is written as:

$$\frac{d\boldsymbol{M}(\boldsymbol{r})}{dt} = -\gamma\mu_0\boldsymbol{M}(\boldsymbol{r}) \times \boldsymbol{H}_{eff}(\boldsymbol{r}) + \frac{\alpha}{M_S}\boldsymbol{M}(\boldsymbol{r}) \times \frac{d\boldsymbol{M}(\boldsymbol{r})}{dt} \tag{I.9}$$

The motion of the magnetisation is thus driven by two phenomena: the precession of the magnetisation around the effective magnetic field $\boldsymbol{H}_{eff}$ (first term) and a damping term that diminishes the amplitude of the precession until the magnetisation aligns with the effective field. Let us examine these two terms in detail, before exploring further terms that were proposed in the past few decades.

I.5.1 Magnetic precession

The evolution of the magnetisation as a function of time is expressed in terms of conservation of the angular momentum. If we consider each magnetic moment carried within the matter $\boldsymbol{\mu}_i$, for each moment, the torque applied by the effective magnetic field can be expressed as:

$$\boldsymbol{\Gamma}_i = -\mu_0\boldsymbol{H}_{eff} \times \boldsymbol{\mu}_i$$

Indeed the derivative of the angular moment of a whole sample can be expressed as:

$$\frac{d\boldsymbol{L}}{dt} = \sum_{i\in sample} -\mu_0\boldsymbol{\mu}_i \times \boldsymbol{H}_{eff} = -V\mu_0\boldsymbol{M} \times \boldsymbol{H}_{eff}$$

Since the angular moment and the magnetisation of a material are linked by the gyromagnetic ratio γ ($V\boldsymbol{M} = \gamma\boldsymbol{L}$), we obtain the evolution of the magnetisation corresponding to the conservation of the angular momentum:

$$\frac{d\boldsymbol{M}}{dt} = -\gamma\mu_0\boldsymbol{M} \times \boldsymbol{H}_{eff}$$

In the following, we will take the convention to call $\gamma_0 = \gamma\mu_0$. Without other terms, this equation of motion is a perpetual precession around $\boldsymbol{H}_{eff}$ at a frequency of $\gamma_0\boldsymbol{H}_{eff}$. This is called the Larmor precession, and $\gamma_0\boldsymbol{H}_{eff}$ is the Larmor frequency (in $rad.s^{-1}$).

I.5.2 Damping term

Even though there was no initial theoretical prediction of any damping term, it is observed experimentally that the magnetisation experiences a damping that lets the magnetisation align on the effective field axis. As a consequence, a phenomenological damping term $\boldsymbol{\Gamma}_{damping}$ was added to the magnetisation dynamics equation. This term has to conserve the magnetisation norm, that is to say be orthogonal to the magnetisation. Indeed, the conservation of the norm can be written as:

$$\frac{d\|\boldsymbol{M}\|}{dt} = 0 \Leftrightarrow \frac{d\boldsymbol{M}}{dt} \cdot \boldsymbol{M} = 0$$

Since the precession torque is already orthogonal to $\boldsymbol{M}$, $\boldsymbol{\Gamma}_{damping}$ also has to be. Furthermore, the damping term must be orthogonal to the precession term, otherwise it does not express a damping, but a change in the precession frequency. This can be written as:

$$\boldsymbol{\Gamma}_{damping} \cdot (\boldsymbol{M} \times \boldsymbol{H}) = 0$$

The only direction left is thus $\boldsymbol{M} \times (\boldsymbol{M} \times \boldsymbol{H})$, or equivalently $\boldsymbol{M} \times \frac{d\boldsymbol{M}}{dt}$. Indeed, eq. (I.9) can also be written as:

$$\frac{d\boldsymbol{M}}{dt} = -\tilde{\gamma_0}\boldsymbol{M} \times \boldsymbol{H}_{eff} + \eta\boldsymbol{M} \times (\boldsymbol{M} \times \boldsymbol{H}_{eff})$$

Where $\tilde{\gamma_0} = \frac{\gamma_0}{1+\alpha^2}$ and $\eta = -\frac{\alpha\gamma_0}{(1+\alpha^2)M_S}$.

Let us represent the magnetisation and the torques applied in a general case under an effective magnetic field $\boldsymbol{H}_{eff}$ on fig. I.4:

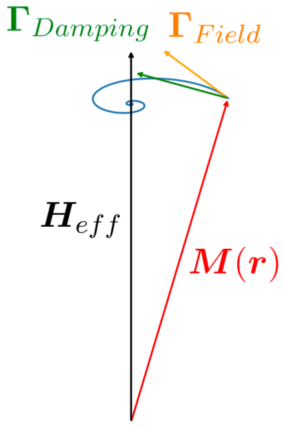

Figure I.4: Schematic of the torques acting on the magnetisation under a static effective magnetic field $\boldsymbol{H}_{eff}$.

I.5.3 Uniform magnetisation motion under a constant applied magnetic field

Let us consider a uniform magnetisation $\boldsymbol{M}$ under an applied magnetic field $\boldsymbol{H}$. Let us call $\boldsymbol{z}$ the direction of the magnetic field. We will consider the magnetisation close to its equilibrium position ($M_z \approx M_S$, $M_j \ll M_z$, $j \in \{x, y\}$). The Landau Lifshitz Gilbert equation (eq. I.9) rewrites:

$$\begin{pmatrix} \frac{dM_x}{dt} \\ \frac{dM_y}{dt} \\ \frac{dM_z}{dt} \end{pmatrix} = -\gamma_0 \begin{pmatrix} M_x \\ M_y \\ M_z \end{pmatrix} \times \begin{pmatrix} 0 \\ 0 \\ H \end{pmatrix} + \frac{\alpha}{M_S} \begin{pmatrix} M_x \\ M_y \\ M_z \end{pmatrix} \times \begin{pmatrix} \frac{dM_x}{dt} \\ \frac{dM_y}{dt} \\ \frac{dM_z}{dt} \end{pmatrix}$$

By linearising this equation, keeping only 1^{st} order terms, we obtain an equation along $\boldsymbol{z}$:

$$\frac{dM_z}{dt} = 0$$

and a coupled system along $\boldsymbol{x}$ and $\boldsymbol{y}$:

$$\begin{pmatrix} \frac{dM_x}{dt} \\ \frac{dM_y}{dt} \end{pmatrix} = -\gamma_0 H \begin{pmatrix} M_y \\ -M_x \end{pmatrix} + \alpha \begin{pmatrix} -\frac{dM_y}{dt} \\ \frac{dM_x}{dt} \end{pmatrix}$$

These equations can be decoupled by derivating each equation and reinjecting it in each other, leading to the equations ($j \in \{x, y\}$):

$$\frac{d^2 M_j}{dt^2} + \left(\frac{2\gamma_0 H\alpha}{1+\alpha^2}\right)\frac{dM_j}{dt} + \left(\frac{(\gamma_0 H)^2}{1+\alpha^2}\right) M_j = 0$$

Let us use the following notations:

$$\begin{cases} \tau = \dfrac{1+\alpha^2}{\gamma_0 H\alpha} \\ \omega_0 = \gamma_0 H\sqrt{\dfrac{1-\alpha^2}{1+\alpha^2}} \end{cases}$$

We can express the transverse magnetisation components, by considering arbitrarily that at $t = 0$ the transverse component of the magnetisation is along the $\boldsymbol{x}$ direction, setting the phase of each component. The resulting expressions are:

$$\begin{cases} M_x(t) = & M_0 e^{-t/\tau}\cos(\omega_0 t) \\ \\ M_y(t) = & M_0 e^{-t/\tau}\sin(\omega_0 t) \end{cases}$$

We represent on fig. I.5 the evolution of the magnetisation in the plane transverse to the magnetisation. If a change in the field value does not change the trajectory, but only affects the speed at which the relaxation occurs, the damping constant α plays a key role in the trajectory. Indeed, the larger the damping parameter, the faster the equilibrium position is reached.

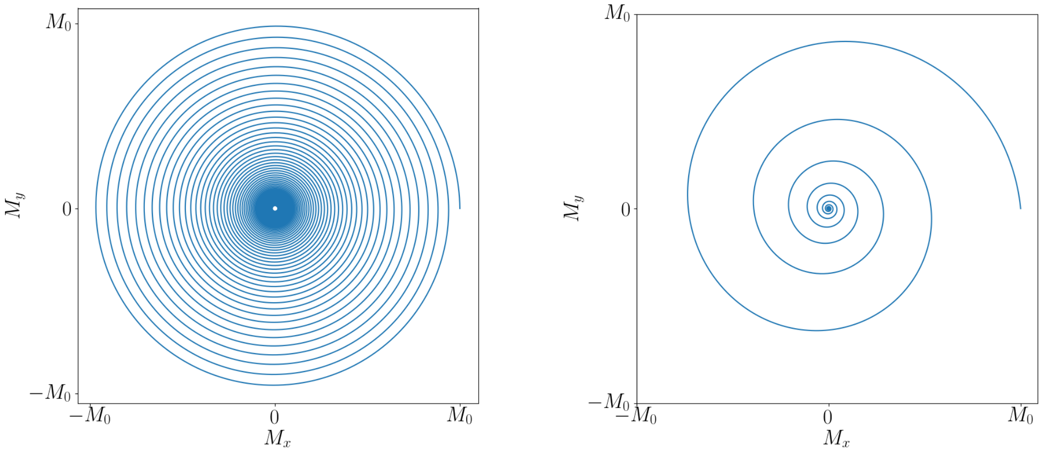

(a) $\alpha = 10^{-2}$ (b) $\alpha = 10^{-1}$

Figure I.5: Trajectory of the magnetisation for two values of the magnetic damping

Let us add the time dependance of each transverse component of the magnetisation presented on fig. I.6, for a value of $\alpha = 0.1$:

I.5.4 Slonczewski torques

The discoveries of Berger and Slonczewski concerning the spin transfer torque lead to a new contribution to the magnetisation dynamics. Indeed, the magnetisation has been proven to be efficiently manipulated using spin polarised currents. It was thus necessary to represent these new contributions in the LLG equation.

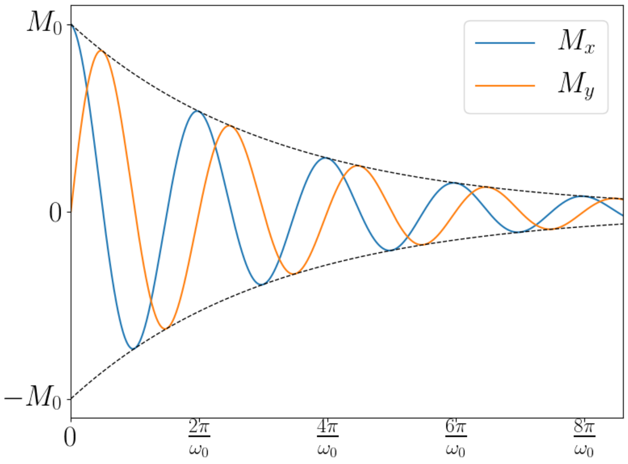

Figure I.6: Time dependence of the transverse components of the magnetisation for $\alpha = 10^{-1}$

As we saw earlier, the time derivative of the magnetisation must be orthogonal to the magnetisation for length conservation of the magnetisation vector. As a consequence, an adequate way to describe the generalised LLG equation is to use the following form:

$$\frac{d\boldsymbol{M}}{dt} = \sum_{i=1}^{n} \boldsymbol{\Gamma}_i$$

where:

$$\forall i \in \{1, ..., n\},\ \boldsymbol{M} \cdot \boldsymbol{\Gamma}_i = 0$$

The most suitable description of the spin torques generated by a spin current, as Slonczewski expressed it [13], is to consider the directions as a function of the spin current polarisation $\boldsymbol{\sigma}$: indeed the equation of motion of magnetisation can be written in terms of $\boldsymbol{m} = \frac{\boldsymbol{M}}{M_S}$:

$$\frac{d\boldsymbol{m}}{dt} = -\gamma_0 \boldsymbol{m} \times \boldsymbol{H}_{eff} + \alpha \boldsymbol{m} \times \frac{d\boldsymbol{m}}{dt} + \Gamma_{\parallel} \frac{\boldsymbol{m} \times (\boldsymbol{m} \times \boldsymbol{\sigma})}{|\boldsymbol{m} \times \boldsymbol{\sigma}|} + \Gamma_{\perp} \frac{\boldsymbol{m} \times \boldsymbol{\sigma}}{|\boldsymbol{m} \times \boldsymbol{\sigma}|}$$

The additionnal torques are called respectively “damping-like” and “field-like”, because in the case where $\boldsymbol{H}_{eff}$ is cancelled, we find the regular LLG equation where the spin polarisation $\boldsymbol{\sigma}$ acts like the effective field. However, in the case where the spin polarisation is not aligned with the effective field, this equation is much more complex, and both additional torques can be expressed in terms of precessional torque and damping torque.

In this section, we have given a short summary of the representation of the magnetisation dynamics. Since we have presented earlier a wey to generate spin currents through spin Hall effect, let us now focus on the action of these on the magnetisation as torques, especially on magnetic domain walls. Let us also disclose results from the literature concerning magnetic domain walls displacements induced by an applied magnetic field.

I.6 Domain wall motion in thin ferromagnetic layers

It has been well-known since the discovery of magnetism that magnetic fields can manipulate the magnetisation. It has thus been an obvious method to achieve magnetic domain wall motion. However, an additional mechanism has been proposed by Berger in 1978, involving only an electric current flowing through the magnetic layer. In this section, we start by introducing the concept of magnetic domains and domain walls. Then, we summarise the progress in field and current induced domain wall motion in ferromagnetic thin layers.

I.6.1 Magnetic domains and domain walls

The interactions presented above give several behaviours that tend to be favoured. First, the Heisenberg exchange is the interaction that tends to align neighbour spins in the case of a ferromagnetic coupling like in iron, cobalt or nickel for instance. Then, the shape and magnetocrystalline anisotropies give preferential directions, that may not be the same. Furthermore, the field gives an additional direction of interest, that can be chosen arbitrarily. Eventually, in the case of multilayers, the RKKY coupling can mimic the interactions between two distinct layers.

From this set of interactions, two simple kinds of magnetic configurations can be studied in particular. First, when the Heisenberg interaction dominates, all the moments must be in the same direction. Since this interaction is very strong, this can lead to what is called a macrospin state. In that case, all the magnetic moments are aligned. We can represent the whole magnetic material as just one spin in this approximation.

However, this representation cannot reflect all the cases. Indeed, in the case of thin films, for instance, the dipolar interaction, which is a long range interaction, does not favour a macrospin state. Indeed, in the case of a strong out-of-plane magnetocrystalline anisotropy that gives rise to an out of plane easy axis of magnetisation, the shape anisotropy is constant, and maximised (in that case, we can use the formula I.4). For large samples, the magnetic configuration is not uniform throughout the sample. In that case, the magnetisation splits into magnetic domains in which the magnetisation is uniform, that are separated by magnetic domain walls, that consist in a continuous rotation of the magnetisation from one direction of the easy axis of magnetisation to the other one. This magnetic structure is called Weiss domains.

Let us consider the simplest model to establish the width of a domain wall under no applied magnetic field in a 1 dimension geometry. In this calculation, we will only consider the magnetocrystalline anisotropy and Heisenberg exchange interactions in terms of energy, and study the competition between both, with the boundary conditions that are a constant rotation of the magnetisation from one direction out of the sample's plane to the other. , as shown on fig. I.7. Let us add eventually the hypothesis that the demagnetising field does not play any role. This is equivalent to consider a perfectly spherical sample, which is not the case, and avoids to compute the value of the dipolar interaction in a non uniform magnetisation configuration.

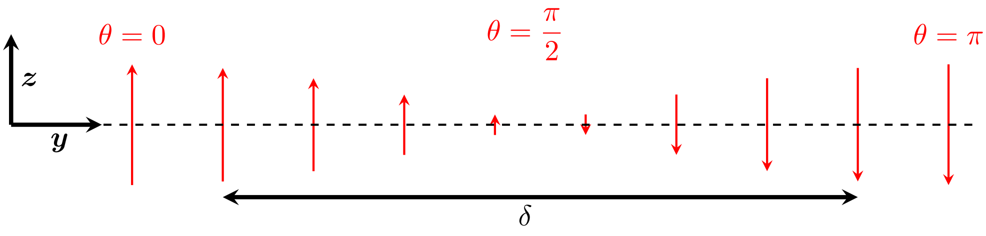

Figure I.7: Simple model representing a Bloch domain wall

Let us consider a Bloch domain wall in the $\boldsymbol{y}$ direction inside a magnetic material of section S. We will consider that the magnetisation can be represented by its angle with respect to an easy axis of magnetisation. Let us call this angle θ. The magnetisation can be described as a function of the angle θ simply as:

$$\boldsymbol{m} = \begin{pmatrix} sin(\theta(y)) \\ 0 \\ \cos(\theta(y)) \end{pmatrix}$$

For the sake of this demonstration, we can consider that the boundary conditions for the function $y \mapsto \theta(y)$ are as follows:

$$\begin{cases} \lim\limits_{y \to -\infty} \theta(y) = 0 \\ \lim\limits_{y \to +\infty} \theta(y) = \pi \\ \lim\limits_{y \to -\infty} \dfrac{\partial \theta}{\partial y}(y) = \lim\limits_{y \to +\infty} \dfrac{\partial \theta}{\partial y}(y) = 0 \end{cases}$$

The exchange interaction for a volume $S \times dy$ in the continuous approach can be written as:

$$dE_E = SA_{ex} \left[(\nabla m_x)^2 + (\nabla m_y)^2 + (\nabla m_z)^2 \right] dy$$

Where A_{ex} is the exchange stiffness. The magnetisation orientation is independent of x and y, which lets us simplify the expression of the exchange interaction as:

$$dE_E = SA_{ex} \left(\frac{\partial \theta}{\partial y} \right)^2 dy$$

The magnetocrystalline anisotropy energy of a volume $S \times dz$ of can be written as a function of the angle θ as:

$$dE_A = -KS \cos^2(\theta) dy$$

For the sake of simplicity, we will use the notation: $f(\theta) = -K \cos^2(\theta)$.

$$dE_A = Sf(\theta) dy$$

At equilibrium, the energy of the Bloch domain wall is minimised. Therfore, the function θ minimises the total energy of the domain wall, expressed as:

$$E = S \int_{-\infty}^{+\infty} \left(A_{ex} \left(\frac{\partial \theta}{\partial y} \right)^2 + f(\theta) \right) dy$$

A small variation of the angle $\delta\theta$ should lead to no variation at the first order in the total energy, which can be expressed using the Euler-Lagrange equation. The Lagrangian function of the system can be expressed as:

$$\mathcal{L}(y, \theta(y), \dot{\theta}(y)) = A_{ex} \dot{\theta}^2 + f(\theta)$$

Where the derivation with respect to y is noted by an upper dot. The Euler-Lagrange equation thus gives:

$$\frac{\partial}{\partial \theta} \mathcal{L} - \frac{\partial}{\partial y} \frac{\partial}{\partial \dot{\theta}} \mathcal{L} = 0$$

Which implies:

$$\frac{\partial f}{\partial \theta} = 2A_{ex} \ddot{\theta}$$

One can multiply each side by $\dot{\theta}$ as follows:

$$\frac{\partial f}{\partial \theta}\dot{\theta} = 2A_{ex}\ddot{\theta}\dot{\theta}$$

Which can be integrated with respect to z as follows:

$$f(\theta) = A_{ex}\dot{\theta}^2 + \lambda$$

Where λ is an integration constant, which can be evaluated to be 0 for positions outside the domain wall, where the magnetocrystalline anisotropy energy is equal to $f(0)$, and the angle θ is constant with respect to the position z.

From this relationship, one can express z as a function of θ by expressing:

$$dy = \sqrt{\frac{A_{ex}}{f(\theta) - f(0)}}d\theta$$

By considering only the first order of a uniaxial magnetocrystalline anisotropy in the $\boldsymbol{z}$ direction, that is to say expressing $f(\theta) = -K\cos^2(\theta)$, one can find:

$$dy = \frac{d\theta}{\sin(\theta)}\sqrt{\frac{A_{ex}}{K}}$$

The integration of this relationship gives:

$$y(\theta) = \sqrt{\frac{A_{ex}}{K}}\ln\left(\tan\left(\frac{\theta}{2}\right)\right)$$

Or equivalently:

$$\theta(y) = 2\arctan\left(\exp\left(\sqrt{\frac{K}{A_{ex}}}y\right)\right)$$

We used the fact that within the domain corresponding to the position $y \rightarrow -\infty$, the angle θ is 0, or equivalently, for $y \rightarrow +\infty$, the angle θ is equal to π to find the integration constant.

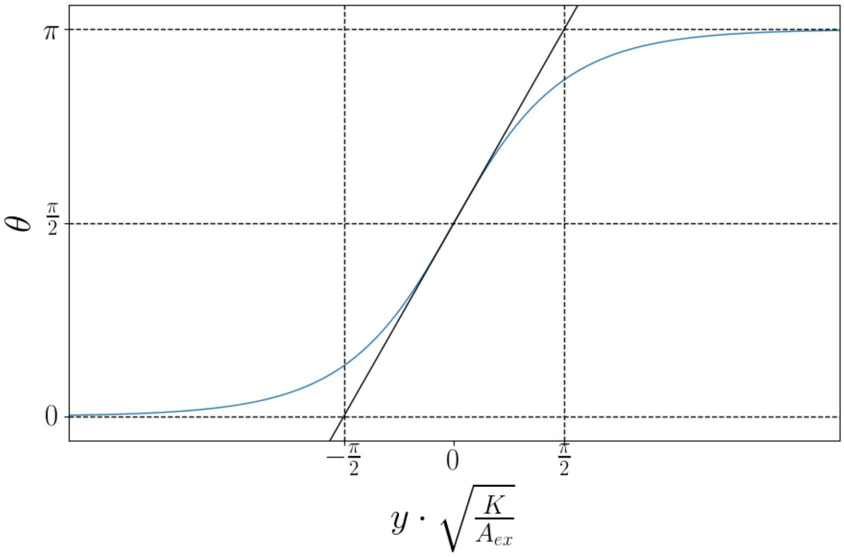

Figure I.8: Evolution of the angle θ representing the local orientation of magnetic momenta as a function of the position z.

This expression, however, does not let θ be equal to 0 nor π for finite values of y, which makes it an infinite domain wall. In order to estimate the domain wall width, one can consider an average variation of the angle as a function of the position as it is in the middle of the domain wall. By doing so, one can find the minimum width δ of the domain wall obtained with this model, which is found to be $\delta = \pi\sqrt{\frac{A_{ex}}{K}}$. In this expression, we can clearly see that the width of the domain wall enlightens the competition between the exchange interaction and the magnetocrystalline anisotropy. Indeed, as expected, a large value of the magnetocrystalline anisotropy tends to decrease δ, leading to a smaller portion of the magnetisation unaligned with the easy axes of magnetisation. Reciprocally, a large value of the exchange interaction leads to small variations of the orientation between neighbour momenta, leading to a wide domain wall, and a large value of δ.

I.6.2 Field induced domain wall motion

A well-known method to manipulate the magnetisation is the application of a magnetic field. The displacement of a magnetic domain wall in the presence of a magnetic field has been studied both theoretically and experimentally. The Landau-Lifshitz-Gilbert equation can be solved analytically, using the Lagrangian method shown in [94], and considering a rigid unidirectional domain wall, and three regimes can be obtained. According to [95], for low fields, inferior to $H_W = \frac{1}{2}\alpha M_S|N_y - N_x|$ (where α is the magnetic damping, M_S is the saturation magnetisation of the magnetic material, and N_x and N_y are diagonal coefficients of the demagnetising tensor corresponding to the geometry of the sample), the speed of the domain wall shows a linear dependence with the applied magnetic field. When the Walker field is reached, the domain wall speed decreases with the applied magnetic field. A third regime is identified in [95]: for larger fields, a precessional propagation regime occurs, linearly with the field, but the slope is much lower than in the low field regime. Thus, the maximum field induced domain wall speed that can be achieved in ferromagnets is small.

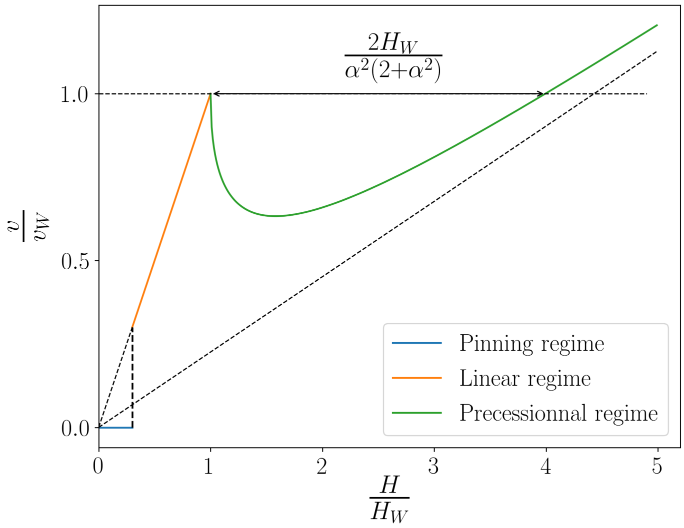

Figure I.9: Evolution of the domain wall velocity as a function of the applied magnetic field, for $\alpha = 0.54$

In the three regimes identified, we have omitted the very low field regime, where no domain wall motion is achieved due to domain wall pinning. The evolution of the domain wall speed as a function of the applied magnetic field can be summarised as shown in fig. I.9. Let us note that in this figure, we have chosen a particularly large value of the damping constant ($\alpha = 0.54$)

to see clearly all the behaviours on the same graph. We can especially notice that, even though for infinite values of the field, the domain wall velocity is supposed to reach arbitrarily large values, the slope of the linear asymptot is $\frac{\alpha^2}{1+\alpha^2}$, which is very slow for usual magnetic materials ($\alpha \leq 0.1$).

Indeed, the Walker breakdown induces a very restrictive limit. For magnetic materials with regular damping ($\alpha = 0.1$) or even lower, the walker speed is overcome in the precessional regime for field values superior to $100 \times H_W$. Experimentally, only low speeds have been achieved in ferromagnets.

I.6.3 Current induced domain wall motion

In 1978, Berger [8] proposed a theoretical mechanism that would enable a charge current to get spin polarised by flowing through a ferromagnetic material, and then being able to transfer angular momentum to the localised moments of the magnetic material [9,10]. This phenomenon, known as spin transfer torque, has also been studied by Slonczewski in the 1990's [12, 13, 96], and these theoretical works predict that a spin polarised charge current could move a magnetic domain wall.

Since the experimental techniques at the time of Berger's first articles on the topic could not achieve the growth of very thin magnets, and considering the current densities that are usually needed (in the order of magnitude of $10^{12} A.m^{-2}$, the experimental confirmation of the analysis of Berger and Slonczewski was impossible to carry out. However, with the enhancement of the materials deposition techniques, the current induced domain wall motion could be observed in the 2000's. Even though rather high speeds could be obtained ($\approx 20 m.s^{-1}$, [97]), a Walker breakdown-like phenomenon occurred for a certain threshold of current density. Indeed this method was also very limited in the scope of magnetic information technologies.

However, this domain wall motion method turns out to be very efficient in peculiar materials such as ferrimagnets around the angular compensation [98, 99], or synthetic ferrimagnets close to the net magnetisation compensation In this manuscript, we are going to investigate the latter in details.

I.6.4 Zhang and Li torques and current induced domain wall motion

Beyond the representation of the torques acting on the magnetisation proposed by Slonczewski, Zhang and Li [14] gave a new representation of the torques acting on a non uniform magnetisation structure, adding displacement terms depending on the spatial variation of the magnetisation. The equation given by Zhang and Li, corresponding to the motion of a non uniform magnetisation in which a spin polarised current displaces along the $\boldsymbol{x}$ direction, is the following:

$$\frac{\partial \boldsymbol{m}}{\partial t} = -\gamma_0 \boldsymbol{m} \times \boldsymbol{H}_{eff} + \alpha \boldsymbol{m} \times \frac{\partial \boldsymbol{m}}{\partial t} - b_J \boldsymbol{m} \times \left(\boldsymbol{m} \times \frac{\partial \boldsymbol{m}}{\partial x} \right) - c_J \boldsymbol{m} \times \frac{\partial \boldsymbol{m}}{\partial x}$$

In this expression, $\boldsymbol{H}_{eff}$ is the effective field, γ_0 is the product of the vacuum permeability and the gyromagnetic ratio, $\boldsymbol{m}$ is the magnetisation divided by the saturation magnetisation M_S, α is the magnetic damping, b_J and c_J are respectively the adiabatic and the non adiabatic torques parameters. These parameters are defined as:

$$\begin{cases} b_J = \dfrac{P J \mu_B}{e M_S (1+\xi^2)} \\ \\ c_J = \dfrac{P J \mu_B \xi}{e M_S (1+\xi^2)} \end{cases}$$

where J is the current density, μ_B is the Bohr magneton, P the spin polarisation, e the electric charge of an electron, M_S the saturation magnetisation. ξ is defined as the ratio of two time constants: $\xi = \frac{\tau_{ex}}{\tau_{sf}}$. τ_{sf} is the spin flip relaxation time in the ferromagnetic material, whereas $\tau_{ex} = \frac{\hbar}{SJ_{ex}}$ is a time parameter of the exchange interaction, defined as the ratio of $\hbar$ by the product of the unitless local spin length S and the exchange interaction J_{ex} between the local and itinerant electron spins.

Another formulation of this physical phenomenon was provided by Thiaville *et al.* [100]. The equation of motion of the magnetisation becomes then:

$$\frac{d\boldsymbol{m}}{dt} = -\gamma_0 \boldsymbol{m} \times \boldsymbol{H}_{eff} + \alpha \boldsymbol{m} \times \frac{d\boldsymbol{m}}{dt} - (\boldsymbol{u} \cdot \boldsymbol{\nabla})\, \boldsymbol{m} + \beta \boldsymbol{m} \times [(\boldsymbol{u} \cdot \boldsymbol{\nabla})\, \boldsymbol{m}]$$

In this equation, $\boldsymbol{u}$ is a vector oriented in the direction of the electrons motion, and which norm u is defined as $u = \frac{1+\xi^2}{\xi} \frac{g}{2} c_J$ where g is the Landé factor and β is the non adiabatic spin transfer parameter, supposed to be small, of the same order of magnitude than α. The u parameter, proportional to the current density flowing through the domain wall, is often the parameter as a function of which the domain wall velocity is studied.

I.7 Field induced domain wall motion in synthetic ferrimagnets

This study that is presented here was carried out by members of the spintronics team of Pr. Mangin [101] in collaboration with other scientists. It is presented as part of the literature. ***I did not contribute to the works that are presented in the section I.7.***

In the previous sections, we have shown several theoretical elements concerning the field- and current-induced magnetisation reversal in a thin ferromagnetic film. Let us now focus on one of the main limitation of the field-induced domain wall propagation in synthetic ferrimagnets. The main point that will be made here is that these materials, the Walker breakdown can occur for values of the applied magnetic field lower than what one could expect.

I.7.1 Description of the experiment

The quantity that we want to characterise is the domain wall speed when a magnetic field is applied. In the case studied, a field pulse is applied during a given period, and the displacement of the domain wall is observed by MOKE means. The speed is estimated to be the ratio of the displacement by the duration of the pulse. This corresponds to a “flight time” measurement. We represent on fig. I.10 the magnetic loop of the sample that was studied in the works of Hamadeh *et al.*. On this, we can mainly distinguish four magnetic stable states noted P^+, AP^+, AP^- and P^-. The P states correspond to a parallel alignment of the magnetisation of both layers whereas the AP states represent an antiparallel alignment of these magnetisations. The + and − exponents correspond to the sign of the projection of the total magnetisation on the axis perpendicular to the sample's plane, ascending from the substrate to towards the capping layer. A more careful representation of these states is presented in subsection I.8.2.

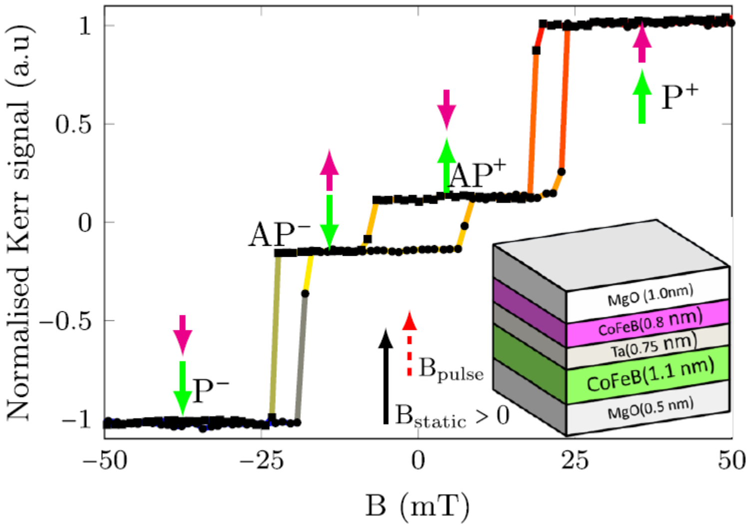

Figure I.10: Magnetic hysteresis loop obtained by MOKE microscopy at room temperature of the system studied: $MgO(0.5)/CoFeB(1.1)/Ta(0.75)/CoFeB(0.8)/MgO(1)$ (the thicknesses are given in nm). (Excerpt from [101])

The measurements that are performed on the $AP^+ \mapsto P^+$ domain wall are prepared in the following way: an AP^+ domain is nucleated in a P^+ saturated state. The whole is stabilised at an applied magnetic field of $\mu_0 H = 19.5$ mT. Then, a rectangular field pulse is applied to the sample. For a given amplitude of the field, several field durations are considered. Then, by measuring the displacement as a function of the pulse duration, a linear dependence is found, and its slope is considered to be the domain wall speed corresponding to the applied magnetic field. We represent the evolution of the domain wall speed recorded by Hamadeh *et al.* for the $AP^+ \mapsto P^+$ transition in fig. I.11:

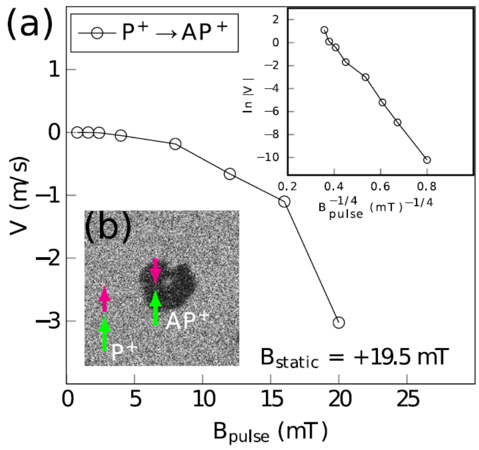

Figure I.11: Domain wall speed for the $AP^+ \mapsto P^+$ transition as a function of the amplitude of the field pulse around the static field $\mu_0 H_{static} = 19.5$ mT. (Excerpt from [101])

The results for this transition give usual results: the inset in fig. I.11 shows the evolution of the logarithm of the speed as a function of $\mu_0 H^{1/4}$. The linear trend is a typical feature of the creep regime of domain wall propagation [102]. However, it is more interesting to consider the $AP^+ \mapsto AP^-$ transition: indeed the static field to apply is zero, and the coherent propagation of two coupled magnetic domains can prevent pinning points issues.

The same experiment as the one showed on fig. I.11 has been carried out for the $AP^- \mapsto AP^+$. We represent the results on fig. I.12.

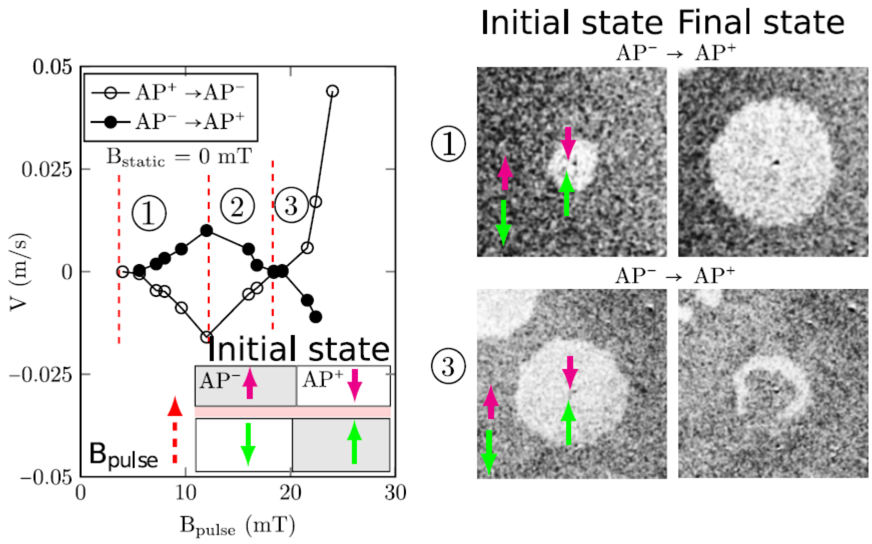

Figure I.12: Domain wall speed for the $AP^- \mapsto AP^+$ transition as a function of the amplitude of the field pulse around the static field $\mu_0 H_{static} = 0$ mT. (Adapted from [101])

The results, however, are significantly different. We can distinguish three regimes in the domain wall speed dependence on the amplitude of the field pulse: for low amplitudes, the propagation of the domain wall occurs, and the most stable magnetic state is favoured. This phenomenon occurs until an amplitude of the field pulse of 12 mT, from where we can observe a decrease of the speed when increasing the amplitude of the field pulse. The end of this second regime occurs around 18–20 mT, which is the exchange field between both layers, as it has been estimated earlier in [101]. Eventually, the third regime corresponds to field pulse amplitudes superior to 18–20 mT. In that case, the state favoured is not the expected one: a positive amplitude favours the AP^- state whereas a negative amplitude lets the AP^+ state propagate. Hamadeh *et al.* provide an explanation to this counter intuitive observation. The understanding of the phenomenon stems from the comparison between the gain of energy of the propagation of two domain walls that are coupled by RKKY exchange, and the propagation of each domain wall alone, breaking the indirect exchange coupling between both magnetic layers. An explanation for these observations is summarised in fig. I.13.

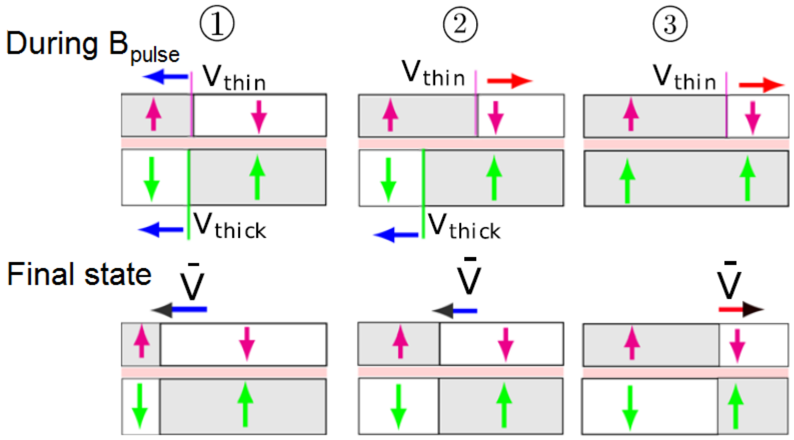

Figure I.13: Evolution of the magnetic configuration during a field pulse in the $AP^- \mapsto AP^+$ transition as a function of the field amplitude regime (1, 2, or 3). (Adapted from [101])

I.7.2 Three domain wall motion regimes

The regime ① corresponds to values of the field where the Zeeman interaction due to this applied field is lower than the indirect exchange between both magnetic layers. In that case, both layers are perfectly coupled and the domain walls in both layers behave as one: the displacement favours the most stable magnetic state, which is AP^+ for positive field pulses B_{pulse}, and AP^- when $B_{pulse} < 0$.

The regime ② appears when the Zeeman interaction and the RKKY coupling are of the same order of magnitude. In that case, each domain wall follows a different direction, and the system relaxes in an intermediate position. Indeed the net displacement at the end of the field pulse is reduced. This phenomenon occurs until the Zeeman energy compensates the indirect coupling, around $B_{pulse} = 19$ mT, where the displacement is null.

Eventually, the regime ③ occurs for higher absolute values of the field pulse. In that case, the AP^- state is not stable anymore, and is assumed to vanish completely during the time of the pulse. Furthermore, the positive field favours the P^+ state, and thus the $P^+ \mapsto AP^+$ domain wall moves in the direction where the AP^+ state is reduced. After the pulse though, the P^+ state is replaced by an AP^- state, due to the exchange coupling that becomes the dominant interaction at zero field. Indeed, in the final state, the AP^- state has grown, and the displacement of the domain wall has an opposite sign to the one of regimes ① and ②.

The main conclusion that one can draw from the results of Hamadeh *et al.* is that a Walker breakdown-like phenomenon, that leads to the limitation of field induced domain wall propagation, occurs at low fields. This phenomenon occurs between the regimes ① and ② presented earlier. However, the sign of the domain wall propagation depends on the amplitude of the field pulse. For the case presented in [101], it is possible to achieve a high domain wall motion for a field pulse that is larger than the exchange field, even though the direction is not intuitive, but the exchange field shown in the article is small. Due to the small exchange energy ($11\mu J.m^{-2}$), the exchange field is estimated to be around 19.5 mT. In the scope of the iridium-based synthetic ferrimagnets, even using the second RKKY peak, the exchange field is around 170 mT. A domain wall displacement at high speeds using field pulses would thus require field amplitudes of a higher order of magnitude than what is shown in this study.

I.8 Quasistatic magnetisation reversal of a synthetic ferrimagnet

In this section, we are going to show a similar study as what was shown earlier in section I.3, but in the case of a synthetic ferrimagnet. This study will be the occasion to compare the Stoner Wohlfarth model to experimental results, and to determine materials parameters, such as the indirect exchange coupling intensity.

In the case of synthetic ferrimagnets, we will consider two ferromagnetic layers represented as macrospins, and coupled via the RKKY interaction. We will thus have to represent two magnetisations M_1 and M_2. Furthermore, since the RKKY interaction does not depend on the volume, we will treat this problem in terms of surface energy, using again an adapted Stoner Wohlfarth model. Eventually, we will not consider the hard axis magnetic loop case, since it is not useful to our study. Let us start with a short presentation of the motivations that lead us to contemplate synthetic ferrimagnets for domain wall motion first.

I.8.1 Synthetic ferrimagnets for current induced domain wall motion

We have seen in the subsection I.6.3 that the current induced domain wall motion is limited by an equivalent of the Walker breakdown observed in field induced domain wall motion. At this point, the current density threshold that is observed for ferromagnetic monolayers is attributed to a destabilisation of the domain wall [103]. Intuitively, a structure with two ferromagnetic layers pointing in opposite directions diminishes the dipolar field radiated by the domain wall on itself. This intuition has been studied experimentally in 2009 by Herranz [104], and with simulations by Kuteifan *et al.* [105] who performed simulations representing a domain wall speed as a function of the spin current density for such structures, and also as a function of the magnetisation of each layer. Indeed, we represent on fig. I.14 the results obtained by Kuteifan *et al.* concerning the evolution of the domain wall speed as a function of the parameter u as defined by [100]: $u = \frac{gJ\mu_B P}{2eM_S}$ is the ratio of the Landé factor g, the current density J, the Bohr magneton μ_B, the spin polarisation P, and the electric charge of an electron e and the saturation magnetisation M_S, in the case of a single ferromagnetic layer for various values of the non adiabatic spin transfer parameter β (a) and in a synthetic ferrimagnet (b) for various values of both layers magnetisations.

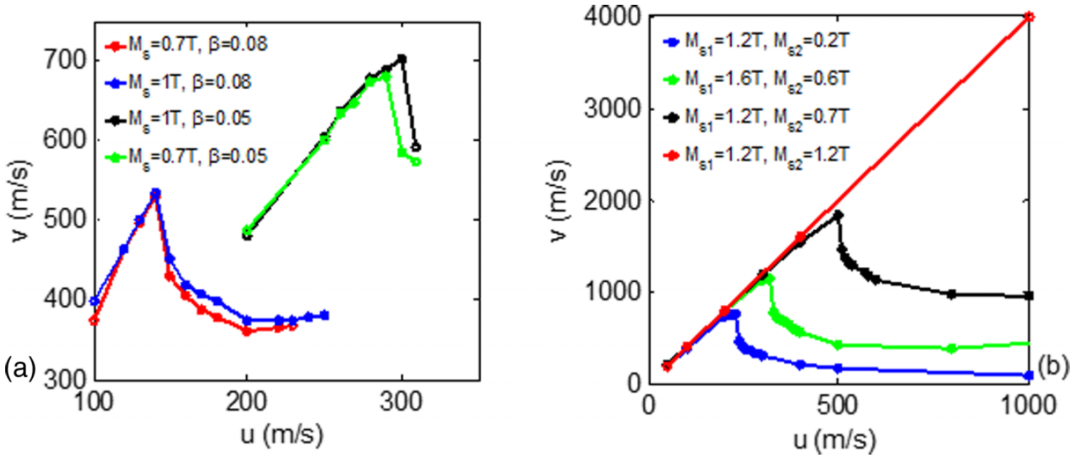

Figure I.14: Evolution of a domain wall speed as a function of the u parameter defined as $u = \frac{gJ\mu_B P}{2eM_S}$: in the case of a single ferromagnetic layer (a), the influence of the saturation magnetisation M_S and the adiabatic spin-transfer parameter β is studied; in the case of a synthetic ferrimagnet (b), the authors focus on the influence of the saturation magnetisation of both layers. **Excerpt from [105]**.

The most striking result is the confirmation of an enhancement of the maximum domain wall velocity achievable with the decrease of the net magnetisation of a bilayer, by means of an increase of the current density threshold. For a perfectly compensated synthetic ferrimagnet (synthetic antiferromagnet, zero net magnetisation out of plane at remanence), the current threshold is pulled to an infinite value, letting the domain wall speed grow arbitrarily large as we increase the current density. This encouraging result leads to the consideration of synthetic ferrimagnets for current-induced domain wall motion.

Indeed, the team of S. S. Parkin carried out many experiments of current-induced domain wall motion in ruthenium based synthetic ferrimagnets. The most impressive result obtained is the domain wall motion speed of $750 m.s^{-1}$ [40], which is thus more than one order of magnitude larger than what was achieved for single ferromagnetic layers.

I.8.2 Most stable states

Let us determine the most stable magnetic states as a function of the applied magnetic field. In order to do so, we will calculate the minima of energy density of the system, but first, let us consider the symmetries of the problem considered: our material was grown by magnetron sputtering using a rotating substrate, leading *a priori* to no preferential axis in the plane of the sample. Furthermore, the magnetisation is expected to have an out-of-plane easy axis. Eventually, the applied magnetic field is applied in the out-of-plane direction. All these arguments let us expect that the magnetisation will have the symmetries of the problem, and will thus be perpendicular to the sample's plane.

Consequently, we can distinguish exactly four magnetic states that can be observed as macromagnetic states: two for which magnetisations are parallel: P^+ when the magnetisation is parallel to the $\boldsymbol{z}$ axis and P^- when the magnetisation is antiparallel to the $\boldsymbol{z}$ axis; and two states where the magnetisations are antiparallel: AP^+ where the net magnetisation is along the $\boldsymbol{z}$ axis, and AP^- where the net magnetisation is along the $-\boldsymbol{z}$ axis.

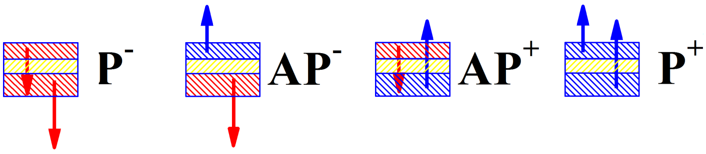

Figure I.15: Representation of the most stable magnetic states under a perpendicular applied magnetic field, as a function of the orientation of the magnetisations of the top and bottom layer. The bottom layer (thicker) is assumed to have a larger net magnetisation than the top layer. We assume an ascending $\boldsymbol{z}$ axis.

A further consequence of the symmetries is that the dipolar energy density, which corresponds to the demagnetising energy density in the case of a macrospin, does not play a role: the magnetisation of each layer can only be in the z direction, which lets invariant the dipolar energy density of each layer. Let us point out that in our approach, we neglect the interaction of the stray field each layer with the other layer's magnetisation. Additionally, the Heisenberg exchange energy density is assumed to be constant (macrospin hypothesis), so we can let it out of all the calculations. Eventually, in all of the possible most stable states, the anisotropy energy density is minimised, beacause the magnetisation is assumed to lie in the easy axis of magnetisation. We can thus exclude this contribution of the energy density from the research of the most stable magnetic configuration as a function of the applied magnetic field.

I.8.3 RKKY coupling

The energy density that one has to consider in this case is a surface energy: in the model we are using, the surface contributions especially due to the magnetocrystalline anisotropy are dominating. Indeed, to determine the lower energy state in the macrospin approximation, we will consider the surface energy ε corresponding to the energy density that follows: $E_{tot} = E_Z + E_{RKKY}$. Let us adapt this formula to compute the energy density of each four states P^+, AP^+, AP^-, P^- as a function of the applied magnetic field:

$$\begin{cases} \varepsilon_{P^+}(H) & = -\mu_0 H(t_1M_1 + t_2M_2) + J_E \\ \varepsilon_{AP^+}(H) & = -\mu_0 H(t_1M_1 - t_2M_2) - J_E \\ \varepsilon_{AP^-}(H) & = \mu_0 H(t_1M_1 - t_2M_2) - J_E \\ \varepsilon_{P^-}(H) & = \mu_0 H(t_1M_1 + t_2M_2) + J_E \end{cases}$$

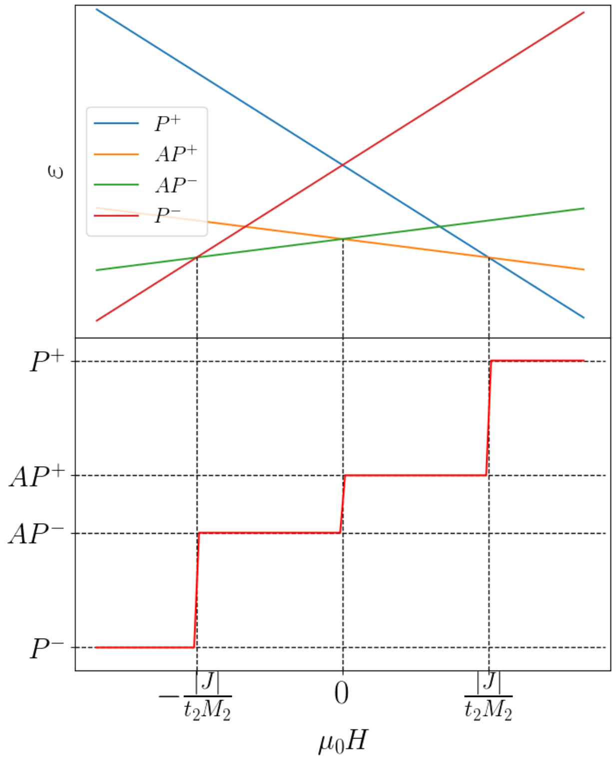

Figure I.16: Most stable states according to a macrospin approach.

The first observation one can make from these four equations is the field symmetry of the expressions. At first sight, we can clearly note that:

$$\begin{cases} \varepsilon_{P^+}(H) = \varepsilon_{P^-}(-H) \\ \varepsilon_{AP^+}(H) = \varepsilon_{AP^-}(-H) \end{cases}$$

Which is a direct consequence of the symmetry of the problem. We can thus only study the most stable states for a positive applied magnetic field, and use the symmetry to complete our study. The expected states for positive fields are P^+ and AP^+, due to their total magnetisation that would then be parallel to the magnetic field. The energy densities of these states are equal at a value of the field given by:

$$\mu_0 H_{AP^+ \leftrightarrow P^+} = \frac{J_E}{t_2M_2} \tag{I.10}$$

The slopes of both linear equations thus state that the state P^+ is the most stable state for $\mu_0 H \geq \frac{J_E}{t_F M_2}$ (and symmetrically, P^- is the most stable state for $\mu_0 H \leq -\frac{J_E}{t_F M_2}$), and AP^+ is the most stable configuration for $0 \leq \mu_0 H \leq \frac{J_E}{t_F M_2}$ (and by symmetry, AP^- is the most stable configuration for $-\frac{J_E}{t_F M_2} \leq \mu_0 H \leq 0$

The energy density description of the samples described above can be represented schematically as shown on fig. I.16.

I.8.4 Influence of the ferromagnetic layers thickness

Let us now consider another parameter of influence, that is the thickness of the magnetic layers of the stack. This dimension is of major importance, because it clearly determines the net magnetisation of the sample. In the following paragraphs, we choose to keep the thickness of the top cobalt layer constant, and we vary the thickness of the bottom cobalt layer. We will divide this study in two parts: first, we consider the evolution of the behaviour of the stacks as a function of the thickness of the bottom cobalt layer in terms of energy density terms, through the Stoner-Wohlfarth model, and then we analyse experimental results obtained from a series of samples corresponding to this parameter study. **Let us point out at first sight that the considerations made here are based on the analysis of the width of an hysteresis loop, which can only be qualitative**.

Stoner-Wohlfarth approach

We have already studied the outer loops switching field in a Stoner-Wohlfarth model, leading to a determination of the RKKY exchange coupling. We only used the centre of the hysteresis loop then, because it is very narrow, according to the experimental results. Concerning the influence of the cobalt thicknesses, we will focus on the $AP^+ \leftrightarrow AP^-$ transition.

In this transition we want to characterise, the switching can occur only because of the difference of Zeeman energy, the two configurations being perfectly symmetric with respect to the sample's plane. The hysteresis loop being centered on 0 field, what matters here is the width of the hysteresis loop. We can then understand the switching of the magnetisation as the crossing of an energy barrier that is caused by the magnetic anisotropy. Let us consider that the orientation of the magnetisation of both layers can be represented by their angle with the perpendicular-to-the-plane direction. Let us consider that the angle is the same for both layers, in a macrospin approximation, leading to minimising the RKKY exchange energy density. We represent the energy densities involved as a function of this angle on fig. I.17.

Let us determine the width of the centered hysteresis loop as a function of the energy barrier represented here. First, the macrospin assumption leads to the following total surface energy of the system, using eqs. (I.2) and (I.5):

$$\varepsilon_{tot} = \varepsilon_Z + \varepsilon_A = -\mu_0(t_1 M_1 - t_2 M_2) H \cos(\theta) - K \cos^2(\theta)$$

We can now express the angle θ_{max} maximising the total energy density by cancelling the derivative of ε_{tot} with respect to θ:

$$\theta_{max} = \arccos\left(\frac{\mu_0(t_2 M_2 - t_1 M_1) H}{2K}\right)$$

The amplitude of the energy barrier is then defined as:

$$\Delta\varepsilon = \max_{\theta \in [0,\pi]} (\varepsilon_{tot}(\theta)) - \max(\{\varepsilon(\theta = 0), \varepsilon(\theta = \pi)\})$$

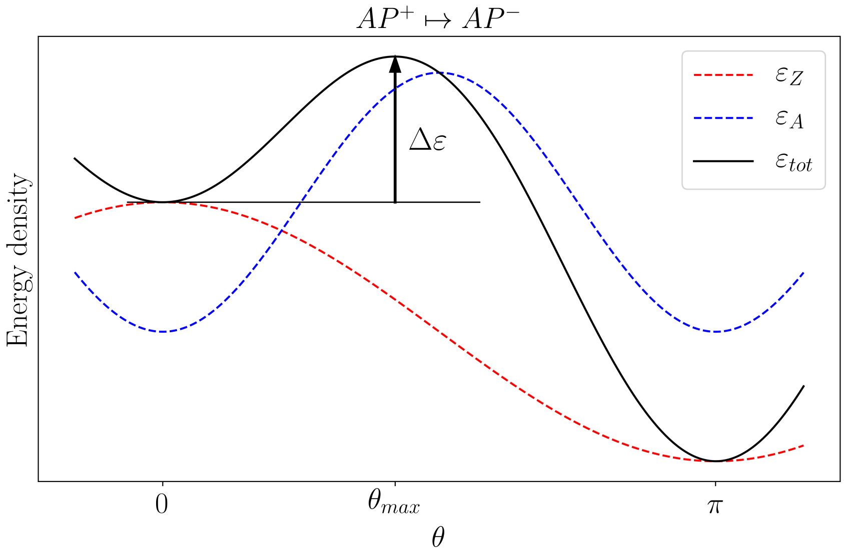

Figure I.17: Macrospin energy density as a function of the angle θ between the magnetisation of the cobalt layers and the out-of-plane axis for the $AP^+ \leftrightarrow AP^-$ transition.

We can evaluate this relationship as a function of the applied magnetic field as:

$$\Delta\varepsilon = \mu_0(t_1M_1 - t_2M_2)H\left(1 - \frac{\mu_0(t_2M_2 - t_1M_1)H}{2K}\right) + K\left(1 - \left(\frac{\mu_0(t_2M_2 - t_1M_1)H}{2K}\right)^2\right)$$

The previous equations enable us to find the coercive field, by letting θ_{max} being equal to 1 or -1, or letting $\Delta\varepsilon$ be null. We obtain thus the expression of the switching field that follows:

$$\mu_0 H_S = \frac{2K}{\Delta tM}$$

In the previous expression, we note ΔM the absolute value of the difference of both magnetisations multiplied by the corresponding thickness: $\Delta tM = |t_1M_1 - t_2M_2|$. If we consider that the magnetisations of both layers should be very close one to another, by calling M_S the common magnetisation, and Δt the absolute value of the difference of both thicknesses, one can express the coercive field as:

$$\mu_0 H_S = \frac{2K}{M_S\Delta t} \tag{I.11}$$

Let us also remember from eq. I.10 that the outer loop switching field is also dependent on the layer of smaller magnetisation, as well as on the total magnetic thickness of both layers. We can thus observe both switching fields as a function of the thicknesses of both cobalt layers.

I.8.5 Magnetic transitions and pinning points

Now that we have a deeper understanding of the magnetic transitions that can occur, and their dependences on the thickness of the layers of materials, let us characterise the shape of the magnetic domain walls. The method that we chose is the magneto-optic Kerr effect imaging. This technique enables us to probe the whole magnetisation of our samples because of their very small thickness. The spatial precision is also adequate, since we can see details down to few micrometers, which is the order of magnitude that matters to us.

We especially want to see the difference between the ferromagnetic to ferrimagnetic and ferrimagnetic to ferrimagnetic transitions. We expect from literature a significant difference between both transitions, due to the fact that ferrimagnetic to ferrimagnetic transitions correspond to simultaneous switching of both magnetisations, whereas ferromagnetic to ferrimagnetic transitions correspond to a monodomain in one of the magnetic layers, and a magnetic domain wall propagating only in the other magnetic layer.

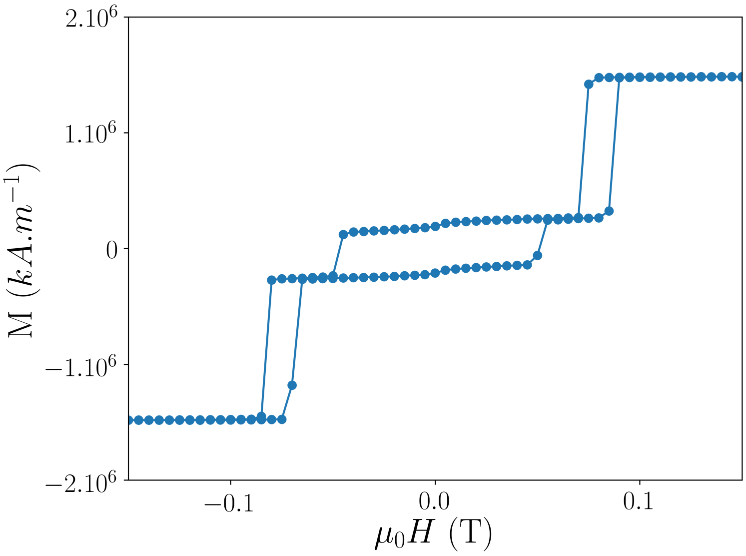

Figure I.18: Magnetic hysteresis loop of the synthetic ferrimagnet $Ta/Pt/Co(0.95)/Ir(1.5)/Co(1)/Pt$: Evolution of the magnetisation as a function of the applied magnetic field

We present the hysteresis loop of a synthetic ferrimagnet at room temperature on fig. I.18. We chose this sample because it exhibits all the transitions by sweeping the field from negative to positive.

On fig. I.19, we present Kerr imaging of the magnetic transitions occurring in the synthetic ferrimagnet during the hysteresis loop displayed on fig. I.18. First, we can notice a field symmetry in the transitions: a and f, b and e, and c and d represent the transitions that are symmetric with respect to the applied magnetic field. The images b and e show smooth bubbles propagating with no noticeable pinning point, with the exception of a scratch that is also visible on images c and d. On the other hand, images a and f show irregular shapes of domain wall, with a dendritic-like appearance, and numerous nuclei. Similarly, on images c and d, the domain wall looks irregular, and numerous pinning points can be seen.

This observation has already been reported in previous works by P. Pirro *et al.* [106]. The explanation that holds from the samples we work on is the following: the magnetic domain wall propagation can be stopped by pinning points due to defects in the material. By only considering these defects, we can expect a 1 layer domain wall to be easily pinned by a simple defect in the layer it is propagating in. However, for a 2 layer domain wall, a pinning point in only one of the layers can be overcome because of the propagation of the domain wall in the layer that is not pinned. The exchange between the domain wall in the pinned layer and the domain wall in the other one can let both domains propagate and diminish the influence of pinning points, unless the defect that pins the domain walls is present at the exact same location in both layers (which can be the case for a deep scratch for instance, as shown on fig. I.19 b – e).

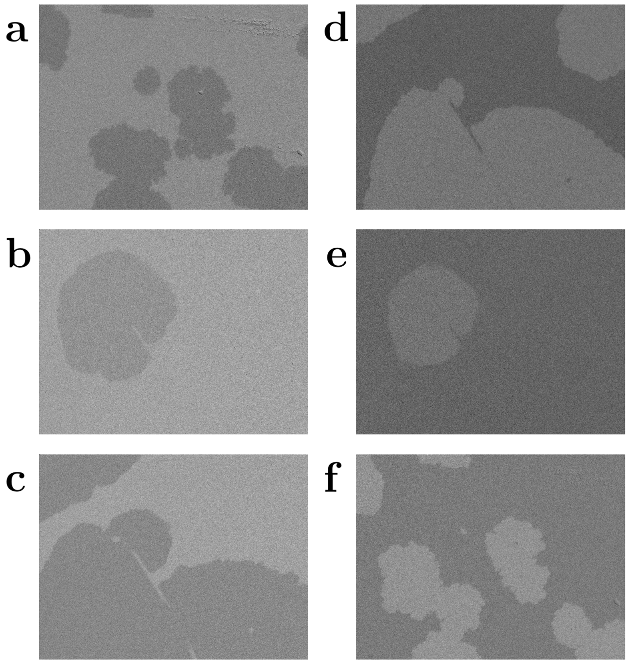

Figure I.19: Propagation of magnetic domain walls under applied field for the transition: $P^- \mapsto AP^-$ (a); $AP^- \mapsto AP^+$ (b); $AP^+ \mapsto P^+$ (c); $AP^- \mapsto P^-$ (d); $AP^+ \mapsto AP^-$ (e); $P^+ \mapsto AP^+$ (f)

I.9 Conclusion

In this chapter, we have provided means of understanding of the field induced behaviour of magnetic thin films that can be considered as macrospins. Indeed we have introduced the main interactions that govern the magnetisation state, as well as the equations of motion of the magnetisation when subjected to various excitations, such as a static field or a spin polarised current. These elements are the basis of further analysis, as well as experimental characterisation of our samples.

Besides, we have presented the chronological progress made in the domain wall motion field induced by current and field. We have given the main steps in the enhancement of the domain wall speed that were achieved in the past decades, and also explained why synthetic ferrimagnetic bilayers are considered as very promising candidates to propagate domain walls at high velocities.

This state of the art chapter lets us now contemplate in details new results about iridium-based synthetic ferrimagnets.

Chapter II

Methods

This chapter is devoted to the presentation of experimental details of the setups that were used to obtain the results presented in the rest of this manuscript. Amongst the tools that were used, we can distinguish three main categories corresponding to the fabrication of the samples, the measurement of the magnetic hysteresis loops, and the spin transport measurement. We will thus present in this order the main devices that were used. Let us note that for the spin transport setups, a more precise study of the methods is given in the last chapter of this manuscript.

II.1 Physical vapor deposition by magnetron sputtering

The magnetron sputtering is a deposition technique that is widely used in the academic field as well as in the industry, for instance in order to make magnetic memories. This deposition technique relies on the fact that high vacuum ($\leq 5 \times 10^{-8}$ mbar) can be achieved in a chamber, in which the deposition process is lead by the sputtering of an ultra pure target of material thanks to argon ions confined by a magnetron field, and accelerated towards the target by an electric field, as shown on fig. II.1. The collision between the argon ions and the materials target results in the sputtering of the target. Atoms are projected in the chamber, and can be collected on a substrate facing the target, leading to a homogeneous layer of material.

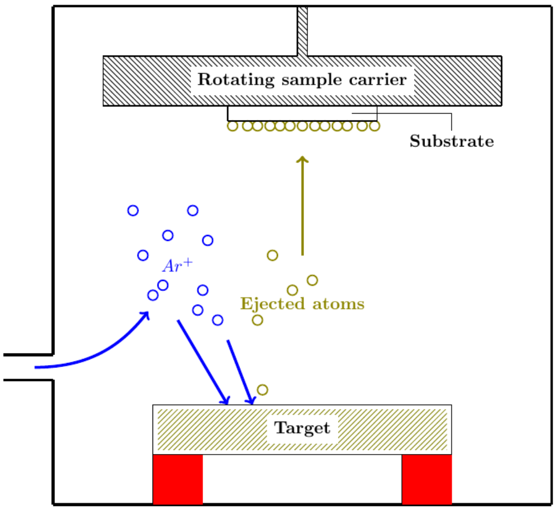

Figure II.1: Physical principle of a magnetron sputtering.

The main parameters of influence to tune the properties of the deposition are the energy of the incident atoms, the purity of the materials supttered and the temperature of the substrate.

The energy of the incident atoms is mainly determined by the argon pressure and the voltage that is applied to the target. On the one hand, the higher the applied voltage, the larger the speed of argon ions that sputter the material target chosen, therefore the larger the incident atoms energy. On the other hand, the pressure of argon is linked to the number of collisions that will occur between an incident atom and the atoms of the argon atmosphere. Indeed, the larger the argon pressure the lower the incident atoms energies.

The energy of the incident atoms can have various effects on the quality of the deposition. It was for example shown by Thornton [107] that the larger the incident energy, the smaller the roughness of the material. This can be understood considering that the incident atoms energy will be transfered to the atoms at the surface of the layer being grown, which can gain a large mobility, leading to a smoother interface. However, it is well known that if the incident atoms energy is too large, some resputtering can occur. This phenomenon corresponds to the sputtering of the deposition caused by the incident atoms, and can be especially dramatic when a heavy material is sputtered with a large incident energy on top of a light element.

Eventually, the temperature of the substrate can be an asset to improve the crystalline quality of the samples grown. A large temperature combined with a low deposition rate can even lead to an epitaxial growth using this method [108, 109]. Even though this method seems appealing, the corresponding drawback is a possible diffusion of the elements of a layer into another, or on the contrary, the segregation of two compounds of an alloy. These are the reasons why we did not try to deposit our stacks at high temperature.

Regarding the thickness of the layers that one can deposit, the precision that can be obtained is the angstrom. Indeed, as we show later in this manuscript, when evaluating experimentally the thickness dependence of the interfacial effect of indirect coupling, a change of 1Å is clearly noticeable on the behaviour of the materials, and easily reproducible.

The sputtering system built by Vinci Technologies is presented on fig. II.2. One of my tasks was to assess the device and try several functionnalities. I could especially perform depositions at temperatures up to 800°C, try both the DC and RF mode, and eventually I performed depositions of titanium in reactive atmospheres composed of O_2 and N_2. From the outstanding quality of the samples grown with this device, I could be certain of the properties of the multilayered stacks that are studied in the rest of this manuscript.

Figure II.2: Sputtering system developped by Vinci Technologies for the Institut Jean Lamour.

II.2 Measurement of a magnetic hysteresis loop

The most interesting properties of the materials that we want to probe are related to the magnetisation. Several tools and methods can lead to a measurement of the magnetisation as a function of the applied magnetic field. In this section, we present two types of effects and devices that are routinely used in magnetometry. These effects can be separated depending on their physical origins. We will first introduce magneto optical effects, and afterwards we are going to describe the superconducting quantum interferometry.

II.2.1 Magneto Optical Faraday and Kerr effects

The interaction of light and magnetised matter has been observed since the 19^{th} century mainly by John Kerr [110, 111]. Amongst numerous magneto optical effects, the Faraday and Kerr effects are very often used to characterise magnetic materials. These effects stem from the same causes, that are an asymmetry in the dielectric tensor induced by the magnetisation of the material. Indeed, the propagation of light within materials is derived from the Maxwell equations, and in anisotropic materials, this propagation depends on the magnetic permeability $\boldsymbol{\mu}$ and the dielectric permittivity $\boldsymbol{\varepsilon}$. Since the magnetic permeability is nearly equal to the one of vacuum for materials [112], magnetic or not, at visible light frequencies, all the magneto-optical effects that are seen with visible light are thus a consequence of the asymmetry of the dielectric permittivity $\boldsymbol{\varepsilon}$ that can be written as a tensor, in the case of linear homogeneous materials. The consequences are a change in the helicity and ellipticity of light. For instance, let us study the Faraday effect in a material acting on a linearly polarised light. We can express the linearly polarised light as the superposition of a right circularly polarised light and left-circularly polarised light. Indeed, the expression of the electric field of left ($\boldsymbol{E}^-$) and right ($\boldsymbol{E}^+$) circularly polarised light is the following:

$$\boldsymbol{E}^{\pm}(\boldsymbol{r},t) = \frac{E_0}{\sqrt{2}} e^{i(\omega t - \boldsymbol{r}\cdot\boldsymbol{k}^{\pm} + \phi_{\pm})}(\boldsymbol{x} \pm i\boldsymbol{y})$$

Therefore, a linearly polarised light along the $\boldsymbol{x}$ axis can be written as $\boldsymbol{E}^L = \frac{1}{\sqrt{2}}\left(\boldsymbol{E}^+ + \boldsymbol{E}^-\right)$. Considering a linearly polarised incident light that flows in the same way in vacuum or air, regardless of its helicity, we can find that within the material the helicity of the light changes: both helicities do not gain the same phase factor and the amplitudes do not decay at the same rate as a function of the depth. Let us consider a light beam that flows in the $\boldsymbol{z}$ direction, perpendicular to the thin film. We express the electric field as a function of the position along the $\boldsymbol{z}$ axis, regardless of the other components of $\boldsymbol{r}$. The electric field can be written as follows at a depth δ in the material, considering $\phi_+ = \phi_- = 0$ and $z = 0$ at the incident surface:

$$\boldsymbol{E}(\delta,t) = \frac{E_0}{\sqrt{2}}\left(\left(e^{i(\omega t - k^+\delta)} + e^{i(\omega t - k^-\delta)}\right)\boldsymbol{x} + i\left(e^{i(\omega t - k^+\delta)} - e^{i(\omega t - k^-\delta)}\right)\boldsymbol{y}\right)$$

Using the notations: $\bar{k} = \frac{k^+ + k^-}{2}$ and $\tilde{k} = \frac{k^+ - k^-}{2}$, one can transform the previous expression as follows:

$$\boldsymbol{E}(\delta,t) = \frac{E_0}{\sqrt{2}}\left(\left(e^{i(\omega t - (\bar{k}+\tilde{k})\delta)} + e^{i(\omega t - (\bar{k}-\tilde{k})\delta)}\right)\boldsymbol{x} + i\left(e^{i(\omega t - (\bar{k}+\tilde{k})\delta)} - e^{i(\omega t - (\bar{k}-\tilde{k})\delta)}\right)\boldsymbol{y}\right)$$

Once the light has travelled through a total thickness t of magnetic material, we can let it flow through a polariser that is along the $\boldsymbol{y}$ axis (perpendicular to the initial polarisation of the light). The electric field measured can thus be expressed as:

$$E_y(z,t) = \frac{2E_0}{\sqrt{2}} e^{i(\omega t - kz - \tilde{k}\delta)} \sin(\tilde{k}\delta)$$

The amplitude measured can be deduced from $\Phi_F = \tilde{k}\delta$, known as the complex Faraday rotation. It is indeed dependent on the difference of k vectors of the right and left circularly polarised lights, and thus, on the magnetisation orientation of the sample. The Kerr effect corresponds to the same exact phenomenon but in reflexion II.3. The complex Kerr rotation can be expressed as [113]:

$$\Phi_K \approx i \frac{\sqrt{k^+} - \sqrt{k^-}}{\sqrt{\frac{ck^+k^-}{\omega}} - 1}$$

The magneto optical Kerr effect (MOKE) can thus be used to probe a small area of the matter, of the size of the light beam that is used. However, a more promising way to benefit from this effect is to build a microscopy technique using this principle. Since the MOKE can be observed by two successive polarisers, it is possible to attribute a value according to the intensity of light measured. This intensity is dependent on the angle between the light polarisation and the polariser. Indeed, this intensity of light gives an image of the projection of the magnetisation pointing out of the plane of the sample. It is thus possible convert a microscopy image that shows variations of light intensity into a magnetisation mapping using shades of grey, for instance. This technique is widely spread, and is usual to observe magnetic domains in wires or full films as a function of time when magnetic fields or current pulses are applied.

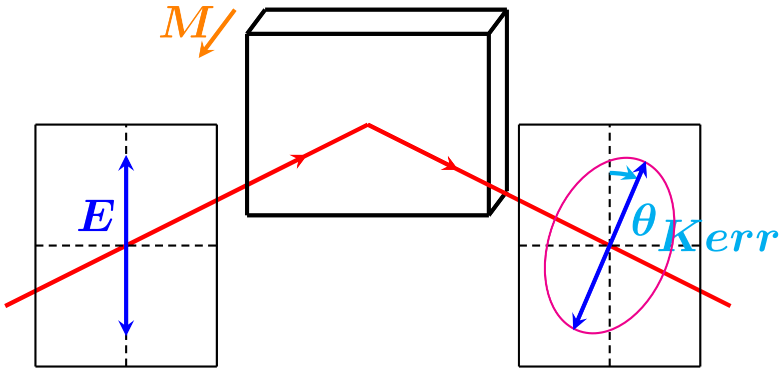

Figure II.3: Representation of the magneto-optical Kerr effect. θ_{Kerr} denotes the rotation of the helicity of the light.

In the setups that are used in Institut Jean Lamour of Nancy, two methods exist. A method consists in converting the helicity rotation into an intensity of light, by using polarisers and measuring the intensity of light. This method gives a local measurement of the magnetisation state, but it does not provide any information concerning the magnetisation evolution as a function of time in the space. For instance, with this tool, it is not possible to observe domain wall motion because the only information displayed concerns the magnetisation state in the small area where the light beam probes the matter. The MOKE equipment available in the Cavendish Lab of Cambridge, that was set up by Jieyi Liu, uses this method in order to probe the magnetisation with a spatial resolution of 3×3 μm^2, for temperatures between 1.6K and room temperature, and for applied fields up to 9 Teslas, which makes it one of the most powerful local MOKE setups. Additionally, it enables the measurement of the magnetisation as a function of time with a time step of around one second. It is also possible to map a surface and measure the MOKE effect over it, but it needs time to sweep the surface, which makes it hard to observe with precision the behaviour of a whole magnetic domain.

Another method is to use the MOKE effect in a microscope. The principle is the same, however the measurement is converted in an image where the black and white contrast corresponds to the magnetisation state. With this microscope, depending on the lens used, it is possible to capture small details, down to the micrometer scale. It is thus possible to observe domains nucleating and domain walls spreading under the action of the field. The setup provided in Nancy enables the direct observation of magnetic domains at room temperature, with a time step that can be tuned between a tenth of a second to several seconds. Indeed, at adequate values of the applied magnetic field, it is possible to observe clearly the nucleation and the propagation of domain walls in many thin layers.

II.2.2 Vibrating Sample Magnetometry (VSM)

It is possible to measure the magnetic moment of a sample using a VSM technique. It consists in making a magnetic sample oscillate over a closed coil, and observe the current induced in it due to the change of magnetic flux that flows through the coil. The mode of detection of the signal can be achieved thanks to various devices. The most precise one is the superconducting quantum interferometer device. This kind of device relies on the Josephson effect that is present in a Josephson ring. This component is composed of a ring of superconducting material in which a weak link is inserted. The DC Josephson effect corresponds to the appearance of a DC current through the non superconducting material in the absence of any applied voltage, referred to as supercurrent. Using the fact that the magnetic flux within a superconductive loop is quantised in units of $\phi_0 = \frac{h}{2e}$, and the relationships between the phase of the supercurrent, it is possible to create a device composed of two Josephson junctions in parallel in which the current flowing in the circuit is modulated by the flux inside the superconducting loop.

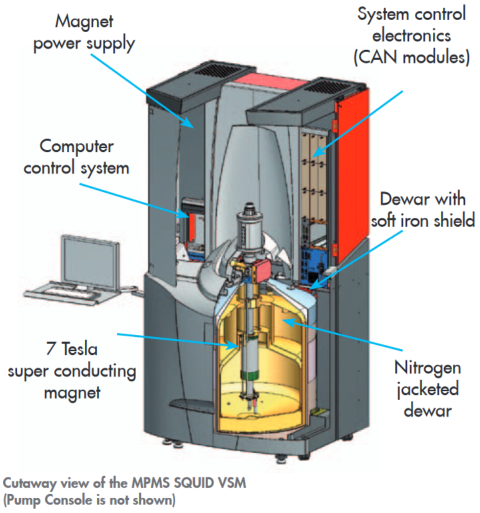

Figure II.4: Schematic of the MPMS SQUID VSM used for the magnetic loops measurements carried out in Nancy. This image was extracted from [114]

The main advantage of this method is that the flux unit of quantisation ϕ_0 is very small, which allows this type of devices to have a great precision. However, it also needs calibrations so as to evaluate the magnetisation of a sample correctly from the magnetic flux that it emits.

The device that I used in Institut Jean Lamour is the MPMS SQUID VSM which is schematically represented in figure II.4.

II.3 Main methods to probe SHE and ISHE

Historically there are two main options to perform a measurement of the direct or inverse spin Hall effects: the spin torque ferromagnetic resonance (ST-FMR) and the spin pumping ferromagnetic resonance (SP-FMR). Both techniques rely on the measurement of the magnetisation dynamics using bilayers composed of a ferromagnetic layer which dynamical behaviour is well-known, and a non magnetic material that we want to characterise. The goal in each case is to measure the interplay between the spin currents and the magnetisation dynamics through rectification effects, and both measurements correspond in the end to an electrical measurement. Accordingly, the samples that we are working on are patterned into wires in both cases. However, there are some major differences between these two experimental techniques that we are going to present.

II.3.1 The spin torque ferromagnetic resonance (STFMR)

The ST-FMR corresponds to the excitation of the magnetisation by injecting an RF charge current that supplies an oscillatory Oersted field and a spin current that acts as an harmonic torque on the magnetisation. The rectification effect that we are probing in this case is the anisotropic magneto resistance (AMR), that is to say the dependence of the electrical resistance on the magnetisation orientation. By this means, we obtain an information on the modification of the magnetisation dynamics, and we can measure the spin current initially supplied thanks to the SHE in the non magnetic material.

This technique is attractive because it relies on the symmetry of the response that is composed of the response to the Oersted field and the response to the spin torques, due to the injected spin current. It is often stated that the symmetric part of the signal is due to the spin torques, whereas the Oersted field produces an antisymmetric response (All the symmetries considered are with respect to the resonance field at the set frequency, or the applied field with respect to the set magnetic field, depending on the type of measurement chosen). This feature makes it an “autocalibrated” measurement: there is no need to characterise the electric circuit in which the excitation propagates, because the Oersted field excitation and the spin torques stem from the same charge current.

The drawback of this method is that the assumption concerning the symmetries of the signal obtained may not always be accurate. Indeed, in usual experimental conditions, the symmetry assumption is due to the fact that the Oersted excitation and the spin torques do not interact with the same coefficients of the magnetic susceptibility χ, and concerning the real part of the matrix, these coefficients are considered as antisymmetric for the diagonal ones, and symmetric for the others, (the imaginary part of the matrix shows an opposite behaviour) which is not exactly true, as shown in the section concerning magnetisation dynamics later in this chapter. Another issue concerning this method is that it does not provide a value of the spin flip length of the non magnetic material that is probed.

II.3.2 The spin pumping ferromagnetic resonance

The spin pumping ferromagnetic resonance represents the “inverse” of ST-FMR. Indeed, in that case, we act on the magnetisation using an antenna generating an Oersted field to drive the magnetisation. We can thus control the magnetisation dynamics without interfering with the non magnetic material in the first place. Then, the magnetisation dynamics is responsible for the generation of a spin current through the spin pumping effect, which is converted in the non magnetic material via ISHE in a transverse charge current. We obtain experimental results by probing the voltage at the terminals of our device.

The main advantage of this technique is that it is supposed to give a signal that is only due to the inverse spin Hall effect. We do not have to face the separation of different components

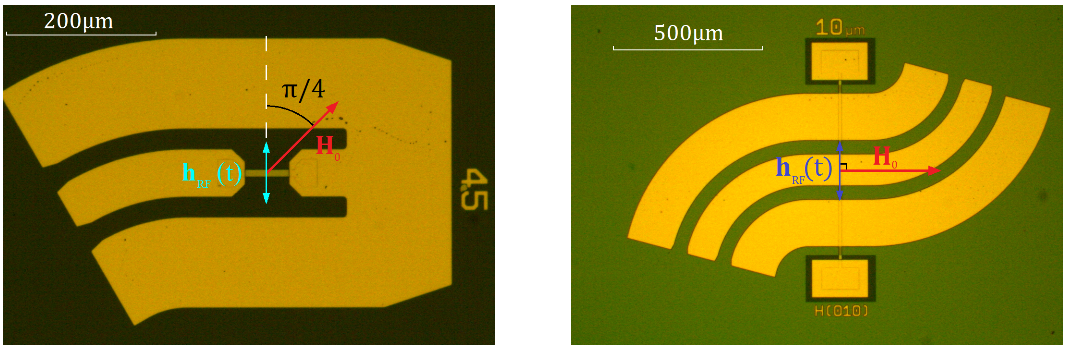

(a) ST-FMR sample (b) SP-FMR sample

Figure II.5: Top view of patterned samples for spin torque (a) and spin pumping (b) ferromagnetic resonances. For STFMR (a), the sample is patterned into an antenna of Ti/Au with a Ground-Signal-Ground (GSG) geometry, and the bilayer is part of the signal. For the SPFMR (b), the sample, patterned into a wire (vertical on the image above), on which an insulating SiO_2 layer has been grown. On top of all this, a Ti/Au curved planar wave guide is deposited (curved yellow lines) in a GSG geometry. The static field $\boldsymbol{H}_0$ and the RF Oersted field $\boldsymbol{h}_{RF}$ applied in the experiment are drawn on the graphs.

in the response. However, the results that are obtained are not easy to quantify since they depend on the amplitude of the Oersted field that is applied to the sample, which is frequency dependant, like all the parts of the propagation line that is used.

We can conclude this section by observing that regardless of the method used, significantly different results have been reported. The same materials have been measured and the values of θ_{SH} and l_{sf} can differ by an order of magnitude. Since there is no clear consensus in the scientific community to unify the method for SHE measurement, it is still up to the experimentalist to choose which of these reciprocal methods is the most suitable.

In our case, we want to measure a material which spin Hall effect was reported only once before, and for which the spin Hall angle is expected to be very small (2%) [43]. After taking a closer look to both methods, we will discuss the choice of the experimental techniques.

Chapter III

Magnetic field study of synthetic ferrimagnets

III.1 Introduction

Now that the physical notions that are needed to understand the whole manuscript have been introduced, let us focus on the magnetic properties of the synthetic ferrimagnets that I have grown. The growth technique has been presented in the introduction, and enables us to fabricate all the samples that are presented in this manuscript.

To start this chapter, I present how we were able to tune the magnetic properties of the synthetic ferrimagnets grown in order to fabricate a model system. In order to do so, we were able to control the exchange coupling between the two magnetic layers that compose our system, and adjust the magnetic compensation to lower the projection of the net magnetisation of the whole stack on the axis perpendicular to the thin film.

Afterwards, I display a study of the magnetic configurations that can be accessed by sweeping the field, depending on the temperature at which the experiment is performed. I could establish three temperature domains that lead to three distinct magnetic loop shapes, according to the possibility to observe various transitions between magnetic configurations.

Eventually, I concentrate on the transitions between two magnetic configurations. We are able to demonstrate non monotonic magnetic aftereffect measurements due to the temperature dependence of the accessible magnetic transitions.

III.2 Magnetic hysteresis loop and quantities of interest

III.2.1 Stacks grown

The stack of the multilayers that were grown and studied by magnetometry is presented in figure III.1. We can especially point out the fact that we use a buffer layer of tantalum. This layer does not play a role for the magnetism, but enables an improvement of the quality of the magnetic layers that were grown above: it is a usual buffer layer. The fact that we use only a small thickness for this layer is mainly due to the fact that above around 5 nm, the tantalum layer gets a preferential crystalline structure that determines the crystalline order of the layers grown on top of it, which is not the effect that we are looking for here. We discuss the role of the platinum layer in the very next paragraph.

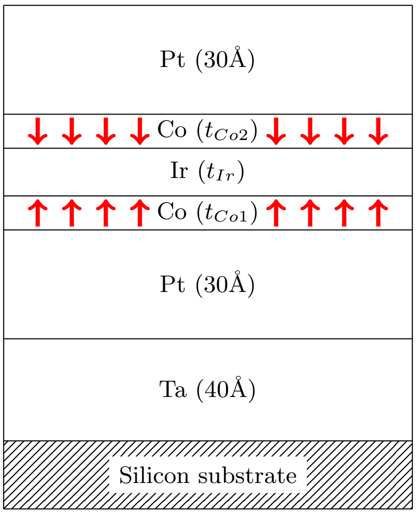

Figure III.1: Stacks grown to optimise the layers thicknesses so as to get a model system for synthetic ferrimagnets for racetrack memory applications. The red arrows represent the magnetisation of the cobalt layers at remanence. The opposite orientation would have been possible as long as both magnetisations were supposed to be aligned in opposite direction so as to satisfy the RKKY interaction. Thus, this configuration was chosen partly arbitrarily.

III.2.2 Perpendicular magnetic anisotropy

One of the features that we want to observe on the magnetic loops measured is the preferred direction of the magnetisation. In order to enable a large storage density as a material for magnetic memory, it is mandatory to obtain an out of plane easy axis of magnetisation. Since the thickness of the magnetic layers in our samples is very small, the demagnetising field makes it challenging to obtain this out of plane magnetisation easy axis. Indeed, the solution that was found is to obtain a large magnetocrystalline perpendicular anisotropy.

The magnetocrystalline anisotropy can be obtained from bulk and surface contributions, as presented in the first chapter. However, the largest contribution that is obtained in our thin films correspond to an interfacial anisotropy. Especially, the Pt/Co interface is well-known for promoting perpendicular magnetic anisotropy. This can be explained by a hybridisation between both materials at the interface, which is due to the large spin orbit coupling of platinum. This hybridisation has been evidenced experimentally, especially by measuring a magnetic enhancement in cobalt as well as in platinum at the interface [115, 116]. Additionally, the strain at the interface because of the lattice mismatch between cobalt and platinum can also play a role in the surface anisotropy [117].

For the materials that we grew, we used the Pt/Co interface that helped us to get perpendicular magnetic anisotropy. It is also likely that the Co/Ir interface helps getting a perpendicular magnetic anisotropy because of a similar lattice mismatch, that would lead to strain at the interface with the cobalt layers, and because of the large spin orbit coupling of iridium. However, let us note that the iridium interface is not sufficient to promote the perpendicular magnetic anisotropy in the stack: all the samples that were grown as multilayers of Ir/Co/Ir had an in-plane remanent magnetisation.

The proof of perpendicular magnetic anisotropy in the magnetic loops is given by the steep transitions that are observed when the magnetic field is applied perpendicularly to the sample's plane. This shows that the out of plane axis is an easy axis of magnetisation. All the hysteresis loops shown in this chapter show sharp transitions as we expect them to be.

III.2.3 Magnetic transitions and remarkable values of the field

In this chapter, we have presented experimental measurements of the magnetisation dependence on the applied magnetic field in an easy axis of magnetisation. As precised in the previous chapter, there are only four accessible magnetic states that we denoted P^+, AP^+, AP^- and P^-. The measurements that we carried out gave us several types of magnetic hysteresis loops, and the most common graphs that we could obtained are schematically represented in fig. III.2.

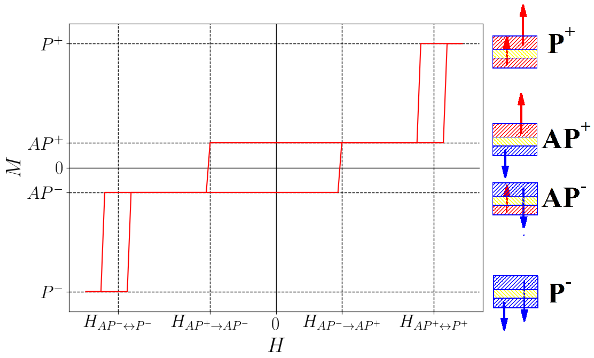

Figure III.2: Schematic of an easy axis magnetic hysteresis loop of a perpendicularly magnetised synthetic ferrimagnet: evolution of the magnetisation as a function of the applied magnetic field along the out-of-plane axis, which is an easy axis of magnetisation.

We can first notice about this cycle that the origin of the graph is a symmetry centre of the curve. Indeed, all the information is contained in a single half of the measurement. We can thus only consider one sign for the applied field. Then, the two most relevant values of the applied magnetic field are obtained when magnetic transitions occur. The field called $H_{AP^-\rightarrow AP^+}$ corresponds to the magnetic transition between the configurations AP^- and AP^+, which involves the switching of the magnetisation of both magnetic layers that compose the synthetic ferrimagnet. The second important value of the magnetic field is the centre of the outer loops, for the transitions $AP^+ \leftrightarrow P^+$. The width of this minor loop is experimentally found to be small, which enables to consider that both switching from AP^+ to P^+ and from P^+ to AP^+ occur at approximately the same value of applied magnetic field.

Now that we have presented the features of a magnetic hysteresis loop that we are going to study, let us focus on the experimental measurements that were carried out in order to characterise the magnetic properties of the synthetic ferrimagnets that we grew.

III.3 Influence of the Iridium thickness on the RKKY coupling amplitude

III.3.1 Measurements

The energetic determination of the most stable magnetic configurations as a function of the applied magnetic field, carried out in the first chapter, provides an easy method for probing the RKKY coupling in synthetic ferrimagnetic structures. However, the determination of the RKKY exchange as we perform it can only give information when the coupling is antiferromagnetic. Indeed when the coupling is ferromagnetic, there is only one main hysteresis loop and two accessible magnetic states, and our method turns out to be ineffective. Therefore, we are only able to measure the RKKY coupling for antiferromagnetic values of the coupling. Fortunately, it corresponds to the effect desired for the applications we consider.

We chose to grow various samples, changing the iridium spacer thickness so as to observe the evolution of the coupling as a function of the iridium thickness, by means of switching fields for the $AP^+ \leftrightarrow P^+$ transition ($H_{AP^+ \leftrightarrow P^+}$), and in an equivalent manner, for the switching fields for the $AP^- \leftrightarrow P^-$ ($H_{AP^- \leftrightarrow P^-} = -H_{AP^+ \leftrightarrow P^+}$).

The measurements that were carried out display the sum of two contributions: the diamagnetic response of the whole stack, and the ferromagnetic contribution that comes from the magnetic materials composing the sample. The diamagnetic part is not a subject of interest to us, and is characterised by a linear response to the field ($\chi_{diamag} \approx -10^{-6}$). We eliminated this part of the signal by subtracting a linear fit of the field dependence of the magnetisation for large values of the field ($1 \leq \mu_0 H \leq 4$ T), where the ferromagnetic contribution is constant.

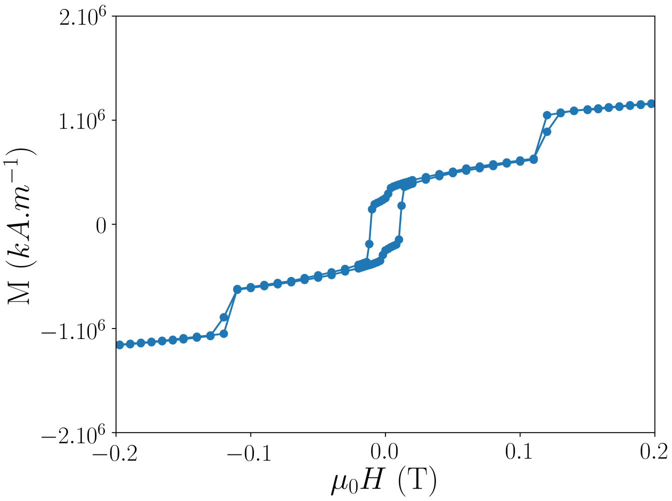

Figure III.3: SQUID magnetic hysteresis loop of a Si//Ta(5)/Pt(3)/Co(0.7)/Ir(1.43)/Co(1)/Pt(3) sample at room temperature. (All thicknesses are in nm)

We also did not take into account a curvy signal in our curves as shown in fig. III.3. This effect has been shown to stem from the edges of the sample where magnetic material was also deposited. We have a confirmation of that conclusion because magneto-optic Kerr microscopy measurements only show the local magnetic behaviour of the material, because the only zone probed corresponds to the location of the light beam, and the results obtained by this local technique do not show this curvy signal. Even though these edges do not represent a large surface, their magnetic signal is not negligible, given the very low thickness of the film. We can also point out that the SQUID measurement is sensitive to the stray field, which can be modified dramatically by the edges.

III.3.2 Results and discussion

On fig. III.4, we represent several easy axis magnetic hysteresis loops of synthetic ferrimagnets of the form: $Si - SiO_2/Ta(5)/Pt(3)/Co(0.7)/Ir(t_{Ir})/Co(1)/Pt(3)$ (All the thicknesses are given in nm). Our interest is to probe the change of switching field ($H_{AP^- \leftrightarrow P^-}$) for the outer loop that is present on all the curves. We interpret the applied magnetic field in the middle of the hysteresis loop as the exact value of transition field predicted by the Stoner-Wohlfarth model as given in eq. (I.10).

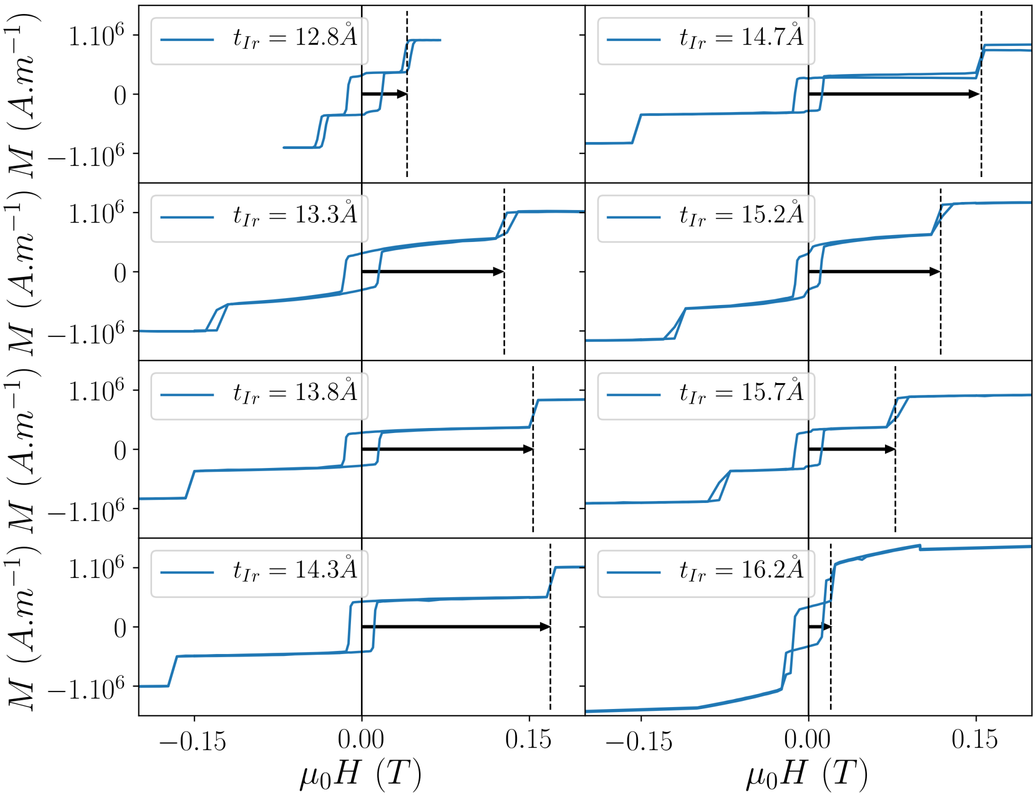

Figure III.4: Magnetisation as a function of the applied magnetic field in Si//Ta(5)/Pt(3)/Co(0.7)/Ir(t_{Ir})/Co(1)/Pt(3) for iridium spacer thicknesses ranging from $t_{Ir} = 12.8$ Å to $t_{Ir} = 16.2$ Å

As expected, the evolution of the switching $H_{AP^+ \leftrightarrow P^+}$ field starts at a low value (around 4 mT) for $t_{Ir} = 12.8$ Å, then increases with the iridium thickness until reaching a maximum of 170 mT for an iridium thickness of 14.3 Å, and eventually plummets until 3 mT for $t_{Ir} = 16.2$ Å. We can compare the values of coupling obtained to what should be obtained according to the RKKY model, and this is what is represented on fig. III.5:

Let us compare the results shown in fig. III.5 with the previous studies published. We can especially compare our findings with the studies of S. S. Parkin [47], in which the author describes a systematic experimental study of the RKKY coupling through various materials, and the article of Yakushiji [118], which focuses on the RKKY coupling in iridium. The value of the exchange coupling found for the first oscillation is 1.85 $erg.cm^{-2}$ (1.85 $mJ.m^{-2}$). According to the literature [58–60], the exchange coupling due to the RKKY interaction decreases as a function of the material thickness as $\frac{\cos(k_F t_{Ir})}{(k_F t_{Ir})^3}$. The period of the oscillations found by Parkin

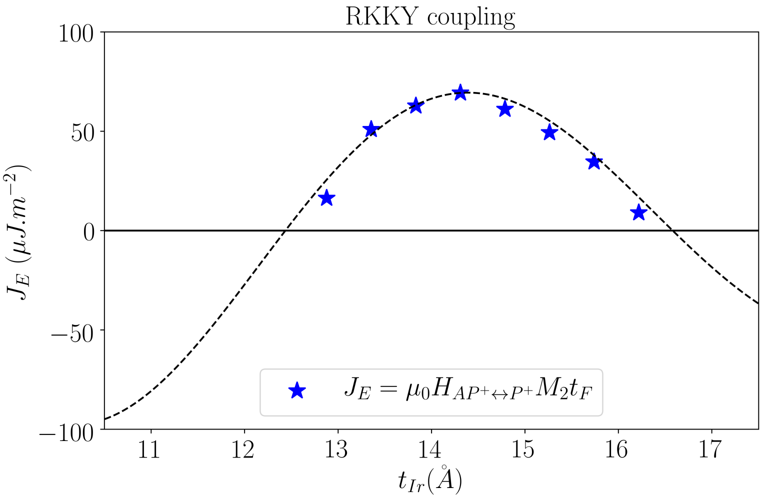

Figure III.5: Measured RKKY exchange constant from Si//Ta(5)/Pt(3)/Co(0.7)/Ir(t_{Ir})/Co(1)/Pt(3) as a function of the iridium thickness (blue stars); The dashed black curve represents the RKKY coupling as predicted by (I.6)

is 9 Å, and the first peak of antiferromagnetic coupling is found at an iridium thickness of $t_{Ir} = 4$ Å. The expected value of the exchange coupling at the second antiferromagnetic peak is thus supposed to be $\left(\frac{4}{4+9}\right)^3$ times smaller than what was found at the first peak, that is to say 54 $\mu J.m^{-2}$. Concerning the study of Yakushiji, both antiferromagnetic peaks are obtained and characterised. The corresponding iridium thickness are 4.5 Å and 14 Å. The amplitudes for these peaks are respectively over than 2 $mJ.m^{-2}$ and 170$\mu J.m^{-2}$.

The value obtained with our experiments show a value of 70 $\mu J.m^{-2}$, which is 30% larger than the value from Parkin, but also less than half of what is obtained by Yakushiji. Concerning the position of the peak, Parkin's study finds the second antiferromagnetic oscillation peak at $t_{Ir} = 13$ Å, and Yakushiji finds it at 14 Å whereas we find it at 14.3 Å. We obtain a difference that is smaller than 10% of the expected value.

The slight difference concerning the position of the RKKY peak can be attributed to the fact that the thickness of the material is not a very precise quantity. Even though the material growth conditions are the best that can be achieved in terms of magnetron sputtering, the interface is very likely to be imperfect and have defects. Furthermore, the roughness of the interfaces might be sufficient to make it hard to define precise thickness of magnetic layers.

Concerning the amplitude of the indirect exchange interaction, since this quantity depends on the surface of the sample, it is likely that a change of quality in the interfaces can modify the observed value of the coupling. Eventually, for both the amplitude and the spatial period of the RKKY coupling, we can argue that the Stoner-Wohlfarth model hypothesis are not perfectly respected, especially due to the fact that the magnetisation is not always behaving as a macrospin, depending on the values of the applied magnetic field. Part of the discrepancies between the different results can thus be imputed to the model. We can conclude from this study that our results are in good quantitative agreement with the previous works of Parkin. However, the large discrepancy between the amplitude of the second antiferromagnetic peak found by Yakushiji and us has to be noted. Our guess is that the quality of the interfaces in our stack does not reach the quality of Yakushiji's. This may be explained by the fact that the stacks of Yakushiji are composed of a buffer and a platinum layer that are initially annealed at 573 K for 300 seconds, which can provide a good crystal quality. Furthermore, between this buffer layer and the iridium one, numerous layers of Co/Pt are grown, which can provide a texture that is likely to improve the interface.

For the rest of the samples that are grown, we set the iridium thickness to 14.3 Å to ensure a maximised antiferromagnetic exchange coupling between both magnetic layers.

III.4 Tuning the magnetic compensation of synthetic ferrimagnets through the cobalt thickness

As mentioned in the first chapter of this manuscript, this cobalt thickness study stems from the comparison of the Zeeman energy and the anisotropy. The latter may be dependent on the position in the sample, and this study assumes no defect leading to an easy nucleation point in the sample, which is very unlikely. ***The theoretical predictions are thus purely qualitative: we do not intend to extract materials parameters here, but to validate a qualitative agreement between the macrospin calculations and the experimental results.***

The experiments that we chose to carry out in order to probe the evolution of the magnetic parameters of the stack are the following: we grew a series of samples with one of the layers with fixed thickness of 1 nm, a constant iridium thickness of 1.43 nm, and a cobalt thickness varying from 7Å to 9.5Å. We measured the magnetisation as a function of the applied magnetic field, and used the previous relation of eq. I.10, I.8.4 in order to estimate materials parameters.

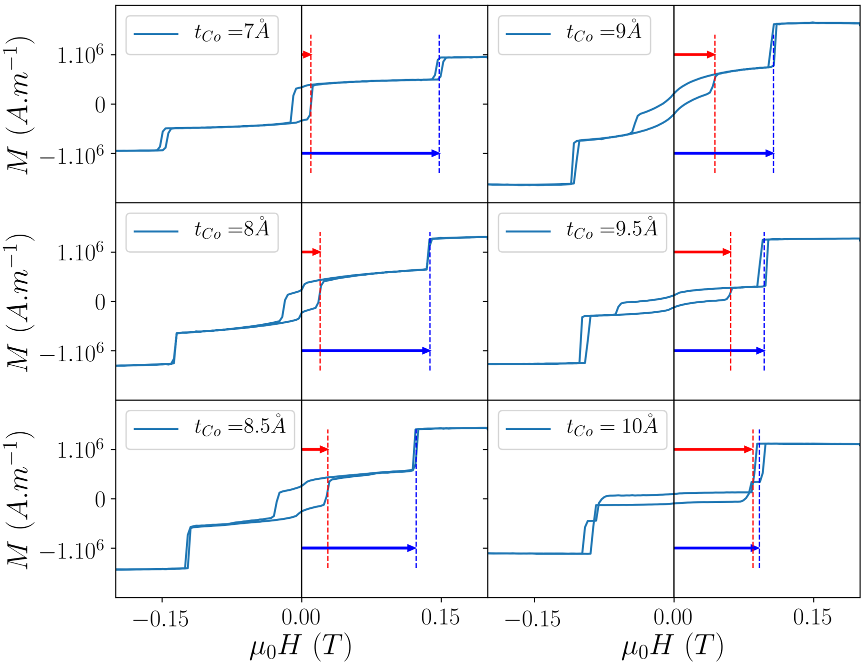

Figure III.6: Magnetisation as a function of the applied magnetic field for Si//Ta(5)/Pt(3)/Co(t_{Co})/Ir(1.43)/Co(1)/Pt(3) with a changing bottom cobalt layer thickness t_{Co} varying from 7Å to 10Å.

We show on fig. III.6 with the red arrow the amplitude of the inner loop coercive field ($H_{AP^+\rightarrow AP^-}$), whereas the blue arrow represents the centre of the outer loop, that we called $H_{AP^+\leftrightarrow P^+}$ in fig. III.2. As we expect from our macrospin calculations, the smaller the difference of thickness between both cobalt layers, the wider the inner loop, due to the competition between the RKKY, which is a surface interaction, and the Zeeman interaction, which is moment (thus volume) dependent. We can also notice a less dramatic decrease of the outer loop switching field when increasing the thickness of the bottom cobalt layer. We represent these evolutions of the switching fields as a function of the thickness of the bottom cobalt layer in fig. III.7.

On this figure, we also add guidelines corresponding to the equations found with the macrospin model in dashed lines (eq. I.10,I.11). However, in order to fit the curves, we had to consider an imperfect sample. In order to do so, we made two assumptions. First, we considered

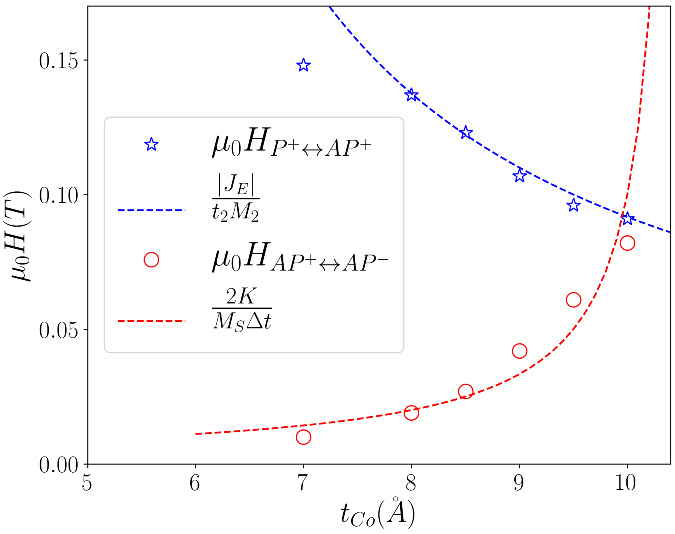

Figure III.7: Evolution of the inner loop (red) and the outer loop (blue) switching fields as a function of the thickness of the bottom cobalt layer in the $Si - SiO_2/Ta/Pt/Co/Ir/Co/Pt$ synthetic ferrimagnet. The dashed blue and red curves represent guide lines which equations are provided ($|\mu_0 H_{P^+ \leftrightarrow AP^+}| = \frac{|J_E|}{t_2 M_2}$ and $|\mu_0 H_{AP^+ \leftrightarrow AP^-}| = \frac{2K}{M_S \Delta t}$), with $|J_E| = 70\ \mu J.m^{-2}$, $M_2 = 1.3 \times 10^6\ A.m^{-1}$ and $K = 3.25 \times 10^{-6}\ J.m^{-2}$.

that the magnetic moment of the layer was proportional to the thickness of the layer, which is theoretically right. Second, however, we assumed that there was a dead layer, that is to say a part of the cobalt layer deposited that was not magnetic. The concept of dead layer has already been widely used, and is often considered in very thin magnetic layers growth. Here, by rewriting the experimentally deposited layer t_{Co} as the sum of an effective layer t_{Co}^{Eff} and a dead layer of thickness t_D, we obtained a 4Å-thick dead layer of cobalt. This explains why the dashed blue line tends to infinite values before zero. The main discrepancy between the values that we obtain and actual plausible material parameters is the surface anisotropy constant. In our model, we assume a 0K temperature, that is to say energy barriers crossings that are not facilitated by thermal energy. Indeed this model tends to overestimate the switching fields with the actual magnetic anisotropy. Therefore, the anisotropy constant value that enables us to mimic the thickness dependence of the inner hysteresis loop is dramatically smaller than what can be found in the literature.

Even though the agreement with both curves is not perfect, especially for the outer loop switching field of the sample with a 7Å-thick bottom cobalt layer, the experimental results seem to follow the trend predicted by the model. The behaviours that are studied are predicted quantitatively for the outer loops switching fields, whereas understanding of the width of the inner loop remains more qualitative.

III.5 State diagram of a synthetic ferrimagnet M(H,T)

All the experiments shown before were performed at room temperature, that is to say around 300K. We did not consider thermal effects in all the previous macrospin calculations, according to the Stoner-Wohlfarth model, which assumes zero temperature. However, a change in the temperature is obviously changing the energy density representation that was presented earlier. For the moment, two extreme cases have been displayed: the 0 temperature results that correspond to the Stoner-Wohlfarth model, and the “infinite temperature” that corresponds to the most stable magnetic states as a function of the field, as shown on fig. I.16. In the latter, thermal energy is assumed to be sufficient to overcome any energy barrier so as to go immediately to the lower energy density state. In this section, we present the evolution of the magnetic hysteresis loops as a function of the temperature at which the experiments are carried out.

III.5.1 Experimental determination of the magnetic transitions

The method we applied in order to probe the magnetic behaviour of our samples as a function of temperature is the following: a synthetic ferrimagnetic sample was grown by magnetron sputtering at room temperature. similarly to what was chosen before, the stack grown was $Si - SiO_2/Ta/Pt/Co(0.7)/Ir(1.5)/Co(1)/Pt$. The experiments consisted in several magnetic hysteresis loop measurements performed with a SQUID at a constant temperature, ranging from 10K to 300K. The measurements that we carried out gave us three types of magnetic hysteresis loops (labelled type I, type II and type III), that depend, for a given sample, on the temperature at which the experiment is performed. Let us have a look at the three types of measurements that we could find on fig. III.8:

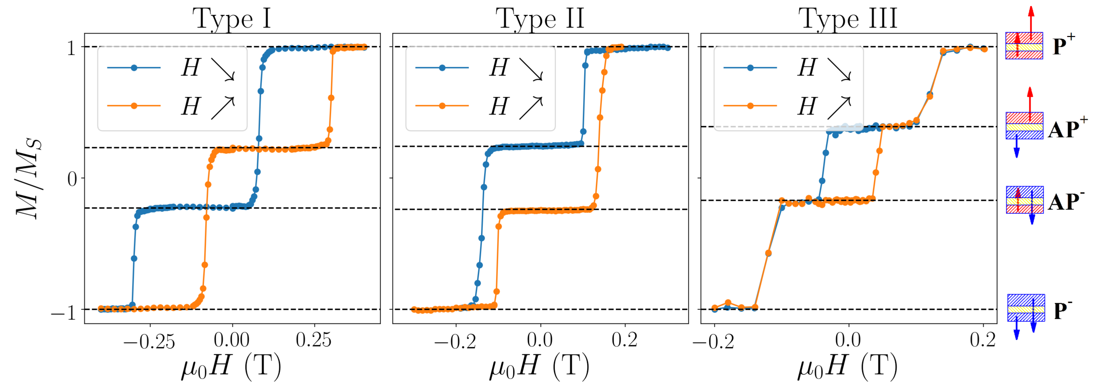

Figure III.8: Magnetic hysteresis loops of a $Si - SiO_2/Ta/Pt/Co(0.7)/Ir(1.5)/Co(1)/Pt$ synthetic ferrimagnet at 50K (left panel), 100K (middle panel) and 300K (right panel) (Adapted from Morgunov, Fache *et al.* [119]).

Although the shape of the magnetisation loops as a function of the applied field display significantly different features, the same magnetic configurations (P^-, AP^-, AP^+ and P^+) are reached. As discussed in section III.5, those states and the corresponding transitions in between these can be understood in terms of competition between energy barriers and thermal activation. The measurements that are the most relevant for our purposes are the hysteresis cycle of type III. We have precised on fig. III.2 the relevant quantities that we will extract from the measurements.

We have represented three temperature domains (noted I, II, and III) for which the hysteresis loops are very different. We provide on fig III.10 a summary of all the transitions that are allowed according to the temperature domain at which the magnetic hysteresis loop is performed.

We present one magnetic hysteresis loop corresponding to each of these temperature domains

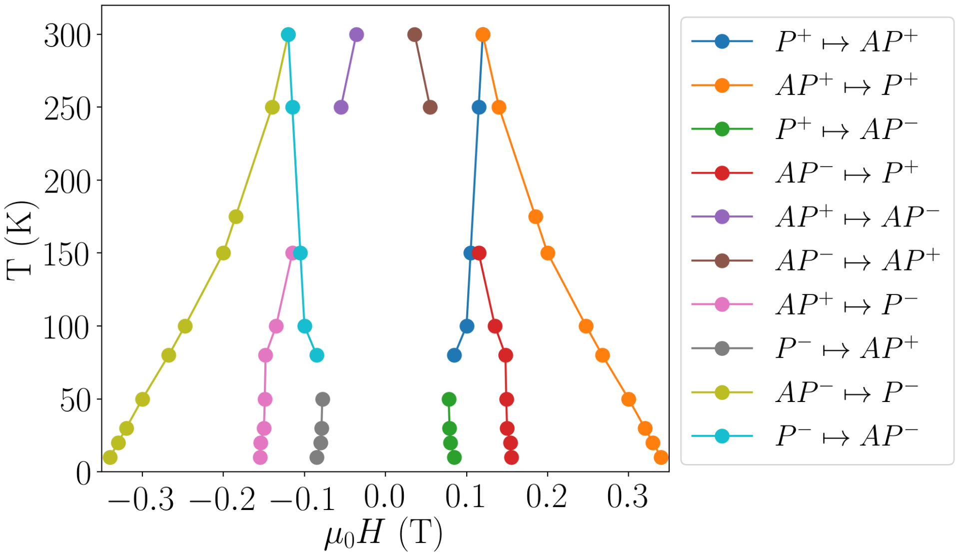

Figure III.9: Magnetic transitions observed as a function of the applied magnetic field for different temperatures in the $Si/Ta/Pt/Co(0.7)/Ir(1.5)/Co(1)/Pt$ synthetic ferrimagnet. (Adapted from Morgunov, Fache *et al.* [119]).

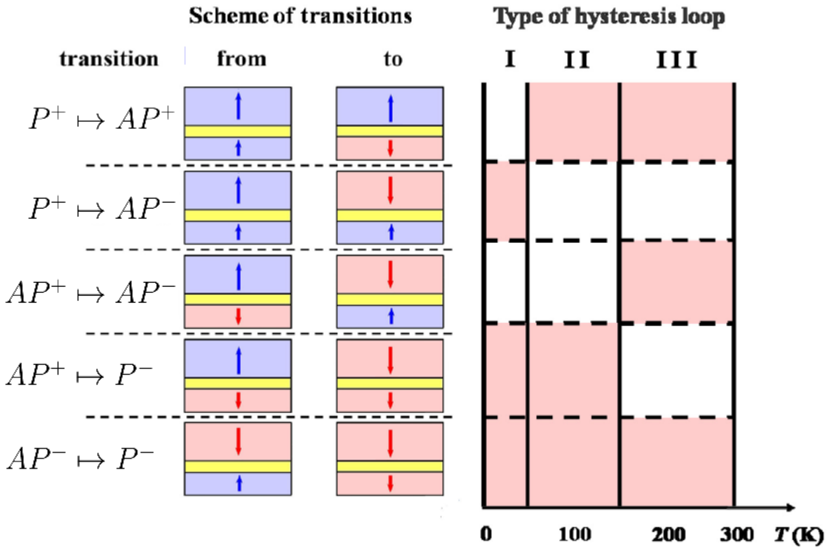

Figure III.10: Summary of the magnetic transitions accessible when sweeping the magnetic field from low to high magnetic field values according to the temperature (Excerpt of Morgunov, Fache *et al.* [119]).

on fig. III.8. We only consider however the transitions occurring when increasing the applied magnetic field, the cycles being perfectly symmetric with respect to the magnetic field.

The hysteresis cycle at room temperature is the usual figure representing a perpendicularly magnetised synthetic ferrimagnet: sharp transitions separate all the states that are accessible by sweeping the magnetic field in one direction. However, as temperature decreases, some states are not accessible in only one field sweep. For instance, in the case of temperature domain II, starting with a low negative field, and ramping up to a large positive field, the sample starts in a P^- state, steps through the AP^- state and ends up in the P^+ state, without accessing the AP^+ configuration.

III.5.2 Temperature addition to the Stoner-Wohlfarth model

We propose an understandig of the changes in the hysteresis loops observed. Let us consider the macrospin approach we have presented in the previous parts. We can assimilate the temperature to an equivalent thermal energy $\varepsilon_T = k_B T$. It is thus possible to consider that the energy density barriers that create the hysteretic behaviour observed can be crossed more easily as the thermal energy density increases.

One way to let that happen mathematically is to modify the initial energy of the system, considering that it possesses a thermal energy that can be expressed as $k_B T$, where k_B is the Boltzmann constant and T is the absolute temperature of the system. Like so, we can define an effective energy barrier ΔE_{eff} that is the difference between the zero temperature energy barrier that is given by the Stoner Wohlfarth model and the thermal energy. The latter reduces the energy density barriers that separate the different configurations. We display this representation on the energy graph shown on fig. III.11.

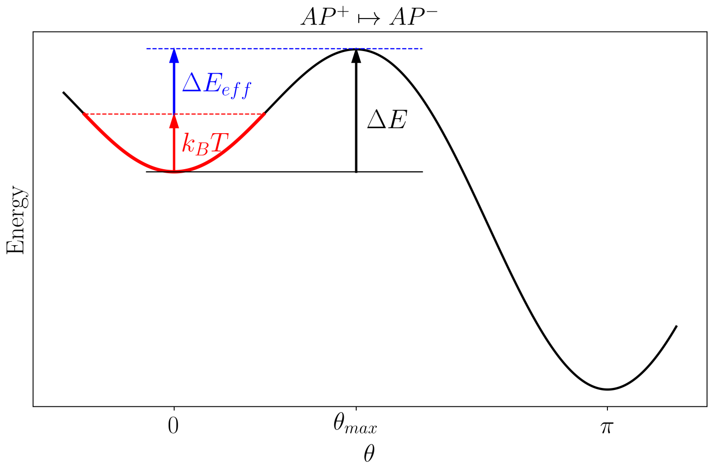

Figure III.11: Representation of the energy as a function of the angular position of a magnetic layer of a synthetic ferrimagnet at a temperature T. The effective energy barrier to cross is represented in blue, whereas the thermal energy is noted in red.

We represent on fig. III.12 three types of magnetic configurations that can occur, similarly to what was previously observed during the experiments. On the top panels, we draw full lines to represent the energy density of each of the four metastable states P^-, AP^-, AP^+, P^+ as a function of the applied magnetic field, and in dashed lines of the same colour, we represent the same energy density with an offset that corresponds to the effective energy barrier that has to be crossed so as to get to this configuration from another. The transition from state AP^+ to P^+ on the type III hysteresis loop occurs when the energy density of the state AP^+ (orange full line) is superior to the energy density of the state P^+ plus the energy barrier, which is represented by the dashed blue line. The inverse transition occurs then at the crossing of the full blue line and the dashed orange one.

Let us notice that, for types II and III, we consider that the energy density barriers to go from any configuration to any other is the same. This is qualitatively true: all the energy barriers are of the same order of magnitude. Consequently, the symmetry of the graphs with respect to $H = 0$ holds. However, in order to get the type I magnetic hysteresis loop, one has to consider that the energy barriers between all configurations are not the same. This is obvious due to the fact that all transitions do not imply the same magnetisation switchings, and thus, not the same anisotropy energy density terms involved. Consequently, for the type I plots, we just consider the sweeping of the field from negative to positive values. Furthermore, we assume that the energy density barrier is smaller from P^- to AP^+ (switching of the layer with the larger

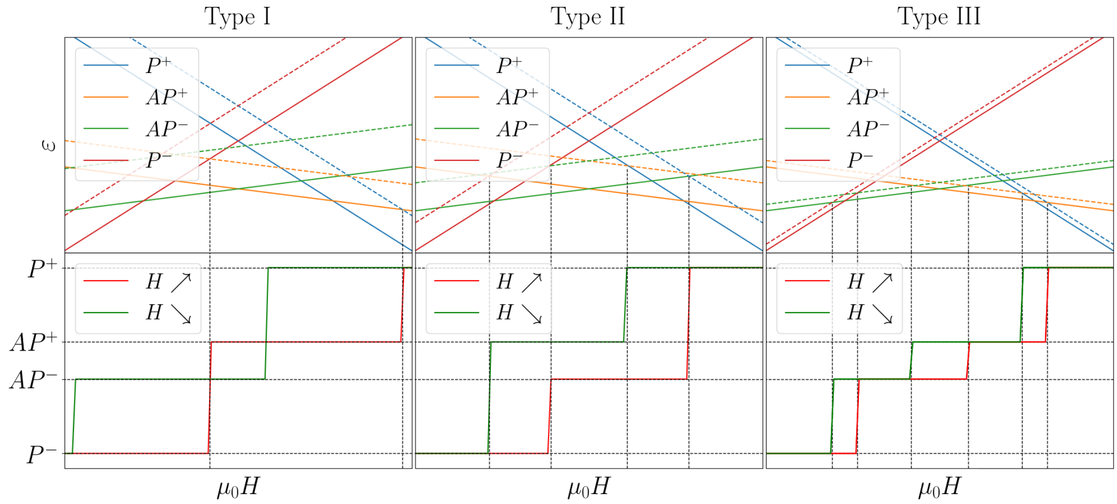

Figure III.12: Energy density as a function of the applied magnetic field for "low" (type I), "medium" (type II) and "high" (type III) temperatures (top panels), leading to magnetic hysteresis loops determined by the temperature dependent Stoner-Wohlfarth model (Adapted from Morgunov, Fache *et al.* [119]).

magnetisation) than from P^- to AP^- (switching of the layer with the lower magnetisation). This hypothesis is equivalent to the assumption of a larger anisotropy energy density for the layer with the smallest magnetic moment. Given the ordering of the stack, this assumption is sensible: indeed the top layer (which magnetic moment is the largest) was grown below a platinum layer. Since Pt is heavier than Co, we can imagine that resputtering can occur, and therefore we expect the top Co layer interface with Pt to be of poorer quality that the bottom Co layer's interface with Pt, leading to these different interfacial magnetic anisotropies. Thus the transitions accessible for this field sweeping are P^- to AP^+ and AP^+ to P^+.

In this section, we have successfully explained the magnetic hysteretic behaviour of a synthetic ferrimagnet as a function of the applied field and the temperature for an easy axis magnetic loop measurement. The addition of a thermal energy to the Stoner-Wohlfarth model lets us consider changing thermal energies of the system, leading to changing effective energy barriers, and thus different switching fields, which is enough to give a satisfactory understanding of the "medium" and "high" temperature regimes (loops of types II and III). A change in the energy density barriers considering the history of the sample is needed to provide an accurate comprehension of the low temperature hysteresis loops (type I). In all these cases, our model can provide a prediction of all the magnetic transitions that can occur, depending on the temperature at which the measurement is carried out.

III.6 Influence of the magnetic field sweeping rate on the magnetic loop

In the previous section, we have seen that the shape of the magnetic hysteresis loop can be significantly modified by the temperature at which the experiment is occuring. Before exploring in more detail a magnetic transition, let us examine the role of the magnetic field sweeping rate on the shape of the magnetic hysteresis loops.

We have measured magnetic hysteresis loops using MOKE microscopy at room temperature on two synthetic ferrimagnetic samples that we are calling samples I and II, which stacks were: $GaAs//MgO(2.5)/CoFeB(1.1)/Ta(0.75)/Co(0.8)/MgO(2.5)/Ta(5)$ for sample I and $SiO_2//Ta(3)/Pt(3)/Co(1.5)/Ir(1.5)/Co(1)/Pt(3)$ for sample II (all the thicknesses are given in nanometers). These samples were grown using magnetron sputtering from elemental targets, at the exception of CoFeB and MgO which were grown using alloy targets. These samples were not grown by myself, but by a collaborator of the Institut Jean Lamour. For that sample, the fact that GaAs is used as a substrate does not change the properties of the stack except for transport measurements, that were not performed on these samples. We present the magnetic hysteresis loops that we obtained with the MOKE measurement for values of the magnetic field sweeping rate of 1, 8 and 50 $mT.s^{-1}$ on figure III.13.

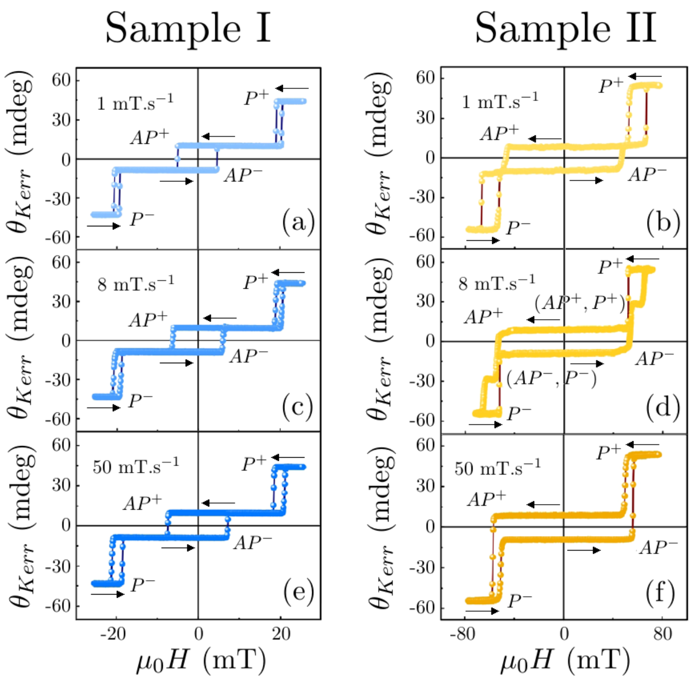

Figure III.13: Kerr rotation as a function of the magnetic applied field for synthetic ferrimagnets $GaAs//MgO/CoFeB/Ta/Co/Ta/MgO$ (a, c, e) and $SiO_2//Ta/Pt/Co/Ir/Co/Pt$ (b, d, f) and at a magnetic field sweeping rate of 1 $mT.s^{-1}$ (a, b), 8 $mT.s^{-1}$ (c, d) and 50 $mT.s^{-1}$ (e, f)(Adapted from Morgunov, Fache *et al.* [120]).

On the figures III.13 a, c and e, we can see that the transitions occurring do not change as a function of the magnetic field sweeping rate: going from positive to negative values of the applied magnetic field or vice versa, all the states are reached as follows: $P^+ \rightarrow AP^+ \rightarrow AP^- \rightarrow P^-$ and vice versa. We can notice a small increase in the value of the field at which the transitions seem to occur. This can be explained easily in a qualitative way. Indeed, the reversal of the magnetisation that occurs in a large sample such as the one that is considered here $(5 \times 5 mm^2)$ needs time, due to the propagation of magnetic domains that nucleate at a given magnetic field. The increasing of the magnetic field sweeping rate does not let enough time for domains to nucleate and/or propagate. The magnetisation reversal is observed not only for an applied field, but also for a time spent to wait for the phenomenon to occur. Therefore the increase of the magnetic field sweeping rate leads to a decrease of the waiting time to let the nucleation of a domain with a magnetisation in the opposite direction, and the domains to propagate.

If we focus on the Pt/Co/Ir/Co/Pt synthetic ferrimagnet (fig. III.13, we can see that the magnetic field sweeping rate changes the magnetic transitions observed. For instance, all the states are accessible by sweeping the field from positive to negative at low magnetic field sweeping rate (b), but one transition is lost at a sweeping rate of $8mT.s^{-1}$, where we can observe an unusual transition from AP^+ to P^- and AP^- at the same time, leading to an intermediary state. For a sweeping rate of $50mT.s^{-1}$, the sweeping of the field only lets two transitions, that are $P^+ \rightarrow AP^+ \rightarrow P^-$ (and symmetrically for an increasing field).

We can go a little deeper in the study of the sweeping rate. We present on figure III.14 the evolution of the field at which some transitions occur, as a function of the magnetic field sweeping rate. We display results that were carried out for a large range of sweeping rates.

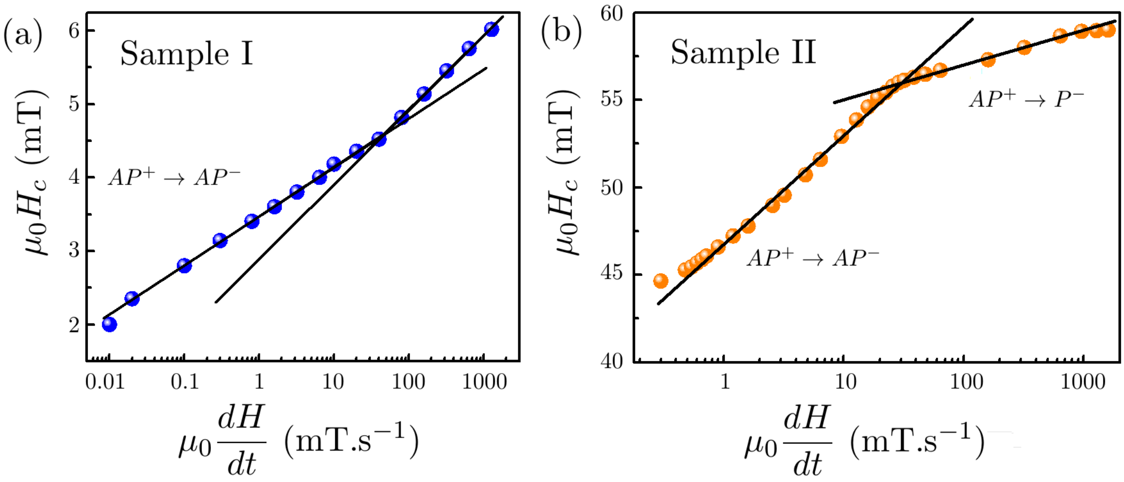

Figure III.14: Coercive field for the samples $GaAs//MgO/CoFeB/Ta/Co/Ta/MgO$ (a) and $SiO_2//Ta/Pt/Co/Ir/Co/Pt$ (b) as a function of the magnetic field sweeping rate. (Adapted from Morgunov, Fache *et al.* [120]).

The linear dependence of the coercive field with respect to the logarithm of the magnetic field sweeping rate is expected: the magnetisation of a material which can be represented as single particles that have an energy barrier to overcome to align with the magnetic field can be represented by an Arrhenius law, as shown in [121, 122]. Therefore, we expect to obtain a relationship of the form:

$$H_C\left(\frac{dH}{dt}\right) = H_f \log\left(\frac{dH}{dt}\right) + H_0$$

Where H_0 is a constant that is linked to the anisotropy constant, and H_f can be expressed as:

$$H_f = \frac{k_B T}{2V_A \mu_0 M_S}$$

Where k_B is the Boltzmann constant, T is the temperature, V_A is the activation volume and M_S is the saturation magnetisation [120]. A detailed calculation can be found in the supplementary material of ref. [120]. However, we can see that on both curves of fig. III.14, a distinct kink appears at a few tens of $mT.s^{-1}$. This kink can be linked to the magnetic hysteresis loops that are obtained on fig. III.13 (d, f): when the magnetic field sweeping rate is too large, when decreasing the magnetic field, the AP^- state is not accessible anymore, and the $AP^+ \rightarrow AP^-$ transition is replaced by the $AP^+ \rightarrow P^-$ transition. The systematic variation of the magnetic field sweeping rate shown in fig. III.14 gives us evidence that this new transition occurs not only in the Pt/Co/Ir/Co/Pt synthetic ferrimagnet, but also in the MgO/CoFeB/Ta/CoFeB/MgO one.

We have thus evidenced an unexpected magnetic transition that could occur at specific magnetic field sweeping rates. In the following, we will keep this rate very low so as to observe in details the transitions that occur, and focus more precisely on the $AP^+ \rightarrow AP^-$ transition in specific temperature conditions.

III.7 Magnetic relaxation in synthetic ferrimagnets

Considering the results obtained by Hamadeh *et al.* [101], we have decided to focus on the magnetic transition occurring between the AP^- and the P^- states, which is where the reversal of the domain wall occurs. Indeed, we performed a magnetic relaxation study of synthetic ferrimagnetic samples, where the magnetisation is subjected to a static magnetic field.

III.7.1 Principle of relaxation measurements

Magnetic relaxation relies on the following physical principle: when a measurement of the magnetisation as a function of the applied magnetic field is performed, the result is often hysteretic. The main reason for this behaviour is that a potential barrier exists between the equilibrium positions of the magnetic system. As a consequence, from a thermodynamic point of view, the most stable state has to be reached, but the kinetics of this phenomenon are not trivial. Thus, the measurement of the magnetisation as a function of the applied field strongly depends on various parameters amongst which the field sweeping rate. In order to overcome that dependence of the experiment on this arbitrary parameter, a kinetic measurement of the magnetisation can be performed so as to understand the mechanisms of field driven magnetisation switching and domain wall motion.

The experimental results as well as the modeling of the experiments that are presented here are the result of a collaboration between several researchers from different teams: the growth of the samples, the room temperature MOKE microscopy, and the theoretical model for the experiments were carried out in Institut Jean Lamour, France; the SQUID magnetometry (relaxation measurements) were performed in the team of Pr. Morgunov, from the Institute of Problems of Chemical Physics in Russia; the low temperature MOKE measurements were carried out in the team of Pr. Barnes, at the Cavendish laboratory, in Cambridge, UK; the simulations were performed by H. S. Tarazona from the Universidad Nacional Mayor de San Marcos, Peru.

III.7.2 Experimental procedure

The relaxation measurements that are presented in this section are performed following the procedure described here: we first set the working temperature, which is one of the parameters of influence of the experiment. Then, according to the magnetic hysteresis loop that was recorded by SQUID at the corresponding temperature, the sample's magnetisation is fully saturated by applying a field H_{sat} larger than the coercive field. Then the magnetic field is set to a value $H^* \approx H_c$ at which the sample is in a metastable state, that is to say a field-driven magnetic transition shall occur. The actual measurement of the magnetisation starts after 30 seconds, so that the magnetic field stabilises at its desired value. We present in fig. III.15 the evolution of the applied magnetic field during the setting of the experiment. On that timeline, the magnetisation recording starts at t_0. Therefore, the measurements that we will display in the rest of the section often start by a large variation of the magnetisation, and the first data acquired do not correspond to the initial magnetisation one expects to obtain according to the state diagrams established by magnetic loops measurements.

III.7.3 Model for a single layer relaxation

Let us examine the expected behaviour of the magnetisation in a single ferromagnetic layer. The experiment relies on the fact that the magnetic system is in a metastable configuration. Let us consider that there are two saturated magnetic states that correspond to the most stable and the metastable states, that we will call up and down. We can represent the energy density as a function of the orientation of the magnetisation as shown on the figure displayed below:

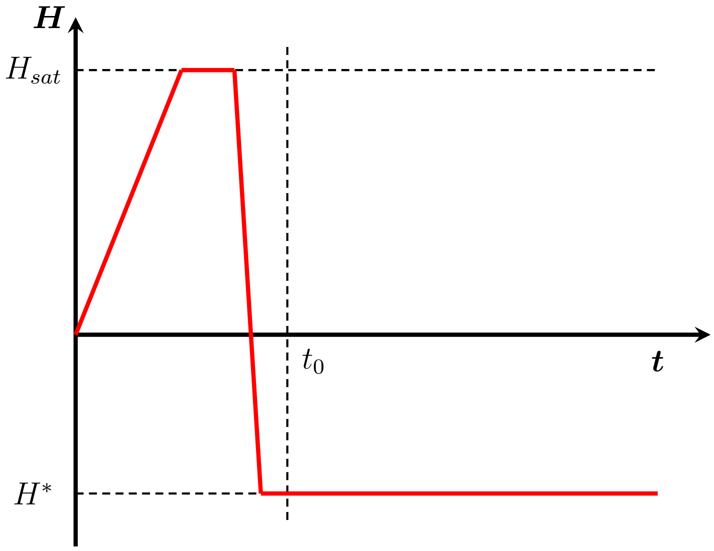

Figure III.15: Evolution of the magnetic field as a function of time in the magnetic relaxation experiments.

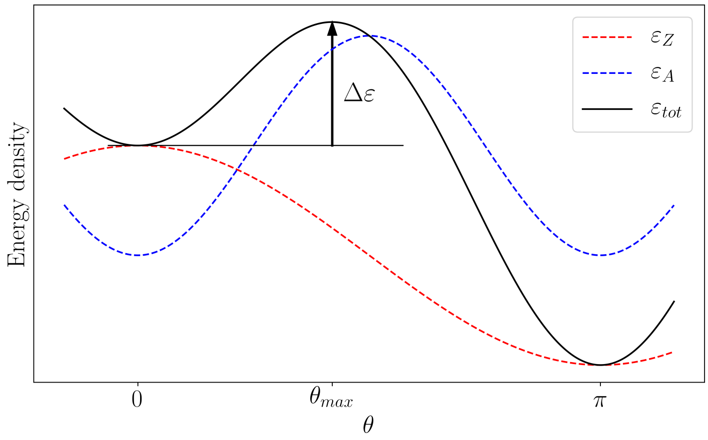

Figure III.16: Energy density landscape in a macrospin approximation for a single layer during a magnetic relaxation experiment

The expected transition corresponds to an exponential decrease of the net magnetisation following an Arrhenius law: the magnetisation is supposed to be likely to switch as a function of the energy barrier that separates states up and down. We consider that the time constant of this reversal is also depending on the temperature at which the experiment is carried out, and is characterised by a frequency attempt to switch.

III.7.4 Experimental relaxation of synthetic ferrimagnets

Room temperature relaxation measurements

The samples on which these measurements were performed were cobalt/iridium based synthetic ferrimagnets, but we chose to grow different thicknesses of cobalt so as to change the net magnetisation of the whole stack. The stacks chosen were Ta(3)/Pt(3)/ Co(1)/Ir(1.43)/Co(0.9)/Pt(3) (sample 1), Ta(3)/Pt(3)/Co(0.7)/Ir(1.43) /Co(1)/Pt(3) (sample 2) and Ta(3)/Pt(3)/Co(0.95)/Ir(1.43)/Co(1)/P (sample 3), all the thicknesses being indicated in nm.

The magnetic hysteresis loop of sample 1 at room temperature is displayed in fig. III.18. On this graph we can notice that all four magnetic states (P^+, AP^+, AP^- and P^-) are accessible

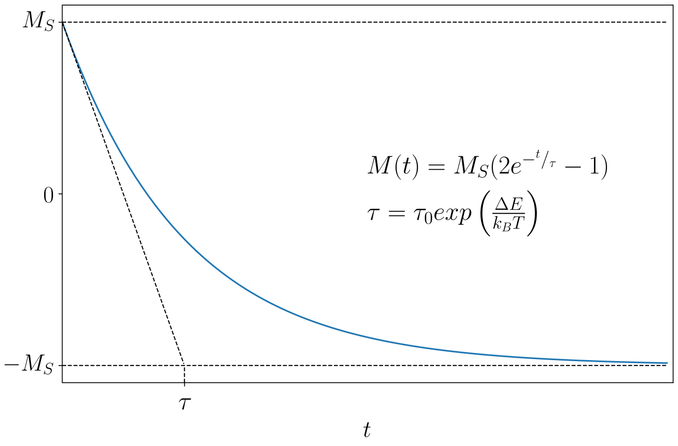

Figure III.17: Usual magnetic relaxation of a perpendicularly magnetised ferromagnetic layer: magnetisation as a function of time.

by sweeping the field from positive to negative. However, the transitions $AP^+ \rightarrow AP^-$ and $AP^- \rightarrow P^-$ seem to occur for similar values of the applied magnetic field. Thus we explored the three transitions $P^+ \rightarrow AP^+$, $AP^+ \rightarrow AP^-$ and $AP^- \rightarrow P^-$. Let us note here that the projection of the magnetisation along the out of plane axis is antisymmetric with the applied magnetic field. Consequently, focusing only on half of the transitions corresponding only to a decreasing magnetic field is enough to get the whole behaviour of the material.

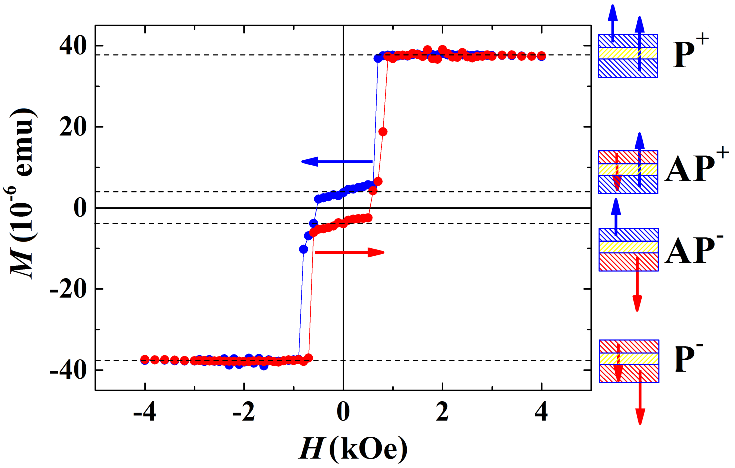

Figure III.18: Magnetisation as a function of the applied magnetic field at room temperature for sample 1 (Excerpt from Fache *et al.* [123])

The graphs shown on fig. III.19 give the time evolution of the magnetisation. Each curve corresponds to a set value of the field H^*. We can see on this graph two types of relaxation. For positive values of the field, at $H^* = 700$ Oe, the relaxation is monotonic. It decreases from its initial value, which corresponds to the positive saturation given by our experimental process, towards the AP^+ value, which is, according to the magnetic hysteresis loop, the final state at that value of the field. We obtain the same kind of curves at -550$\leq H^* \leq$-500 Oe, where we have a monotonic transition between the AP^+ state and the AP^- one.

For the values -625 $\leq H^* \leq$ -575 Oe, we observe an unexpected relaxation curve: the magnetisation that was set in the $P+$ state begins at a value between the ones of the P^- and the AP^- configurations at t_0, and increase with time. This observation does not fit with the magnetic hysteresis loop recorded on fig. III.18 where magnetisation had a monotonic increasing evolution with respect to the applied magnetic field.

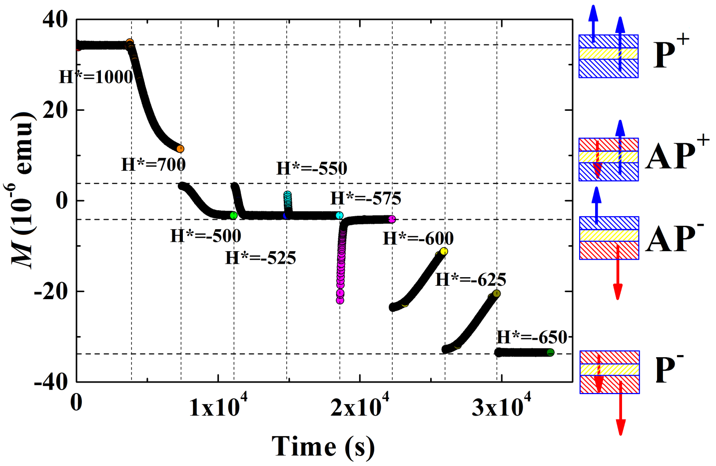

Figure III.19: Magnetisation as a function of time for various applied magnetic field values H^* (in Oe) at room temperature for sample 1 (Excerpt from Fache *et al.* [123])

These counter intuitive results correspond to the whole sample's response to a magnetic field. In order to have a more precise understanding of the causes of this phenomenon, the next step was to perform magneto-optic Kerr effect microscopy (MOKE). This technique offers in particular the possibility to observe the domains forming and propagating, and have a local observation of the sample.

The experiment that was performed under the MOKE microscope is very similar to the relaxation measurements on the SQUID. The images displayed in fig. III.20 show black and white contrast corresponding to the out of plane projection of the magnetisation of the sample. The darkest regions at the very centre of the images b) to f) corresponds to the AP^- configuration. The lightest region in the centre of the a) image corresponds to the P^- configuration (present on all the images). Eventually, the middle grey colour that is on the sides of the a) image, and present on images a) to e) corresponds to the initial AP^+ configuration. These colour/magnetic configuration equivalences were made thanks to a measurement of the magnetisation as a function of the applied magnetic field.

The magnetic reversal mechanism that we can observe on these images is clear. At first, from the AP^+ saturated sample, a P^- nucleus appears (a) and spreads slowly. After a while, from the expanding P^- domain, an AP^- domain nucleates, from the exact same spot as the first nucleation (b). Then both domains (P^- and AP^- propagate, until the initial AP^+ domain (e) and the transient P^- domain (f) vanish.

The transitions that were observed in fig. III.20 correspond to a decrease of the magnetisation corresponding to the disappearance of the AP^+ phase, replaced by domains of lower levels of magnetisation, and an eventual increase, from the moment when the AP^+ configuration has completely disappeared, and the AP^- configuration progressively replaces the P^- one. This experiment is thus in good agreement with the relaxation observed with the SQUID in fig. III.19.

A way to understand the phenomenon is to see it occurring under different conditions, for another sample for instance. In order to do so, we used a similar sample with different cobalt thickness (sample 2). We found out that it was possible to observe a similar magnetic hysteresis loop than for sample 1, but at a lower temperature (fig.III.21).

At this temperature, the magnetisation as a function of the applied magnetic field does not show for sure the $AP^+ \rightarrow AP^-$ transition. Thus we investigated the magnetic relaxation at this temperature. The results are displayed on fig. III.22

Again on that sample, it was possible to observe for magnetic field values from -1360 to -1420

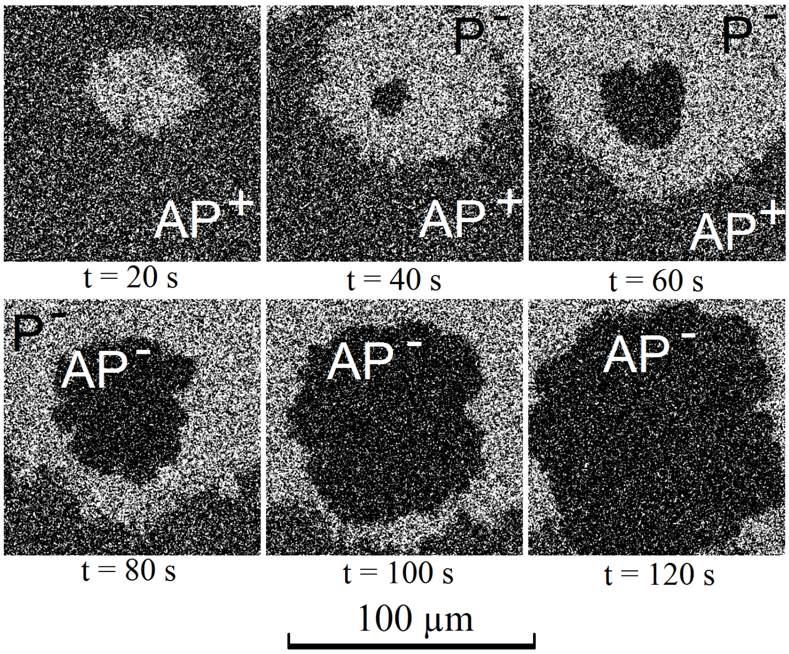

Figure III.20: MOKE imaging of sample 1 at a field value of H^*=-600G at different times. (Excerpt from Fache *et al.* [123])

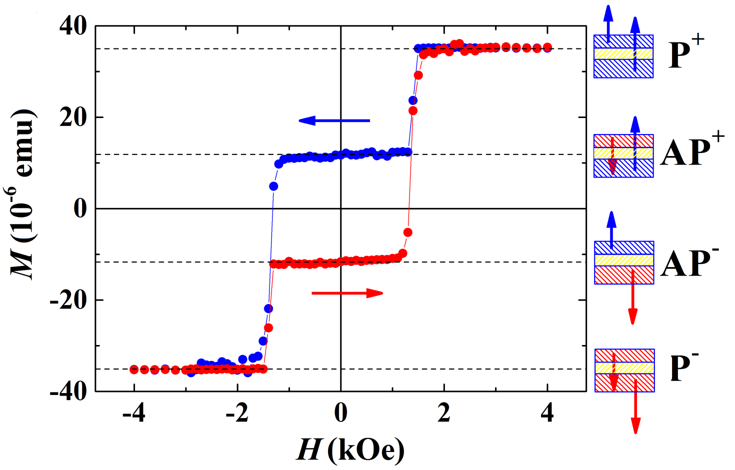

Figure III.21: Magnetisation as a function of the applied magnetic field at a temperature of T=150K. (Excerpt from Fache *et al.* [123])

Oe non monotonic magnetic relaxation, which leads us to think that the relevant parameter that would enable this physical phenomenon was the shape of the hysteresis loop. In order to have local information on the magnetic relaxation at low temperature, we performed low temperature MOKE measurements on a third sample (sample 3). We obtained the magnetic hysteresis loop at 232K that is shown on fig. III.23 a). The corresponding relaxation (fig. III.23 b) gives an image of the magnetisation of a 3x3 mm^2 part of the sample, where the light beam probes the matter.

On that figure, we can clearly see that the magnetsation is constant in the AP^+ state for around 40 seconds after the beginning of the measurement, before dropping dramatically at the APˆ- state for a few seconds, and then dropping to nearly the P^- configuration.

From these observations, one can conclude that the mechanisms of reversal for all the non monotonic transitions that we have seen for different samples at various temperatures are the

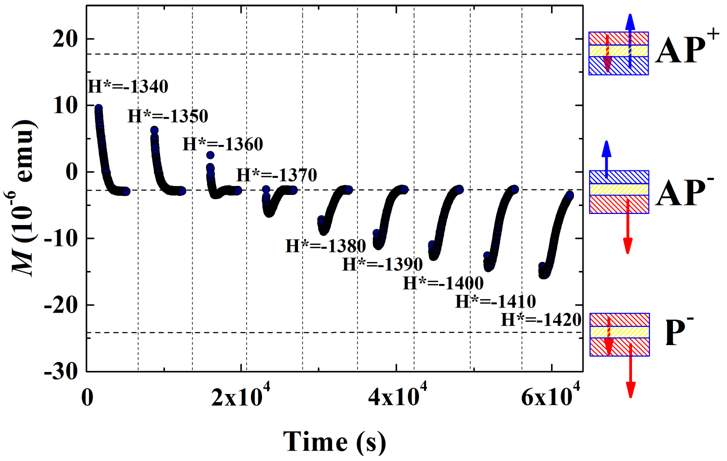

Figure III.22: Magnetisation as a function of time for various applied magnetic field values H^* (in Oe) at T=150K for sample 2. (Excerpt from Fache *et al.* [123])

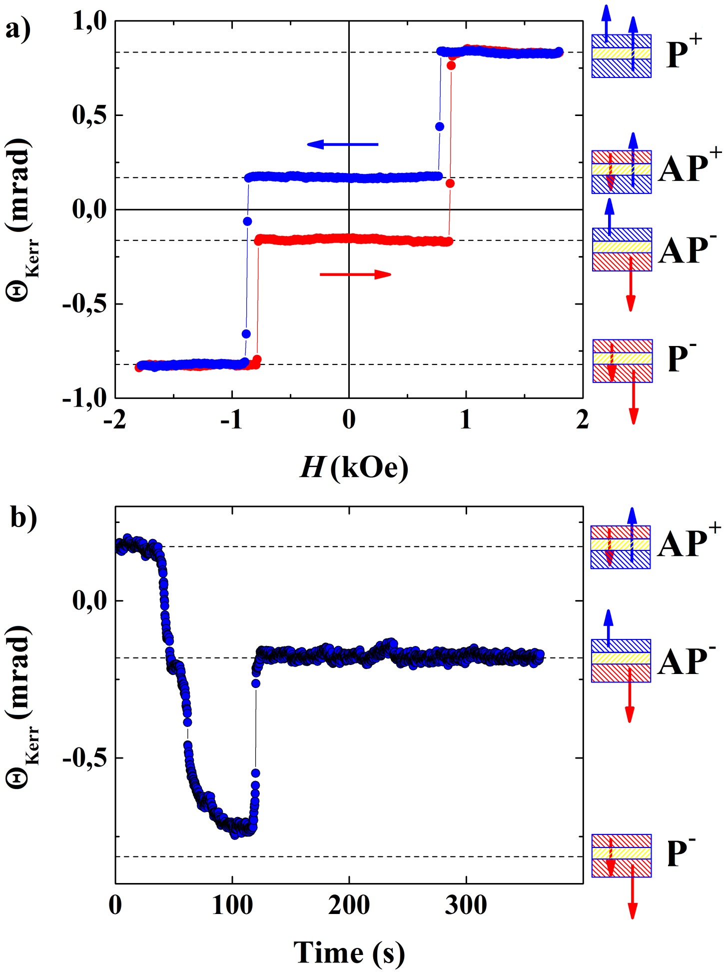

Figure III.23: a) Magnetisation as a function of the applied magnetic field at 232K for sample 3; b) magneto-optic Kerr signal as a function of time at an applied magnetic field of -880 Oe. (Excerpt from Fache *et al.* [123])

same, that is to say a first $AP^+ \to P^-$ transition quickly followed by a $P^- \to AP^-$ transition. We will now focus on an approach that can describe theoretically the phenomena that we just reported.

Modeling the non monotonic magnetic relaxation

Our approach to model the magnetic behaviour that we reported is to consider a lattice of moments represented in the macrospin approximation without interactions between them. Here, since we want to describe two magnetic layers, we will consider every small element of our system as if it were composed of two single magnetic moments on which magnetic interactions apply. The way to describe the moments is the following: we describe the direction of the local moments thanks to an angle couple $(\theta_1, \theta_2)_i$ (i indexes the cells of the model) with respect to the out of plane direction $\boldsymbol{z}$, which is, according to the experiments (III.18), an easy axis of magnetisation.

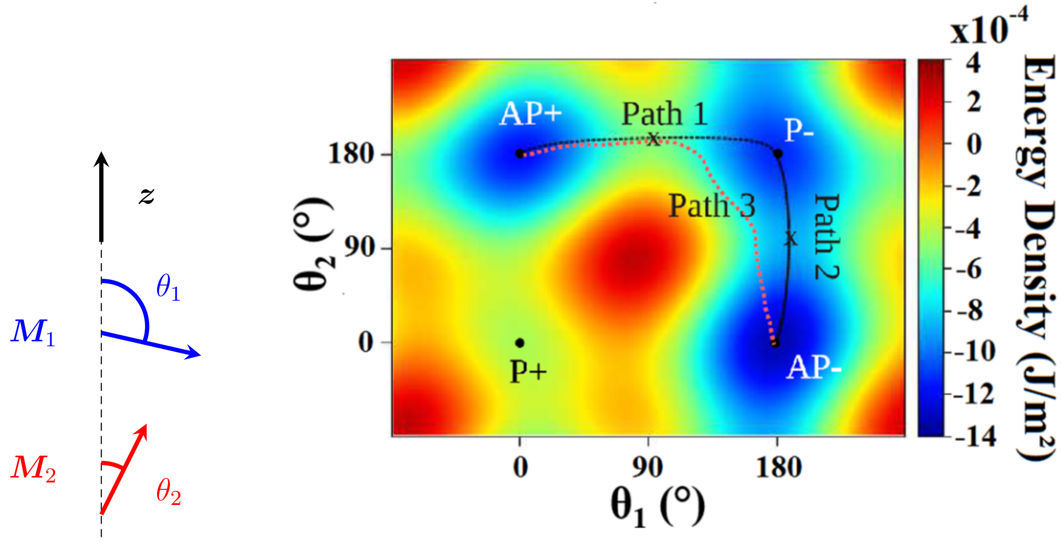

(a) Orientation of the magnetisations

(b) Energy landscape

Figure III.24: (a) Representation of the synthetic ferrimagnet as two macrospins; (b) Energy lanscape of a two macrospin cell at a magnetic applied field of -1500 Oe for the parameters presented in the table III.1. (Excerpt from Fache *et al.* [123])

For each cell, we considered four interactions, namely the Zeeman interaction (representing the applied magnetic field), the magnetocrystalline anisotropy, the demagnetising field, and the RKKY exchange coupling between two corresponding moments of the different magnetic layers. For each macrospin, the surface energies were then:

$$\begin{cases} E_Z = -\mu_0 H(t_1 M_1 \cos(\theta_1) + t_2 M_2 \cos(\theta_2)) \\ E_A = t_1 K_1^{eff} \cos^2(\theta_1) + t_2 K_2^{eff} \cos^2(\theta_2) \\ E_E = J_E \cos(\theta_1 - \theta_2) \end{cases} \tag{III.1}$$

Where t_i, M_i, K_i^{eff} are the thickness, the magnetisation, and the effective anisotropy constant of the layer i. The expression of the effective anisotropy constants was of the form:

$$K_i^{eff} = \frac{\mu_0 M_i^2}{2} - \frac{K_s^i}{t_i} \tag{III.2}$$

Where K_s^i is the surface anisotropy constant. The out of plane magnetisation of the samples is equivalent to the condition $K_i^{eff} < 0$.

According to the interactions presented here, it is possible to plot an energy map of a cell composed of two macrospins, according to the two degrees of freedom of this system, θ_1 and θ_2. This landscape is presented on fig. III.24. On that graph, we can see that three metastable states exist (P^+, AP^+, and P^-), and the most stable equilibrium position is AP^-.

The way we express the transitions using this energetic representation of the magnetic configurations is the following. We consider that at the beginning, our sample is fully saturated in the AP^+ state. Then, we consider that all the 2-spin cells can achieve a switching with a probability that depends on the possible transitions between their actual configurations. We show on fig. III.24 three paths representing a direct $AP^+ \rightarrow P^-$ (Path 1), $P^- \rightarrow AP^-$ (Path 2) and $AP^+ \rightarrow AP^-$ (Path 3) transitions. If we plot the energy density as a function of the curvilinear coordinates, we obtain the graph shown on fig. III.25.

The magnetic state of the sample can thus be described as a proportion P_{AP^+} in the state AP^+, another one P_{P^-} in the state P^-, and the rest of it $P_{AP^-} = 1 - P_{AP^+} - P_{P^-}$ in the configuration AP^-. The projection of the average magnetisation along the $\boldsymbol{z}$ axis is then given by the expression: $\langle M_z \rangle = M_{AP^+}P_{AP^+} + M_{P^-}P_{P^-} + M_{AP^-}P_{AP^-}$. On the other hand, the probability for a cell to switch from state i to state j ($(i,j) \in \{AP^+, P^-, AP^-\}^2$) is then considered as $\omega_{ij} = \tau_{ij} \exp\left(\dfrac{\Delta E_{ij}}{k_B T}\right)$, where τ_{ij} is a frequency attempt parameter. The energy barriers E_{ij} depend on the magnetisation position as a function of time during the magnetisation reversal. On fig. III.24, we represented the different paths that magnetisation can follow during this process: an indirect transition from AP^+ to AP^- stepping by P^- is described in two parts by the consecutive paths labelled 1 and 2, whereas a direct magnetic transition from AP^+ to AP^- is drawn as path 3. The energy barriers to cross are represented by the crosses, and depend on the path chosen. We can represent the evolution of the state of our system by noting:

$$\boldsymbol{X} = \begin{pmatrix} P_{AP^+} \\ P_{P^-} \\ P_{AP^-} \end{pmatrix} \tag{III.3}$$

Which lets us extract the average of the magnetisation along $\boldsymbol{Z}$ as:

$$\langle M_z \rangle = \boldsymbol{X} \cdot \begin{pmatrix} M_{AP^+} \\ M_{P^-} \\ M_{AP^-} \end{pmatrix} \tag{III.4}$$

The equation that describes the temporal evolution of our system is thus:

$$\frac{d\boldsymbol{X}}{dt} = \begin{pmatrix} -(\omega_{AP^+P^-} + \omega_{AP^+AP^-}) & \omega_{P^-AP^+} & \omega_{AP^-AP^+} \\ \omega_{AP^+P^-} & -(\omega_{P^-AP^+} + \omega_{P^-AP^-}) & \omega_{AP^-P^-} \\ \omega_{AP^+AP^-} & \omega_{P^-AP^-} & -(\omega_{AP^-AP^+} + \omega_{AP^-P^-}) \end{pmatrix} \cdot \boldsymbol{X} \tag{III.5}$$

The parameters chosen for the calculations are summarised on table III.1. We especially specify the frequency attempts τ_{ij} corresponding to the transitions between states. These frequency attempts are theoretically linked to the curvature of the energy wells of each state among P^+, AP^+, AP^- and P^-. In our case, we only chose values so that the magnetic relaxation simulated in fig. III.26 would be in qualitative agreement with the experimental results displayed earlier in this chapter. However, we are not expecting these values and this simulation to reproduce quantitatively the experiment. Indeed, we have proven that the main mechanism at stake during the non monotonic magnetic relaxation was a nucleation-propagation phenomenon, whereas the representation that we choose only considers nucleation, since no interaction between neighbour moments.

The evolution of the magnetisation of a sample of size 20×20 nm^2 as a function of time is plotted on fig.III.26. This graph shows a good qualitative agreement with the experimental data shown in fig. III.19, III.22, III.23. As for the experiments, we can see that the relaxation is very sensitive to the applied magnetic field. The time scale is not of the same order of magnitude, though. This discreapancy can be related to the size of the sample, which is $2.5.10^{11}$ times

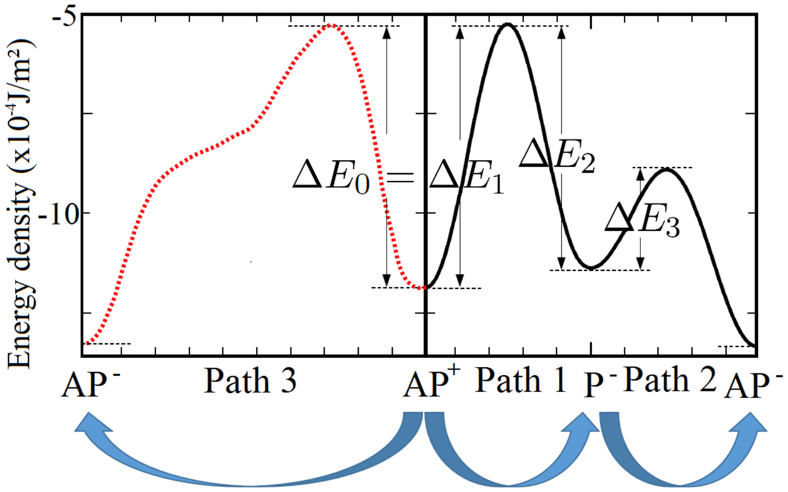

Figure III.25: Magnetic transitions corresponding to paths 1, 2 and 3 on fig. III.24. For the sake of simplicity,we have chosen the notations $\Delta E_0 = \Delta E_{AP^+ \to AP_-}$, $\Delta E_1 = \Delta E_{AP^+ \to P_-}$, $\Delta E_2 = \Delta E_{P_- \to AP^+}$ and $\Delta E_3 = \Delta E_{P^- \to AP_-}$. (Adapted from Fache *et al.* [123])

PARAMETER	VALUE
t_1^{Co}	0.7 nm
t_2^{Co}	1.0 nm
M_1^{Co}	$1.3.10^6$ $A.m^{-1}$
M_2^{Co}	$1.4.10^6$ $A.m^{-1}$
K_s^1	$1.1.10^{-3}$ $J.m^{-2}$
K_s^2	$1.9.10^{-3}$ $J.m^{-2}$
J_E	286 $\mu J.m^{-2}$
τ_{12}	$1.0.10^{10}$ Hz
τ_{13}	$1.0.10^{15}$ Hz
τ_{31}	$2.0.10^{13}$ Hz
τ_{32}	$1.0.10^4$ Hz

Table III.1: Values of the parameters used for the simulation.

larger than the simulated area. Another element that could explain that difference is the value of frequency attempts. However, the most striking difference between our model and the experiment is the absence of coupling between the cells that we have considered. Indeed, no propagation of magnetic domains can be observed, and the simulation only represents local nucleation of magnetic domains. This first approach leads thus to qualitatively reliable results, but could be completed by the addition of coupling between cells.

The temporal evolution of the proportion of the sample in the states AP^+, AP^- and P^- is represented in fig. III.27. In black and blue, the proportions of the initial AP^+ state and the final AP^- state, whereas in red, we can see the proportion of cells in the transient P^- state. These curves show usual behaviours for AP^+ and AP^- populations, with exponential-like curves, and an unusual apparition and vanishing of the P^- state. We can especially see

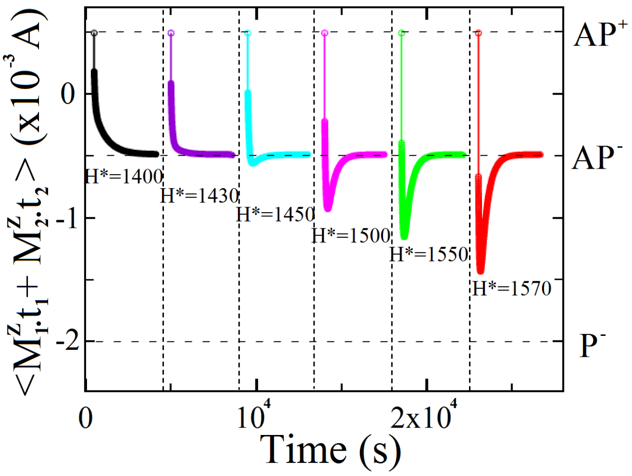

Figure III.26: Magnetic relaxation simulated for a 20 × 20 nm^2 sample at room temperature. (Excerpt from Fache *et al.* [123])

that the following results are verified:

$$\begin{cases} \lim_{t\to\infty} P_{AP^-}(t) & = 1 \\ \lim_{t\to\infty} P_{AP^+}(t) & = \lim_{t\to\infty} P_{P^-}(t) = 0 \\ P_{AP^+}(t=0) & = 1 \\ P_{P^-}(t=0) & = P_{AP^-}(t=0) = 0 \end{cases} \tag{III.6}$$

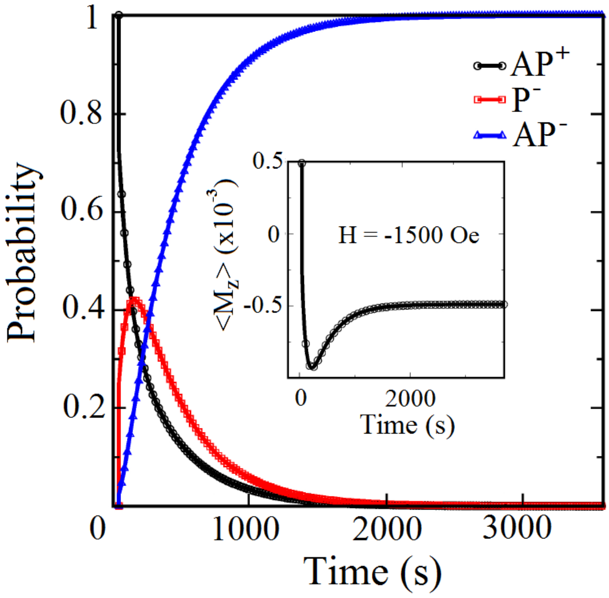

Figure III.27: Proportions P_{AP^+} (black), P_{P^-} (red) and P_{AP^-} (blue) of AP^+, P^- and AP^- cells. The inset shows the corresponding time dependence of the projection of the magnetisation along $\boldsymbol{z}$. (Excerpt from Fache *et al.* [123])

The coherence between the simulation, the model and the experimental results gives a good insight to understand the mechanism that enables the non monotonic relaxation observed, and the counter intuitive transition that occurs. However, the complete kinetics of this transition is not described perfectly. We can point out that our approach does not take into account the domain wall propagation process, which is, according to the low temperature MOKE results shown in fig. III.23, of major importance in the process. More appropriate considerations could lead to a more credible and quantitative model, using for instance the magnetisation reversal studies proposed by Fatuzzo and Labrune.

From this study, and given the model that we could establish to reproduce the experimental results, we can see that the intermediary states observed in the non monotonic relaxation measurements are not very likely to occur at some point in the magnetic history of the material. Indeed, they can only exist in a narrow range of temperatures, and at a specific value of the applied magnetic field. Furthermore, these states are metastable, and thus cannot survive long periods of time, due to the propagation of domain walls. In the case of our samples, the intermediary P^- states have been observed for around an hour, in conditions that were set to maximise this period.

In the scope of current induced domain wall motion, the nucleation and propagation of such metastable states is not a concern. Indeed, due to the change of temperature that must occur during a current pulse, it is very unlikely that the intermediary state stays stable enough to survive for a long period of time, or even nucleate in the first place.

III.8 Conclusion

In this chapter, we have presented an experimental study of synthetic ferrimagnets under an applied magnetic field. First, we have been able to characterise the indirect exchange interaction using the Stoner Wohlfarth model presented in the first chapter, with qualitative results in agreement with the values found in the literature. Then, with a more qualitative approach, we could validate the Stoner Wohlfarth approach using the thickness dependence of the cobalt layers of our stack. The last part of this materials characterisation was the temperature dependence of the magnetic hysteresis loops of our samples, explained by the addition of the temperature to the Stoner Wohlfarth model.

Afterwards, we displayed a field induced domain wall motion study in synthetic ferrimagnets extracted from the literature, and considering the results disclosed, we performed a study of the magnetic transitions under a static applied magnetic field, corresponding to the relaxation of the magnetisation, which lead to unusual non monotonic results. A simple energetic model could explain the kinetics of the relaxation, and even though the results obtained need to be completed by domain wall propagation phenomena, the origin of the transitions is understandable using our simple model.

From these results, we have been able to confirm the relevance of the Stoner Wohlfarth representation of the synthetic ferrimagnetic system. The materials characterisation gives us a reliable way to check the properties of samples that will be grown further, and sets an adequate frame for the comparison between several samples. Furthermore, the fact that the unexpected non monotonic magnetic behaviour that is disclosed in the magnetic relaxation study can also be treated correctly using the Stoner Wohlfarth model validates the latter. Eventually, the existence of the transient metastable states appearing in the magnetic relaxation in very specific circumstances as we understand it is not expected to matter for the current induced domain wall propagation, due to the perturbation that this is supposed to generate in terms of heating of the sample. The metastable state would thus be very unstable, and is likely not to appear at all.

Chapter IV

Spin dependant transport in Iridium

IV.1 Introduction

Numerous materials are well-known for their direct (charge-to-spin conversion) and inverse (spin-to-charge conversion) spin Hall effects (SHE) that lead to major spintronics applications. In the scope of spintronics devices, the application of spin currents is the key to current induced domain wall motion, and it is mandatory to select the best materials for that purpose. For instance, the materials for the buffer and capping layers are chosen partly for their charge-to-spin conversion efficiency.

In the case of synthetic ferrimagnets, in order to optimise the materials, we aim at finding a material for the spacer that can both induce a large antiferromagnetic coupling between both magnetic layers (RKKY interaction) and an efficient spin Hall effect. In the previous chapter, we have characterised iridium for its well known RKKY behaviour. The aim of the present chapter is to study the spin Hall effect in iridium.

If direct and inverse spin-Hall effects are already widely used in spintronics, the best materials for that property might not be the more adequate as spacers in synthetic ferrimagnets, especially regarding the RKKY interaction. For instance, for materials with large spin-Hall effect efficiencies like platinum or tungsten the RKKY coupling is very small [47], and for materials like copper with rather large RKKY coupling, the spin-Hall effect is expected to be very small due to a very small spin orbit coupling, caused by its small atomic number ($Z_{Cu} = 29$). Tantalum combines both effects [86, 106], but its electrical resistivity is very high, and the efficiency of spin current generation is consequently reduced.

In this chapter, we will study the spin-Hall and inverse spin-Hall effects (SHE and ISHE) in iridium so as to characterise the efficiency of this material to enhance the current induced domain wall motion in iridium-based synthetic ferrimagnets. We have aleady presented in the chapter devoted to methods the quantities of interest that need to be determined, as well as the methods that can lead to the characterisation of SHE and ISHE in a general manner. In this chapter, we start by we describing the experiment with a general formalism so as to represent the problem as generally as possible. Then, we have a closer look at the assets and drawbacks of each method (SP and ST-FMR). Eventually, we display measurements that were performed on two series of bilayers, probing ISHE in iridium and platinum, and show the full characterisation of SHE in iridium.

IV.2 Magnetisation dynamics in ferromagnetic materials

In this section, we develop the calculation that enables to characterise the magnetisation dynamics as a function of the frequency of an applied periodic magnetic field, in a general framework. We start by defining some notations and the representation of the physical system, and then solve the linearised LLG equation (eq. I. 10), which leads us, using the linear response theory, to the magnetic susceptibility of the material studied.

IV.2.1 Notations and representation of the problem

The study of ferromagnetic resonance is well known and has been treated many times before. Despite the fact we can often take advantage of a symmetry by rotation around the equilibrium position around which we will make the magnetisation precess, or from the fact that the magnetisation amplitude can be assumed to be constant, many authors choose to represent it using a Cartesian coordinates system. However, this approach imply a loss of generality, and we will provide here a description of the problem using spherical coordinates. The only limitation of this representation corresponds to the case of a magnetisation along the $\boldsymbol{z}$ axis, which is a singularity in this description. However, this specific case can be obtained by continuity of the spherical general solution.

The coordinates system is depicted in the scheme presented on fig. IV.1. It is defined in the following way: at any instant, the vector $\boldsymbol{r}$ is aligned with the magnetisation. We will also consider that the magnetisation is a vector of constant length M_S, being thus completely determined by the couple (θ, φ).

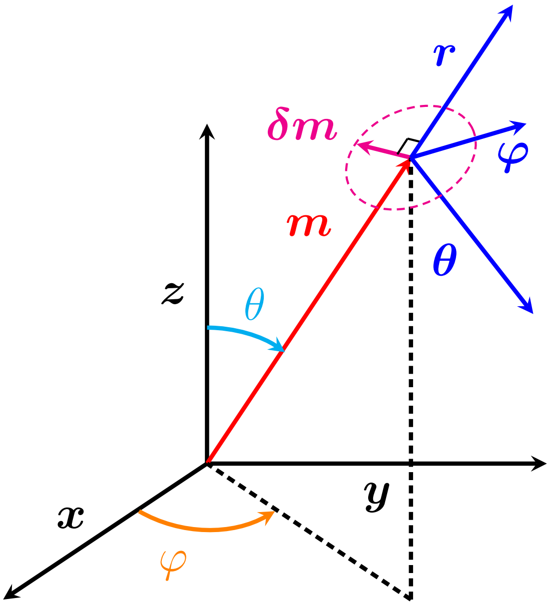

Figure IV.1: Representation of the magnetic oscillations around the equilibrium position

The way to switch from Cartesian coordinates to spherical coordinates uses the transformation matrix written as follows:

$$\mathcal{M}_{\mathcal{B}_1 \mapsto \mathcal{B}_2} = \begin{bmatrix} \sin(\theta)\cos(\varphi) & \cos(\theta)\cos(\varphi) & -\sin(\varphi) \\ \sin(\theta)\sin(\varphi) & \cos(\theta)\sin(\varphi) & \cos(\varphi) \\ \cos(\theta) & -\sin(\theta) & 0 \end{bmatrix}$$

We took here the convention $\mathcal{B}_2 = \{\boldsymbol{x}, \boldsymbol{y}, \boldsymbol{z}\}$ as the cartesian basis and $\mathcal{B}_1 = \{\boldsymbol{r}, \boldsymbol{\theta}, \boldsymbol{\varphi}\}$ as the spherical basis so that we have the relationship:

$$X_{\mathcal{B}_2} = \mathcal{M}_{\mathcal{B}_1 \mapsto \mathcal{B}_2} \cdot X_{\mathcal{B}_1}$$

Here, since $\mathcal{M}_{\mathcal{B}_1 \mapsto \mathcal{B}_2}$ represents an orthogonal symmetry, we can benefit from the relationship:

$$\mathcal{M}_{\mathcal{B}_2 \mapsto \mathcal{B}_1} = \mathcal{M}^{-1}_{\mathcal{B}_1 \mapsto \mathcal{B}_2} = {}^t\mathcal{M}_{\mathcal{B}_1 \mapsto \mathcal{B}_2}$$

We can thus represent vectors from cartesian coordinates in our spherical system easily with the relationship:

$$X_{\mathcal{B}_1} = \mathcal{M}_{\mathcal{B}_2 \mapsto \mathcal{B}_1} \cdot X_{\mathcal{B}_2}$$

With:

$$\mathcal{M}_{\mathcal{B}_2 \mapsto \mathcal{B}_1} = \begin{bmatrix} \sin(\theta)\cos(\varphi) & \sin(\theta)\sin(\varphi) & \cos(\theta) \\ \cos(\theta)\cos(\varphi) & \cos(\theta)\sin(\varphi) & -\sin(\theta) \\ -\sin(\varphi) & \cos(\varphi) & 0 \end{bmatrix}$$

Concerning the derivatives, let us apply the convention presented in Chapter I: the derivatives with respect to time will be noted with overdots as follows: $\dfrac{\partial X}{\partial t} = \dot{X}$; the position derivatives will only be used for the energy density, in which case they will be noted by subscripts as shown here: $\dfrac{\partial \varepsilon}{\partial \varphi} = \varepsilon_\varphi$. For second derivatives, we will add another subscript as follows: $\dfrac{\partial^2 \varepsilon}{\partial \theta \partial \varphi} = \varepsilon_{\theta\varphi}$. For the matricial quantities X, let us point out that the subscripts $X_{\theta\varphi}$ represent the element of the matrix X in the line corresponding to θ and the column corresponding to φ. A single subscript stands for the projection of the vector X on the vector $\boldsymbol{\theta}$ or $\boldsymbol{\varphi}$.

We will use the Schwarz theorem, stating that the functions that we want to derivate with respect to the spatial coordinates (θ and φ) are derivable twice, and that their second derivatives are continuous, the order of derivation does not matter: $\dfrac{\partial^2}{\partial \theta \partial \varphi} = \dfrac{\partial^2}{\partial \varphi \partial \theta}$. Especially, applied to the energy density, we will consider that $\varepsilon_{\theta\varphi} = \varepsilon_{\varphi\theta}$.

We will also represent the vectorial space of square matrices of size 2 with real coefficient by $\mathcal{M}_2(\mathbb{R})$.

We will also use the symmetric part and antisymmetric part operators defined by the property:

$$\begin{cases} \mathcal{S}_{x_0}(f)(x_0 + x) = & \mathcal{S}_{x_0}(f)(x_0 - x) \\ \mathcal{A}_{x_0}(f)(x_0 + x) = & -\mathcal{A}_{x_0}(f)(x_0 - x) \\ \mathcal{A}_{x_0} + \mathcal{S}_{x_0} = \mathcal{I} \end{cases}$$

Where $\mathcal{I}$ is the identity operator.

In order to distinguish real variables and complex ones, we will use the notation:

$$\begin{cases} x \implies x \in \mathbb{R} \\ \underline{x} \implies \underline{x} \in \mathbb{C} \end{cases}$$

We will also denote the real part and the imaginary as follows:

$$\forall \underline{z} \in \mathbb{C}, \underline{z} = \Re(\underline{z}) + i\Im(\underline{z}) \ \textit{such that} \ (\Re(\underline{z}), \Im(\underline{z})) \in \mathbb{R}^2$$

Since we will focus on resonant problems, and consider frequency dependent variables, we will use the complex notations to improve the clarity of the calculations as follows: a quantity X that evolves periodically at a frequency ω, usually noted $X(t) = X_0 \cos(\omega t + \phi_X)$ will be referred to as $\underline{X}(t) = \underline{X}_0 e^{i\omega t}$ where the phase term is included in the prefactor: $\underline{X}_0 = X_0 e^{i\phi_X}$.

For the sake of clarity, we will group the vacuum permeability and the gyromagnetic ratio as follows: $\gamma\mu_0 = \gamma_0$, where γ_0 can thus be expressed in $rad.s^{-1}.(A.m^{-1})^{-1}$.

Eventually, since the magnetisation can be represented by a vector of constant magnitude (M_S), we will work on the normalised magnetisation $\boldsymbol{m} = \frac{1}{M_S}\boldsymbol{M}$.

IV.2.2 Excitation of the ferromagnetic layer by an RF-magnetic field

Experimentally, we pattern the sample in a wire shape so that we can apply an RF current, letting the induced Oersted field be the main excitation of the magnetic material. However, in a more general case, even though the RF magnetic field may not stem from an Oersted field, the results are exactly the same, the only change will be in the expression of $\boldsymbol{h}_{RF}$ that we do not explicit for the moment.

It is worth noticing that the current density in the material must be small so that we keep the excitation small in comparison with the effective magnetic field $\boldsymbol{H}_{eff}$. This feature is mandatory to use the linear response theory, letting all the following formulas be true, and the calculations to be valid. If not, what will be considered as oscillations at the same frequency as the excitation will be actually changes in the equilibrium position, and the resonance phenomena that we wish to observe will be biased.

The magnetisation dynamics is governed by the Landau-Lifschitz-Gilbert (LLG) equation presented in the section I.5:

$$\dot{\boldsymbol{m}} = -\gamma_0 \boldsymbol{m} \times \boldsymbol{H}_{eff} + \alpha \boldsymbol{m} \times \dot{\boldsymbol{m}} + \boldsymbol{\tau}_{ext} \tag{IV.1}$$

We represent here the effective magnetic field $\boldsymbol{H}_{eff}$, the normalised magnetisation $\boldsymbol{m}$, the damping α and the other external torques acting on the magnetisation $\boldsymbol{\tau}_{ext}$. In a first approximation, we will neglect $\boldsymbol{\tau}_{ext}$, and we will consider them later.

The LLG equation is clearly not linear, and the approximation of a small excitation leading to a linear response allows us to linearise the problem. We will thus consider only the transverse part of the magnetisation, that is to say the components in the linear span of $\{\boldsymbol{\theta}_0, \boldsymbol{\varphi}_0\}$

We can divide the applied field in two different parts: the effective field, and the RF applied field. The effective field is defined as $\boldsymbol{H}_{eff} = -\frac{1}{\mu_0 M_S}\nabla_{\boldsymbol{m}}\varepsilon$, where ε is the total energy density. This field gives the direction of the equilibrium position, and is defined according to that property. The RF field $\underline{\boldsymbol{h}_{RF}}$ is defined by the current flowing through our wire-shaped material. We can represent our objects as follows:

$$\boldsymbol{m} = \begin{bmatrix} 1 \\ 0 \\ 0 \end{bmatrix} \;;\; \dot{\boldsymbol{m}} = \begin{bmatrix} 0 \\ \dot{\theta} \\ \dot{\varphi}\sin(\theta) \end{bmatrix} \;;\; \nabla_{\boldsymbol{m}}\varepsilon = \begin{bmatrix} 0 \\ \varepsilon_\theta \\ \frac{1}{\sin(\theta)}\varepsilon_\varphi \end{bmatrix} \;;\; \boldsymbol{h}_{RF} = \begin{bmatrix} h_r\cos(\omega t + \phi_r) \\ h_\theta\cos(\omega t + \phi_\theta) \\ h_\varphi\cos(\omega t + \phi_\varphi) \end{bmatrix}$$

Let us now use the complex notations of frequency dependant quantities for the sake of calculations simplicity, as mentioned in the section IV.2.1. We can especially express the RF field as:

$$\underline{\dot{\boldsymbol{m}}} = \begin{bmatrix} 0 \\ \dot{\underline{\theta}} \\ \dot{\underline{\varphi}}\sin(\underline{\theta}) \end{bmatrix} \;;\; \nabla_{\boldsymbol{m}}\varepsilon = \begin{bmatrix} 0 \\ \varepsilon_\theta \\ \frac{1}{\sin(\underline{\theta})}\varepsilon_\varphi \end{bmatrix} \;;\; \underline{\boldsymbol{h}}_{RF} = e^{i\omega t}\begin{bmatrix} \underline{h}_r \\ \underline{h}_\theta \\ \underline{h}_\varphi \end{bmatrix}$$

Let us call (θ_0, φ_0) the equilibrium position of the magnetisation. We will linearise the equation of motion around that position. We will thus consider the following forms for the angles θ and φ, with constants θ_0, φ_0, and unknown time-dependent functions $\underline{\delta\theta}, \underline{\delta\varphi}$.

$$\begin{cases}\underline{\theta} = & \theta_0 + \underline{\delta\theta}\\ \underline{\varphi} = & \varphi_0 + \underline{\delta\varphi}\end{cases}$$

By using these expressions in the Landau Lifshitz Gilbert equation (eq.(IV.1)), we obtain:

$$\begin{cases}\dot{\underline{\theta}} = -\dfrac{\gamma}{\sin(\theta)M_S}\varepsilon_\varphi(\theta,\varphi) - \alpha\dot{\underline{\varphi}}\sin(\theta) + \gamma_0\underline{h}_\varphi e^{i\omega t}\\ \dot{\underline{\varphi}}\sin(\theta) = \dfrac{\gamma}{M_S}\varepsilon_\theta(\theta,\varphi) + \alpha\dot{\underline{\theta}} - \gamma_0\underline{h}_\theta e^{i\omega t}\end{cases} \tag{IV.2}$$

The assumption of a linear response to the RF field $\boldsymbol{h}_{RF}$, meaning that the angles θ and φ will follow the oscillations at the same frequency as the excitation, leads to the expressions of the the time derivatives that follow:

$$\begin{cases}\dot{\underline{\theta}} = \dot{\underline{\delta\theta}} = i\omega\underline{\delta\theta}_0 e^{i\omega t}\\ \dot{\underline{\varphi}} = \dot{\underline{\delta\varphi}} = i\omega\underline{\delta\varphi}_0 e^{i\omega t}\end{cases}$$

Where $(\underline{\delta\theta}_0, \underline{\delta\varphi}_0) \in \mathbb{C}^2$ are the amplitudes of the functions, evaluated in (θ_0, φ_0) including a phase. The 1^{st} order linearisation of ε gives us the following:

$$\begin{cases}\varepsilon_\theta(\theta_0 + \underline{\delta\theta}, \varphi_0 + \underline{\delta\varphi}) = \varepsilon_\theta(\theta_0,\varphi_0) + \underline{\delta\theta}\varepsilon_{\theta\theta}(\theta_0,\varphi_0) + \underline{\delta\varphi}\varepsilon_{\theta\varphi}(\theta_0,\varphi_0)\\ \varepsilon_\varphi(\theta_0 + \underline{\delta\theta}, \varphi_0 + \underline{\delta\varphi}) = \varepsilon_\varphi(\theta_0,\varphi_0) + \underline{\delta\theta}\varepsilon_{\varphi\theta}(\theta_0,\varphi_0) + \underline{\delta\varphi}\varepsilon_{\varphi\varphi}(\theta_0,\varphi_0)\end{cases}$$

This system of equations is simplified when we take into account the fact that (θ_0, φ_0) is an equilibrium position of the magnetisation. The derivative of the total energy with respect to both spatial coordinates cancels out, leading to the following relations:

$$\begin{cases}\varepsilon_\theta(\theta_0 + \underline{\delta\theta}, \varphi_0 + \underline{\delta\varphi}) = \underline{\delta\theta}\varepsilon_{\theta\theta}(\theta_0,\varphi_0) + \underline{\delta\varphi}\varepsilon_{\theta\varphi}(\theta_0,\varphi_0)\\ \varepsilon_\varphi(\theta_0 + \underline{\delta\theta}, \varphi_0 + \underline{\delta\varphi}) = \underline{\delta\theta}\varepsilon_{\varphi\theta}(\theta_0,\varphi_0) + \underline{\delta\varphi}\varepsilon_{\varphi\varphi}(\theta_0,\varphi_0)\end{cases}$$

In the following, the derivatives of the energy density will be implicitly evaluated at the equilibrium position. We can thus rewrite the system IV.2.2, as the following system:

$$\begin{cases}i\omega\underline{\delta\theta}_0 = -\dfrac{\gamma}{\sin(\theta_0)M_S}\left(\underline{\delta\theta}_0\varepsilon_{\varphi\theta} + \underline{\delta\varphi}_0\varepsilon_{\varphi\varphi}\right) - i\omega\alpha\underline{\delta\varphi}_0\sin(\theta_0) + \gamma_0\underline{h}_\varphi\\ i\omega\underline{\delta\varphi}_0\sin(\theta_0) = \dfrac{\gamma}{M_S}\left(\underline{\delta\theta}_0\varepsilon_{\theta\theta} + \underline{\delta\varphi}_0\varepsilon_{\varphi\theta}\right) + i\omega\alpha\underline{\delta\theta}_0 - \gamma_0\underline{h}_\theta\end{cases}$$

Or in matricial notations, we obtain the system $\mathcal{D}$:

$$\begin{bmatrix}\dfrac{\gamma}{M_S}\varepsilon_{\theta\theta} + i\omega\alpha & -i\omega + \dfrac{\gamma}{\sin(\theta_0)M_S}\varepsilon_{\varphi\theta}\\ i\omega + \dfrac{\gamma}{\sin(\theta_0)M_S}\varepsilon_{\varphi\theta} & \dfrac{\gamma}{\sin^2(\theta_0)M_S}\varepsilon_{\varphi\varphi} + i\omega\alpha\end{bmatrix}\cdot\begin{bmatrix}\underline{\delta\theta}_0\\ \sin(\theta_0)\underline{\delta\varphi}_0\end{bmatrix} = \gamma_0\begin{bmatrix}\underline{h}_\theta\\ \underline{h}_\varphi\end{bmatrix}$$

The determinant of that system has a great impact on the magnetic susceptibility since the amplitude of the coefficients are proportionnal to the modulus of its inverse. Let us explicit that value, that we will interpret as a function of the excitation frequency:

$$\det(\mathcal{D})(\omega) = \begin{vmatrix}\dfrac{\gamma}{M_S}\varepsilon_{\theta\theta} + i\omega\alpha & -i\omega + \dfrac{\gamma}{M_S\sin(\theta_0)}\varepsilon_{\theta\varphi}\\ i\omega + \dfrac{\gamma}{M_S\sin(\theta)}\varepsilon_{\varphi\theta} & \dfrac{\gamma}{\sin^2(\theta_0)M_S}\varepsilon_{\varphi\varphi} + i\omega\alpha\end{vmatrix}$$

Thus we obtain a 2^{nd} order polynomial equation for the frequency:

$$\det(\mathcal{D})(\omega) = -\omega^2(1+\alpha^2) + i\omega\frac{\alpha\gamma}{M_S}\left(\varepsilon_{\theta\theta} + \frac{1}{\sin^2(\theta_0)}\varepsilon_{\varphi\varphi}\right) - \left(\frac{\gamma}{M_S\sin(\theta_0)}\right)^2(\varepsilon_{\theta\varphi}^2 - \varepsilon_{\theta\theta}\varepsilon_{\varphi\varphi})$$

At this point, let us define:

$$\boxed{\omega_0 = \frac{\gamma}{\sin(\theta_0)M_S\sqrt{1+\alpha^2}}\sqrt{\varepsilon_{\theta\theta}\varepsilon_{\varphi\varphi} - (\varepsilon_{\theta\varphi})^2}} \tag{IV.3}$$

And:

$$\boxed{\Delta = \frac{\gamma\alpha}{(1+\alpha^2)M_S}\left(\varepsilon_{\theta\theta} + \frac{1}{\sin^2(\theta_0)}\varepsilon_{\varphi\varphi}\right)} \tag{IV.4}$$

With this definition, ω_0 matches the definition of the resonant frequency, and Δ corresponds to the linewidth of the resonant peak that can be observed in the magnetic response of the material as a function of the frequency. For the lorentzian-like coefficients of the susceptibility (expressed later, in eq. (IV.6)), it is the width of the peak at the half of the maximum height), and for the antilorentzian-like coefficients, it corresponds to the difference of frequency of the two peaks of the curve. With these conventions, we can express in a general way, the determinant of the system eq. (IV.2) as follows:

$$\det(\mathcal{D})(\omega) = -(1+\alpha^2)(\omega^2 - \omega_0^2) + i\omega\Delta(1+\alpha^2)$$

In that expression, it is remarkable that $\Delta \ll 1$ for low values of damping, for instance $\alpha \leq 0.1$. Consequently, the modulus of the determinant is minimum approximately when $\omega \approx \omega_0$. Thus, with the interpretation of the system $\mathcal{D}$ in terms of magnetic susceptibility $\underline{\chi}$ as defined in eq. IV.5, in a first approach, we can consider that the modulus of the coefficients of the magnetic susceptibility $\underline{\chi}$ will be maximised at that position, even though this is just an approximate result. We will nonetheless call ω_0 the resonance frequency.

$$\underline{\chi}^{-1}(\omega)\delta\boldsymbol{m}M_S = \underline{\boldsymbol{h}}_{RF} \tag{IV.5}$$

We can inverse that system so as to express the magnetic susceptibility, that is to say the material response to the applied magnetic excitation.

$$\boxed{\underline{\chi}(\omega) = \frac{\gamma_0 M_S}{\left[(\omega_0^2 - \omega^2) + i\omega\Delta\right](1+\alpha^2)}\begin{bmatrix}\frac{\gamma}{\sin^2(\theta_0)M_S}\varepsilon_{\varphi\varphi} + i\omega\alpha & i\omega - \frac{\gamma}{\sin(\theta_0)M_S}\varepsilon_{\varphi\theta} \\ -i\omega - \frac{\gamma}{\sin(\theta_0)M_S}\varepsilon_{\varphi\theta} & \frac{\gamma}{M_S}\varepsilon_{\theta\theta} + i\omega\alpha\end{bmatrix}} \tag{IV.6}$$

We can separate that susceptibility as a real part and an imaginary part that we will note as follows:

$$\underline{\chi} = \chi' + i\chi'' = \begin{bmatrix}\chi'_{\theta\theta} & \chi'_{\theta\varphi} \\ \chi'_{\varphi\theta} & \chi'_{\varphi\varphi}\end{bmatrix} + i\begin{bmatrix}\chi''_{\theta\theta} & \chi''_{\theta\varphi} \\ \chi''_{\varphi\theta} & \chi''_{\varphi\varphi}\end{bmatrix}$$

Where $(\chi', \chi'') \in (\mathcal{M}_2(\mathbb{R}))^2$. Following that decomposition, we find:

$$\boxed{\chi'(\omega) = \frac{\gamma_0 M_S}{f(\omega)(1+\alpha^2)}\begin{bmatrix}\frac{\gamma\left(\omega_0^2 - \omega^2\right)}{\sin^2(\theta_0)M_S}\varepsilon_{\varphi\varphi} + \omega^2\alpha\Delta & \omega^2\Delta - \frac{\gamma\left(\omega_0^2 - \omega^2\right)}{\sin(\theta_0)M_S}\varepsilon_{\varphi\theta} \\ -\omega^2\Delta - \frac{\gamma\left(\omega_0^2 - \omega^2\right)}{\sin(\theta_0)M_S}\varepsilon_{\varphi\theta} & \frac{\gamma\left(\omega_0^2 - \omega^2\right)}{M_S}\varepsilon_{\theta\theta} + \omega^2\alpha\Delta\end{bmatrix}} \tag{IV.7}$$

$$\boxed{\chi''(\omega)=\frac{\gamma_0 M_S\omega}{f(\omega)(1+\alpha^2)}\begin{bmatrix}-\dfrac{\gamma\Delta}{\sin^2(\theta_0)M_S}\varepsilon_{\varphi\varphi}+\left(\omega_0^2-\omega^2\right)\alpha & \left(\omega_0^2-\omega^2\right)+\dfrac{\gamma\Delta}{\sin(\theta_0)M_S}\varepsilon_{\varphi\theta}\\ -\left(\omega_0^2-\omega^2\right)+\dfrac{\gamma\Delta}{\sin(\theta_0)M_S}\varepsilon_{\varphi\theta} & -\dfrac{\gamma\Delta}{M_S}\varepsilon_{\theta\theta}+\left(\omega_0^2-\omega^2\right)\alpha\end{bmatrix}} \tag{IV.8}$$

Where the function f is defined as:

$$f(\omega)=\left(\omega_0^2-\omega^2\right)^2+(\omega\Delta)^2$$

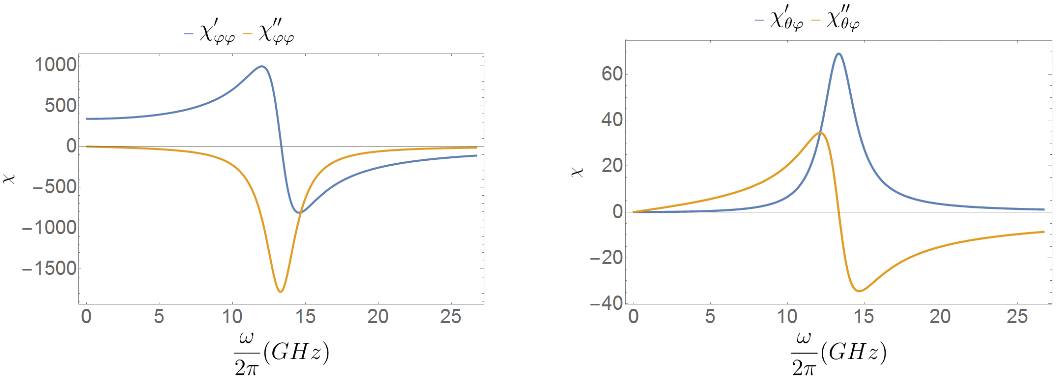

(a) Case of a diagonal coefficient: $\chi_{\varphi\varphi}$

(b) Case of a non-diagonal coefficient: $\chi_{\theta\varphi}$

Figure IV.2: Representation of the real parts (blue) and imaginary parts (orange) diagonal (a) and non-diagonal (b) coefficients of the magnetic susceptibility χ in the case of a material with a saturation magnetisation of $M_S = 1.45\times10^6\ A.m^{-1}$, a magnetic damping of $\alpha = 7\times10^{-3}$, an in-plane uniaxial anisotropy in the $\boldsymbol{x}$ direction with a constant $K = 3.3\times10^4\ J.m^{-3}$, the demagnetising field of a perfect infinite thin film, and an applied magnetic field of $\mu_0 H = 0.1\ T$ in the direction defined by $\theta = \dfrac{\pi}{2}$ and $\varphi = \dfrac{\pi}{4}$.

We have analytically determined the response of a ferromagnetic material to a monochromatic magnetic perturbation as a function of the frequency of the perturbation, and of materials parameters in the limits of the linear response regime. The results we displayed enable us to evaluate the response of the magnetisation in all the geometric configurations that are possibly achievable, except the case of an out of plane magnetisation, which has already been solved numerous times, and only needs Cartesian coordinates, and which can be obtained by continuity of the expressions we obtained for $\theta_0 \to 0$. Before using these results to treat ST-FMR and SP-FMR experiments, let us first focus on a short example of the study of the frequency resonance as a function of the applied field in two well-known cases, and for a less standard geometry.

IV.2.3 Examples using a standard configuration

We have seen in the first chapter that several magnetic interactions govern the magnetisation dynamics. Here, we explicit several energy terms that we shall consider for further numerical applications. We will consider especially three cases corresponding to the orientation of the magnetic field with respect to the easy axis of magnetisation. All of these cases involve a magnetisation in the plane of the sample, which is equivalent in terms of coordinates to $\theta = \frac{\pi}{2}$. Let us call φ_H the angle between the applied magnetic field and the easy axis of magnetisation. We are especially interested in common experimental cases that can be useful for the rest of the manuscript. First, we will consider the case in which the magnetic field is along an easy axis of magnetisation ($\varphi_H = 0$). This case can be solved entirely analytically as long as the macrospin approximation holds. Then, we will focus on the hard axis case, corresponding to ($\varphi_H = \frac{\pi}{2}$) , which is also analytically solvable, and which represents a usual experimental configuration of the spin pumping experiment. Eventually, we present an intermediate case in which the magnetisation is tilted from the easy axis ($\varphi_H = \frac{\pi}{4}$), which is particularly interesting because it is the experimental configuration that is often used for spin torque ferromagnetic resonance experiments. This last case, however, is not explicitly treatable analytically, since the solutions of the equilibrium position of the magnetisation of the macrospin are implicit. Indeed the results must be obtained by a numerical analysis.

The only energy density term that differs in these three cases is the one corresponding to the action of the magnetic field, ε_Z. We will take that aspect into account by examining three different expressions of the Zeeman energy density labelled ε_Z^0, $\varepsilon_Z^{\frac{\pi}{2}}$ and $\varepsilon_Z^{\frac{\pi}{4}}$, labelled after the corresponding values of φ_H respectively.

Since all the calculations are based on the macrospin hypothesis, we can use the energies detailed in the first chapter, especially ignoring the direct exchange, and taking into account the Zeeman interaction ε_Z, the demagnetising term ε_D, due to the shape of the sample, and less dramatically the magnetic anisotropy ε_A. We will consider the latter in this calculation to see the influence of this parameter on the results, but we will not keep it for the rest of the analysis, the magnetic anisotropy in the plane of the sample being absent in the samples presented in the rest of the manuscript. Let us call $\boldsymbol{x}$ the wire's long axis and $\boldsymbol{y}$ the direction perpendicular to it, in the plane of the sample. Then, the energy densities are written as follows:

$$\begin{cases} \varepsilon_Z^0 = & -\mu_0 \boldsymbol{M} \cdot \boldsymbol{H} = -\mu_0 M_S H (\boldsymbol{r} \cdot \boldsymbol{x}) \\ \varepsilon_Z^{\frac{\pi}{4}} = & -\mu_0 M_S H (\boldsymbol{r} \cdot \dfrac{\boldsymbol{x} + \boldsymbol{y}}{\sqrt{2}}) \\ \varepsilon_Z^{\frac{\pi}{2}} = & -\mu_0 M_S H (\boldsymbol{r} \cdot \boldsymbol{y}) \\ \varepsilon_A = & -\dfrac{K}{M_S} (\boldsymbol{M} \cdot \boldsymbol{x})^2 \\ \varepsilon_D = & \dfrac{1}{2} \mu_0 \boldsymbol{M} \cdot \boldsymbol{N} \cdot \boldsymbol{M} = \dfrac{1}{2} \mu_0 M_S^2 (\boldsymbol{r} \cdot \boldsymbol{z})^2 \end{cases}$$

In the last expression, we chose the demagnetising tensor as:

$$\boldsymbol{N} = \begin{bmatrix} 0 & 0 & 0 \\ 0 & 0 & 0 \\ 0 & 0 & 1 \end{bmatrix}$$

We chose the axes $\boldsymbol{x}$ and $\boldsymbol{y}$ corresponding to the image shown in fig. IV.3. Let us point out here that the model we choose is to put a large demagnetising field in the out of plane direction, neglecting the shape anisotropy in the other directions. Actually, the addition of a small uniaxial magnetocrystalline anisotropy is equivalent to an additional component in the demagnetising tensor. For further measurements, the dimensions of the wires that we will consider will be 100 $\mu m \times 10$ $\mu m \times 5$ nm. Indeed, we computed approximate values of the coefficients of the demagnetising tensor according to [57] in the table IV.1:

Using the angular coordinates, these energies are expressed as follows:

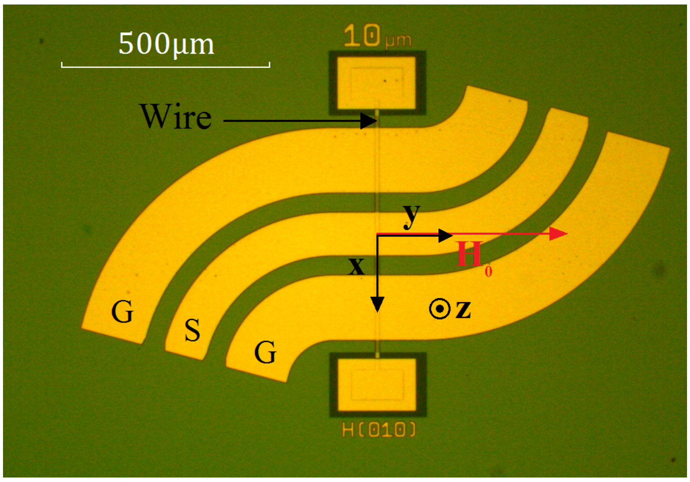

Figure IV.3: Schematic of the axes corresponding to the expression of the demagnetising tensor expressed as a diagonal.

t_{FM} (nm)	N_{xx} ($\times 10^{-4}$)	N_{yy} ($\times 10^{-6}$)	N_{zz}
1	1.059850	3.059736	0.999899
2	2.119700	6.119473	0.999798
3	3.179551	9.179210	0.999697
5	5.299251	15.298683	0.999496
10	10.598502	30.597365	0.998991
15	15.897753	45.896048	0.998487
20	21.197005	61.194730	0.997982

Table IV.1: Values of the demagnetising tensor for a 100μm-long and 10μm-wide wire as a function of its thickness t_{FM}.

$$\begin{cases} \varepsilon_Z^0 = -\mu_0 M_S H \sin(\theta)\cos(\varphi) \\ \varepsilon_Z^{\frac{\pi}{4}} = -\dfrac{\mu_0 M_S H}{\sqrt{2}} \sin(\theta)(\sin(\varphi)+\cos(\varphi)) \\ \varepsilon_Z^{\frac{\pi}{2}} = -\mu_0 M_S H \sin(\theta)\sin(\varphi) \\ \varepsilon_A = -K\sin^2(\theta)\cos^2(\varphi) \\ \varepsilon_D = \dfrac{1}{2}\mu_0 M_S^2 \cos^2(\theta) \end{cases}$$

The 2^{nd} derivatives of the energy density $\varepsilon = \varepsilon_Z + \varepsilon_A + \varepsilon_D$ with respect to the position are then:

$$\begin{cases} \varepsilon_{\theta\theta}^0 = \mu_0 M_S H \sin(\theta)\cos(\varphi) - 2K\cos(2\theta)\cos^2(\varphi) - \mu_0 M_S^2 \cos(2\theta) \\ \varepsilon_{\varphi\varphi}^0 = \mu_0 M_S H \sin(\theta)\cos(\varphi) + 2K\sin^2(\theta)\cos(2\varphi) \\ \varepsilon_{\theta\varphi}^0 = \varepsilon_{\varphi\theta} = \mu_0 M_S H \cos(\theta)\sin(\varphi) + K\sin(2\theta)\sin(2\varphi) \end{cases}$$

$$\begin{cases} \varepsilon_{\theta\theta}^{\frac{\pi}{2}} = \mu_0 M_S H \sin(\theta)\sin(\varphi) - 2K\cos(2\theta)\cos^2(\varphi) - \mu_0 M_S^2 \cos(2\theta) \\ \varepsilon_{\varphi\varphi}^{\frac{\pi}{2}} = \mu_0 M_S H \sin(\theta)\sin(\varphi) + 2K\sin^2(\theta)\cos(2\varphi) \\ \varepsilon_{\theta\varphi}^{\frac{\pi}{2}} = \varepsilon_{\varphi\theta} = -\mu_0 M_S H \cos(\theta)\cos(\varphi) + K\sin(2\theta)\sin(2\varphi) \end{cases}$$

$$\begin{cases} \varepsilon_{\theta\theta}^{\frac{\pi}{4}} = \dfrac{\mu_0 M_S H}{\sqrt{2}} \sin(\theta)(\sin(\varphi) + \cos(\varphi)) - 2K\cos(2\theta)\cos^2(\varphi) - \mu_0 M_S^2 \cos(2\theta) \\ \varepsilon_{\varphi\varphi}^{\frac{\pi}{4}} = \dfrac{\mu_0 M_S H}{\sqrt{2}} \sin(\theta)(\sin(\varphi) + \cos(\varphi)) + 2K\sin^2(\theta)\cos(2\varphi) \\ \varepsilon_{\theta\varphi}^{\frac{\pi}{4}} = \varepsilon_{\varphi\theta} = -\mu_0 M_S H \cos(\theta)(\cos(\varphi) - \sin(\varphi)) + K\sin(2\theta)\sin(2\varphi) \end{cases}$$

The expressions given in these three cases need to be evaluated at the equilibrium positions of the magnetisation, which depends on the applied field. In our case, we consider that the magnetic anisotropy is dominated by the demagnetising field, leading to a magnetisation that lies in the plane of the sample as long as we do not apply a magnetic field out of the plane. Indeed we will consider $\theta_0 = \frac{\pi}{2}$. The simplest case is definitely the easy axis measurement, in which the magnetisation is always aligned with the easy axis of magnetisation ($\varphi \in \{0, \pi\}$), with a switching predicted for an applied field equal to the anisotropy field H_K defined as: $H_K = \frac{2K}{\mu_0 M_S}$. The hard axis measurement also shows a simple field dependence, with a saturation for an absolute value of the field superior to H_K, and a linear dependence in between $-H_K$ and H_K. The case corresponding to $\varphi_H = \frac{\pi}{4}$ is the only one that we have to solve numerically. All the magnetic hysteresis loops are represented on the top panels of fig. IV.4.

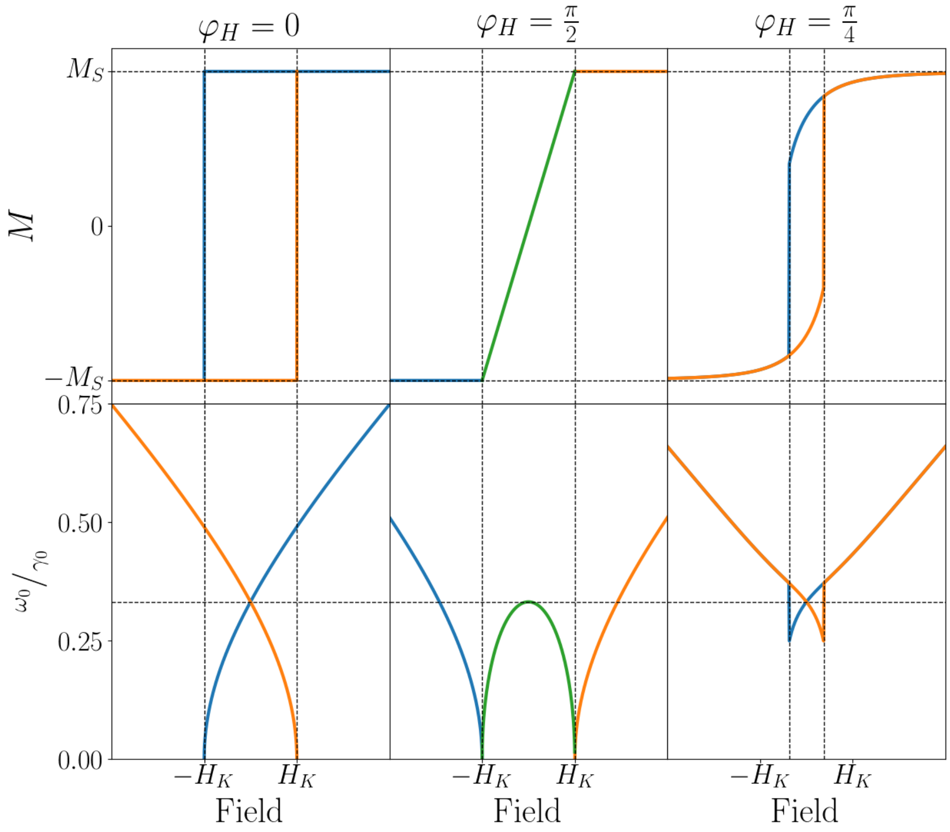

Figure IV.4: Correspondance between the hysteresis magnetic loop and the dependence of the resonant frequency as a function of the applied magnetic field in three different geometries: easy axis of magnetisation ($\varphi_H = 0$, eq. (IV.9)), hard axis of magnetisation ($\varphi_H = \frac{\pi}{2}$, eq. (IV.10)) and for a field tilted from both the easy and hard axes of magnetisation ($\varphi_H = \frac{\pi}{4}$): the top panels represent the magnetic hysteresis loops whereas the lower panels represent the resonant frequency as a function of the amplitude of the applied magnetic field.

Thus, from eq. (IV.3), we can write the Kittel law (for low magnetic damping, that is to say $1+\alpha^2 \approx 1$) for the two branches of the easy axis case:

$$\begin{cases} \dfrac{\omega_0}{\gamma_0} = \sqrt{(H-H_K)(H-M_S-H_K)} & for\ \varphi_0 = \pi \\ \\ \dfrac{\omega_0}{\gamma_0} = \sqrt{(H+H_K)(H+M_S+H_K)} & for\ \varphi_0 = 0 \end{cases} \tag{IV.9}$$

and for the hard axis case:

$$\begin{cases} \dfrac{\omega_0}{\gamma_0} = \sqrt{(H+H_K)(H-M_S)} & for\ H < -H_K,\ \varphi_0 = -\dfrac{\pi}{2} \\ \\ \dfrac{\omega_0}{\gamma_0} = \sqrt{H_K(H_K+M_S)\left(1-\left(\dfrac{H}{H_K}\right)^2\right)} & for\ H \in [-H_K, H_K] \\ \\ \dfrac{\omega_0}{\gamma_0} = \sqrt{(H-H_K)(H+M_S)} & for\ H > H_K,\ \varphi_0 = \dfrac{\pi}{2} \end{cases} \tag{IV.10}$$

We can also express the dependence of the linewidth of the ferromagnetic resonance with the applied magnetic field. In the case of the easy and hard axis (for $|H| > H_K$) measurements, we obtain the following equations:

$$\begin{cases} \Delta = \gamma_0\alpha(2|H|+M_S+H_K) & \varphi_H = 0 \\ \Delta = \gamma_0\alpha(2|H|+M_S-H_K) & \varphi_H = \dfrac{\pi}{2} \end{cases}$$

For further calculation, since the materials considered have low magnetic damping ($\alpha \approx 10^{-2}$), we will consider that $1+\alpha^2 = 1$.

We have now described explicitly the magnetisation dynamical response to an RF perturbation at a given frequency, with an applied field and various magnetic interactions, in a general manner that enables us to deal with all the geometries where the magnetisation is not perpendicular to the sample's plane. We have presented an application of the literal results that we displayed, for an in plane magnetisation with a uniaxial anisotropy, and studied three cases corresponding to three different relative orientations between the anisotropy axis and the applied magnetic field, showing that we can perfectly reproduce the Kittel law. We also linked that evolution of the resonant frequency dependence on the applied magnetic field to the magnetic hysteresis loops that the macrospin model provides. We shall now present the physical phenomena that will enable us to use the previous results in order to determine the SHE and ISHE in a material.

IV.3 SHE and ISHE characterisation from spin currents

Since the years 1970, several researchers have predicted the existence of spin currents and their action on the magnetisation. From these works, the discovery of methods to generate spin currents gathered a lot of attention from the scientific community. The main means for this purpose were the magnetisation dynamics, and also to study the interplay between a spin current and the magnetisation of materials. In this section, we will present first the spin currents generation and its consequence on the magnetisation dynamics. Then, we will see how both parts of the problem lead to two distinct methods to probe the SHE and ISHE in a non magnetic material using an auxiliary ferromagnetic material.

IV.3.1 Interplay between spin currents and magnetisation

Spin current carried by electrons

Since the theoretical prediction of spin currents, several options have been considered to achieve experimentally those. Theoretically, two mechanisms have been proposed for spin transport. First, Berger evidenced that the electrical current is able to carry a spin current. This phenomenon can occur within a magnetic material when a charge current is flowing through it. Indeed the spin of the electrons aligns with the local magnetisation of the ferromagnetic material.

This mechanism can be a powerful mean to obtain the spin polarisation of a charge current. However, it is a source of heat in the material where it propagates through the Joule effect, and is therefore not very efficient in terms of energy consumption. Moreover, the spin polarisation P that one can achieve with such method is not always large. We define the spin polarisation as a function of the Fermi vectors $k^{\uparrow}$ and $k^{\downarrow}$:

$$P = \frac{k^{\uparrow} - k^{\downarrow}}{k^{\uparrow} + k^{\downarrow}}$$

This spin polarisation, which is a way to represent the efficiency of spin current generation, can vary between 0 and 1, but the maximum polarisation is only achieved in semi-metals, which is not the most common case in spintronics. This kind of spin currents is responsible for the effect called spin transfer torque (STT) that we discuss in IV.3.1.

Spin current by spin Hall effect

Through the discovery of spin Hall effect, another spin current generation method was found. The principle lies in spin dependent scatterings and intrinsic effects that can be observed in materials showing strong spin orbit coupling. In this case, we observe a pure spin current that is not carried by charge carriers. Indeed we can diminish dramatically the thermal effects experienced usually. Indeed, even though Joule effect is not cancelled during spin current generation, it can be much smaller than in spin transfer torque techniques due to the low resistivity of materials showing SHE, and therefore enable the generation of a large spin current with a small heating effect. The efficiency of this conversion is given by the spin Hall angle of the chosen material.

Since this spin current is stemming from the spin orbit coupling, the resulting action of the spin current produced by these means on the magnetisation is named spin orbit torques (SOT).

The representation of a spin current density $\boldsymbol{j_s}$ can be achieved using a vector which components are also vectors, in the following form:

$$\boldsymbol{j_s} = \begin{bmatrix} \boldsymbol{j_s^x} \\ \boldsymbol{j_s^y} \\ \boldsymbol{j_s^z} \end{bmatrix}$$

The spin polarisation directions of the components of the spin currents can be noted $\boldsymbol{\sigma}_k$ where $k \in \{x, y, z\}$ such that the spin current can be written:

$$\boldsymbol{j}_s = \begin{bmatrix} j_s^{\boldsymbol{x}} \boldsymbol{\sigma}_x \\ j_s^{\boldsymbol{y}} \boldsymbol{\sigma}_y \\ j_s^{\boldsymbol{z}} \boldsymbol{\sigma}_z \end{bmatrix}$$

Following this representation, $\boldsymbol{j}_s^{\boldsymbol{u}}$ is the spin current density flowing in the $\boldsymbol{u}$ direction ($\boldsymbol{u} \in \{\boldsymbol{x}, \boldsymbol{y}, \boldsymbol{z}\}$), and the spin polarisation is given by the unit vector $\boldsymbol{\sigma}_u$. The amplitude of the spin current flowing along $\boldsymbol{u}$ is thus given by the magnitude of $\boldsymbol{j}_s^{\boldsymbol{u}}$.

Spin current by spin pumping

The evolution of the magnetisation dynamics in a ferromagnet creates a spin current transverse to the magnetisation, which polarisation is colinear with the equilibrium position of the magnetisation, and which expression is [88,124,125]:

$$\boldsymbol{j}_s^{\boldsymbol{u}} = \frac{\hbar}{4\pi} \frac{1}{M_s^2} A_r \left(\boldsymbol{M} \times \frac{d\boldsymbol{M}}{dt} \right) \tag{IV.11}$$

Here, $\boldsymbol{u}$ is the unit vector along which the spin current propagates, and A_r is the sample's spin pumping conductance, which is usually considered to be close to the real part of the spin mixing conductance at the interface where the spin current is injected [125]. A careful examination of this formula show a clear proportionality of the spin current generated to the damping torque acting on the magnetisation. This relationship can be understood from qualitative considerations: when precessing around an equilibrium position with a static excitation, the magnetisation experiences a damped motion in which the angular momentum aligns with the effective field. The magnetic damping corresponds thus to the dissipation of angular momentum on the directions transverse to the effective field to other degrees of freedom of the system. The fact that the precession is maintained leads to a continuous emission of angular momentum along the effective field axis, maintaining a component of the magnetisation out of the effective field axis, hence a proportionality between the spin current density and the damping torque.

Spin transfer torque (STT)

When a spin current flows through a ferromagnetic material, the spin current and the magnetisation of the lattice can exchange angular momentum. Indeed, the flow of the spin current can act on the magnetisation, which is modeled by a torque added in the Landau Lifshitz Gilbert equation eq. (IV.1). This phenomenon is called Spin Transfer Torque (STT). The first prediction of this phenomenon is due to Berger, who described it from 1978 and in the following decade, especially in the case of current induced domain wall motion [8–10]. Slonczewski [13,96] and Berger [126,127] predicted simultaneously the reorientation of the magnetisation of a layer using spin transfer torques. The common way to represent the torques acting on the magnetisation is to define a base of the plane transverse to the magnetisation by considering a “field-like” ($\boldsymbol{\tau}_{FL}$) and a “damping-like” ($\boldsymbol{\tau}_{DL}$) torque. Unless the spin polarisation is colinear with the magnetisation, in which case the spin current does not interact with the magnetisation at first order, the expression of these torques is the following:

$$\begin{cases} \boldsymbol{\tau}_{DL} = a(\boldsymbol{m}, \boldsymbol{j}_s, \boldsymbol{\sigma}, \omega) \boldsymbol{m} \times (\boldsymbol{m} \times \boldsymbol{\sigma}) \\ \boldsymbol{\tau}_{FL} = b(\boldsymbol{m}, \boldsymbol{j}_s, \boldsymbol{\sigma}, \omega) \boldsymbol{m} \times \boldsymbol{\sigma} \end{cases} \tag{IV.12}$$

Here, the amplitude of these torques is defined by the functions a and b, which can depend on many parameters in a general way. If several expressions of torques have been proposed in the literature, this general approach enables a general representation of the torque applicable to the magnetisation.

We have seen two types of effects: the action of a spin current on the magnetisation (spin torques) and the generation of a spin current from magnetisation dynamics (spin pumping). Let us now consider the techniques that stem from these two effects in order to probe direct (spin torques) and inverse (spin pumping) spin Hall effects.

IV.3.2 Spin Torque Ferromagnetic Resonance (ST-FMR)

Let us consider a bilayer where a charge current at RF frequency flows through a nonmagnetic material, creating both a spin current that flows through a magnetic layer, and an RF Oersted field. The magnetic layer's behaviour is described by the dynamic susceptibility calculated in eq. (IV.6).

The effect of spin torques that we represented on equation (IV.12) are especially visible at FMR frequencies. By considering the expressions of the torques, one can see that the temporal average of the field-like torque is null, at the first order: $\overline{\boldsymbol{m} \times \boldsymbol{\sigma}} = \mathbf{0}$. However, the damping-like torque does not seem to cancel. From now on, we will assume that the time average of the damping-like torque is small enough not to change the equilibrium position of the magnetisation. This approximation accuracy increases with the amplitude of the applied magnetic field. One can easily observe that the addition of an oscillating field-like torque on the LLG equation leads to the transformation: $\boldsymbol{h}_{RF} \mapsto \boldsymbol{h}_{RF} + b\boldsymbol{\sigma}$. In that case, all the magnetisation dynamics study that was carried out earlier holds. However, the damping like torque is more complex to handle. In the approximation where the damping-like torque is small compared to the field torque generated by the RF excitation, which is the assumption that is made when using the linear response theory for the treatment of the problem, we will consider that the addition of this torque does not change the magnetic susceptibility obtained in eq. (IV.6). Indeed, we can consider an additional transverse field equal to $\boldsymbol{m} \times \boldsymbol{\sigma}$. In that case, the torque added will change the way that the material is probed, leading to the appearance of different terms of the magnetic susceptibility in the signals observed. In the spherical coordinates system that we use, the oscillating torques can be written after simplification as follows:

$$
\begin{cases}
\boldsymbol{\tau}_{DL} = a(\boldsymbol{m})\boldsymbol{m} \times \begin{bmatrix} 0 \\ -\sigma_\varphi \\ \sigma_\theta \end{bmatrix} e^{i(\omega t + \psi)} = a(\boldsymbol{m})\boldsymbol{m} \times \begin{bmatrix} 0 \\ -\underline{\sigma}_\varphi \\ \underline{\sigma}_\theta \end{bmatrix} e^{i\omega t} \\
\boldsymbol{\tau}_{FL} = b(\boldsymbol{m})\boldsymbol{m} \times \begin{bmatrix} \sigma_r \\ \sigma_\theta \\ \sigma_\varphi \end{bmatrix} e^{i(\omega t + \psi)}
\end{cases}
$$

Here, without any loss of generality, we add a phase term in the time dependence of the torque. We assume that the origin for the phase is relative to the RF field. We will thus express the projections of $\boldsymbol{\sigma}$ as complex numbers, including that phase term: $\underline{\sigma}_j = \sigma_j e^{i\psi}$ where $j \in \{\theta, \varphi\}$. We can note however that in the special case where the field excitation is only due to current effects, the phase cancels out because it is the same between the Oersted field and the SHE effect, stemming from the same source.

Let us consider that the vector $\boldsymbol{\sigma}$ can be represented by the angles $(\theta_\sigma, \varphi_\sigma)$ in the spherical coordinates system, (θ, φ) given by the position of the magnetisation, as represented in fig. IV.5. We can explicit the terms σ_θ and σ_φ as follows:

$$
\begin{cases}
\sigma_\theta = \cos(\theta)\sin(\theta_\sigma)\cos(\varphi - \varphi_\sigma) - \cos(\theta_\sigma)\sin(\theta) \\
\sigma_\varphi = \sin(\theta_\sigma)\sin(\varphi_\sigma - \varphi))
\end{cases}
$$

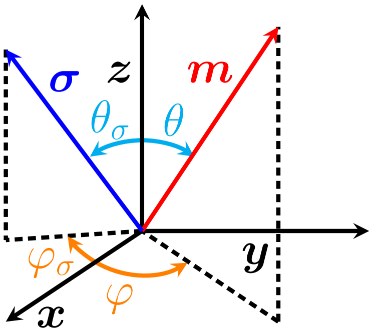

Figure IV.5: Representation of the normalised magnetisation $\boldsymbol{m}$ and the spin polarisation direction σ with spherical coordinates.

We can see that this additional torque modifies the excitation in the form of a change in the polarisation of the excitation, and in its amplitude. We can represent the new excitation as follows:

$$\boldsymbol{h}'_{RF} = \boldsymbol{h}_{RF} + \boldsymbol{h}_{SHE} = \begin{bmatrix} \underline{h}_\theta + b\underline{\sigma}_\theta - a\underline{\sigma}_\varphi \\ \underline{h}_\varphi + b\underline{\sigma}_\varphi + a\underline{\sigma}_\theta \end{bmatrix} e^{i\omega t} \tag{IV.13}$$

Resistance measurement by Anisotropic Magnetoresistance (AMR)

The anisotropic magnetoresistance is a well known phenomenon that leads one of the major electric properties of the magnetic materials: when a current flows through a magnetic wire, the resistance shows a dependence on the angle between the magnetisation $\boldsymbol{m}$ and the direction of the current flow density $\boldsymbol{j}$. We can represent the resistance as a function of these parameters as follows:

$$R = R_0 + \Delta R \left(\frac{\boldsymbol{j} \cdot \boldsymbol{m}}{\|\boldsymbol{j}\|} \right)^2$$

In our experimental study, the current density is along the $\boldsymbol{x}$ axis, and the magnetisation is assumed to precess around the (θ_0, φ_0) position with respective amplitudes (including a phase term) $\underline{\delta\theta}_0$ and $\underline{\delta\varphi}_0$, giving the following expression:

$$\underline{R}(\omega) = R_0 + \Delta R (\sin(\theta_0 + \underline{\delta\theta}_0 e^{i\omega t}) \cos(\varphi_0 + \underline{\delta\varphi}_0 e^{i\omega t}))^2$$

We can develop that expression, keeping only the 1^{st} order terms as follows:

$$\underline{R}(\omega) = R_0 + \Delta R \left(\sin(\theta_0)\cos(\varphi_0) + e^{i\omega t} \left(\underline{\delta\theta}_0 \cos(\varphi_0)\cos(\theta_0) - \underline{\delta\varphi}_0 \sin(\varphi_0)\sin(\theta_0) \right) \right)^2$$

By expanding the square, and again, keeping only the 1^{st} order, we obtain the linearised expression of the resistance:

$$\underline{R}(\omega) = R_0 + \Delta R \left(\sin^2(\theta_0)\cos^2(\varphi_0) + e^{i\omega t} \left(\underline{\delta\theta}_0 \cos^2(\varphi_0)\sin(2\theta_0) - \underline{\delta\varphi}_0 \sin(2\varphi_0)\sin^2(\theta_0) \right) \right)$$

Let us remember that the charge current is linked to the current density by the section of the material it flows through: $I = jS$. This relationship also applies to complex variables: $\underline{I} = \underline{j}S$. The AMR voltage measured during the spin-torque ferromagnetic resonance measurement (ST-FMR) can thus be expressed as follows:

$$\begin{aligned} V_{AMR} = \Re(j(\omega)S\ \Re(R(\omega)) =& \Re(j_0 S e^{i\omega t})\Re(R_0 + \Delta R \sin^2(\theta_0)\cos^2(\varphi_0) \\ &+ \Delta R\ e^{i\omega t}\left(\underline{\delta\theta}_0 \cos^2(\varphi_0)\sin(2\theta_0) - \underline{\delta\varphi}_0 \sin(2\varphi_0)\sin^2(\theta_0)\right)) \end{aligned}$$

Where S is the transverse section of the wire, and j_0 the current density flowing through it. Let us note that we choose here the following convention: the current density phase is zero. This implies, due to the Maxwell equations ($\nabla \times \boldsymbol{H} = \boldsymbol{j}$) that the Oersted induced current also has a null phase, leading to a real value of h_{RF}. In order to explicit the terms of the previous equation, we have to express the complex amplitude of the oscillations. We choose the following notation:

$$\begin{cases} \underline{\delta\theta}_0 = |\underline{\delta\theta}_0| e^{i\psi_\theta} \\ \underline{\delta\varphi}_0 = |\underline{\delta\varphi}_0| e^{i\psi_\varphi} \end{cases}$$

This voltage can thus be divided in three parts, according to the frequency of the signal that can be 0 (DC signal), ω, or 2ω. The following expressions are written as follows:

$$\begin{cases} V_{AMR}^{DC} = V_{AMR}^{2\omega} = \dfrac{1}{2} j_0 S \Delta R \left(\Re(\underline{\delta\theta}_0)\cos^2(\varphi_0)\sin(2\theta_0) - \Re(\underline{\delta\varphi}_0)\sin(2\varphi_0)\sin^2(\theta_0)\right) \\ V_{AMR}^{\omega} = j_0 S \left(R_0 + \Delta R(\sin^2(\theta_0)\cos^2(\varphi_0)\right) \end{cases} \tag{IV.14}$$

The main interest in having such general formulas is that we can evaluate the susceptibility according to the geometry we use. In our experimental case, let us agree on some geometric features. We will consider that the sample is a wire along the $\boldsymbol{x}$ axis. We define the direct orthonormal coordinates system $(\boldsymbol{x}, \boldsymbol{y}, \boldsymbol{z})$ so that the $\boldsymbol{z}$ axis corresponds to the ascending out-of-plane axis. The spherical coordinates system is defined corresponding to it.

The sample that we consider is a bilayer of non magnetic metal of thickness t_N and a ferromagnetic layer of thickness t_F, capped with aluminum oxide. This type of sample allows a current density that will be essentially in the non magnetic metal, leading to an Oersted field in a special configuration: given the symmetry of the problem, and assuming a perfect shape for the wire, the spatial average of the Oersted field is along the $\boldsymbol{y}$ axis. A simple geometric approach gives hints about that result. The current density distribution is assumed to be uniform in the sample and its barycentre is supposed to be displaced towards the layer with the largest electric conductivity, that is to say the non magnetic layer (usually Pt, Ir, Ta). We represent this situation on fig. A.1, representing the layers as well as the Oersted field analytically computed. The Oersted field that is emitted from this is radial with respect to the barycentre of the current density distribution (for detailed calculation, see the Appendix A). Therefore, when averaging the magnetic field experienced by the ferromagnetic layer, one can separate the contributions along $\boldsymbol{y}$ and $\boldsymbol{z}$. We will express the space average of a quantity X as follows: $\langle X \rangle$. In a general way, we can express:

$$\langle \boldsymbol{h}_{RF}^{Oersted} \rangle = \langle \boldsymbol{h}_{RF} \cdot \boldsymbol{y} \rangle \boldsymbol{y} + \langle \boldsymbol{h}_{RF} \cdot \boldsymbol{z} \rangle \boldsymbol{z}$$

The radial dependence in amplitude, and azimutal direction imply that the Oersted field along $\boldsymbol{z}$ is antisymmetric with respect to the plane orthogonal to $\boldsymbol{y}$ at the half width of the sample. Therefore, $\langle \boldsymbol{h}_{RF} \cdot \boldsymbol{z} \rangle = 0$. As a consequence, we can express the spatial average of the Oersted field as:

$$\langle \boldsymbol{h}_{RF}^{Oersted} \rangle = \langle \boldsymbol{h}_{RF} \cdot \boldsymbol{y} \rangle \boldsymbol{y}$$

From now on, let us consider that spatial average as the field exciting the magnetisation, that is to say a uniform RF applied field. Let us define: $\langle \boldsymbol{h}_{RF}^{Oersted} \rangle = h_{RF}\boldsymbol{y}$, as it is according to

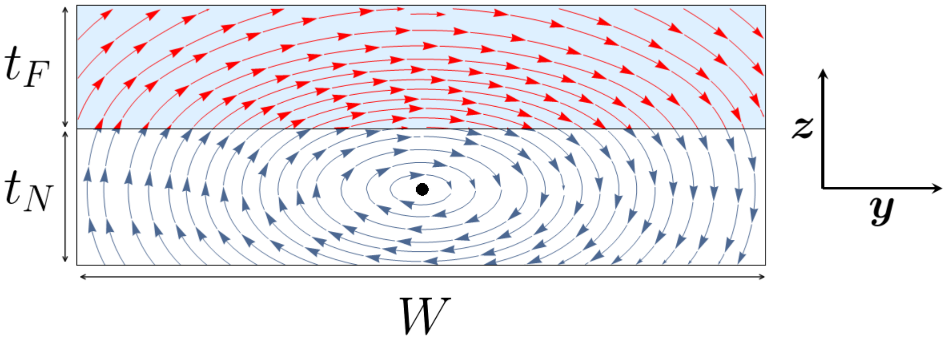

Figure IV.6: Schematic of the cross section of a STFMR sample with the Oersted field at a given moment. The black dot represent the barycentre of the current density in the material. The lower layer represents the non magnetic material of thickness t_N, whereas the upper layer, coloured in light blue, represents the ferromagnetic material. The arrows represent the Oersted field lines in the non magnetic material (blue) and in the ferromagnet (red). The spacial average of the field that is relevant to us is the average on the upper layer (red arrows).

the geometry. Similarly, the spin current injected is polarised along the $\boldsymbol{y}$ axis ($\boldsymbol{\sigma} = \boldsymbol{y}$) given the fact that the charge current is injected along the $\boldsymbol{x}$ axis, and that the spin current propagates along the $\boldsymbol{z}$ axis. We can note that we work with a linear polarisation of the field. In order to be able to use the magnetic susceptibility that was calculated earlier, we have to express that exciting RF field in the spherical base, which is done as follows:

$$\langle \boldsymbol{h}_{RF}^{'} \rangle(\omega) = \langle \boldsymbol{h}_{RF}^{Oersted} \rangle(\omega) + \langle \boldsymbol{h}_{RF}^{SHE} \rangle(\omega) = (h_{RF}+b) \begin{bmatrix} \sin(\theta_0)\sin(\varphi_0) \\ \cos(\theta_0)\sin(\varphi_0) \\ \cos(\varphi_0) \end{bmatrix} + a \begin{bmatrix} 0 \\ -\cos(\varphi_0) \\ \cos(\theta_0)\sin(\varphi_0) \end{bmatrix} = \begin{bmatrix} h_r^{`} \\ h_\theta^{`} \\ h_\varphi^{`} \end{bmatrix}$$

Using the equation IV.6, and expressing the matrix $\underline{\chi}$ as follows:

$$\underline{\chi} = \begin{bmatrix} \underline{\chi_{\theta\theta}} & \underline{\chi_{\theta\varphi}} \\ \underline{\chi_{\varphi\theta}} & \underline{\chi_{\varphi\varphi}} \end{bmatrix}$$

For the sake of clarity, let us use the notations: $A(\omega, \theta_0, \varphi_0) = \cos(\theta_0)\sin(\varphi_0)\chi'_{\theta\theta} + \cos(\varphi_0)\chi'_{\theta\varphi}$ and $B(\omega, \theta_0, \varphi_0) = \cos(\theta_0)\sin(\varphi_0)\chi'_{\varphi\theta} + \cos(\varphi_0)\chi'_{\varphi\varphi}$. We obtain without expliciting all the terms, and using the fact that $h_{RF} \in \mathbb{R}$:

$$\begin{cases} \Re(\underline{\delta\theta}_0) & = \dfrac{h_{RF}+b}{M_S} A(\omega, \theta_0, \varphi_0) - \dfrac{a}{M_S \sin(\theta_0)} B(\omega, \theta_0, \varphi_0) \\ \Re(\underline{\delta\varphi}_0) & = \dfrac{h_{RF}+b}{M_S \sin(\theta_0)} B(\omega, \theta_0, \varphi_0) + \dfrac{a}{M_S} A(\omega, \theta_0, \varphi_0) \end{cases}$$

From eq. (IV.14) we obtain the DC AMR voltage written as follows:

$$V_{AMR}^{DC} = \frac{1}{2} j_0 S \Delta R \Bigg(\left(\frac{h_{RF}+b}{M_S} A(\omega, \theta_0, \varphi_0) - \frac{a}{M_S \sin(\theta_0)} B(\omega, \theta_0, \varphi_0) \right) \cos^2(\varphi_0) \sin(2\theta_0) \\ - \left(\frac{h_{RF}+b}{M_S \sin(\theta_0)} B(\omega, \theta_0, \varphi_0) + \frac{a}{M_S} A(\omega, \theta_0, \varphi_0) \right) \sin(2\varphi_0) \sin^2(\theta_0) \Bigg) \tag{IV.15}$$

Experimental application

In this expression, the angles (θ_0, φ_0) are given by the equilibrium position of the magnetisation, that is defined by the applied magnetic field $\boldsymbol{H}_0$. However, in order to make it easier to use the formula, we can study the case when the amplitude of $\boldsymbol{H}_0$ is larger than the coercive field, letting the equilibrium position to be around the applied magnetic field direction. In our experimental setup, the applied magnetic field is along the vector $\frac{1}{\sqrt{2}}(\boldsymbol{x} - \boldsymbol{y})$ (45°), leading to the equilibrium position $(\theta_0, \varphi_0) = \left(\frac{\pi}{2}, -\frac{\pi}{4}\right)$. This angle was chosen because it is close to the maximum of the signal that can be achieved. Indeed, as shown in fig. IV.8, both the symmetric and the antisymmetric parts of the signal are maximised at an angle around 35°. Let us note that this evaluation of (θ_0, φ_0) is only valid for high values of the applied field, when the magnetisation is aligned with the applied field. In other cases, one has to evaluate that position, by minimising the total energy density for instance. For these specific angular values, one finds $A(\omega, \theta_0, \varphi_0) = \cos(\varphi_0)\chi'_{\theta\varphi}$ and $B(\omega, \theta_0, \varphi_0) = \cos(\varphi_0)\chi'_{\varphi\varphi}$, leading to the final voltage expression:

$$V_{DC} = -\frac{j_0 \Delta R}{2\sqrt{2} M_S}((h_{RF} + b)\chi'_{\varphi\varphi} + a\chi'_{\theta\varphi}) \tag{IV.16}$$

From here, a method to analyse the experimental data was proposed, relying on the symmetries of the signals obtained. Let us have a closer look to this side of the problem.

Fitting procedure and data analysis

Let us now focus on the data treatment that links the experimental curves of ST-FMR and the determination of the spin Hall angle θ_{SH}. If we consider the DC voltage given in eq. IV.16, that is to say the actual experimental curve obtained, we can see that two parts are involved, which correspond to $\chi'_{\theta\varphi}$ and $\chi'_{\varphi\varphi}$. The usual manner to find the amplitudes of the torques, and thus the amplitude of the spin current present in the ferromagnetic material, is to consider that the spin torques are purely damping-like (b=0), and that they do not change the equilibrium position. We also postulate the coefficients of the magnetic susceptibility present perfect behaviours regarding the symmetries, that is to say $\chi'_{\theta\varphi}$ is perfectly antisymmetric with respect to the resonant frequency, and $\chi'_{\varphi\varphi}$ is supposed to be perfectly symmetric. The DC is fitted with the sum of a Lorentzian-like and an anti-Lorentzian-like functions using the following form:

$$fit(\omega) = S\frac{\Delta^2}{\Delta^2 + (\omega - \omega_0)^2} + A\frac{(\omega - \omega_0)\Delta}{\Delta^2 + (\omega - \omega_0)^2} \tag{IV.17}$$

The symmetric amplitude S is attributed to $\chi'_{\theta\varphi}$, that is to say to the damping like torque, and thus the spin current action, whereas the antisymmetric amplitude A is attributed to $\chi'_{\varphi\varphi}$, which is linked to the effect of the Oersted field. Hence the determination of the best fitting parameters let us compute the ratio of the amplitudes of the signals found, and since both contributions have the same linear dependence on the RF current flowing through the device, the ratio of the amplitudes does not depend on the actual current in the wire. This is a huge asset, because the determination of the current flowing through a circuit at FMR frequencies can turn out to be very complex. Let us now study the symmetry of the coefficients of the magnetic susceptibility that are of interest in our case.

Symmetries of $\chi'_{\theta\varphi}$ and $\chi'_{\varphi\varphi}$

Let us compare the amplitudes of the symmetric and antisymmetric parts of $\chi'_{\varphi\theta}$ and $\chi'_{\varphi\varphi}$, using the results given in the Appendix B.

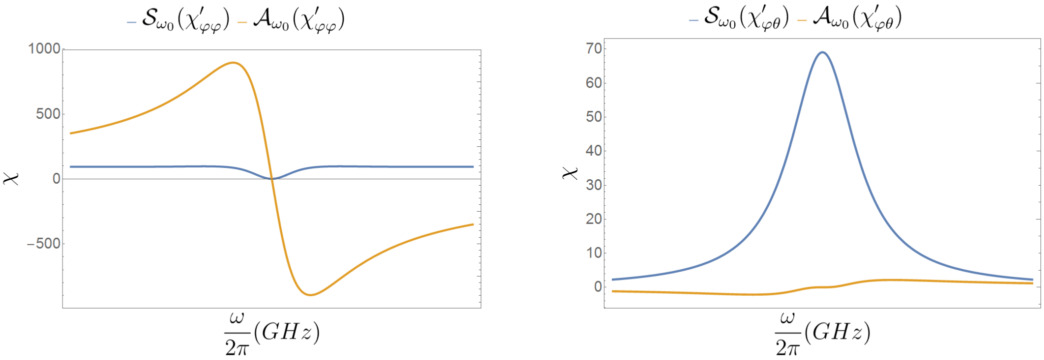

(a) $\mathcal{S}(\chi')$ (b) $\mathcal{A}(\chi')$

Figure IV.7: Comparison of the symmetric and antisymmetric parts of $\chi'_{\varphi\theta}$ and $\chi'_{\varphi\varphi}$

The analysis of the antisymmetric parts presented above on the right is favourable since the contribution of $\chi'_{\varphi\theta}$ is negligible. It is thus totally justified to consider that the antisymmetric part of the signal only corresponds to $\chi'_{\varphi\varphi}$.

However, the comparison of the symmetric parts is not as obvious. The amplitudes of both contributions are of the same order of magnitude, the one corresponding to $\chi'_{\varphi\varphi}$ being even a little larger than the one of $\chi'_{\varphi\theta}$. Considering the amplitude of the symmetric part of the signal as the effect of spin-torques is thus not an analytic result, but an approximation.

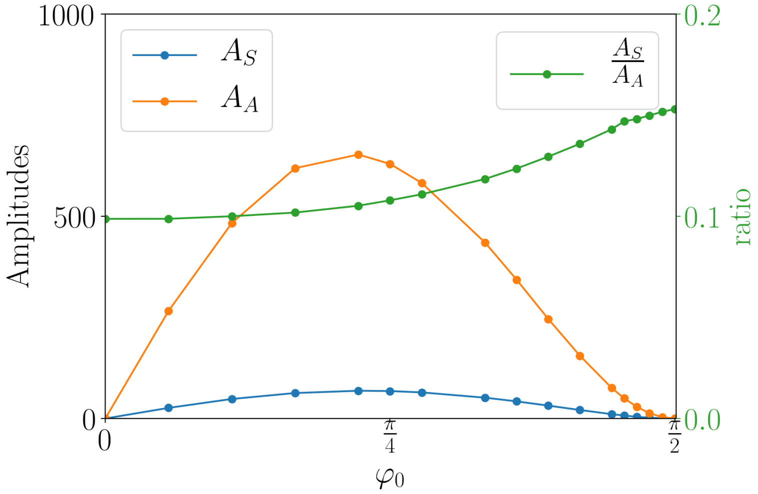

Figure IV.8: Dependance of the amplitudes of symmetric (blue) and antisymmetric (orange) parts of the real part of $\chi'_{\varphi\varphi}$ modulated by AMR angular dependence as a function of the in-plane angle of the applied field φ_0. The ratio is plotted in green.

We have represented the ratio between the peak height of the symmetric part divided by the amplitude of the antisymmetric part as a function of the value of the angle φ_0 for real part of the diagonal coefficient $\chi_{\varphi\varphi}$, as shown on fig. IV.8 (green curve). We can first point out that both components, symmetric and antisymmetric, reach a maximum for a value of φ_0 close to 35°. This angle maximises the function $\varphi_0 \mapsto \cos(\varphi_0)\sin(2\varphi_0)$, which is the dependence found in eq. (IV.15). As we can notice, there is approximately an order of magnitude between these components, and the ratio, which is assumed to be equal to zero in the ST-FMR treatment approximation can be around 14%, and is always superior to 10%. Let us evaluate the consequences of this approximation using the usual fitting procedure. We choose two cases: first, we consider a case where we only want to fit $\chi_{\varphi\varphi}$. What an experimentalist would wish is to find only an antisymmetric contribution, due to the absence of spin torques. Second, we fit $\chi_{\varphi\varphi} - \chi_{\varphi\theta}$, where we expect to obtain a symmetric contribution from $\chi_{\varphi\theta}$ additioned to the antisymmetric part already obtained for $\chi_{\varphi\varphi}$. We disclose the results of the fitting on fig. IV.10.

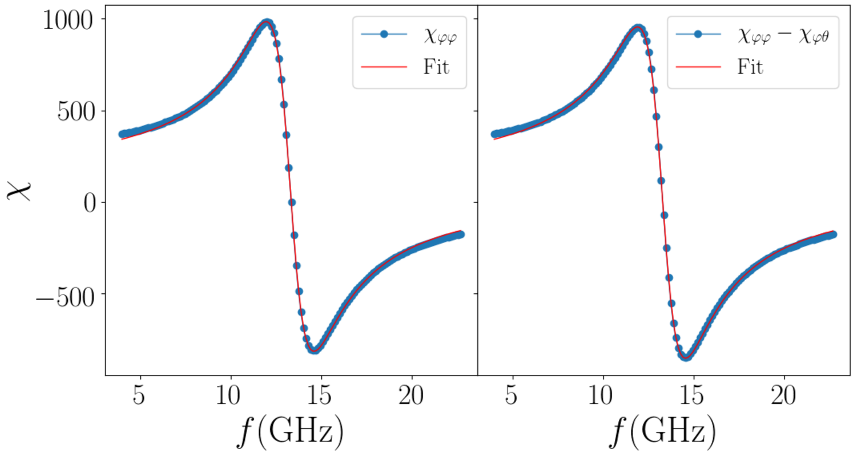

Figure IV.9: Fitting of the analytical expressions of $\chi_{\varphi\varphi}$ (left panel) and $\chi_{\varphi\varphi} - \chi_{\varphi\theta}$ with the usual fitting method.

The amplitudes ratios that we find are 8.5×10^{-3} for $\chi_{\varphi\varphi}$ and 4.5×10^{-2} for $\chi_{\varphi\varphi} - \chi_{\varphi\theta}$. The values that were expected from the calculations made earlier were respectively 1.1×10^{-1} and 1.8×10^{-1}, which is a non negligible difference. Our understanding of this discrepancy is that the symmetric contribution brought by $\chi_{\varphi\varphi}$ does not have the same linewidth as $\chi_{\theta\varphi}$ and $\mathcal{A}_{\omega_0}(\chi_{\varphi\varphi})$. Thus, since this contribution is in all cases an order of magnitude smaller than the contributions with the expected linewidth, the algorithm seems to neglect this part and converge to the solution that is physically correct, that is to say cancel the symmetric contribution of $\chi_{\varphi\varphi}$. In a more general way, we represent the evolution of the parameter a^* obtained by the fitting function $fit(\omega)$ defined in eq. IV.17, that is to say the result that would be given by a data processing of results, as a function of the parameter a of the theoretical signal defined as $\chi'_{\varphi\varphi} + a\chi'_{\theta\varphi}$, that is to say the exact value that should be obtained.

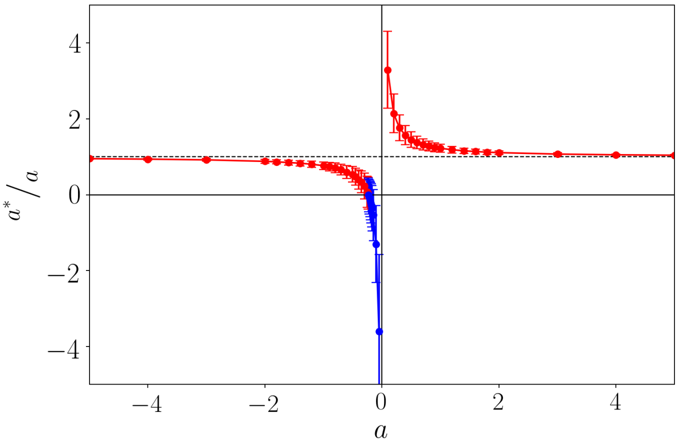

Figure IV.10: Evolution of the ratio of the fitted amplitude a^* of the symmetric part of a theoretical defined as $\chi'_{\varphi\varphi} + a\chi'_{\theta\varphi}$ as a function of the value of a.

As expected, for small values of the a parameter, the ratio between the fitted value and the value we wish to obtain differs from what one would expect. More importantly, the sign of the ratio can switch from positive to negative (the blue part of the curve shows this sign discrepancy around zero). Precisely, we can observe a zero antisymmetric part (a^*=0) for $a \approx 0.21$. Indeed such an analysis would lead to a determination of a non zero value of the spin Hall angle for materials without spin Hall effect.

IV.3.3 Spin Pumping Ferromagnetic resonance (SP-FMR)

Principle of spin pumping

The measurement that is carried out is the voltage as a function of the applied magnetic field and the frequency of the RF applied magnetic field. The RF excitation triggers the magnetisation dynamics, which can be represented by the magnetic susceptibility χ that was previously expressed on eq. (IV.6). The evolution of the magnetisation dynamics creates a spin current which flows perpendicularly to the magnetisation direction, as shown on eq. (IV.11). When the spin current crosses the ferromangnetic/nonmagnetic interface, it experiences spin dependent scatterings and reflexions that are described by the spin mixing conductance $g^{\uparrow\downarrow}$. The generated spin current density at the interface with the non magnetic material can be expressed as [77]:

$$\boldsymbol{j}_s^{\boldsymbol{z}} = \frac{\omega}{2\pi}\int_0^{\frac{2\pi}{\omega}} \frac{\hbar}{4\pi}\Re\left(g^{\uparrow\downarrow}\right)\frac{1}{M_s^2}\left(\boldsymbol{M}\times\frac{d\boldsymbol{M}}{dt}\right)dt \qquad \text{(IV.18)}$$

Here, $\boldsymbol{z}$ represents the direction perpendicular to the interface, along which the spin current expressed in eq. (IV.18)is flowing. This expression can be detailed easily using the dynamic susceptibility obtained in eq. (IV.6).

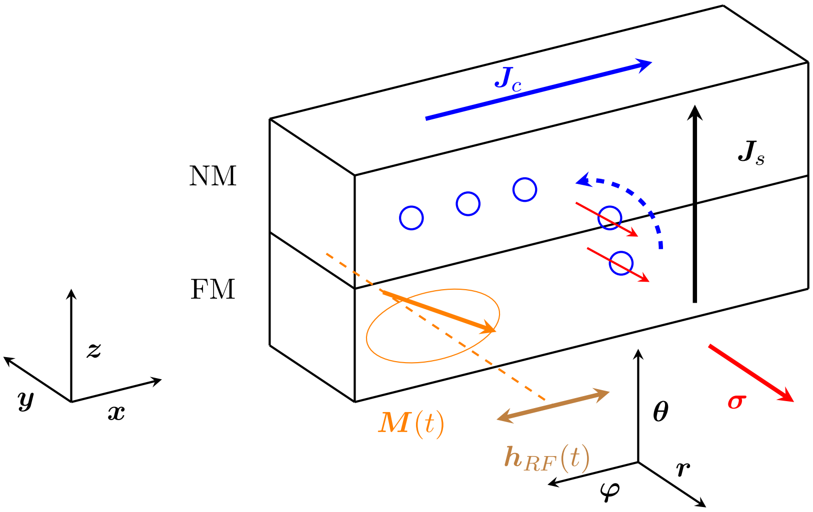

Figure IV.11: Generation of a spin current by spin pumping

Expression of the spin current

Let us consider now the actual contributions. Let us consider that $\underline{h} = h_{RF}\exp(i\omega t)\boldsymbol{\varphi}$, as represented on fig. IV.11, which is a simple transverse RF magnetic field applied to the magnetisation. The magnetisation writes:

$$\boldsymbol{M} = h_{RF}\begin{pmatrix} \dfrac{M_S}{h_{RF}} \\ \chi'_{\theta\varphi}\cos(\omega t) - \chi''_{\theta\varphi}\sin(\omega t) \\ \chi'_{\varphi\varphi}\cos(\omega t) - \chi''_{\varphi\varphi}\sin(\omega t) \end{pmatrix}$$

Its temporal derivative can thus be expressed as:

$$\frac{d\boldsymbol{M}}{dt} = h_{RF}\omega \begin{pmatrix} 0 \\ \\ -\chi'_{\theta\varphi}\sin(\omega t) - \chi''_{\theta\varphi}\cos(\omega t) \\ \\ -\chi'_{\varphi\varphi}\sin(\omega t) - \chi''_{\varphi\varphi}\cos(\omega t) \end{pmatrix}$$

The integral over a precession period of the cross product only gives a component on the $\boldsymbol{m}_{eq}$ direction, (which is the direction of the magnetisation at equilibrium in the absence of time dependent perturbation), which is then the spin polarisation direction $\boldsymbol{\sigma}$. We can thus write the spin current flowing in the $\boldsymbol{z}$ direction as: $\boldsymbol{j}_s^{\boldsymbol{z}} = j_s^{\boldsymbol{z}}\boldsymbol{\sigma}$. Its amplitude is given by:

$$j_s^{\boldsymbol{z}} = \frac{\hbar}{4\pi}\Re\left(g^{\uparrow\downarrow}\right)\frac{h_{RF}^2\omega}{M_S^2}\left(\chi'_{\varphi\varphi}\chi''_{\theta\varphi} - \chi'_{\theta\varphi}\chi''_{\varphi\varphi}\right)$$

The component of the spin current density that corresponds to the spin current flowing perpendicularly to the interface with the non magnetic material can thus be written generally as:

$$\boxed{\boldsymbol{j}_s^{\boldsymbol{z}} = \frac{\hbar}{4\pi}\Re\left(g^{\uparrow\downarrow}\right)\frac{h_{RF}^2\omega}{M_S^2}\left(\chi'_{\varphi\varphi}\chi''_{\theta\varphi} - \chi'_{\theta\varphi}\chi''_{\varphi\varphi}\right)\boldsymbol{\sigma}} \tag{IV.19}$$

Experimental application

Now that we have determined analytically the general amplitude of the spin current generated by spin pumping as a function of the analytical expression of the magnetic susceptibility, we can evaluate this result to the actual experiment that we are carrying out. Let us express that component using the terms of the magnetic susceptibility for the energy densities previously chosen (case study IV.2.3 for $\phi_H = \frac{\pi}{2}$, with no magneto crystalline anisotropy), at the resonance $\omega = \omega_0$ (and equivalently, $H = H_r$ where H_r is the resonance field), where:

$$\begin{cases} \underline{\chi}_{\theta\varphi} = \dfrac{\gamma_0 M_S}{\Delta} \\ \underline{\chi}_{\varphi\varphi} = \dfrac{\gamma_0 M_S\alpha}{\Delta} - i\dfrac{\gamma_0^2}{\Delta\omega}(H_r + M_S)M_S \end{cases}$$

The expression in eq. (IV.19) is then simplified as:

$$j_s^{\boldsymbol{z}} = \frac{\hbar}{4\pi}\Re\left(g^{\uparrow\downarrow}\right)\frac{\gamma_0^3 h_{RF}^2}{\Delta^2}(H_r + M_S)$$

Using the fact that: $\omega_0 = \gamma\mu_0\sqrt{H_r(H_r + M_S)}$, we can show that at the resonance, by replacing the field in the previous expressions, at the interface between the ferromagnetic material and the non magnetic one, the following relationship holds:

$$j_s^{\boldsymbol{z}} = \frac{\hbar}{4\pi}\Re\left(g^{\uparrow\downarrow}\right)\frac{1}{2}\left(\frac{\gamma_0 h_{RF}}{\alpha}\right)^2\frac{\gamma_0 M_S + \sqrt{(\gamma_0 M_S)^2 + 4\omega_0^2}}{(\gamma_0 M_S)^2 + 4\omega_0^2}$$

Since we are studying here the spin pumping spin current density at the resonance frequency, and at the interface between the ferromagnetic layer and the non magnetic material, that is to say at a specific spatial position, we will note $j_s^{\boldsymbol{z},0}$ this quantity, that will be useful in the expression of the spin current density within the non magnetic material.

$$j_s^{\boldsymbol{z},0} = \frac{\hbar}{8\pi\alpha^2}\Re(g^{\uparrow\downarrow})\,(\gamma_0 h_{RF})^2\,\frac{\gamma_0 M_S + \sqrt{(\gamma_0 M_S)^2 + 4\omega_0^2}}{(\gamma_0 M_S)^2 + 4\omega_0^2} \tag{IV.20}$$

We find here the result obtained by Ando *et al.* [128]. We represent the spin current density at the resonance as a function of the resonance frequency on fig. IV.12

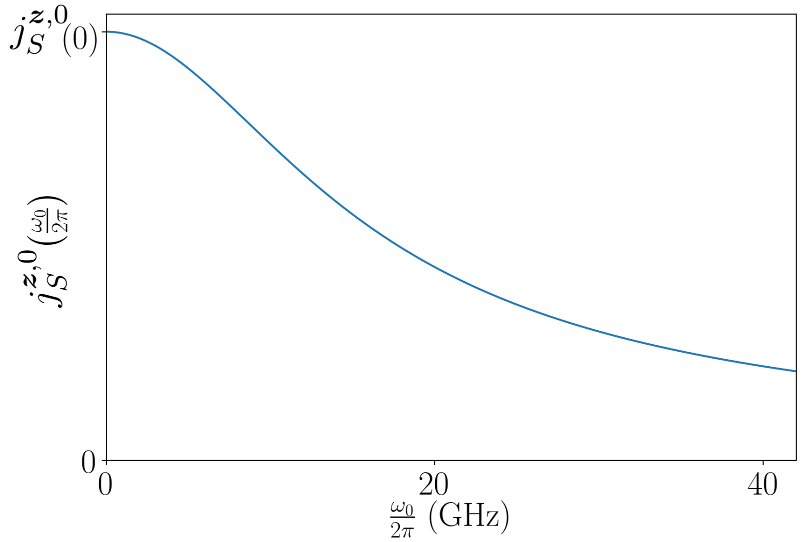

Figure IV.12: Spin current density at the resonance as a function of the resonance frequency. $j_S^{z,0}$ is given by eq. (IV.20), with a saturation magnetisation of $\mu_0 M_S = 1T$.

Diffusion of the spin current in the non magnetic material

Let us now consider the spin-to-charge conversion occurring within the material in which shows ISHE. The diffusion of the spins at a ferromagnetic-paramagnetic interface has already been treated by Johnson *et al.* [129], and lead to a diffusion equation that give the amplitude of the spin current density flowing along the direction $\boldsymbol{z}$ (perpendicular to the interface magnetic/nonmagnetic material) that can be expressed as a function of the spin flip length l_{sf} and the depth t into the non magnetic material which thickness is t_N, as [130]:

$$j_s^{\boldsymbol{z}}(t) = j_s^{\boldsymbol{z},0} \frac{\sinh\left(\dfrac{t_N - t}{l_{sf}}\right)}{\sinh\left(\dfrac{t_N}{l_{sf}}\right)} \tag{IV.21}$$

Where $j_s^{\boldsymbol{z},0}$ is the spin current density amplitude at the ferromagnetic/non magnetic interface materials. Let us now consider the spin-to-charge conversion occurring. Since the charge current density generated is proportional to the spin current density, one can calculate directly the charge current by integrating the previous equation over the whole section of the material, which is equivalent to integrate on the thickness where the conversion is located, and multiply by the width W of the sample:

$$i_c = \frac{2e}{\hbar}\theta_{SH} W \int_0^{t_N} j_s^{\boldsymbol{z}}(t)dt = \frac{2e}{\hbar}\theta_{SH} W l_{sf} j_s^{\boldsymbol{z},0} \tanh\left(\frac{t_N}{2l_{sf}}\right) \tag{IV.22}$$

The thickness dependence of the current density is evolving as $\tanh(\frac{t_N}{2l_{sf}})$, regardless on the amplitude. It is thus possible to obtain the spin flip length easily as long as the data provided show thicknesses that are in the order of magnitude of l_{sf}. We represent this thickness dependence on fig. IV.14.

On the few previous paragraphs, we have seen that the effective current density due to the ISHE in the material we want to probe is proportional to the product of the spin flip length,

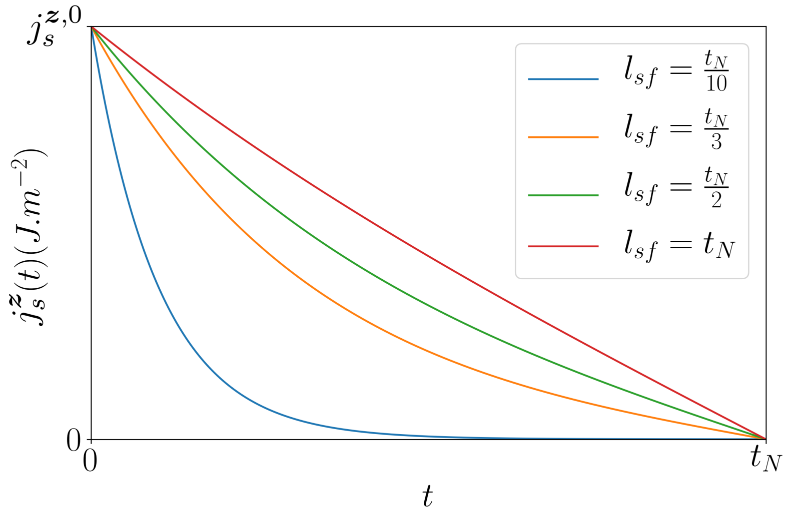

Figure IV.13: Spin current density as a function of the depth within the non magnetic material, given by eq. (IV.21).

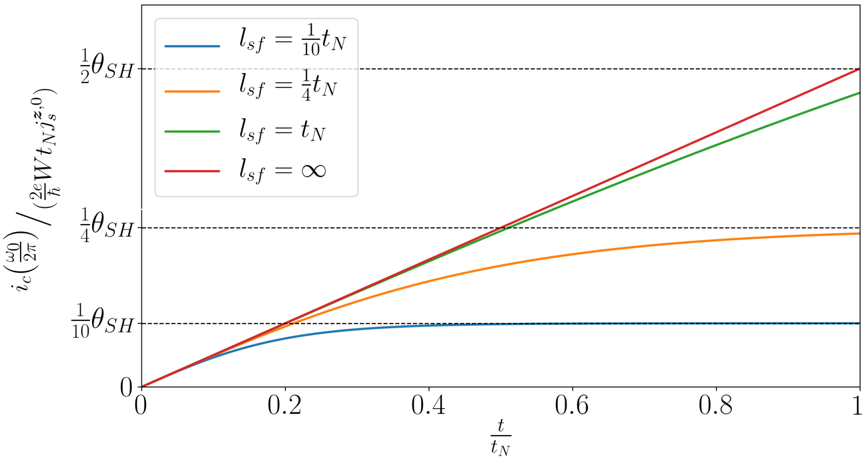

Figure IV.14: Charge current density as a function of the thickness of the non magnetic material given by eq. (IV.22).

the spin Hall angle, and an hyperbolic tangent of the inverse of l_{sf}. This means that the spin flip length is as influential than the spin Hall angle. Indeed, the final current density that will quantify the spin Hall effect is proportional to the product of these two quantities.

Magnetic damping enhancement

The spin pumping phenomenon was found to be responsible for an increasing of the magnetic damping of the non magnetic material [124]. Consequently, as the spin-to-charge conversion increases, the observed magnetic damping increases until it reaches a maximum, when the conversion is at its maximum, that is to say when the non magnetic material thickness is much larger than the spin flip length. The measurement of the magnetic damping can be made from the dependence of the linewidth of the spin pumping voltage on the applied magnetic field. Indeed, the dependence of the linewidth of the spin pumping signal is expected to be linear with respect to the applied magnetic field, as showed in eq. IV.4, and the damping coefficient is proportional to the slope of the line obtained.

According to Tserkovnyak *et al.* [124,131], the spin mixing conductance can be calculated by the damping enhancement, that is to say the difference of the damping measured for a thickness of non magnetic material largely superior to the spin flip length ($\alpha_{t_N \gg l_{sf}}$), and the intrinsic damping (α_0) of the ferromagnetic material used as follows:

$$\alpha_{t_N \gg l_{sf}} - \alpha_0 = \frac{g\mu_B}{4\pi M_S t_{FM}} \Re(g_{eff}^{\uparrow\downarrow}) \approx \frac{g\mu_B}{4\pi M_S t_{FM}} g_{eff}^{\uparrow\downarrow} \tag{IV.23}$$

Where g is the Landé factor and μ_B the Bohr magneton. This equation enables the characterisation of the interface between the ferromagnetic and non magnetic materials considered. This characterisation has been extended by Rojas-Sanchez *et al.* [82] by noticing that the charge current thickness dependence and the magnetic dependence with respect to the thickness of the non magnetic material are not the same. This has been understood in terms of spin memory loss at the interface, which explicits the fact that the interfaces are not transparent for the spin currents. Therefore, the effective spin mixing conductance also expresses the reduction of spin current occuring at the ferromagnetic/non magnetic materials interface, thus this quantity as well as an effective spin Hall angle can be estimated for a couple of materials in a more relevant way than just for a single material.

Summary of the measurements

Since we have presented all the steps that lead to a characterisation of a bilayer composed of a non magnetic material showing spin Hall effect and a ferromagnetic material, let us summarise these steps in order.

For a given sample, the data that need to be acquired are the evolution of the spin pumping voltage as a function of the magnetic field for a set frequency. This experiment has to be carried out at various values of the set frequency. From this, one can obtain the relation between the applied magnetic field and the resonance frequency, which enables to determine the effective field in the material, as well as the saturation magnetisation. One can also plot the evolution of the linewidth of the spin pumping voltage as a function of the frequency, which gives access to the magnetic damping. Eventually, one can obtain the evolution of the spin current generated by spin pumping as a function of the frequency, which is proportional to the spin pumping voltage measured experimentally.

The comparison of the latter for various samples can lead to the spin pumping voltage as a function of the thickness of non magnetic material, for each frequency studied. These can lead to the determination of the spin flip length of the non magnetic material. The evolution of the damping as a function of the non magnetic material thickness allows to observe the magnetic damping enhancement that is required to estimate the spin mixing conductance of the interface ferromagnetic/non magnetic materials. Eventually, now that all of the materials parameters have been evaluated except the spin Hall angle of the non magnetic material, one can get from the fitting of the spin pumping voltage as a function of the frequency the amplitude and the sign of the spin Hall angle.

We have now presented the experimental methods that lead to the determination of the relevant materials parameters. Let us now focus on the measurements that were carried out, and the analysis of these results.

IV.4 Experimental measurements in Iridium

Now that the main physical phenomena have been described and analysed, let us present the measurements that I performed to characterise the spin Hall effect in iridium. First, let us point out that the spin Hall effect in iridium was scarcely studied. The only reports in the literature were carried out by Zhang [43], and by White [49]. In the former, the system studied is a bilayer of permalloy/iridium, and the spin Hall angle is evaluated at $\theta_{SH}^{Ir} = 0.02 \pm 0.005$. In both studies, the spin flip length in iridium is found to be $l_{sf}^{Ir} = 0.5 \pm 0.1$ nm. Since the system $CoFeB/Ir$ has not been studied yet, there is no spin mixing value that was ever reported for that interface.

Even though the information contained in the literature is scarce, we obtain an order of magnitude, especially for the spin flip length, which is the parameter that determines the thickness range for the iridium layer that we want to consider. Indeed we want to start with thicknesses that are of the same order of magnitude than l_{sf} and increase the thickness until we can consider that $t_{Ir} \gg l_{sf}$.

IV.4.1 Choice of the method

As we have seen in the analysis of both resonance methods, there are assets and drawbacks to STFMR and SPFMR. Basically, the main advantages of STFMR are to provide a self calibrated measurement of the spin Hall angle: benefiting from symmetries, we are supposed to be able to separate the main components of the AMR signal observed, and thus be able to compute the relative action of the spin torques with respect to the Oersted field. Let us point out that this assertion is only valid for values of the spin Hall angle that are not too low. Indeed for very small values, the fitting using usual algorithms and fitting procedures might not converge to the correct values of the amplitudes of the signals. This limitation can however be ruled out due to the expected spin Hall angle, that is supposed to be non negligible in iridium. However, this method implies that the spin torques acting on the magnetisation are exclusively damping-like. Moreover, the method does not provide a robust way to access the spin flip length of the non magnetic material that is probed.

On the other hand, the SPFMR technique has the advantage to use only the amplitude of the lorentzian-like signal obtained (as seen on Ando's formula eq. (IV.20) [128]), on which there is little doubt about the precision of the fitting. Furthermore, the determination of the spin flip length is expected to be easy to carry out. Nevertheless, the obtention of the exact value of the spin Hall angle is dependent on the knowledge of the electric circuit that transports the RF field that is applied to the system. This part is the main limitation of this method: it is however possible to characterise the spin Hall angle of a material by comparing it to another, which is only a comparative study, without absolute results for this quantity.

Having contemplated these elements lead us to the choice of spin pumping FMR as a method to characterise SHE in iridium. Indeed, the knowledge of the spin flip length seems to be mandatory, in order to be able to evaluate the efficiency of the charge to spin conversion in the scope of current induced domain wall propagation of an iridium based synthetic ferrimagnet. By doing so, we give up our ambition to give an absolute value of the spin Hall angle of iridium. This renunciation does not seem to be too limiting: since numerous measurements of spin Hall angles of platinum have given significantly changing results in various reports using the same method, we prefer to quantify materials in comparison to others so as to be able to trust the comparisons made, regardless on the method used.

Therefore, we will focus on the next part of this chapter on the spin pumping experiments, first analytically, and then experimentally, in the scope of the characterisation of iridium.

IV.4.2 Choice of the samples

We chose to grow series of bilayers of materials including a ferromagnetic layer of $Co_{40}Fe_{40}B_{20}$ (in atomic proportions) and iridium. The main quality of the ferromagnetic layer that we chose is its low intrinsic magnetic damping (our calculations assume $1 + \alpha^2 \approx 1$ for most of the applicable results). Furthermore, this ternary alloy is a typical compound of spintronics devices, and has therefore been studied numerous times.

We chose a thickness for the ferromagnetic layer of $t_{FM} = 5$nm. This value was chosen so as to avoid the interfacial anisotropy contributions, and obtain an in plane magnetic anisotropy dominated by the demagnetising field. We did not use a larger thickness, however, so as to keep a large resistance for that layer, and not shunt the sample.

The choice of the thickness of the non magnetic layers (Ir, Pt) was made by considering three things. First, we wanted this range to be around the spin flip length value of iridium that was not known for sure at that time, but was supposed to be around 0.5 nm. Second, we wanted to perform a comparative study of iridium and platinum, and the latter has a spin flip length between 1 nm and 12 nm according to the literature. Thus, the thickness of non magnetic materials was chosen in a range from 1 to 15 nm. A sample with no non magnetic material was also grown so as to measure the properties of the CoFeB layer alone, especially the intrinsic magnetic damping. Third, we wanted to compare two materials with similar resistivities, due to the fact that the experiments that are carried out in this section involve the propagation of an RF magnetic field through a GSG antenna, which transmission parameters are very sensitive to materials properties such as conductivity. We display on fig. IV.15 the evolution of the resistance of our devices, composed as follows: $Si - SiO_2//CoFeB(5nm)//NM(t_{NM})$ where NM represents Pt or Ir, and t_{NM} represents the thickness of the corresponding layer. Both materials seem to have very similar resistivity values for samples with a small non magnetic material thickness ($t_{NM} \leq 6$ nm). There is a larger difference for the thicker sample, where we find a behaviour that gets closer to the one of bulk materials: in this latter case, the iridium conductivity is twice smaller than the one of platinum. Another remark we can make is that the inverse of the resistance does not follow a linear behaviour, which leads us to think that the quality of the thinner layers might be poorer than the quality of the thick samples. If we use the thicker samples to estimate the resistivity of the samples, we obtain the following values: $\rho_{Pt} = 245\ \Omega$.m and $\rho_{Ir} = 250\ \Omega$.m.

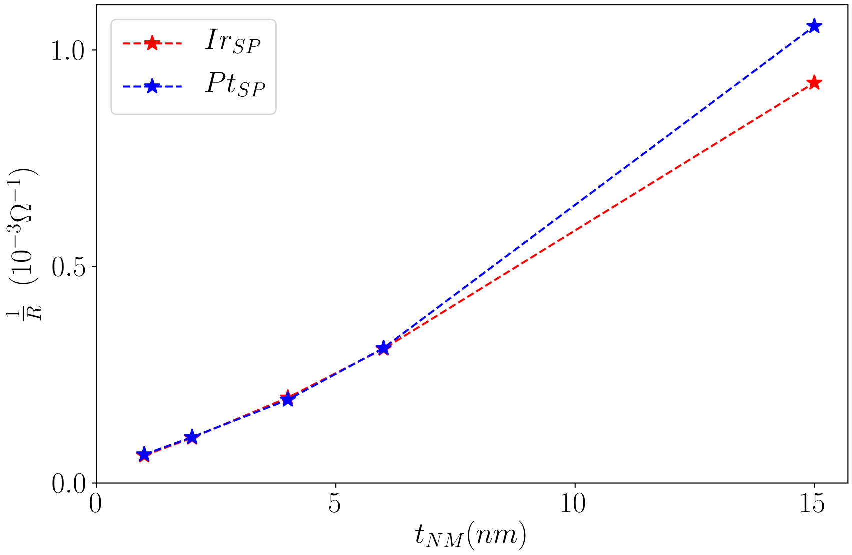

Figure IV.15: Inverse of the resistance of spin pumping devices composed of CoFeB and iridium (red stars) or platinum (blue stars).

All the samples were grown using magnetron sputtering from an elemental source of iridium of high purity ($\geq$99.95%). The deposition of CoFeB was made using an alloy target.

IV.4.3 Spin pumping ferromagnetic resonance experiments

The principle of the SP-FMR experiment was already described in subsection II.3.2. Here are the practical details that enable the measurement.

First, the samples measured are patterned in wire shapes of aspect ratio of 100. These wires are contacted to DC probes, where the quantity measured is the voltage at the terminals. On top of the wire, a 75nm thick insulating SiO_2 layer was deposited by reactive magnetron sputtering, from an elemental source of silicon. Eventually, on top of this insulating layer, an antenna composed of two grounds and a signal was patterned, so as to benefit from a GSG geometry to apply an RF magnetic field to the magnetisation. The signal of the antenna is orthogonal to the sample's wire.

In this configuration, the sample is contacted with two RF probes at the terminals of the antenna. The static magnetic field is applied perpendicular to the sample's wire, and thus parallel to the signal of the antenna. This configuration leads to an RF field perpendicular to the static field, which maximises the pumping. Moreover, all AMR effects are cancelled since the magnetisation precesses around a direction perpendicular to the sample's wire.

For each sample, that is to say for each value of the thickness of the non magnetic material, we perform a series of measurements. We set the frequency of the RF field injected in the antenna, and we sweep the magnetic field from high absolute values to lower absolute values, crossing the resonant point. We repeat the experiment for each integer value of GHz starting from 4 to 27, unless the signal gets to small to be detected accurately, or the resonant field gets higher than the maximum magnetic field that our experimental setup can supply, which is 0.6 T.

We do not perform measurements for frequencies lower than 4 GHz because the resonant condition is reached for very small values of the magnetic field. Indeed the resonance overlaps the magnetisation switching around 0 applied magnetic field, and the signal is not well represented by the calculations presented earlier, that assume a saturated homogeneous magnetisation. Furthermore, it was already shown by Guillemard *et al.* [132] that the precession of the magnetisation is homogenous for frequency values higher than 4 GHz, which is a crucial hypothesis of the experiment.

Let us represent one measurement carried out at a frequency of 5 GHz on the bilayer $CoFeB(5)/Ir(2)$ on fig. IV.16. As expected, we obtain a purely symmetric response that can be fitted by a lorentzian function. (By using eq. IV.19, and using the fact that $\chi''_{\theta\varphi} = \chi''_{\varphi\theta} = 0$ when $\theta = \frac{\pi}{2}$, we can rewrite the spin current as:

$$j_s^z = -\frac{\hbar}{4\pi}\Re\left(g^{\uparrow\downarrow}\right)\frac{h_{RF}^2\omega}{M_S^2}\chi'_{\theta\varphi}\chi''_{\varphi\varphi} = \frac{\hbar}{4\pi}\Re\left(g^{\uparrow\downarrow}\right)\frac{\gamma_0^2\gamma\omega^2\varepsilon_{\theta\theta}}{M_S}\frac{1}{f(\omega)}$$

where the last factor gives the lorentzian shape). The amplitude S corresponds to the heigth of the peak, and the parameter Δ corresponds to the half width at half maximum, $\mu_0 H_0$ is the resonant field and we add a baseline y_0. As we can see, the baseline is the only parameter that we do not attribute to the effect we want to measure. Indeed, we have noticed that in a general manner, the offset is antisymmetric with the field: when we change the sign of the field, the whole signal changes sign, including the offset. However, given the geometric symmetries of our system, the only effects that we can think of that could explain that offset are the ordinary and anomalous Nernst effects (ONE and ANE) where a voltage is obtained in the presence of a temperature gradient and an applied field (ONE) [133, 134] or a magnetisation (ANE) [135]. The thermal gradient is likely to stem from the Joule effect that occurs in the wire, where a current is flowing. The heat should dissipate by conduction in the substrate, which would act as a thermodynamical bath. Therefore the temperature would be higher at the top of the wire, and lower towards the substrate, leading to a local gradient. Since this matter is not directly linked to our topic, we present a few more experimental results about the offset in the Appendix C.

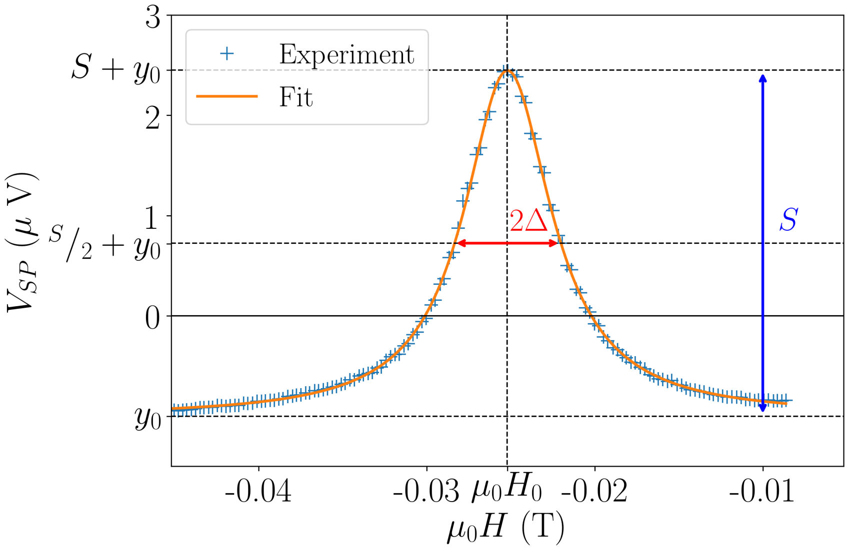

Figure IV.16: Measurement of the spin pumping voltage as a function of the applied magnetic field. The frequency of the RF field is set at $f = 5$ GHz. Over the experimental signal (crosses), we plot the fitting obtained using the function f presented in eq. (IV.17). The measurement shown corresponds to the bilayer $Si - SiO_2/Co_{40}Fe_{40}B_{20}(5nm)/Ir(2nm)$, and the experiment is carried out at room temperature.

The measurements obtained for one sample can be represented on the graph IV.17. All of them are fitted using lorentzian functions (for the sake of clarity, we do not represent all the curves available). Let us notice that the physical problem we study is antisymmetric with respect to the applied magnetic field. However, the fittings are done separately with independent parameters. The systematic identity between the fitted parameters for the couples of measurements at the same frequency for positive and negative fields confirms the precision of the measurements.

IV.4.4 Magnetic properties of the ferromagnetic layer

The first characterisation that can be performed is by fitting the field dependence of the resonant frequency by a Kittel law, as presented in eq. (IV.10). Here, we can choose to let a free parameter corresponding to a uniaxial anisotropy in the plane of the sample, additionally to the demagnetising field. This characterisation is not dependent on the thickness of the non magnetic material. We disclose this measurement for the sample corresponding to t_{Ir}=2nm.

As expected, the uniaxial magnetic anisotropy, that can be represented by a field $\mu_0 H_K$, is very weak. It lies in the length of the wire, which can thus be understood as a small shape anisotropy, with values that correspond to the demagnetising values calculated in the table IV.1. This confirms our assumption to neglect any uniaxial magnetic anisotropy term. The magnetisation at saturation of the sample is evaluated to be around 1.1×10^6 A.m^{-1} ($\mu_0 M_S \approx$ 1.4T) for all the thicknesses of iridium and platinum, as displayed on fig. IV.19:

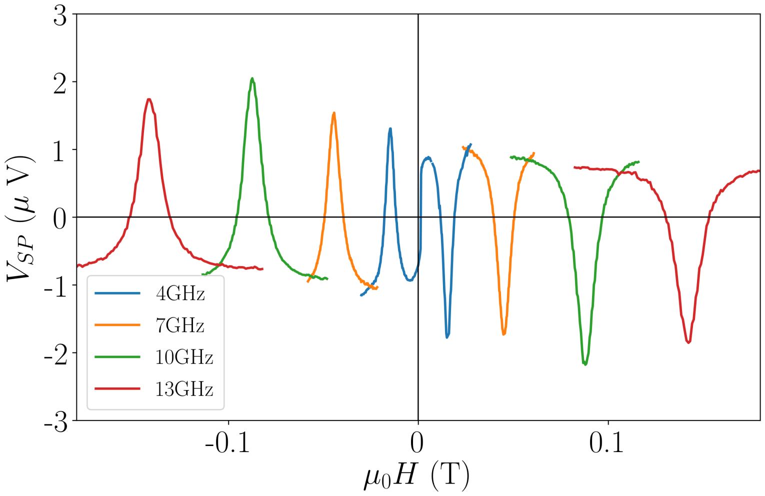

Figure IV.17: Measurement of the spin pumping voltage as a function of the applied magnetic field for several frequencies. We can especially notice that for a given frequency, the measurements are antisymmetric with respect to the applied magnetic field. The measurement shown corresponds to the bilayer $Si - SiO_2/Co_{40}Fe_{40}B_{20}(5nm)/Ir(2nm)$, and the experiment is carried out at room temperature.

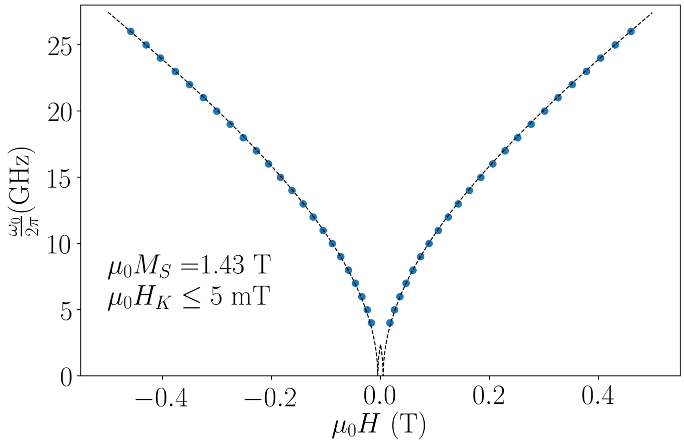

Figure IV.18: Evolution of the resonant frequency as a function of the amplitude of the static applied field (blue dots), fitted by a Kittel law (dashed black lines). The measurement shown corresponds to the bilayer $Si - SiO_2/Co_{40}Fe_{40}B_{20}(5nm)/Ir(2nm)$, and the experiment is carried out at room temperature.

IV.4.5 Damping enhancement and determination of $g_{eff}^{\uparrow\downarrow}$ in the CoFeB/NM interface

Now that this characterisation is done, let us study the evolution of the magnetic damping as a function of the thickness of the non magnetic material. As explained earlier, we expect to see the damping enhancement phenomenon. In order to do so, let us observe the evolution of the linewidth of the spin pumping voltage as a function of the frequency. For each sample, we can fit that curve with a linear model that is obtained with the calculation of the magnetic susceptibility presented earlier, in eq. IV.4.

We display on fig. IV.20 the evolution of the linewidth as a function of the frequency for the different thicknesses of iridium. From the evolution of the slope of the linear interpolations we expect to see the phenomenon of damping enhancement, for thicknesses of the non magnetic

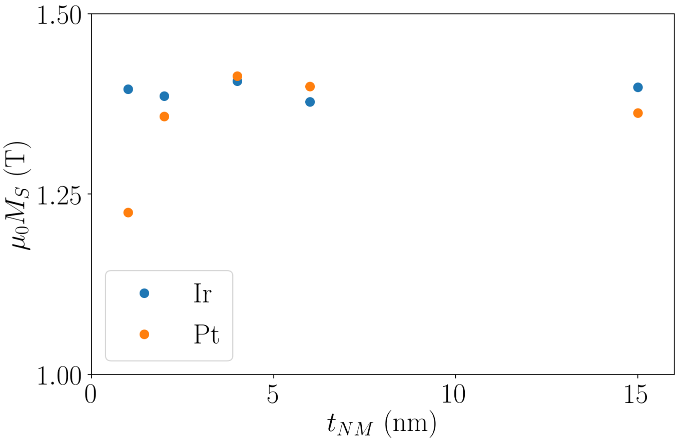

Figure IV.19: Evolution of the saturation magnetisation as a function of the thickness of the iridium (blue dots) or platinum (orange dots) in the bilayers $Si-SiO_2/Co_{40}Fe_{40}B_{20}(5nm)/Ir(t_{NM})$ and $Si-SiO_2/Co_{40}Fe_{40}B_{20}(5nm)/Pt(t_{NM})$.

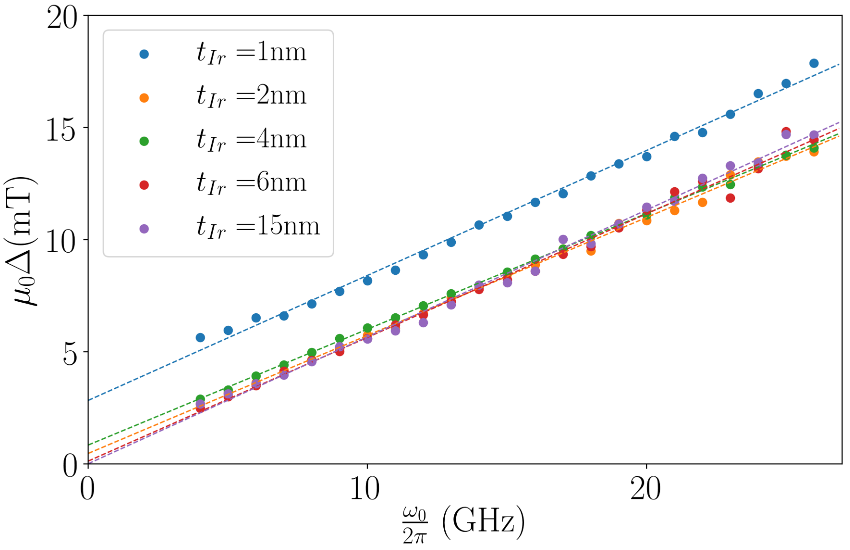

Figure IV.20: Evolution of the spin pumping voltage linewidth as a function of the frequency for several values of the iridium thickness (dots), fitted with a linear model (dashed lines), for the bilayers $Si-SiO_2/Co_{40}Fe_{40}B_{20}(5nm)/Ir(t_{Ir})$

material superior to the spin flip length. On the other hand, the intercept of the linear fit is often referred to as the inhomogeneous broadening [136]. We can see on fig. IV.20 that this intercept is very small, around 1mT for all the thicknesses of iridium, except for the thinnest sample, where only 1 nm was deposited. We can interpret this as an inhomogeneity of this 1 nm-thick iridium layer. Therefore, we have to consider carefully the results obtained for that sample: indeed the spin-to-charge and charge-to-spin conversion shall be smaller than expected. We display on fig.IV.21 the evolution of the magnetic damping as a function of the non magnetic material thickness.

At the opposite of what was expected, we can see that the damping is not monotonically increasing: there is an ascending trend from a non magnetic thickness of 2nm for platinum, and 4nm for iridium, but the values obtained on the samples with 1nm of non magnetic material show an unexpectedly large magnetic damping. This irregularity can be explained by the fact that for this thickness range, the quality of the deposition might be a little inferior, due to

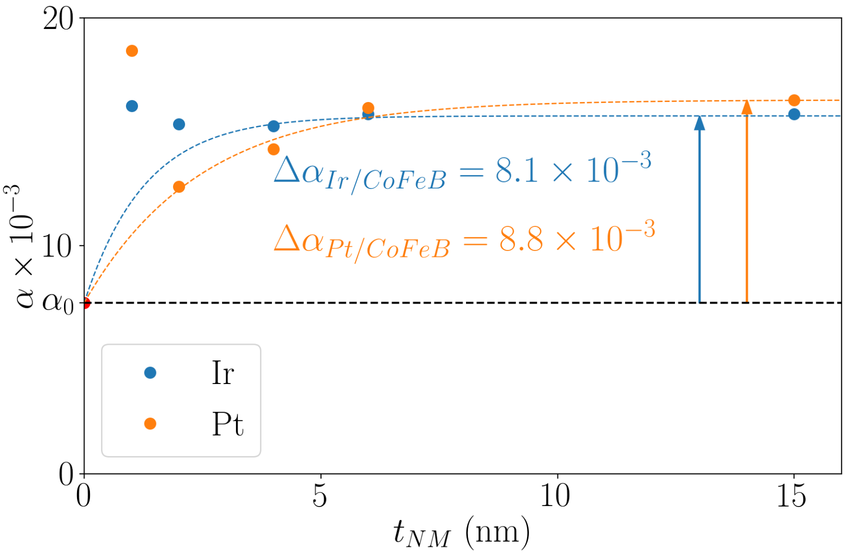

Figure IV.21: evolution of the magnetic damping as a function of the thickness of iridium (blue) and platinum (orange) for the bilayers $Si - SiO_2/Co_{40}Fe_{40}B_{20}(5nm)/Ir(t_{NM})$ and $Si - SiO_2/Co_{40}Fe_{40}B_{20}(5nm)/Pt(t_{NM})$. The guidelines were added after the determination of the spin flip lengths in the next subsection.

the roughness of the material. Indeed a slight roughness could lead to non continuous films, or with thicknesses varying a lot depending on the position. The interfacial effects could also be amplified due to the roughness, which could lead to an unexpected behaviour. We can also point out that the fact that iridium and platinum, which are heavier elements than cobalt, iron and boron, might also have resputtered the magnetic layer, which would lead to a poor interface quality, more visible at low thicknesses of Pt and Ir.

The values of magnetic damping obtained for large thicknesses of non magnetic material seem to stabilise, which advocates for the fact that the maximum non magnetic thickness chosen is several times superior to the spin flip length of both materials studied, which was one of the goals of the experiment.

Let us use the damping enhancement phenomenon to characterise the spin mixing conductance at the interface between CoFeB and Pt or Ir. We can benefit from the relationship eq. (IV.23) to estimate this parameter. In order to do that, we choose to use the average saturation magnetisation value, since it has a low dependence on the non magnetic thickness, as shown on fig. IV.19. Furthermore, if we observe that the damping enhancement $\Delta\alpha$ (fig. IV.21) and the saturation magnetisation M_S (fig. IV.19) are approximately the same for CoFeB/Ir and CoFeB/Pt, we expect both interfaces to give very similar values of the spin mixing conductance. The numerical values that we obtain are $g^{\uparrow\downarrow}_{eff,\ Ir/CoFeB} = 31nm^{-2}$ and $g^{\uparrow\downarrow}_{eff,\ Pt/CoFeB} = 33nm^{-2}$.

IV.4.6 Determination of l_{sf} in iridium

The value of the spin flip length can be determined with the method developped earlier, leading to eq. (IV.22): setting the frequency to a certain value and looking at the amplitude of the spin pumping current should give a trend that can be fitted by an hyperbolic tangent function that gives the spin flip length, regardless the prefactors.

Even though we only have 5 data points for each frequency, we can estimate this length accurately because we can analyse each frequency data to obtain a value.

We show the fitting corresponding to the thickness dependence of the spin pumping charge

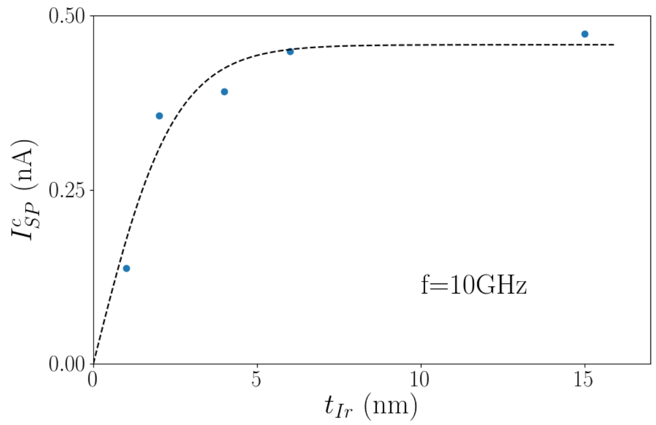

Figure IV.22: Evolution of the spin pumping charge current as a function of the iridium thickness for SP-FMR experiments carried out at 10GHz in the bilayers $Si-SiO_2/Co_{40}Fe_{40}B_{20}(5nm)/Ir(t_{NM})$ for $t_{NM} \in \{1,2,4,6,15\}$ nm, obtained by measurements carried out at room temperature. The dashed line corresponds to the fitting function used: $f(t_{Ir}) = \lambda \tanh\left(\frac{t_{Ir}}{2l_{sf}}\right)$ where λ is let as a free parameter, and l_{sf} is obtained from the curve fitting.

current I^c_{SP} for one frequency on fig. IV.22, and the evolution of the l_{sf} values obtained by fitting as a function of the frequency on fig. IV.23. Let us notice here that what we call “charge current” is actually the ratio between the voltage measured at the terminals due to the charge accumulation obtained by ISHE and the DC resistance of the device that was measured before SPFMR measurements.

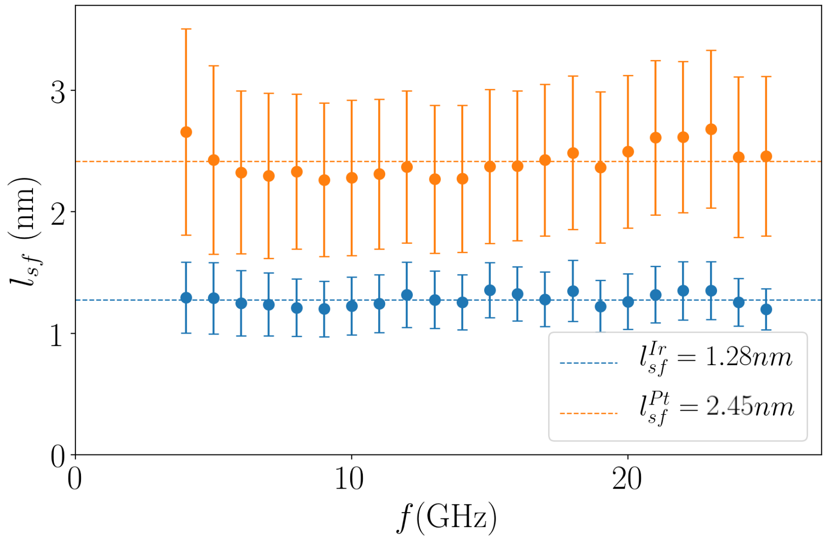

Figure IV.23: Evolution of the spin flip length as a function of the frequency for Ir and Pt. Each dot corresponds to the fitted value of the spin flip length from the curve representing I^c_{SP} as a function of the non magnetic layer thickness (as in fig. IV.22), using all the series of samples $Si-SiO_2/Co_{40}Fe_{40}B_{20}(5nm)/Ir(t_{NM})$ or $Si-SiO_2/Co_{40}Fe_{40}B_{20}(5nm)/Pt(t_{NM})$ for $t_{NM} \in \{1,2,4,6,15\}$ nm. All the experiments were carried out at room temperature.

The value of spin flip length for platinum that we find is 2.45 nm, which is in the order of magnitude of what can be found in the literature. Even though numerous values were reported, ranging from 1nm to 12nm, we shall not try to discuss the relevance of each measurement reported earlier. Our point is to provide results that are consistent between two materials, Pt and Ir, and not try to find the exact accurate value of l_{sf}.

The value obtained for iridium is consistent with our predictions, that is to say inferior to 10nm. The value of 1.28 nm that we found is small, but is of the same order of magnitude than the thickness of the iridium spacer used in iridium based synthetic ferrimagnets. Consequently, all the charge to spin conversion that could occur in this layer would be useful, and a larger spin flip length would be of no use.

IV.4.7 Comparison of θ_{SH} in iridium and platinum

The determination of the spin Hall angle is obtained using the amplitude of the "charge current", that is to say its value at the ferromagnetic resonance. We define the charge current as the ratio between the voltage measured at the terminals of the device due to the ISHE and the DC resistance of the device. Let us remember that from eq. (IV.20, IV.22), the charge current at the magnetic resonance can be written as:

$$I_c^{SP} = \frac{2e}{\hbar}\frac{\hbar\Re(g^{\uparrow\downarrow})\theta_{SH}l_{sf}W}{8\pi\alpha^2}(\gamma_0 h_{RF})^2\tanh\left(\frac{t_N}{2l_{sf}}\right)\frac{\gamma_0 M_S+\sqrt{(\gamma_0 M_S)^2+4\omega^2}}{(\gamma_0 M_S)^2+4\omega^2}$$

Let us call f the function that corresponds to the magnetic susceptibility:

$$f(\omega, M_S) = \frac{\gamma\mu_0 M_S+\sqrt{(\gamma\mu_0 M_S)^2+4\omega^2}}{(\gamma\mu_0 M_S)^2+4\omega^2}$$

As we see, the device that we consider corresponds to a current source in the part where the spin-to-charge conversion occurs, that is to say under the GSG wave guide. The voltage measured is thus corresponding to the resistivity of the sample. Experimentally, the charge current I_c^{SP} is obtained by the ratio of the measured spin pumping voltage by the measured resistance of the ferromagnetic/nonmagnetic wire.

The main difficulty to evaluate the formula obtained is the knowledge of the RF magnetic field applied, since it depends on the propagation line studied. We display a detailed study of this propagation line on the Appendix D. However, another strategy is to compute the ratio between the spin pumping charge currents for iridium and platinum. This is the choice we make by introducing a new quantity that is the corrected current, that can be expressed as follows:

$$\mathcal{R}_{NM} = \frac{I_{c,NM}^{SP}\alpha^2_{CoFeB/NM}}{f(\omega, M_S)l_{sf}^{NM}\Re(g^{\uparrow\downarrow}_{CoFeB/NM})}$$

The ratio of this new quantity for iridium and platinum can thus be expressed as:

$$\frac{\mathcal{R}_{Ir}}{\mathcal{R}_{Pt}} = \frac{\theta_{SH}^{Ir}}{\theta_{SH}^{Pt}}\frac{\tanh(\frac{t_N}{2l_{sf}^{Ir}})}{\tanh(\frac{t_N}{2l_{sf}^{Pt}})} \tag{IV.24}$$

Where t_N is the thickness of non magnetic material, that must be the same for the iridium- and the platinum-based samples. Let us plot the corrected ratio, doing away with the frequency dependant part by evaluating it at the chosen frequencies and the measured M_S values.

We represent the ratio of corrected currents as a function of the frequency on fig. IV.24:

As expected, the ratio of the $\mathcal{R}$ quantities for a given thickness of the non magnetic materials is mainly flat, and the variations decrease as the non magnetic thickness increases. This lack of noise in the ratio of our data is the confirmation that the amplitude of the RF field as a function of the frequency of the excitation is the same for the iridium based and the platinum based samples: a slight difference would be amplified by the ratio of the square of the RF applied fields, resulting in a curve showing strong irregularities.

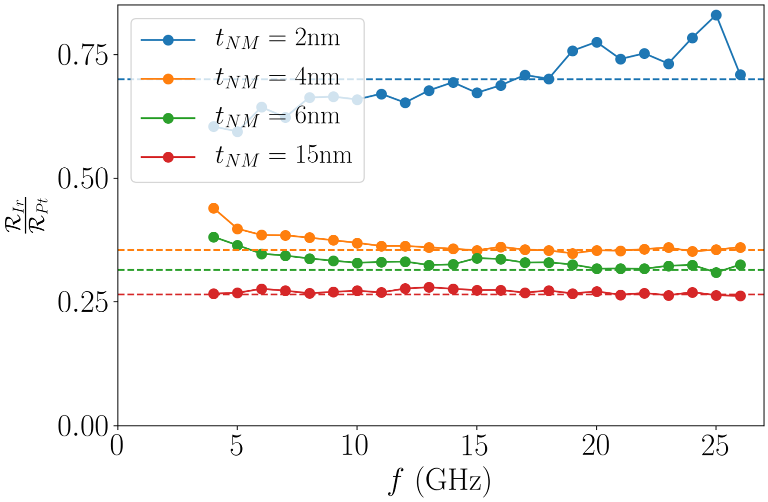

Figure IV.24: Evolution of the $\frac{\mathcal{R}_{Ir}}{\mathcal{R}_{Pt}}$ ratio as a function of the frequency. Each dot corresponds to the comparison of the measurements carried out on the samples $Si - SiO_2/Co_{40}Fe_{40}B_{20}(5nm)/Ir(t_{NM})$ and $Si - SiO_2/Co_{40}Fe_{40}B_{20}(5nm)/Pt(t_{NM})$ for $t_{NM} \in \{2, 4, 6, 15\}$ nm (one thickness per curve, see the legend) at the given frequency, at room temperature.

The most relevant value of the ratio of the $\mathcal{R}$ quantities is the limit obtained for high frequencies. Indeed, this limit also corresponds to large applied fields, which tend to validate the macrospin hypothesis on which the whole model and interpretation of the results holds. We can thus plot this limit as a function of the non magnetic thickness. We understand this evolution as representing the ratio of hyperbolic tangents presented in eq. (IV.24), multiplied by the ratio of both spin Hall angles. The ratio is obtained by considering that in our experiments, the maximum value of t_{NM} is superior to both spin flip lengths (which is experimentally validated), and thus using the result:

$$\lim_{t_{NM}\to\infty} \frac{\mathcal{R}_{Ir}}{\mathcal{R}_{Pt}} = \frac{\theta_{SH}^{Ir}}{\theta_{SH}^{Pt}}$$

On fig. IV.25, we can see that the agreement between the theory and the experiment is good except for the 2nm-thick samples. It is even worse for the 1nm-thick samples that we did not even represent on figs. IV.24 and IV.25. These discrepancies can be explained by the fact that the uncertainty in the thicknesses of materials increase, which lead to larger errors in the results. Overall, the interface effects that we do not take into account with great precisions in the models that are used can become larger, and the roughness can cause more unexpected features. For this reason, we are still confident in the rest of the results, since the agreement with the model improves as the thickness of non magnetic material increases.

We obtain a spin Hall angle ratio of 0.26. The first qualitative remark about this result is that iridium and platinum have spin Hall angles with the same sign. This element is of major importance, because the relative spin Hall angles signs of the non magnetic layers that share an interface with a magnetic layer determine the complementary action of the spin currents acting on the magnetisation, or the cancellation of the effects desired.

In a more quantitative perspective, we have determined the spin-Hall efficiency of iridium with respect to platinum. Indeed we do away with the uncertainties due to the reproducibility of the experiments that lead to more than an order of magnitude between the results reported by different research groups. The fact that we used exactly the same ferromagnetic material, substrates, deposition and patterning materials and procedures, allows us to be confident in

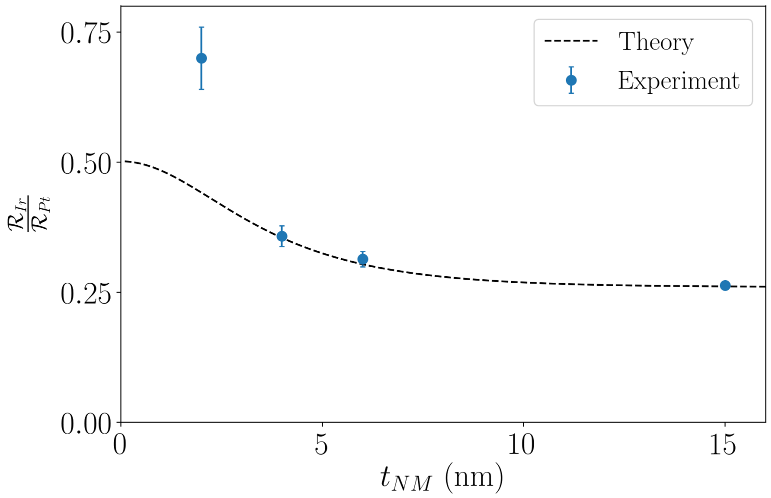

Figure IV.25: Evolution of the ratio $\dfrac{\mathcal{R}_{Ir}}{\mathcal{R}_{Pt}}$ as a function of the non magnetic thickness, using the samples $Si-SiO_2/Co_{40}Fe_{40}B_{20}(5nm)/Ir(t_{NM})$ and $Si-SiO_2/Co_{40}Fe_{40}B_{20}(5nm)/Pt(t_{NM})$ for $t_{NM} \in \{2, 4, 6, 15\}$ nm (one thickness per dot), by averaging the results obtained in all the frequency range displayed in fig. IV.24. The dashed line represents the theoretical formula that is expected from eq. (IV.24). The only fitted parameter is the ratio of the spin Hall angles of Ir and Pt

this relative characterisation.

The method by which we could obtain the previous results is as interesting as the results themselves. If the values for the spin flip length and the spin mixing conductance are obtained similarly to what was done in earlier publications, the relative measurement of the spin Hall angles of a material in comparison to another is a promising new option in order to obtain a standard measurement for the spin Hall effect in materials. Indeed, since no consensus seems to be found for the best measurements to carry out, just taking a reference material and measuring the spin pumping on the same geometry is a step further for the comparison of the results. It is much more likely to reach a clear experimental consensus in that case than only with separate measurements on experimental setups that can change from an institute to another.

About the possible enhancement of the propagation of domain walls in an iridium-based synthetic ferrimagnet, the result that we obtain is not very favourable: since iridium and platinum have spin Hall angles of the same sign, the spin current injection enabled by both materials will tend to cancel each other. Fortunately, the small charge to spin conversion efficiency in iridium let us hope that this will let the Pt layer dominate the domain wall propagation. The small thickness of iridium in synthetic ferrimagnets (around 1.5nm) will also decrease the charge current density flowing through it, and therefore limit the undesired effects. On the other hand, in a further step, it would be possible to contemplate a sample capped with tantalum, which spin Hall angle sign is opposite to the one of Pt and Ir, leading to an addition of the effects in the top layer of the synthetic ferrimagnets stacks that can be grown.

IV.5 Conclusion

In this chapter, we have characterised the ability of iridium to generate a spin current and thus act on the magnetisation when a current flows through it. By studying the magnetisation dynamics in the presence of an oscillatory excitation, we have been able to characterise the magnetic susceptibility of a material depending on the geometry of the experiment, with the most general approach. Therefore, after a careful analysis of the techniques that could lead us to a characterisation of the spin Hall efficiency in a material, we have been able to choose the most relevant experiments to carry out.

Then, we have presented an experimental procedure that leads to the determination of quantities that characterise the SHE/ISHE properties of a material with respect to another one's, leading to a good confidence in the numeric results obtained, and getting rid of doubts that are still nowadays inherent to such experiments, and that lead to a great dispersion in the experimental results reported even for the same experimental technique.

We have eventually estimated the spin flip length of the materials that we studied to be $l_{sf}^{Ir} = 1.28$ nm and $l_{sf}^{Pt} = 2.45$ nm; the spin mixing conductances that characterise the interfaces between these non magnetic materials and the ferromagnetic layer chosen were evaluated at: $g_{eff,Ir/CoFeB}^{\uparrow\downarrow} = 31nm^{-2}$ and $g_{eff,Pt/CoFeB}^{\uparrow\downarrow} = 33nm^{-2}$. The spin Hall angle of iridium turns out to have the same sign as platinum's, and its value corresponds to 26% of the spin Hall angle of platinum.

This study is a mandatory step in the understanding of the role played by iridium in any transport experiment carried out in an iridium-based synthetic ferrimagnetic sample. We can appreciate the fact that the spn flip length in iridium is typically of the same order of magnitude than the iridium thickness at which we obtain adequate values for the RKKY coupling in synthetic ferrimagnets, which should enable the maximisation of the SHE in the iridium spacer despite its very low thickness.

Conclusion

In this manuscript, we have focused on a type of heterostructures, synthetic ferrimagnets, in order to optimise this kind of materials for the spintronic application of racetrack memories, using iridium as a spacer layer for its promising potentialities. We have thus performed characterisations regarding the static field response of the materials grown with a temperature dependence, and considered with a special interest iridium for its spintronics properties.

In this manuscript, we start by giving a short state of the art and stating the motivation of an in-depth study of iridium-based synthetic ferrimagnets in the introduction. Then, in the first chapter, we present a few basic concepts of magnetism that enable the good understanding of the rest of this manuscript. We especially give clues to understand the quantities of interest and the approximations and models that are used all along. We present in particular the magnetisation dynamics equations, models for domain walls and experimental studies extracted from literature. Eventually, we provide a way to characterise synthetic ferrimagnets using only magnetic hysteresis loops.

In the second chapter, we display the experimental results of the characterisation of synthetic ferrimagnets that were grown in the frame of this thesis. We present the experimental techniques that enable us to measure the magnetic hysteresis loops, and display corresponding experimental results. We analyse the data to show the evolution of the synthetic ferrimagnets properties as a function of the thicknesses of the iridium layer and the ferromagnetic layers involved. Afterwards, we study the temperature dependence of the magnetic hysteresis loops by SQUID means, and evidence the fact that three types of magnetic cycles can be obtained. By observing the transitions between the various magnetic hysteresis loops, we explore the time dependence of the magnetisation as a function of the applied field for various magnetic fields. We are able in this frame to evidence non monotonic magnetic aftereffects, that we are able to understand and explain with a 2-spin energetic model.

The third chapter is devoted to the study of the spin transport in iridium. This part is crucial because it shows the interest in using iridium to grow synthetic ferrimagnets for racetrack memory, but also in a wider framework for other spintronics applications. In order to do so, we first present the direct and inverse spin Hall effects (SHE and ISHE), which are amongst the most efficient ways to generate a spin current. We then provide a detailed study of the magnetisation dynamics in a ferromagnet at RF frequencies, which enables us to introduce two of the most routinely used techniques to probe SHE and ISHE in a material. From this study, we draw the conclusion that the most relevant measurements that can be carried out are comparative measurements: indeed, the most reliable way to estimate the actual spin Hall effect behaviour of two materials is to use the very same experimental technique and materials, so as to be able to know where the differences stem from. This method would avoid the enormous discrepancies that exist in the literature for the very same experiments on the same stacks grown by the same methods. We conclude this chapter by disclosing a comparative experimental characterisation of the spin Hall effect in iridium and platinum.

Let us point out that this manuscript does not provide current-induced magnetic domain wall motion, as it would be needed in order to create a racetrack memory. However, this thesis is the first step towards a systematic study of the non magnetic spacer of a synthetic ferrimagnet for racetrack memories. The perspectives of this thesis correspond to the switching of the magnetisation of the stack by spin orbit torque, to demonstrate a possibility of nucleation of a magnetic domain by current means, and a study of the propagation of magnetic domains by current pulses, so as to evaluate the efficiency of this stack for an application in the racetrack memory field. One of the options that is also explored to improve the stack in this perspectives is the change of the capping material used in the iridium-based synthetic ferrimagnets grown. During this thesis, several options have been already tested for the growth, such as iridium, tantalum and aluminum. This change in materials for one layer will thus be the object of another thesis in the group of nanomagnetism and spintronics of Institut Jean Lamour.

Appendix A

Calculation of the Oersted field in a simple model

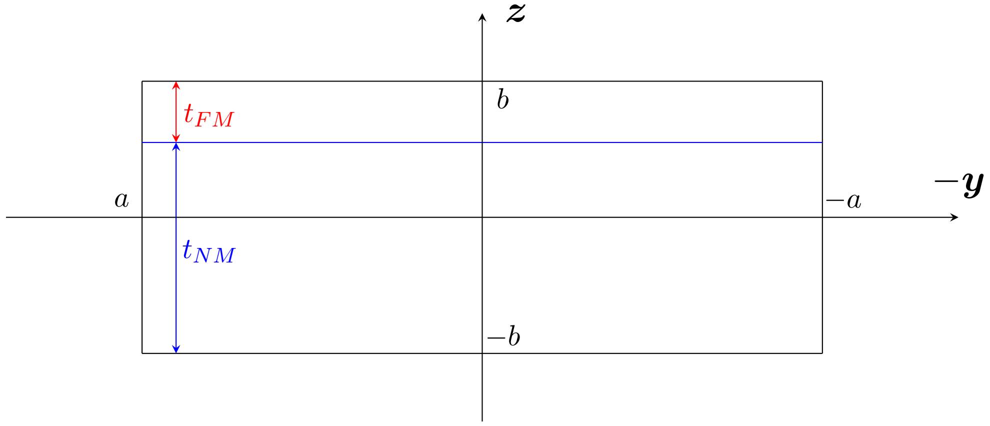

Figure A.1: Oersted field in the wire

Here, we consider a uniform current density $\boldsymbol{J} = J\boldsymbol{x}$ in the whole sample. Let us divide the wire in a multiplicity of wires of section $dydz$. Let us consider the field produced by an infinite wire in the $\boldsymbol{x}$ direction passing at the position (y_0, z_0) at a position M (x_M, y_M, z_M). It is given by the formula:

$$d\boldsymbol{H}(M) = \frac{Jdydz}{2\pi r}\boldsymbol{e}_\theta \tag{A.1}$$

Where we define $r = \sqrt{(y_0 - y_M)^2 + (z_0 - z_M)^2}$ and $\boldsymbol{e}_\theta = \frac{z_M - z_0}{r}\boldsymbol{y} + \frac{y_0 - y_M}{r}\boldsymbol{z}$.

The total magnetic field can thus be calculated as follows:

$$\boldsymbol{H}(M) = \frac{J}{2\pi}\int_{-a}^{a}\int_{-b}^{b}\left(\frac{z_M - z_0}{(y_0 - y_M)^2 + (z_0 - z_M)^2}\boldsymbol{y} + \frac{y_0 - y_M}{(y_0 - y_M)^2 + (z_0 - z_M)^2}\boldsymbol{z}\right) dydz \tag{A.2}$$

We can thus integrate both components of the field separately as follows:

$$\begin{cases} H_y = & -\dfrac{J}{2\pi}\displaystyle\int_{-a}^{a}\left[\ln((y_0 - y_M)^2 + (z_0 - z_M)^2)\right]_{z_0=-b}^{z_0=b} dy \\ H_z = & \dfrac{J}{2\pi}\displaystyle\int_{-b}^{b}\left[\ln((y_0 - y_M)^2 + (z_0 - z_M)^2)\right]_{y_0=-a}^{y_0=a} dz \end{cases} \tag{A.3}$$

Rewriting explicitly:

$$\begin{cases} H_y = & -\dfrac{J}{2\pi}\displaystyle\int_{-a}^{a}\Big(\ln[(y_0-y_M)^2+(b-z_M)^2]-\ln[(y_0-y_M)^2+(b+z_M)^2]\Big)dy \\ H_z = & \dfrac{J}{2\pi}\displaystyle\int_{-b}^{b}\Big(\ln[(a-y_M)^2+(z_0-z_M)^2]-\ln[(a+y_M)^2+(z_0-z_M)^2]\Big)dz \end{cases} \tag{A.4}$$

We obtain by performing the second spatial integral the following result:

$$\begin{aligned} H_y = -\frac{J}{4\pi}\Bigg[&(y_0-y_M)[\ln((y_0-y_M)^2+(b-z_M)^2)-\ln((y_0-y_M)^2+(b+z_M)^2)] \\ &+(b-z_M)\arctan\left(\frac{y_0-y_M}{b-z_M}\right)-(b+z_M)\arctan\left(\frac{y_0-y_M}{b+z_M}\right)\Bigg]_{-a}^{a} \end{aligned} \tag{A.5}$$

$$\begin{aligned} H_y = -\frac{J}{4\pi}\Bigg(&(a-y_M)[\ln((a-y_M)^2+(b-z_M)^2)-\ln((a-y_M)^2+(b+z_M)^2)] \\ &+(a+y_M)[\ln((a+y_M)^2+(b-z_M)^2)-\ln((a+y_M)^2+(b+z_M)^2)] \\ &+(b-z_M)\Bigg(\arctan\left(\frac{a-y_M}{b-z_M}\right)+\arctan\left(\frac{a+y_M}{b-z_M}\right)\Bigg) \\ &-(b+z_M)\Bigg(\arctan\left(\frac{a-y_M}{b+z_M}\right)+\arctan\left(\frac{a+y_M}{b+z_M}\right)\Bigg)\Bigg) \end{aligned} \tag{A.6}$$

And similarly for H_z, inverting the variables (y_M, a) and (z_M, b), with a $-$ sign. We can especially enjoy the following symmetries:

$$\begin{cases} y \mapsto -y \implies H_y \mapsto H_y \\ y \mapsto -y \implies H_z \mapsto -H_z \\ z \mapsto -z \implies H_z \mapsto H_z \\ z \mapsto -z \implies H_y \mapsto -H_y \end{cases} \tag{A.7}$$

We can visalise that vector field in the form of a stream plot as shown on fig.A.2:

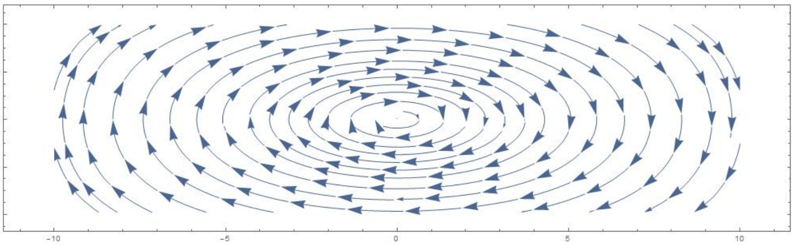

Figure A.2: Oersted field produced by a square conductor

If we wish to calculate the spatial average of the field induced by the current $\langle \boldsymbol{h}_{RF} \rangle$ in the ferromagnetic layer, we have to sum the magnetic field over the spatial domain defined by: $\{(y_M, z_M)\ such\ that\ y_M \in [-a; a]\ and\ z_M \in [b-t_{FM}, b]\}$. This set is symmetric with respect to y, and we have the antisymmetry: $H_z(-y, z) = -H_z(y, z)$, leading to the following: $\langle \boldsymbol{h}_{RF} \rangle = \langle h_{RF} \rangle \boldsymbol{y}$. We then have to calculate it as follows:

$$\langle h_{RF} \rangle = \frac{1}{2at_{FM}}\int_{-a}^{a}\int_{b-t_{FM}}^{b} H_y(y,z)dydz = \frac{1}{at_{FM}}\int_{0}^{a}\int_{b-t_{FM}}^{b} H_y(y,z)dydz \tag{A.8}$$

Appendix B

Symmetries of the coefficients of χ

We have seen the expression of the real part of the magnetic susceptibility χ' presented in eq. (IV.7). Let us notice that the components of this matrix are all composed of the sum of two functions: $f_1(\omega) = \dfrac{\omega^2 - \omega_0^2}{f(\omega)}$ and $f_2(\omega) = \dfrac{\omega^2}{f(\omega)}$:

$$\boxed{\chi'(\omega) = \frac{\gamma\gamma_0}{1+\alpha^2} f_1(\omega) \begin{bmatrix} -\dfrac{\varepsilon_{\varphi\varphi}}{\sin^2(\theta_0)} & \dfrac{\varepsilon_{\theta\varphi}}{\sin(\theta_0)} \\ \dfrac{\varepsilon_{\varphi\theta}}{\sin(\theta_0)} & -\varepsilon_{\theta\theta} \end{bmatrix} + \frac{\gamma_0 M_S \Delta}{1+\alpha^2} f_2(\omega) \begin{bmatrix} \alpha & 1 \\ -1 & \alpha \end{bmatrix}}$$

If we divide the functions f_1 and f_2 as shown below, we can separate χ' as a sum of a symmetric and an antisymmetric matrices.

$$\chi'(\omega) = \mathcal{S}_{\omega_0}(\chi')(\omega) + \mathcal{A}_{\omega_0}(\chi')(\omega)$$

Where:

$$\mathcal{S}_{\omega_0}(\chi')(\omega) = \frac{\gamma\gamma_0}{1+\alpha^2} \mathcal{S}_{\omega_0}(f_1)(\omega) \begin{bmatrix} -\dfrac{\varepsilon_{\varphi\varphi}}{\sin^2(\theta_0)} & \dfrac{\varepsilon_{\theta\varphi}}{\sin(\theta_0)} \\ \dfrac{\varepsilon_{\varphi\theta}}{\sin(\theta_0)} & -\varepsilon_{\theta\theta} \end{bmatrix} + \frac{\gamma_0 M_S \Delta}{1+\alpha^2} \mathcal{S}_{\omega_0}(f_2)(\omega) \begin{bmatrix} \alpha & 1 \\ -1 & \alpha \end{bmatrix}$$

And:

$$\mathcal{A}_{\omega_0}(\chi')(\omega) = \frac{\gamma\gamma_0}{1+\alpha^2} \mathcal{A}_{\omega_0}(f_1)(\omega) \begin{bmatrix} -\dfrac{\varepsilon_{\varphi\varphi}}{\sin^2(\theta_0)} & \dfrac{\varepsilon_{\theta\varphi}}{\sin(\theta_0)} \\ \dfrac{\varepsilon_{\varphi\theta}}{\sin(\theta_0)} & -\varepsilon_{\theta\theta} \end{bmatrix} + \frac{\gamma_0 M_S \Delta}{1+\alpha^2} \mathcal{A}_{\omega_0}(f_2)(\omega) \begin{bmatrix} \alpha & 1 \\ -1 & \alpha \end{bmatrix}$$

We explicit these symmetric and antisymmetric parts to make :

$$\begin{cases} \mathcal{S}_{\omega_0}(f_1)(\omega) = \dfrac{(\omega-\omega_0)^6 + (\omega-\omega_0)^4(\Delta^2 - 4\omega_0^2) - 3(\omega-\omega_0)^2\omega_0^2\Delta^2}{g(\omega)} \\ \mathcal{A}_{\omega_0}(f_1)(\omega) = -\dfrac{2\omega_0(\omega-\omega_0)\Big((\omega-\omega_0)^4 - 4\omega_0^2(\omega-\omega_0)^2 - \omega_0^2\Delta^2\Big)}{g(\omega)} \end{cases}$$

$$\begin{cases} \mathcal{S}_{\omega_0}(f_2)(\omega) = \dfrac{(\omega-\omega_0)^6 + (\omega-\omega_0)^4(\Delta^2 - 3\omega_0^2) + 2\omega_0^2(\omega-\omega_0)^2(2\omega_0^2 - \Delta^2) + \omega_0^4\Delta^2}{g(\omega)} \\ \mathcal{A}_{\omega_0}(f_2)(\omega) = -\dfrac{2\omega_0(\omega-\omega_0)^3((\omega-\omega_0)^2 - 2\omega_0^2)}{g(\omega)} \end{cases}$$

Where:

$$g(\omega) = \big((\omega-\omega_0)^4 + (\omega-\omega_0)^2(4\omega_0^2+\Delta^2) + \omega_0^2\Delta^2\big)^2 - \big(2\omega_0(\omega-\omega_0)(2(\omega-\omega_0)^2+\Delta^2)\big)^2$$

is a symmetric function with respect to ω_0.

Appendix C

Study of the offset in the spin pumping measurements

We have extracted numerous informations from the spin pumping measurements that were carried out. However, we have not studied the offset of the signal that was obtained, and that was not expected. We have observed peculiar features about this offset that is noted y_0 on fig. IV.16. This offset is antisymmetric with respect to the applied magnetic field and the magnetisation. Indeed, we represent on fig. C.1 the value of the offset that was found for CoFeB(5nm)/Ir(t_{Ir}) samples ($t_{Ir} \in \{1, 2, 4, 6, 15\ nm\}$) as a function of the frequency, and for various thicknesses of iridium. Both positive and negative applied magnetic field values are represented.

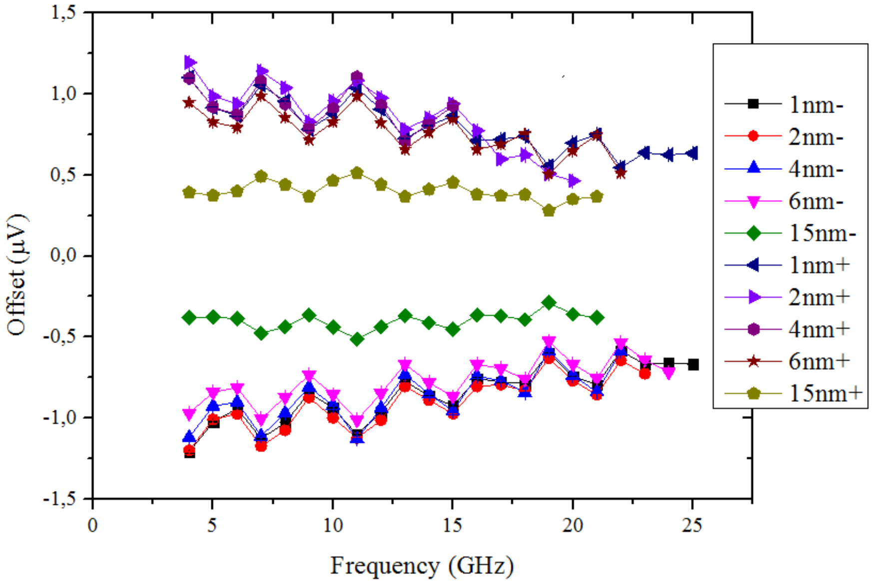

Figure C.1: Measurement of the offset y_0 of the spin pumping voltage as a function of the frequency for CoFeB(5nm)/Ir(t_{Ir}) samples for $t_{Ir} \in \{1, 2, 4, 6, 15\ nm\}$

Furthermore, due to the symmetries of our samples, for the coplanar waveguide that propagates the RF signal as well as for the bilayer wire in which the spin to charge conversion is occuring, we are looking for a phenomenon belonging to the Nernst/Hall effects family, as those presented in [137]. Since we have an applied magnetic field and the magnetisation that lie perpendicularly to the wire, and we measure a longitudinal voltage, we are looking for either a temperature gradient or a spin current that would be transverse to the wire and orthogonal to the magnetic field and magnetisation.

Given that the spin current emmited is the one that is already probed in the inverse spin Hall effect through the conversion of spin current into a charge current, we can rule out this origin. Concerning the appearance of a thermal gradient within the thickness of the magnetic layer, we can easily imagine that the current flowing through the CoFeB/Ir bilayer can lead to this phenomenon. In order to get insight about this, we represent on fig. C.2 the offset measured as a function of the thickness of iridium of the sample, for several frequencies.

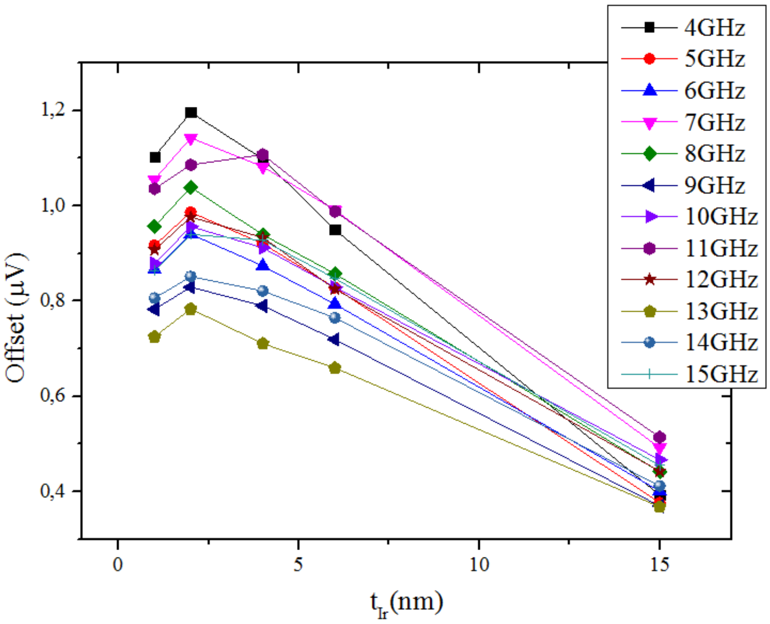

Figure C.2: Measurement of the offset y_0 of the spin pumping voltage as a function of the iridium thickness $t_{Ir} for$ CoFeB(5nm)/Ir(t_{Ir}) samples at various frequencies ranging from 4 to 15 GHz

We can see that the offset is maximised for a value of the iridium thickness of 2 nm for all the frequencies (except 11GHz). In order to understand this phenomenon, let us consider two situations that are the very low thickness regime and the large thickness regime. The former is for thicknesses that are smaller than 2 nm. In the corresponding samples, the iridium layer is thin enough to be more resistive than bulk iridium. Therefore, the resistivity of this layer is not much higher than the one of the CoFeB layer. The Joule heating occuring in the sample is thus close in both layers, and only a small transverse thermal gradient appears.

On the opposite, for large values of the iridium thickness, the iridium resistivity is significantly lower than the one of CoFeB. In that case, the current flowing in the bilayer is mainly propagating in the iridium layer. Consequently, the thicker the iridium layer the smaller the current density in the CoFeB layer, and the smaller the Joule heating in the whole sample. In this large iridium thickness regime, an increase of the iridium thickness decreases the transverse thermal gradient in the bilayer.

This analysis advocates for a Nernst effect enabled by a thermal gradient. Indeed, the figure C.2 shows an effect that is low for a very low thickness regime, a maximum obtained around $t_{Ir} = 2nm$, and a decrease of the amplitude with the iridium thickness in the large iridium thickness regime.

The undetermined issue at this point is the differenciation between the ordinary Nernst effect (ONE), in which a charge current can be obtained transverse to a thermal gradient and an applied magnetic field that are orthogonal, or the anomalous Nernst effect (ANE), where the charge current is generated perpendicularly to a thermal gradient and an orthogonal magnetisation. These effects should be easy to discriminate, because one should depend linearly with the applied magnetic field whereas the other one should be constant once the magnetisation is saturated in the field direction. However, since the change in the applied magnetic field during a spin pumping measurement is also affecting the spin pumping current, it is directly changing the Joule effect in the wire, and thus the thermal gradient also modified. As a consequence, we currently do not have arguments that would favour one contribution or another amongst these two effects.

Appendix D

Modelling of a RF spin pumping line

The measurement that we want to carry out during the SP-FMR experiment corresponds to the injection of a RF current in an antenna so as to induce an RF Oersted field that can excite a ferromagnetic layer. One of the key parameters of this experiment is the RF induced field. However, the knowledge of this parameter depends on the whole experimental setup, that is to say all the geometric and electric properties of the components of the circuit, and their behaviour as a function of the frequency.

In this part, we are going to describe the electronic characterisation of the experimental setup, so as to get a quantitative description of our experiment.

Representation of the electric signal

There are three main ways to characterise an electric quadrupole, which are the impedance, the transmission and the scattering matrices. These three representations link the entrance signal, noted (v_e, i_e), and the signal flowing out of the quadrupole (v_s, i_s).

- The impedance matrix: This representation gives the relationship between the voltages and the currents at the entrance and the exit of the quadrupole. This quantity is not considered in our calculations.
- The transmission matrix:

  This matrix links easily the entrance signal to the outgoing signal. Indeed, thus representation implies that a convention of entrance and exit is chosen. We can express the relationship between the voltages and currents as follows:

  $$\begin{pmatrix} v_e \\ i_e \end{pmatrix} = T \cdot \begin{pmatrix} v_s \\ i_s \end{pmatrix}$$

  For clarity, we will express the transmission matrix with the following convention:

  $$T = \begin{pmatrix} A & B \\ C & D \end{pmatrix}$$

  This representation has the advantage to chain the blocks by multiplicating the matrices as follows: for a circuit described by n quadrupoles described by the transmission matrices T_n, the total quadrupole is then represented by the transmission matrix T_{tot} calculated as follows:

  $$T_{tot} = \prod_{i=1}^{n} T_i \tag{D.1}$$

However, experimentally, this is not the matrix that is usually measured. This formalism is mainly efficient as a calculation tool, and equivalences have to be used in order to step from one formalism to another.

- The scattering matrix:

  This representation of a quadrupole represents the part of the signal that flows from one port to another. Here, let us forget for a moment the notion of entrance and way out of the quadrupole, and only consider that it has two ports, namely 1 and 2. The coefficients of the matrix S_{ij} represent the signal going from port j to port i. For instance, S_{21} is the transmission coefficient from 1 to 2.

  This is the matrix that is experimentally measured using a vectorial Network Analyser (VNA) in a 2-port measurement. However, the S matrices cannot be multiplied to represent several quadrupoles in one single matrix. This representation has then to be converted in terms of transmission matrix in order to represent the whole experimental setup.

The matrices represented here can be linked by the following relationships [138]:

$$\begin{cases} A = & \dfrac{(1+S_{11})(1-S_{22})+S_{12}S_{21}}{2S_{21}} \\[2ex] B = & Z_0\dfrac{(1+S_{11})(1+S_{22})-S_{12}S_{21}}{2S_{21}} \\[2ex] C = & \dfrac{1}{Z_0}\dfrac{(1-S_{11})(1-S_{22})-S_{12}S_{21}}{2S_{21}} \\[2ex] D = & \dfrac{(1-S_{11})(1+S_{22})+S_{12}S_{21}}{2S_{21}} \end{cases}$$

Scattering parameter measurement with a vectorial network analyser (VNA)

The easiest way to characterise a quadrupole is to plug it on a VNA using the four poles of the device. In this case, the measurement of each of the R coefficients of the scattering matrix can be measured easily. However, in some cases, the device is not meant to be plugged on a VNA on both sides, because the end of the line consists in a patterned sample. In that case, we can only perform 1 port measurements, and we have to achieve a total characterisation using adequate loads at the terminal of the device studied.

It is possible to characterize a quadrupole using only 1-port scattering measurements with a VNA. The usual way to do so is to load the quadrupole with three well known loads, which are usually an open circuit, a short circuit, and a 50 Ω load so as to math the impedances. In these cases, we will obtain three frequency dependant scattering measurements, that we will refer to as S_{11}^O, S_{11}^S, S_{11}^M respectively. We can link these scattering measurements to the reflexion coefficient due to the impedance mismatch, considering the quadrupole loaded as a dipole. We can thus define the measured entrance impedances M^O, M^S and M^M as a function of the intern impedance of the VNA Z_0^{VNA} (supposed to be 50 Ω) as:

$$M^k = Z_0^{VNA}\frac{1+S_{11}^k}{1-S_{11}^k}$$

Ideal case

For each entrance impedance obtained, it is possible to link the parameters to the load and the transmission matrix of the quadrupole. We can have two cases: the open circuit and the match (the short circuit corresponds to a match with an impedance equal to $Z_M = 0\ \Omega$).

The open circuit equations are the following:

$$\begin{pmatrix} V_e \\ I_e \end{pmatrix} = \begin{pmatrix} A & B \\ C & D \end{pmatrix} \cdot \begin{pmatrix} V_s \\ 0 \end{pmatrix}$$

Leading to:

$$M^O = \frac{V_e}{I_e} = \frac{A}{C}$$

The match equations give the slightly different system:

$$\begin{pmatrix} V_e \\ I_e \end{pmatrix} = \begin{pmatrix} A & B \\ C & D \end{pmatrix} \cdot \begin{pmatrix} Z_M I_s \\ I_s \end{pmatrix}$$

Leading to:

$$M^M = \frac{V_e}{I_e} = \frac{A.Z_M + B}{C.Z_M + D}$$

And:

$$M^S = \frac{V_e}{I_e} = \frac{B}{D}$$

Using the fact that the transmission matrix has a unit determinant, ($AD - BC = 1$), one can get the following system:

$$\left\{ \begin{array}{rcl} A & = & \pm M^O \sqrt{\dfrac{(M^M - M^S)}{Z_M(M^O - M^S)(M^O - M^M)}} \\ B & = & \pm M^S \sqrt{\dfrac{Z_M(M^O - M^M)}{(M^O - M^S)(M^M - M^S)}} \\ C & = & \pm \sqrt{\dfrac{(M^M - M^S)}{Z_M(M^O - M^S)(M^O - M^M)}} \\ D & = & \pm \sqrt{\dfrac{Z_M(M^O - M^M)}{(M^O - M^S)(M^M - M^S)}} \end{array} \right.$$

Non-ideal loads – General case

Let us now consider that the loads of the calibration kit that are given are not ideal, which is the case. Some slight corrections can be applied to the determination of the transmission matrix through the series of the 3 1 port measurements. Let us consider that for each measurement, the load has the impedance Z_i ($i \in \{0, 1, 2\}$). Let us note the entrance impedances measured as M_i. We thus have the following system to solve:

$$\left\{ \begin{array}{rcl} AZ_i + B & = & CZ_iM_i + DM_i \\ AD - BC & = & 1 \end{array} \right.$$

From the first equation comes the relation:

$$B = CZ_0M_0 + DM_0 - AZ_0$$

Leading, for the second equation, to:

$$A = \frac{M_1Z_1 - M_0Z_0}{Z_1 - Z_0}C + \frac{M_1 - M_0}{Z_1 - Z_0}D$$

The third equation then links C to D as follows:

$$\frac{C}{D} = \frac{M_0(Z_2 - Z_1) + M_1(Z_0 - Z_2) + M_2(Z_1 - Z_0)}{M_0Z_0(Z_1 - Z_2) + M_1Z_1(Z_2 - Z_0) + M_2Z_2(Z_0 - Z_1)} = c$$

We can thus express the ratios as follows:

$$\frac{A}{D} = \frac{M_0M_1(Z_0 - Z_1) + M_1M_2(Z_1 - Z_2) + M_2M_0(Z_2 - Z_0)}{M_0Z_0(Z_1 - Z_2) + M_1Z_1(Z_2 - Z_0) + M_2Z_2(Z_0 - Z_1)} = a$$

And

$$\frac{B}{D} = \frac{Z_0M_1M_2(Z_2 - Z_1) + Z_1M_2M_0(Z_0 - Z_2) + Z_2M_0M_1(Z_1 - Z_0)}{M_0Z_0(Z_1 - Z_2) + M_1Z_1(Z_2 - Z_0) + M_2Z_2(Z_0 - Z_1)} = b$$

Let us note that these expressions of the ratios a, b, and c are independant of the choice of the indexes 0, 1 and 2, which translates the fact that the three first equations are exactly the same for (Z_i, M_i) $(i \in \{0, 1, 2\})$. It is thus possible to choose that the indexes $\{0, 1, 2\}$ correspond to the measurements $\{short, open, load\}$ in whatever order. Let us solve the system thanks to the fourth equation:

$$\left\{ \begin{array}{lcl} A & = & aD \\ B & = & bD \\ C & = & cD \\ D & = & \pm\frac{1}{\sqrt{a - bc}} \end{array} \right. \tag{D.2}$$

Modeling of the transmission line

The transmission line that we consider is similar to a planar cable with losses. In order to do so, the transmission matrix proposed by Pozar can be written as:

$$T_{lossy} = \begin{pmatrix} \cos(\beta l) & Z_0 \sin(\beta l) \\ \frac{1}{Z_0}\sin(\beta l) & \cos(\beta l) \end{pmatrix}$$

Where Z_0 is the characteristic impedance of the line, β the propagation coefficient and l the length. The length is easily measurable. However, Z_0 and β need to be determined and explicited. We can consider the losses on the line by considering a conductance G, a resistance R, a capacitance C and an inductance L, all these quantities being defined per length unit. With these notations, according to Pozar, the terms Z_0 and β of the line can be expressed as:

$$Z_0 = \sqrt{\frac{R + jL\omega}{R + jG\omega}}$$

and

$$\beta = \sqrt{(R + jL\omega)(R + jG\omega)}$$

We now need to determine the parameters R, L, C and G. The parameter R is easy to obtain thanks to a DC measurement of the resistance of the grounds and the signal. The division by the length of the line gives the value of R.

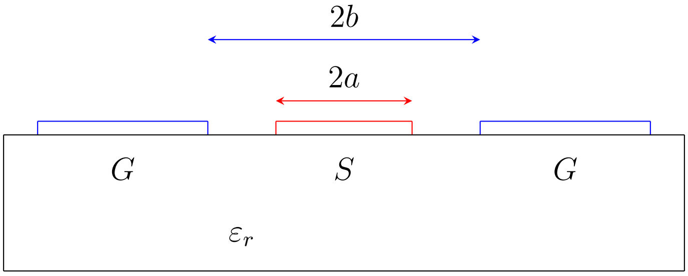

Figure D.1: Representation of a coplanar waveguide in a ground-signal-ground (GSG) configuration.

One way to express the capacitance per unit length was established by Gupta [139] in the case of a planar geometry for a signal and two grounds. Considering the schematic given in fig. D.1, the capacitance per unit length can be expressed as:

$$C = 2\varepsilon_0 \left(\varepsilon_r + 1\right) \frac{K_1(k)}{K_2(k)} = \varepsilon_0 \varepsilon_{re} \frac{K_1(k)}{K_2(k)}$$

Where $k = \frac{a}{b}$ is the ratio of the dimensions of the cable as noted on fig. D.1, ε_{re} is the effective dielectric constant of the coplanar waveguide, K_1 is the complete elliptic integral of the first kind, and K_2 is its complement.

In order to obtain the value of L, one can make the approximation that the line is lossless, compute the characteristic impedance, and consider that the relation $Z_0 = \sqrt{\frac{L}{C}}$ holds. This is what we did, using the relation of Gupta for the lossless characteristic impedance with the notations previously introduced:

$$Z_0 = \frac{30\pi}{\sqrt{\varepsilon_{re}}} \frac{K_1(k)}{K_2(k)}$$

We have represented on fig. D.2 the real and imaginary part of each coefficient of the transfer matrix of the antenna that we measured with a VNA. We have plotted in solid lines the coefficients obtained by using the analytical formulas presented above. We can see that the agreement is nearly perfect, which proves the validity of the approach and the quality of the antenna.

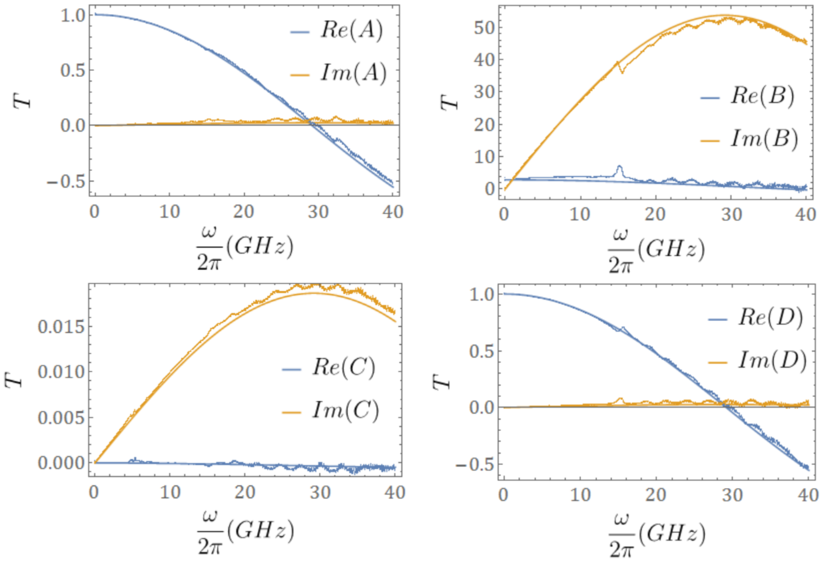

Figure D.2: Real and imaginary parts of each coefficient of the transmission matrix of the antenna studied as a function of the frequency. All the dot curves represent the experimental measurements, whereas the solid lines correspond to the model presented above.

Bibliography

[1] M. N. Baibich, J. M. Broto, A. Fert, F. N. V. Dau, F.Petroff, P. Eitenne, G. Creuzet, A. Friederich, and J. Chazelas, “Giant magnetoresistance of (001)Fe/(001)Cr magnetic superlattices,” *Physical Review Letters*, vol. 61, nov88 1988.

[2] G. Binasch, P. Grunberg, F. Saurenbach, and W.Zinn, “Enhanced magnetoresistance in layered magnetic structures with antiferromagnetic interlayer exchange,” *Physical Review B*, vol. 39, mar 1989.

[3] S.-G. Je, J.-C. Rojas-Sanchez, T. H. Pham, P. Vallobra, G. Malinowski, D. Lacour, T. Fache, M.-C. Cyrille, D.-Y. Kim, S.-B. Choe, M. Belmeguenai, M. Hehn, S. Mangin, G. Gaudin, and O. Boulle, “Spin-orbit torque-induced switching in ferrimagnetic alloys: Experiments and modeling,” *Applied Physics Letters*, vol. 112, feb 2018.

[4] T. H. Pham, S.-G. Je, P. Vallobra, T.Fache, D. Lacour, G. Malinowski, M.-C. Cyrille, G. Gaudin, O. Boulle, M. Hehn, J.-C. Rojas-Sanchez, and S. Mangin, “Thermal contribution to the spin-orbit torque in metallic-ferrimagnetic systems,” *Physical Review Applied*, vol. 9, jun 2018.

[5] S. S. Parkin, M. Hayashi, and L. Thomas, “Magnetic domain-wall racetrack memory,” *Science*, vol. 11, pp. 190–194, apr 2008.

[6] Z. Sun, X. Bi, W. Wu, S. Yoo, and H. Li, “Array organization and data management exploration in racetrack memory,” *IEEE Transactions on Computers*, vol. 65, sep 2014.

[7] S. Parkin and S. H. Yang, “Memory on the racetrack,” *Nature*, vol. 10, pp. 195–198, mar 2015.

[8] L. Berger, “Low-field magnetoresistance and domain drag in ferromagnets,” *Journal of Applied Physics*, vol. 49, pp. 2156–2161, mar 1978.

[9] L. Berger, “Exchange interaction between ferromagnetic domain wall and electric current in very thin metallic films,” *Journal of Applied Physics*, vol. 55, pp. 1954–1956, mar 1984.

[10] L. Berger, “Exchange forces between domain wall and electric current in permalloy films of variable thickness,” *Journal of Applied Physics*, vol. 63, pp. 4276–4278, apr 1988.

[11] L. Berger, “Motion of a magnetic domain wall traversed by fast-rising current pulses,” *Journal of Applied Physics*, vol. 71, pp. 2721–2726, mar 1992.

[12] J. C. Slonczewski, “Conductance and exchange coupling of two ferromagnets separated by a tunneling barrier,” *Physical Review B*, vol. 39, apr 1989.

[13] J. C. Slonczewski, “Current-driven excitation of magnetic multilayers,” *Journal of Magnetism and Magnetic Materials*, vol. 159, oct 1996.

[14] S. Zhang and Z. Li, “Roles of nonequilibrium conduction electrons on themagnetization dynamics of ferromagnets,” *Physical Review Letters*, vol. 93, sep 2004.

[15] G. Tatara and H. Kohno, “Theory of current-driven domain wall motion: Spin transfer versus momentum transfer,” *Physical Review Letters*, vol. 92, feb 2004.

[16] M. Hayashi, L. Thomas, Y. B. Bazaliy, C. Rettner, R. Moriya, X. Jiang, and S. S. P. Parkin, “Influence of current on field-driven domain wall motion in permalloy nanowires from time resolved measurements of anisotropic magnetoresistance,” *Physical Review Letters*, vol. 96, may 2006.

[17] G. S. D. Beach, C. Knutson, C. Nistor, M. Tsoi, and J. L. Erskine, “Nonlinear domain-wall velocity enhancement by spin-polarized electric current,” *Physical Review Letters*, vol. 97, aug 2006.

[18] A. Yamaguchi, T. Ono, S. Nasu, K. Miyake, K. Mibu, and T. Shinjo, “Real-space observation of current-driven domain wall motion in submicron magnetic wires,” *Physical Review Letters*, vol. 92, feb 2004.

[19] M. Klaui, P.-O. Jubert, R. Allenspach, A. Bischof, J. A. C. Bland, G. Faini, U. Rudiger, C. A. F. Vaz, L. Vila, and C. Vouille, “Direct observation of domain-wall configurations transformed by spin currents,” *Physical Review Letters*, vol. 95, feb 2004.

[20] A. Yamaguchi, D. Chiba, F. Matsukura, T. Dietl, and T. Ono, “Velocity of domain-wall motion induced by electrical currentin the ferromagnetic semiconductor (Ga,Mn)As,” *Physical Review Letters*, vol. 96, mar 2006.

[21] M. Hayashi, L. Thomas, C. Rettner, R. Moriya, Y. B. Bazaliy, and S. S. P. Parkin, “Current driven domainwall velocities exceeding the spin angular momentum transfer rate in permalloy nanowires,” *Physical Review Letters*, vol. 98, pp. 1–4, jan 2007.

[22] M. Hayashi, L. Thomas, R. Moriya, C. Rettner, and S. S. P. Parkin, “Current-controlled magnetic domain-wall nanowire shift register,” *Science*, vol. 11, pp. 209–211, apr 2008.

[23] I. M. Miron, T. Moore, H. Szambolics, L. D. Buda-Prejbeanu, S. Auffret, B. Rodmacq, S. Pizzini, J. Vogel, M. Bonfim, A. Schuhl, and G. Gaudin, “Fast current-induced domain-wall motion controlled by the rashba effect,” *Nature Materials*, vol. 10, pp. 419–423, jun 2011.

[24] K. S. Ryu, L. Thomas, S. H. Yang, and S. S. Parkin, “Chiral spin torque at magnetic domain walls,” *Nature Nanotechnology*, vol. 8, pp. 527–533, jul 2013.

[25] K. S. Ryu, L. Thomas, S. H. Yang, and S. S. Parkin, “Chiral spin torque arising from proximity-induced magnetization,” *Nature Communication*, vol. 5, pp. 1–8, may 2014.

[26] S. Parkin and L. Thomas, “Sequence of current pulses for depinning magnetic domain walls,” US Patent 7 492 622, june, 12 2007.

[27] S. S. P. Parkin and L. Thomas, “Sequence of current pulses for depinning magnetic domain walls,” US Patent 7 760 535, February 23 2010.

[28] S. S. P. Parkin, “Unidirectional racetrack memory device,” US Patent 7 551 469, June 23 2009.

[29] F. Ummelen, H. Swagten, and B. Koopmans, “Racetrack memory based on in-plane-field controlled domain-wall pinning,” *Scientific Reports*, vol. 7, apr 2017.

[30] R. Moriya, S. S. P. Parkin, and L. Thomas, “Magnetic racetrack with current-controlled motion of domain walls within an undulating energy landscape,” US Patent 7 626 844, December 1 2009.

[31] R. Moriya, S. S. P. Parkin, and L. Thomas, “Magnetic racetrack with current-controlled motion of domain walls within an undulating energy landscape,” US Patent 7 667 994, February 23 2010.

[32] S. S. P. Parkin, L. Thomas, and S. H. Yang, “Domain wall motion in perpendicularly magnetized wires having magnetic multilayers with engineered interfaces,” US Patent 8 638 601, January 28 2014.

[33] S. S. P. Parkin, L. Thomas, and S. H. Yang, “Domain wall motion in perpendicularly magnetized wires having artificial antiferromagnetically coupled multilayers with engineered interfaces,” US Patent 8 687 415, July 6 2014.

[34] J. Z. Sun, R. Allenspach, S. S. P. Parkin, J. C. Slonczewski, and B. D. Terris, “Spin-current switched magnetic memory element suitable for circuit integration and method of fabricating the memory element,” US Patent 8 860 105, October 14 2014.

[35] T. Phung, A. Pushp, L. Thomas, C. Rettner, S.-H. Yang, K.-S. Ryu, J. Baglin, B. Hughes, and S. Parkin, “Highly efficient in-line magnetic domain wall injector,” *Nano Letters*, vol. 15, jan 2015.

[36] Y. Zhang, W. S. Zhao, J.-O. Klein, C. Chappert, and D. Ravelosona, “Current induced perpendicular-magnetic-anisotropy racetrack memory with magnetic field assistance,” *Applied Physical Letters*, vol. 104, jan 2014.

[37] Y. Zhang, W. S. Zhao, J.-O. Klein, C. Chappert, and D. Ravelosona, “Implementation of magnetic field assistance to current-induced perpendicular-magnetic-anisotropy racetrack memory,” *Journal of Applied Physics*, vol. 115, feb 2014.

[38] Y. Zhang, W. S. Zhao, D. Ravelosona, J.-O. Klein, J. V. Kim, and C. Chappert, “Perpendicular-magnetic-anisotropy CoFeB racetrack memory,” *Journal of Applied Physics*, vol. 111, may 2012.

[39] S. Fukami, T. Suzuki, Y. Nakatani, N. Ishiwata, M. Yamanouchi, S. Ikeda, N. Kasai, and H. Ohno, “Current-induced domain wall motion in perpendicularly magnetized CoFeB nanowire,” *Applied Physics Letters*, vol. 98, feb 2011.

[40] S. H. Yang, K. S. Ryu, and S. Parkin, “Domain-wall velocities of up to $750m.s^{-1}$ driven by exchange-coupling torque in synthetic antiferromagnets,” *Nature Nanotechnology*, vol. 10, pp. 221–226, mar 2015.

[41] L. Caretta, M. Mann, F. Buttner, K. Ueda, B. Pfau, C. M. Gunther, P. Hessing, A. Churikova, C. Klose, M. Schneider, D. Engel, C. Marcus, D. Bono, K. Bagschik, S. Eisebitt, and G. S. D. Beach, “Fast current-driven domain walls and small skyrmions in a compensated ferrimagnet,” *Nature Nanotechnology*, vol. 13, pp. 1154–1160, sep 2018.

[42] L. D. Geng and Y. M. Jin, “Magnetic vortex racetrack memory,” *Journal of Magnetism and Magnetic Materials*, vol. 423, sep 2016.

[43] W. Zhang, M. B. Jungfleisch, W. Jiang, J. Sklenar, F. Y. Fradin, J. E. Pearson, J. B. Ketterson, and A. Hoffmann, “Spin pumping and inverse spin hall effects – insights for future spin-orbitronics (invited),” *Journal of Applied Physics*, vol. 117, mar 2015.

[44] W. Kang, Y. Huang, C. Zheng, W. Lv, N. Lei, Y. Zhang, X. Zhang, Y. Zhou, and W. Zhao, “Voltage controlled magnetic skyrmion motion for racetrack memory,” *Scientific Reports*, vol. 6, mar 2016.

[45] W. Kang, C. Zheng, Y. Huang, X. Zhang, W. Lv, Y. Zhou, and W. Zhao, "Compact modeling and evaluation of magnetic skyrmion-based racetrack memory," *IEEE Transactions on Electron devices*, vol. 64, feb 2017.

[46] R. T. V. Puliafito, E. Martinez, A. Manchon, M. Ricci, M. Carpentieri, and G. Finocchio, "Performance of synthetic antiferromagnetic racetrack memory: domain wall versus skyrmion," *Journal of Physics D: Applied Physics*, vol. 50, jul 2017.

[47] S. S. P. Parkin, "Systematic variation of the strength and oscillation period of indirect magnetic exchange coupling through the 3d, 4d, and 5d transition metals," *Physical Review Letters*, vol. 67, pp. 3598–3601, dec 1991.

[48] S. S. P. Parkin and D. Mauri, "Spin engineering: Direct determination of the Ruderman-Kittel-Kasuya-Yosida far-field function in ruthenium," *Physical Review B*, vol. 44, pp. 7131–7134, oct 1991.

[49] T. White, T. Bailey, M. Pierce, and C. W. Miller, "Strong spin pumping in permalloy-iridium heterostructures," *IEEE Magnetic Letters*, vol. 8, aug 2017.

[50] D. D. Sarma, "Nature dependance of spin-orbit splittings on atomic number," *Procedures of Indian Academic Science*, vol. 90, jan 1981.

[51] H. L. Wang, C. H. Du, Y. Pu, R. Adur, P. C. Hammel, and F. Y. Yang, "Scaling of spin Hall angle in 3d, 4d, and 5d metals from $Y_3Fe_5O_{12}$/metal spin pumping," *Physical Review Letters*, vol. 112, jan 2014.

[52] R. A. Duine, K.-J. Lee, S. S. P. Parkin, and M. D. Stiles, "Synthetic antiferromagnetic spintronics," *Nature Physics*, vol. 14, mar 2018.

[53] G. S. Abo, Y.-K. Hong, J. Park, J. Lee, W. Lee, and B.-C. Choi, "Definition of magnetic exchange length," *IEEE Transactions on Magnetics*, vol. 49, pp. 4937–4939, aug 2013.

[54] L. Néel *Cahiers de Physique*, vol. 25, no. 1, 1944.

[55] C. Kittel, "Physic al theory of ferromagnetic domains," *Review of Modern Physics*, vol. 21, pp. 541–592, mar 1949.

[56] R. Moskowitz and E. D. Torre, "Theoretical aspects of demagnetization tensors," *IEEE Transactions on Magnetic Materials*, vol. 2, dec 1966.

[57] J. A. Obsorn, "Demagnetizing factors of the general ellipsoid," *Physical Review*, vol. 77, pp. 351–357, jun 1945.

[58] M. Ruderman and C. Kittel, "Indirect exchange coupling of nuclear magnetic moments by conduction electrons," *Physical Review*, vol. 96, pp. 99–102, jun 1954.

[59] T. Kasuya, "A theory of metallic ferro- and antiferromagnetism on Zener's model," *Progress of Theoretical Physics*, vol. 16, pp. 45–57, feb 1956.

[60] K. Yosida, "Magnetic properties of Cu-Mn alloys," *Physical Review*, vol. 106, pp. 893–898, feb 1957.

[61] P. Bruno and C. Chappert, "Ruderman-Kittel theory of oscillatory interlayer exchange coupling," *Physical Review B*, vol. 46, jul 1992.

[62] E. C. Stoner, F. R. S., and E. P. Wohlfarth, "A mechanism of magnetic hysteresis in heterogenous alloys," *Philosophical transactions of the Royal Society A*, vol. 240, may 1948.

[63] R. J. Elliott, “Theory of the effect of spin-orbit coupling on magnetic resonance in some semiconductors,” *Physical Review*, vol. 96, pp. 266–279, may 1954.

[64] Y. Yafet, “g factors and spin-lattice relaxation of conduction electrons,” *Solid State Physics*, vol. 14, pp. 1–98, 1963.

[65] D. Ralph and M. Stiles, “Spin transfer torques,” *Journal of Magnetism and Magnetic Materials*, vol. 320, pp. 1190–1216, Apr. 2008.

[66] J. A. Katine and E. E. Fullerton, “Device implications of spin-transfer torques,” *Journal of Magnetism and Magnetic Materials*, vol. 320, dec 2007.

[67] M. I. D’Yakonov and V. I. Perel, “Spin orientation of electrons associated with the interband absorption of light in semi conductors,” *Soviet Journal of Experimental and Theoretical Physics*, vol. 33, nov 1971.

[68] N. F. Mott, “The scattering of fast electrons by atomic nuclei,” *Proceedings of the Royal Society A*, vol. 124, jun 1929.

[69] J. Sinova, D. Culcer, Q. Niu, N. A. Sinitsyn, T. Jungwirth, and A. H. MacDonald, “Universal intrinsic spin Hall effect,” *Physical Review Letters*, vol. 92, mar 2004.

[70] J. Wunderlich, B. Kaestner, J. Sinova, and T. Jungwirth, “Experimental observation of the spin-Hall effect in a two-dimensional spin-orbit coupled semiconductor system,” *Physical Review Letters*, vol. 94, feb 2005.

[71] C. Hahn, G. de Loubens, O. Klein, and M. Viret, “Comparative measurements of inverse spin Hall effects and magnetoresistance in YIG/Pt and YIG/Ta,” *Physical Review B*, vol. 87, pp. 1–8, may 2013.

[72] L. Liu, T. Moriyama, D. C. Ralph, and R. A. Buhrman, “Spin-torque ferromagnetic resonance induced by the spin Hall effect,” *Physical Review B*, vol. 106, pp. 1–4, jan 2011.

[73] O. Mosendz, J. E. Pearson, F. Y. Fradin, G. E. W. Bauer, S. D. Bader, and A. Hoffmann, “Quantifying spin Hall angles from spin pumping: Experiments and theory,” *Physical Review Letters*, vol. 104, pp. 1–4, jan 2010.

[74] K. Ando, S. Takahashi, J. Ieda, H. Kurebayashi, T. Trypiniotis, C. H. W. Barnes, S. Maekawa, and E. Saitoh, “Electrically tunable spin injector free from the impedance mismatch problem,” *Nature Materials*, vol. 10, pp. 655–659, jun 2011.

[75] A. Azevedo, L. H. Vilela-Leao, R. L. Rodriguez-Suarez, A. F. L. Santos, and S. M. Rezende, “Spin pumping and anisotropic magnetoresistance voltages in magnetic bilayers: Theory and experiment,” *Physical Review B*, vol. 83, pp. 1–6, apr 2011.

[76] Z. Feng, J. Hu, L. Sun, B. You, D. Wu, J. Du, W. Zhang, A. Hu, Y. Yang, D. M. Tang, B. S. Zhang, and H. F. Ding, “Spin pumping and anisotropic magnetoresistance voltages in magnetic bilayers: Theory and experiment,” *Physical Review B*, vol. 85, pp. 1–7, jun 2012.

[77] H. Nakayama, K. Ando, K. Harii, T. Yoshino, R. Takahashi, Y. Kajiwara, K. Uchida, and Y. Fujikawa, “Geometry dependence on inverse spin Hall effect induced by spin pumping in $Ni_{81}Fe_{19}$/Pt films,” *Physical Review B*, vol. 85, pp. 1–7, apr 2012.

[78] V. Vlaminck, J. E. Pearson, S. D. Bade, and A. Hoffmann, “Dependence of spin-pumping spin Hall effect measurements on layer thicknesses and stacking order,” *Physical Review B*, vol. 88, pp. 1–8, apr 2013.

[79] H. Y. Hung, G. Y. Luo, Y. C. Chiu, P. Chang, W. C. Lee, J. G. Lin, S. F. Lee, M. Hong, and J. Kwo, "Detection of inverse spin Hall effect in epitaxial ferromagnetic Fe_3Si films with normal metals Au and Pt," *Journal of Applied Physics*, vol. 113, pp. 1–3, apr 2013.

[80] L. Bai, P. Hyde, Y. S. Gui, C.-M. Hu, V. Vlaminck, J. E. Pearson, S. D. Bader, and A. Hoffmann, "Universal method for separating spin pumping from spin rectification voltage of ferromagnetic resonance," *Physical Review Letters*, vol. 111, pp. 1–5, nov 2013.

[81] M. Obstbaum, M. Hartinger, H. G. Bauer, T. Meier, F. Swientek, C. H. Back, and G. Woltersdorf, "Inverse spin Hall effect in $Ni_{81}Fe_{19}$ /normal-metal bilayers," *Physical Review B*, vol. 89, pp. 1–5, feb 2014.

[82] J.-C. Rojas-Sánchez, N. Reyren, P. Laczkowski, W. Savero, J.-P. Attané, C. Deranlot, M. Jamet, J.-M. George, L. Vila, and H. Jaffrès, "Spin pumping and inverse spin Hall effect in platinum: The essential role of spin-memory loss at metallic interfaces," *Physical Review Letters*, vol. 112, pp. 1–5, mar 2014.

[83] K. Kondou, H. Sukegawa, S. Mitani, K. Tsukagoshi, and S. Kasai, "Evaluation of spin Hall angle and spin diffusion length by using spin current-induced ferromagnetic resonance," *Applied Physics Express*, vol. 5, pp. 1–3, jul 2012.

[84] M. Althammer, S. Meyer, H. Nakayama, M. Schreier, S. Altmannshofer, M. Weiler, H. Huebl, S. Geprags, M. Opel, R. Gross, D. Meier, C. Klewe, T. Kuschel, J.-M. Schmalhorst, G. Reiss, L. Shen, A. Gupta, Y.-T. Chen, G. E. W. Bauer, E. Saitoh, and S. T. B. Goennenwein, "Quantitative study of the spin Hall magnetoresistance in ferromagnetic insulator/normal metal hybrids," *Physical Review B*, vol. 87, pp. 1–15, jun 2013.

[85] H. Nakayama, M. Althammer, Y.-T. Chen, K. Uchida, Y. Kajiwara, D. Kikuchi, T. Ohtani, S. Geprags, M. Opel, S. Takahashi, R. Gross, G. E. W. Bauer, S. T. B. Goennenwein, and E. Saitoh, "spin Hall magnetoresistance induced by a nonequilibrium proximity effect," *Physical Review Letters*, vol. 110, pp. 1–5, may 2013.

[86] L. Liu, C.-F. Pai, Y. Li, H. W. Tseng, D. C. Ralph, and R. A. Buhrman, "Spin-torque switching with the giant spin Hall effect of tantalum," *Science*, vol. 336, may 2012.

[87] J. E. Gomez, B. Z. Tedlla, N. R. Alvarez, G. Alejandro, E. Goovaerts, and A. Butera, "Spin transport parameters in $Ni_{80}Fe_{20}$/Ru and $Ni_{80}Fe_{20}$/Ta bilayers," *Physical Review B*, vol. 90, pp. 1–8, nov 2014.

[88] J. Sinova, S. O. Valenzuela, J. Wunderlich, C. H. Back, and T. Jungwirth, "Spin Hall effects," *Reviews of Modern Physics*, vol. 87, pp. 1–47, oct 2015.

[89] L. Vila, T. Kimura, and Y. Otani, "Evolution of the spin Hall effect in Pt nanowires: Size and temperature effects," *Physical Review Letters*, vol. 99, pp. 1–4, nov 2007.

[90] W. Zhang, V. Vlaminck, J. E. Pearson, R. Divan, S. D. Bader, and A. Hoffmann, "Determination of the Pt spin diffusion length by spin-pumping and spin Hall effect," *Applied Physics Letters*, vol. 103, pp. 1–4, dec 2013.

[91] A. Ganguly, K. Kondou, H. Sukegawa, S. Mitani, S. Kasai, Y. Niimi, Y. Otani, and A. Barman, "Thickness dependence of spin torque ferromagnetic resonance in $Co_{75}Fe_{25}$/Pt bilayer films," *Applied Physics Letters*, vol. 104, pp. 1–5, feb 2014.

[92] K. Xia, P. J. Kelly, G. E. W. Bauer, A. Brataas, and I. Turek, "Spin torques in ferromagnetic/normal-metal structures," *Physical Review B*, vol. 65, may 2002.

[93] W. Skowronski, L. Karwacki, S. Zietek, J. Kanak, S. Lazarski, K. Grochot, T. Stobiecki, P. Kuswik, F. Stobiecki, and J. Barna, "Determination of spin Hall angle in heavy-metal/CoFeB-based heterostructures with interfacial spin-orbit fields," *Physical Review Applied*, vol. 11, feb 2019.

[94] J. Shibata, G. Tatara, and H. Kohno, "A brief review of field- and current-driven domain-wall motion," *Journal of Physics D: Applied Physics*, vol. 44, sep 2011.

[95] A. Mougin, M. Cormier, J. P. Adam, P. J. Metaxas, and J. Ferré, "Domain wall mobility, stability and Walker breakdown in magnetic nanowires," *European Physics Letters*, vol. 78, jun 2007.

[96] J. C. Slonczewski, "Excitation of spin waves by an electric current," *Journal of Magnetism and Magnetic Materials*, vol. 195, aug 1999.

[97] M. Yamanouchi, D. Chiba, F. Matsukura, and H. Ohno, "Current-induced domain-wall switching in a ferromagnetic semiconductor structure," *Nature*, vol. 428, apr 2004.

[98] K. J. Kim, S. K. Kim, Y. Hirata, S. H. Oh, T. Tono, D. H. Kim, T. Okuno, W. S. Ham, S. K. G. Go, Y. Tserkovnyak, A. Tsukamoto, T. Moriyama, K. J. Lee, and T. Ono, "Fast domain wall motion in the vicinity of the angular momentum compensation temperature of ferrimagnets," *Nature Materials*, vol. 16, sep 2017.

[99] M. Imai, H. Chudo, M. Matsuo, S. Maekawa, and E. Saitoh, "Enhancement of domain-wall mobility at the angular momentum compensation temperature detected by NMR," *arXiv*, vol. 1911.02207, nov 2019.

[100] A. Thiaville, Y. Nakatani, J. Miltat, and Y. Suzuki, "Micromagnetic understanding of current-driven domain wall motion in patterned nanowires," *Europhysics Letters*, vol. 69, feb 2005.

[101] A. Hamadeh, P. Pirro, J.-P. Adam, Y. Lu, M. Hehn, S. Petit-Watelot, and S. Mangin, "Inversion of the domain wall propagation in synthetic ferrimagnets," *Applied Physics Letters*, vol. 111, jul 2017 hal-01654267.

[102] P. J. Metaxas, J. P. Jamet, J. Ferre, B. Rodmacq, B. Dieny, and R. Stamps, "Magnetic domain wall creep in the presence of an effective interlayer coupling field," *Journal of Magnetism and Magnetic Materials*, vol. 320, apr 2008.

[103] J. Y. Lee, K. S. Lee, S. Choi, K. Y. Guslienko, and S. K. Kim, "Dynamic transformations of the internal structure of a moving domain wall in magnetic nanostripes," *Physical Review B*, vol. 76, apr 2004.

[104] D. Herranz, R. Guerrero, R. Villar, F. G. Aliev, A. C. Swaving, R. A. Duine, C. van Haesendonck, and I. Vavra, "Anomalous low-frequency noise in synthetic antiferromagnets: Possible evidence of current-induced domain-wall motion," *Physical Review B*, vol. 79, apr 2009.

[105] M. Kuteifan, M. V. Lubarda, S. Fu, R. Chang, M. A. Escobar, S. Mangin, E. E. Fullerton, and V. Lomakin, "Large exchange-dominated domain wall velocities in antiferromagnetically coupled nanowires," *AIP Advances*, vol. 6, apr 2016 hal-02070472.

[106] P. Pirro, A. Hamadeh, M. Lavanant, T. Meyer, B. Tao, E. Rosario, Y.Lu, M. Hehn, S. Mangin, and S. Petit-Watelot, "Perpendicularly magnetized CoFeB multilayers with tunable interlayer exchange for synthetic ferrimagnets," *Journal of Magnetism and Magnetic Materials*, vol. 432, pp. 260–265, feb 2017.

[107] J. A. Thornton, "High rate thick film growth," *Annual Review of Materials Science*, vol. 7, aug 1977.

[108] E. E. Fullerton, J. S. Jiang, M. Grimsditch, C. H. Sowers, and S. D. Bader, "Exchange-spring behavior in epitaxial hard/soft magnetic bilayers," *Physical Review B*, vol. 58, nov 1998.

[109] E. E. Fullerton, J. S. Jiang, C. Rehm, C. H. Sowers, S. D. Bader, J. B. Patel, and X. Z. Wu, "High coercivity, epitaxial sm-co films withuniaxial in-plane anisotropy," *Applied Physics Letters*, vol. 71, jul 1998.

[110] J. Kerr, "On rotation of the plane of polarization by reflection from the pole of a magnet," *London, Edimburgh and Dublin philosophical magazine*, vol. 3, may 1877.

[111] J. Kerr, "On reflection of polarized light from the equatorial surface of a magnet," *London, Edimburgh and Dublin philosophical magazine*, vol. 5, may 1878.

[112] T. Haider, "Micromagnetic understanding of current-driven domain wall motion in patterned nanowires," *International Journal of Electromagnetics and Applications*, vol. 7, feb 2017.

[113] H. Ebert, "Magneto-optical effects in transition metal systems," *Reports of Progress in Physics*, vol. 59, may 1996.

[114] "MPMS SQUID VSM documentation." `http://www.lao.cz/data/ke-stazeni/MPMS_SQUID_VSM_eu_1_.pdf`. Accessed: 2019-12-16.

[115] D. Weller, Y. Wu, J. Stohr, M. Samant, B. Hermsmeier, and C. Chappert, "Orbital magnetic moments of Co in multilayers with perpendicular magnetic anisotropy," *Physical Review B*, vol. 49, dec 1993.

[116] G. Schutz, S. Stahler, M. Knulle, P. Fischer, S. Parkin, and H. Ebert, "Distribution of magnetic moments in Co/Pt and Co/Pt/Ir/Pt multilayers detected by magnetic x-ray absorption," *Journal of Applied Physics*, vol. 73, mar 1993.

[117] K. Kyuno, J.-G. Ha, R. Yamamoto, and S. Asan, "Theoretical study on the strain dependence of the magnetic anisotropy of X/Co(X=Pt, Cu,Ag, and Au) metallic multilayers," *Journal of Applied Physics*, vol. 79, jan 1996.

[118] K. Yakushiji, A. Sugihara, A. Fukushima, H. Kubota, and S. Yuasa, "Very strong antiferromagnetic interlayer exchange coupling with iridiumspacer layer for perpendicular magnetic tunnel junctions," *Applied Physics Letters*, vol. 110, feb 2017.

[119] R. Morgunov, A. Hamadeh, T. Fache, G. Lvova, O. Koplak, A. Talantsev, and S. Mangin, "Magnetic field and temperature control over Pt/Co/Ir/Co/Pt multistate magnetic logic device," *Superlattices and Microstructures*, vol. 104, pp. 1–9, feb 2017.

[120] R. B. Morgunov, E. I. Kunitsyna, A. D. Talantsev, O. V. Koplak, T. Fache, Y. Lu, and S. Mangin, "Influence of the magnetic field sweeping rate on magnetic transitions in synthetic ferrimagnets with perpendicular anisotropy," *Applied Physics Letters*, vol. 114, mar 2019.

[121] P. Bruno, G. Bayreuther, P. Beauvillain, C. Chappert, G. Lugerta, D. Renard, J. P. Renard, and J. Seiden, "Hysteresis properties of ultrathinferromagnetic films," *Journal of Applied Physics*, vol. 68, jul 1990.

[122] M. El-Hilo, A. de Witte, K. O'Grady, and R. Chantrell, "The sweep rate dependence of coercivity in recording media," *Journal of Magnetism and Magnetic Materials*, vol. 117, jun 1992.

[123] T. Fache, H. S. Tarazona, J. Liu, G. Lvova, M. J. Applegate, J. C. Rojas-Sanchez, S. Petit-Watelot, C. V. Landauro, J. Quispe-Marcatoma, R. Morgunov, C. H. W. Barnes, and S. Mangin, "Nonmonotonic aftereffect measurements in perpendicular synthetic ferrimagnets," *Physical Review B*, vol. 98, aug 2018.

[124] Y. Tserkovnyak, A. Brataas, and G. E. W. Bauer, "Enhanced Gilbert damping in thin ferromagnetic films," *Physical Review Letters*, vol. 88, pp. 1–4, mar 2002.

[125] Y. Tserkovnyak, A. Brataas, and G. E. W. Bauer, "Spin pumping and magnetization dynamics in metallic multilayers," *Physical Review B*, vol. 66, pp. 1–10, dec 2002.

[126] L. Berger, "Emission of spin waves by a magnetic multilayer traversed by a current," *Physical Review B*, vol. 54, oct 1996.

[127] L. Berger, "Effect of interfaces on Gilbert damping and ferromagnetic resonance linewidth in magnetic multilayers," *Journal of Applied Physics*, vol. 90, mar 2001.

[128] K. Ando, T. Yoshino, and E. Saitoh, "Optimum conditions for spin-current generation from magnetization precession in thin film systems," *Applied Physics Letters*, vol. 94, apr 2009.

[129] M. Johnson and R. Silsbee, "Coupling of electronic charge and spin at a ferromagnetic-paramagnetic metal interface," *Physical Review B*, vol. 37, apr 1988.

[130] A. Brataas, Y. Tserkovnyak, G. E. W. Bauer, and B. I. Halperin, "Spin battery operated by ferromagnetic resonance," *Physical Review B*, vol. 66, pp. 1–4, aug 2002.

[131] Y. Tserkovnyak, A. Brataas, G. E. W. Bauer, and B. I. Halperin, "Nonlocal magnetization dynamics in ferromagnetic heterostructures," *Reviews of Modern Physics*, vol. 77, pp. 1375–1421, oct 2005.

[132] C. Guillemard, S. Petit-Watelot, S. Andrieu, and J.-C. R. Sanchez, "Charge-spin current conversion in highquality epitaxial Fe/Pt systems: Isotropic spin Hall angle along different in-plane crystalline directions," *Applied Physics Letters*, vol. 113, dec 2018.

[133] A. von Ettingshausen and W. Nernst, "Ueber das auftreten electromotorischer kräfte in metallplatten, welche von einem wärmestrome durchflossen werden und sich im magnetischen felde befinden," *Annalen der Physik*, vol. 265, 1886.

[134] N. F. Mott, "Ueber die electromotorischen kräfte, welche durch den magnetismus in von einem wärmestrome durchflossenen metallplatten geweckt werden," *Annalen der Physik*, vol. 267, jun 1887.

[135] A. W. Smith, "The transverse thermomagnetic effect in nickel and cobalt," *Physical Review*, vol. 33, oct 1911.

[136] W. Chen, J.-M. L. Beaujour, G. de Loubens, A. D. Kent, and J. Z. Sun, "Spin-torque driven ferromagnetic resonance of Co/Ni synthetic layers in spin valves," *Applied Physics Letters*, vol. 92, jan 2008.

[137] A. Bose and A. Tulapurkar, "Recent advances in the spin Nernst effect," *Journal of Magnetism and Magnetic Materials*, vol. 491, jul 2019.

[138] D. M. Pozar, *Microwave Engineering*, vol. 1 of *1.* John Wiley Sons Inc., 4 ed., 2012.

[139] K. C. Gupta, R. Garg, I. Bahl, and P. Bhartia, *Microstrip Lines and Slotlines*, vol. 1 of *1.* Artech House, 2 ed., 1996.

Résumé

Les matériaux ferrimagnétiques de synthèse à aimantation perpendiculaire ont été étudiés extensivement lors de la dernière décennie. Leurs propriétés d'électronique de spin, notamment en ce qui concerne les propagations de parois magnétiques par l'injection d'un courant, en font des candidats idéaux pour les applications de mémoires magnétiques de type racetrack. Du fait de propriétés remarquables concernant d'une part la génération et le transport de courant de spin par couple de spin orbite, et d'autre part le couplage d'échange de type RKKY, l'iridium est un excellent candidat en tant que matériau de spacer pour les matériaux ferrimagnétiques de synthèse. Dans ce manuscrit, nous étudions des multicouches ferrimagnétiques de synthèse composées de deux couches de cobalt séparées par un spacer d'iridium. Nous présentons d'une part l'optimisation de la croissance de tels matériaux, de sorte à obtenir un système modèle en vue d'applications pour des ≪ racetrack memories ≫. Nous maximisons ainsi le couplage d'échange antiferromagnétique entre les couches de cobalt et l'aimantation à rémanence. D'autre part, nous étudions les propriétés de transport de spin de l'iridium grâce à des méthodes de résonance magnétique par pompage en spin. Nous en concluons que les matériaux ferrimagnétiques de synthèse à base d'iridium sont des systèmes modèles pour la fabrication de ≪ racetrack memories ≫.

Mots clefs : couple de spin orbite, mémoires magnétiques racetrack, nanomagnétisme, couches minces, iridium , électronique de spin.

Abstract

Synthetic ferrimagnets with perpendicular magnetic anisotropy have been studied extensively in the past decades. Their outstanding properties in terms of spintronics, especially concerning the current-induced magnetic domain wall propagation lead us to contemplate them as promising candidates as materials for magnetic racetrack memories. Besides, considering the remarkable properties of iridium concerning the transport and the generation of pure spin currents by means of spin orbit torque, as well as its large RKKY coupling properties, this material seems to be an excellent material as a spacer for synthetic ferrimagnets. In this manuscript, we study magnetic multilayers composed of two magnetic layers of cobalt separated by an iridium spacer. We optimise the growth of these multilayers by choosing the most adequate thicknesses, so as to obtain a model system for racetrack memories applications. Thus, we maximise the antiferromagnetic exchange between the cobalt layers, and the remanence magnetisation. Besides, we study the spin current generation and transport properties of iridium by spin pumping ferromagnetic resonance means. We draw the conclusion that iridium-based synthetic ferrimagnets can be considered as model systems for racetrack memory technology.

Key words: Spin orbit torque, magnetic racetrack memory, nanomagnetism, thin films, iridium, spintronics.